Exotic Decay Measurements at the Experimental Storage Ring for Neutron Capture Processes

by

Guy Leckenby

Bachelor of Philosophy (Science), The Australian National University, 2017

A THESIS SUBMITTED IN PARTIAL FULFILLMENT OF
THE REQUIREMENTS FOR THE DEGREE OF

DOCTOR OF PHILOSOPHY

in

The Faculty of Graduate and Postdoctoral Studies

(Physics)

THE UNIVERSITY OF BRITISH COLUMBIA

(Vancouver)

December 2024

© Guy Leckenby 2024

The following individuals certify that they have read, and recommend to the Faculty of Graduate and Postdoctoral Studies for acceptance, the dissertation entitled:

> **Exotic Decay Measurements at the Experimental Storage Ring for Neutron Capture Processes**

submitted by **Guy Leckenby** in partial fulfillment of the requirements for the degree of **Doctor of Philosophy** in **Physics**.

Examining Committee:

Reiner Kruecken, Adjunct Professor, Physics and Astronomy, UBC
Supervisor

Iris Dillmann, Senior Researcher, Physical Sciences, TRIUMF
Co-supervisor

Jeremy Heyl, Professor, Physics and Astronomy, UBC
Supervisory Committee Member

Andrew MacFarlane, Professor, Physics and Astronomy, UBC
University Examiner

Douglas Bryman, Professor, Physics and Astronomy, UBC
University Examiner

Sarah Naimi, Researcher, IJCLab, Université Paris-Saclay
External Examiner

Additional Supervisory Committee Members:

Alannah Hallas, Associate Professor, Physics and Astronomy, UBC
Supervisory Committee Member

Alison Lister, Professor, Physics and Astronomy, UBC
Supervisory Committee Member

Abstract

The slow (s) and rapid (r) neutron capture processes are responsible for producing almost all elements heavier than iron. Both processes require a lot of nuclear data to make more reliable predictions, and heavy-ion storage rings provide unique methods for measuring nuclear masses and exotic decay modes that can play an important role in these processes. A prime example is bound-state β^- decay, where the β-electron is produced in a bound state of the decaying nucleus. This decay mode for highly-charged ions can currently only be measured at the Experimental Storage Ring (ESR) at the GSI Helmholtz Centre in Darmstadt, Germany.

This thesis describes the analysis of the bound-state β^- decay of fully ionised $^{205}Tl^{81+}$ at the ESR. ^{205}Tl is a particularly interesting isotope due to its applications in solar neutrino spectrometry and for dating the early Solar System. A bound β-decay half-life of 291^{+33}_{-27} days was measured, which is much longer than the value previously used in astrophysical models. The experimental half-life was used to extract the nuclear matrix element of this transition, which allows for the calculation of accurate astrophysical decay rates of ^{205}Tl and ^{205}Pb in the stellar plasma. This enables models of the s process in asymptotic giant branch (AGB) stars to provide accurate ^{205}Pb yields, which are essential for using ^{205}Pb as a cosmochronometer to date processes in the early Solar System. Specifically, this thesis reports on a preliminary determination of the collapse time of our Sun's parent molecular cloud using ^{205}Pb.

In complement, a heavy-ion detector called PLEIADES was constructed and commissioned at the ESR, which will be used to detect decay products leaving the storage ring acceptance. PLEIADES is a δE–E telescope that uses silicon pads to measure the ion energy loss and a scintillator stopper to measure the total ion energy. It was commissioned with a ^{208}Pb beam at the ESR, and achieved a full-width half-maximum resolution of $\delta Z = 0.66$ for proton number and $\delta A = 1.14$ for mass. PLEIADES and its predecessor CsISiPHOS will be used as multi-purpose detectors for future measurements in the ESR.

Lay Summary

The chemical elements are created in very hot and energetic locations like the centre of stars and their explosive deaths. In these violent conditions, nuclear reactions create new nuclei. Newly created nuclei can spontaneously change their composition, which is called nuclear decay. Understanding nuclear reactions and decay pathways allows us to explain the origin of the elements.

Heavy-ion storage rings are machines that confine charged nuclei in a circular orbit, where nuclear properties and decay lifetimes can be measured. This thesis reports on the measurement of an exotic type of decay of the thallium-205 nucleus that only occurs in the core of stars, and explains how this measurement is integral for predicting the collapse time of the gas and dust that formed our Solar System. Additionally, the construction of a new particle detector is reported, which will be used for future measurements to understand how the elements were created.

Preface

The work presented in this thesis has been heavily collaborative. All of the text of this thesis is of my own formulation, none of the text has been taken directly from previous or published work, and no generative AI models were used. Where figures are reproduced or inspired from published work, the source and copyright is indicated in the caption.

The experiment presented in Chapter 3 was only possible due to relentless work of many people over the 30 years before I started this thesis work. Some key individuals include F. Bosch, G. Münzenberg, F. Nolden, H. Geissel, P. Kienle, K. Takahashi, and Y.A. Litvinov. I was one of three early career scientists who worked on the data analysis, the other two being R.S. Sidhu (at the time a PhD candidate) and R.J. Chen. R.S. Sidhu and R.J. Chen worked collaboratively to lay the groundwork for the analysis, handling the Schottky data analysis and constructing the methods for most of the corrections. I initially worked on the charge-changing cross-section ratio, which used the CsISiPHOS detector. Later I helped iterate the corrections to be more statistically robust, and developed the Monte Carlo analysis to extract the final bound-state β^--decay rate of $^{205}\mathrm{Tl}^{81+}$. Throughout the analysis, we consulted heavily with the E121 analysis group, which featured J. Glorius, R. Gernhäuser, Y.A. Litvinov, I. Dillmann, M.S. Sanjari, and C.J. Griffin.

The astrophysical impact presented in Chapter 4 has been published in Leckenby *et al.* (2024), *Nature* **634**:321–326. The astrophysical weak decay rates discussed in Section 4.2 were calculated by our GSI theory colleagues R. Mancino, G. Martínez-Pinedo, T. Neff, and K. Langanke. Of the AGB models discussed in Section 4.3, the Monash models were implemented by M. Lugaro, B. Szányi, and A.I. Karakas; the FUNS models were implemented by S. Cristallo and D. Vescovi; and the NuGrid models were implemented by U. Battino. Section 4.4, 4.5, and 4.6 presents my literature summary that expands on the Methods section of our *Nature* paper written by M. Lugaro. The calculation of the isolation time distributions was done by me with guidance from M. Lugaro and A. Yagüe Lopéz. Thanks also go to K. Takahashi, B. Meyer, and M. Pignatari for enlightening discussions throughout the analysis process. Figures 4.1, 4.2, 4.7 and Table 4.3 were created by myself, and are reproduced directly from Leckenby *et al.* (2024), *Nature* **634**:321–326.

The construction and commissioning of PLEIADES described in Chapter 5 was primarily done C.J. Griffin and myself. The design philosophy was developed by A. Najafi, R. Gernhäuser, and I. Dillmann prior to the start of this thesis work. C.J. Griffin and I assembled all the detector components with assistance from many technical staff at TRIUMF and GSI; they are thanked by name in the acknowledgements. The commissioning experi-

ment at GSI was conducted by C.J. Griffin, I. Dillmann, J. Glorius, and myself. N. Kurz provided assistance in assembling the data acquisition setup. I wrote the data analysis software, with support from J. Adamczewski-Musch, and I analysed the commissioning data.

The experiment and analysis described in Chapter 3 has led to four publications:

1. G. Leckenby, R.S. Sidhu, R.J. Chen, Y.A. Litvinov, J. Glorius, C.J. Griffin, I. Dillmann, and the E121 Collaboration, "Analysis methods to determine the bound-state beta-decay half-life of Thallium-205." *EPJ Web of Conferences* **279**:06010 (2023). I wrote the proceedings, which covered a basic description of the experiment and some of the analysis corrections mentioned above.
2. G. Leckenby, R.S. Sidhu, R.J. Chen, R. Mancino, B. Szányi, *et al.* "High-temperature ^{205}Tl decay clarifies ^{205}Pb dating in early Solar System." *Nature* **634**:321–326 (2024). M. Lugaro, Y.A. Litvinov, and I wrote the manuscript. R. Mancino, G. Martínez-Pinedo, and I. Dillmann also contributed to the Methods section. The breakdown of the work presented is described above when addressing Chapter 4.
3. R.S. Sidhu, G. Leckenby, R.J. Chen, R. Mancino, Y.A. Litvinov, G. Martínez-Pinedo, *et al.* "Bound-state beta decay of ^{205}Tl^{81+} ions and the LOREX project." *Physical Review Letters* **133**:232701 (2024). R.S. Sidhu and R. Mancino wrote the manuscript, with edits from myself. I contributed to the Supplementary material.
4. R.J. Chen, G. Leckenby, R.S. Sidhu, J. Glorius, M.S. Sanjari, *et al.* "Half-life determination with included feeding and depleting background processes in a heavy-ion storage ring." Submitted (2024). R.J. Chen and R.S. Sidhu wrote the manuscript, with edits from myself.

The work presented in Chapter 5 on the PLEIADES detector is under preparation for publication, and the manuscript is being written by C.J. Griffin with edits from myself.

In addition to the work described in this thesis, I have also participated in radioactive beam experiments at TRIUMF, Vancouver and GSI, Darmstadt, which have led to publications. However, they are not described in this thesis.

Table of Contents

Appendices

List of Tables

List of Figures

List of Abbreviations

ADC	analogue-to-digital converter
AGB	asymptotic giant branch
CCSNe	core-collapse supernovae
CEMP	carbon-enhanced metal-poor
DAQ	data acquisition
DCCT	DC current transformer
DSSD	double-sided silicon strip detector
ESS	early Solar System
ESR	Experimental Storage Ring
FFT	fast Fourier transform
FPGA	field programmable gate array
FRS	Fragment Separator
GCE	galactic chemical evolution
GMC	giant molecular cloud
ISM	interstellar medium
MACS	Maxwellian-averaged cross section
MWPC	multi-wire proportional chamber
NME	nuclear matrix element
NTCAP	new time capture
PCB	printed circuit board
REC	radiative electron capture
RF	radiofrequency
SiPD	silicon photodiode
SLR	short-lived radionuclide
TDU	third dredge-up
UNILAC	Universal Linear Accelerator
UHV	ultra-high vacuum

Acknowledgements

Firstly, I would like to acknowledge that this thesis work was conducted at TRIUMF on the traditional, ancestral, and unceded territory of the Musqueam People.

My deepest gratitude goes to my research supervisor Dr. Iris Dillmann, your patience with my perfectionist tendencies and focused feedback has made me a better scientist. Thank you to Dr. Reiner Kruecken for your academic supervision, even through your move south of 49^{th} parallel. Many thanks to my supervisory committee, Prof. Alannah Hallas, Prof. Alison Lister, and Prof. Jeremy Heyl, for challenging and supporting me over the years. Thank you to my external examiner Dr. Sarah Naimi for your kind words and helpful feedback. Also thanks to my two university examiners, Prof. Doug Bryman and Prof. Andrew MacFarlane for reading my manuscript and for the engaging questions that made my defence a pleasure.

Throughout this PhD, I was lucky enough to have mentors on both sides of the Atlantic. Special thanks to Prof. Yuri Litvinov for your wisdom, humility, and desire to put your early career researchers first. Many thanks to Dr. Jan Glorius, your generosity without hesitation has made this research possible. Thank you to Dr. Mohammed Shahab Sanjari, Dr. Roman Gernhäuser, Dr. Thomas Faestermann, and Dr. Uwe Spillmann for your technical support and friendship whilst in Darmstadt. To Dr. Ragandeep Singh Sidhu and Dr. Rui Jiu Chen, thank you for putting up with my perfectionism and endless debates across the years of analysis, I hope you agree with me that it was worth it in the end! Immense thanks to Dr. Maria Lugaro for your enthusiasm, I really had a lot of fun getting into the weeds of the astrophysics. Thanks also to Prof. Gabriel Martínez-Pinedo for your attention to detail, our paper is significantly better for it. Thank you to Dr. Riccardo Mancino, Dr. Sergio Cristallo, Dr. Umberto Battino, Dr. Marco Pignatari, Dr. Diego Vescovi, Balázs Szányi, Prof. Bradley Meyer, Dr. Amanda Karakas, and Dr. Andés Yagüe Lopéz for your commitment and making our collaboration such a breeze, it was a pleasure.

Heartfelt thanks to the GSI accelerator teams for enabling such amazing science! Special mention must go to the FRS and ESR wizards, Dr. Helmut Weick and Dr. Markus Steck. Another special thank you to Dr. Beatriz Jurado for generously providing us with a shift during her experiment to test our detector. Many thanks to Dr. Nikolaus Kurz for your patient support with FEBEX, and to Dr. Jörn Adamczewski-Musch for the best coding support anyone could ever hope for. Thank you to Davide Racano for graciously handling our last minute machining requests for the pocket holding structure. Last but definitely not least, thank you to Lea Wunderlich for always making GSI feel like a second home!

At TRIUMF, many thanks to the technical staff who made PLEIADES possible. In particular, thank you Shaun Georges for engineering guidance on the housing design, thank you Dr. Nicolas Massacret for showing us the wonders of wirebonding, and thank you Daryl Bishop for your assistance with PCB construction. To Dr. Greg Hackman, thank you for always picking up my late night calls, sometimes the LN2 system just needs your gentle touch. Endless thanks goes to the GAPS members who made TRIUMF a community I wanted to turn up for and give back to. To name just a few, thank you Louis Croquette, Dr. Daniel Yates, Dr. Chris Chambers, Dr. Helena Koniar, Heinz Asch, Maeve Cockshutt, and many more for your friendship and smiles around the lab!

Over the course of my PhD, I was given several opportunities to develop my teaching skills for which I am very grateful for. In particular, thank you to Dr. Joss Ives and Dr. Georg Rieger for giving me a chance to challenge myself! Thanks also to Dr. Adele Ruosi for your kindness and support, you are a pleasure to work with.

To my friends at Green College, we were separated too soon, but I look forward to catching up in the future. Especially to my long lost greenies Caleb Marshall and Rodney Stehr, I miss you! To Yotam Ronen and Noga Vieman, thank you for your wicked humour, delicious treats, and tough love, you keep Vancouver 'hot grape' spicy! To Cheryl Ng, Rosalie Gunawan, Erin Socholotiuk, and Justin Sze, thank you for sharing the joy of climbing rocks with me. To Sam Porter, Dr. Michael Zurel, Gareth Smith, Ashley Warner, Lara Bartels, Tim Branch, Perrin Waldock and the rest of the physics MSc cohort who made grad school such a pleasure, thank you! To Megan Waldock, thank you for the chaos and letting me borrow the brain cell when I need it most; you can add this citation to your physics CV.

To my housemates Emily Cadger, Hannah-Ruth Engelbrecht, Elaina Nguyen, and Jaye Sudweeks, my immense gratitude for all your kindness and support over the years. This thesis would not have been possible without the joy of coming home to our family every night. Thank you for making Vancouver a home! To my Australian family, my dearest parents Lisa Holley and David Leckenby, my brother Josh Leckenby, thank you for visiting my new home and welcoming me back when the winters got too dark over here. You helped me create this dream of a PhD when I was 12, and so much credit goes to your support over the years! Thank you also to my grandmother, Elaine Sherwood, for the best cheering squad a grandson could ever hope for.

And finally, saving the best for last, thank you to my primary partner in crime, adventure, and science, Dr. Chris Griffin. May there always be one last Schweinshaxe...

Chapter 1

Introduction

The essence and origin of the fundamental 'elements' of nature is a central question in understanding our reality. Modern science has allowed us to definitively answer these questions. We now know that our world is constructed of atoms, at the centre of which are atomic nuclei, whose elemental character is determined by the number of protons in the nucleus Z. The field of nuclear astrophysics primarily aims to describe the events that create the variety of atoms we observe in the world around us. This requires understanding both the nuclear physics that defines the microscopic interactions, the astrophysics of the events that generate and sustain these nuclear reactions, and the interplay between them.

Nuclear fusion as the energy source at the cores of stars was first proposed by Eddington in 1920 [1]. The specific details on the fusion of four protons into helium as the primary fuel source was then established by Bethe [2] and Weizsäcker [3, 4] in the late 1930s. Fusion beyond helium and up to iron was largely pioneered by Hoyle in the late 1940s [5, 6]. Finally, the processes behind the synthesis of the heavy elements was outlined in the works of Burbidge, Burbidge, Fowler, & Hoyle (1957) [7]—commonly referred to as B^2FH—and Cameron (1957) [8]. These seminal works established the astrophysical processes that create the elements, and the underlying physical principles of their description are still accurate to this day. However, in the last 67 years, enormous work has been done uncovering the details of these processes, which has lead to a very rich understanding of the depth and diversity of events that shape the elemental distribution we see today.

This thesis aims to describe how heavy-ion storage rings are being used to investigate exotic β-decay modes that play crucial roles in a variety of nucleosynthesis processes. First, the fundamentals of stellar evolution, heavy element nucleosynthesis, and nuclear β decay are presented in the introduction. Then, the experimental methods of storage rings are introduced in Chapter 2. A summary of the data analysis of the measurement of the bound-state β decay of $^{205}Tl^{81+}$ at the Experimental Storage Ring (ESR) at GSI, Darmstadt, is given in Chapter 3. This experiment is an excellent example of how storage rings are uniquely capable of measuring exotic decay modes like bound-state β decay. The astrophysical impact of this measurement on early Solar System studies is discussed in Chapter 4. In addition to the experimental analysis, a particle detector was constructed for the ESR that will be used in future exotic decay experiments. The construction and commissioning of this PLEIADES detector is outlined in Chapter 5. Finally, the conclusion summarises the contributions of this thesis to heavy-ion storage ring methods, and how they can help us understand the nucleosynthetic process that shape our galaxy.

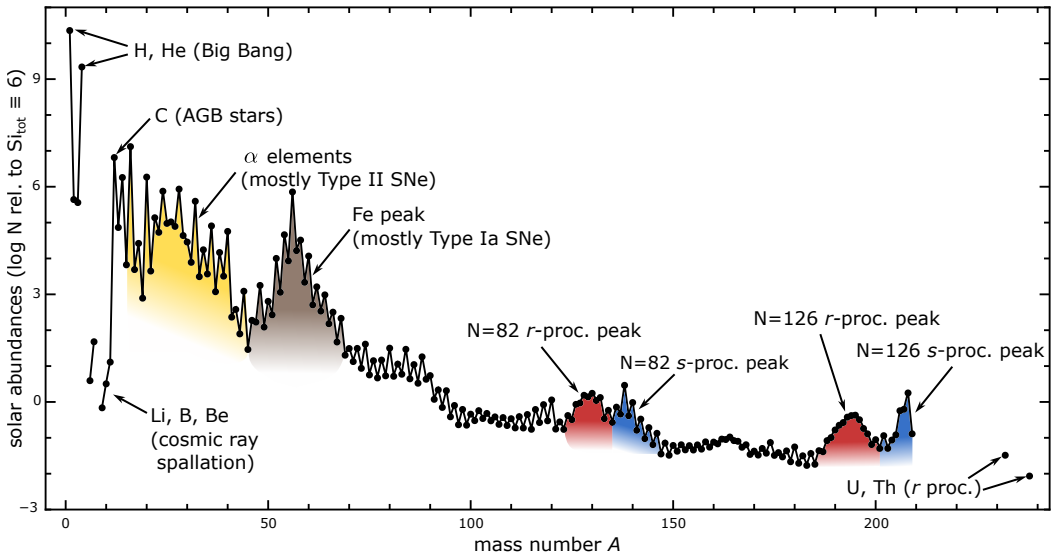

Figure 1.1: The dominant astrophysical sites associated with the solar abundance distribution. Isotopic solar abundances are from Lodders *et al.* (2003) [13] relative to 10^6 stable Si atoms. Figure inspired by Diehl *et al.* (2022) [14].

1.1 The abundances of chemical elements

When nuclear astrophysicists try to describe the origin of the chemical elements, the distribution that we repeatedly turn to are the solar abundances. Shown in Figure 1.1, the solar abundances are such a reliable guide in understanding the chemical richness of our galaxy because they are determined very accurately from absorption lines in the Sun's light and from the isotopic composition of meteorites that fall to Earth [9–12]. The absorption lines in solar light originate at the surface of the Sun—the photosphere—and the intensity of solar light provides a very detailed spectrum to which the underlying abundances can be fit. Meteorites provide complementary data as the isotopic ratios of certain heavier elements can be determined much more accurately by mass spectrometry. The solar abundances are representative of the interstellar gas from which the Solar System formed, both because the Sun contains 99% of the mass in the Solar System and we know that the Sun has not polluted the solar abundances through nuclear reactions since it is still undergoing hydrogen burning.

The fact that the abundances span over 12 orders of magnitude indicates that a variety of sources must have contributed, each with very different probabilities. The scale of the contribution from each source is evident in the abundances themselves. Big Bang nucleosynthesis happened everywhere throughout the universe, and thus unsurprisingly dominates the abundance chart with values of $\sim 10^{10}$. Burning processes in stars and

the supernova explosions from their deaths occurs regularly throughout the galaxy, and thus abundances from carbon up to iron form the next grouping with values of 10^{2-7}. Finally heavy element production—powered by neutron capture processes—occurs in rare scenarios and thus produces the smallest abundances of $10^{(-2)-1}$. Galactic cosmic-ray spallation provides another rare production process for several light elements that are not produced by stellar burning.

Whilst the solar abundances provide a detailed picture of the chemical diversity across the entire nuclear chart, the Sun formed from a specific parcel of gas and dust at a specific time and location in the galaxy. But because the solar material was enriched by many generations of nucleosynthetic events, the overall abundance distribution is broadly representative of the galaxy at large and the physical processes that contributed. By combining the production abundances and frequencies of the various nucleosynthetic events with observed galactic constraints on parameters like star formation, gas inflow, etc., a consistent story of galactic chemical evolution can be assembled by modelling the Milky Way from its birth [15–19]. Doing so allows us to provide a testable prediction of the solar abundances, ensuring we fully understand the origin of the chemical elements.

1.2 Stellar evolution

Big Bang nucleosynthesis produced the majority of ordinary matter in the universe as the hot soup from the Big Bang cooled to form predominantly 75% ^{1}H and 25% ^{4}He [20, 21]. The subtle inhomogeneities left behind by the Big Bang caused the gas to collapse under gravitational attraction forming the earliest stars and galaxies. A cloud of gas that collapses will heat up as gravitational potential energy is converted into thermal pressure, which then counterbalances the gravitational pull establishing *hydrostatic equilibrium*. If the temperature in the core becomes high enough to overcome the Coulomb repulsion between nuclei (the Coulomb barrier), nuclear fusion reactions will begin. The energy generated by fusion provides additional thermal pressure that sustains the hydrostatic equilibrium whilst there are nuclei available to fuse, and this process is called *hydrostatic burning*.

Species in a stellar plasma follow a Maxwell-Boltzmann distribution,[1] so there are overwhelmingly more nuclei available to fuse via quantum mechanical tunnelling than to cross the Coulomb barrier directly. It is the product of the Maxwell-Boltzmann population versus the tunnelling penetration at that energy that defines the probability for fusion to occur, and the region of astrophysically relevant energy/temperature where this probability is maximised is called the *Gamow window*.

[1] Because the mean energy of a thermalised plasma can be directly related to the temperature by the Maxwell-Boltzmann distribution, the energy and temperature of the stellar plasma are often used interchangeably and are related by $kT = 86.173\,T_9$ keV, where $T_9 = T/10^9$ is the temperature in GK.

1.2.1 Stellar burning

Nuclear pairs with the smallest Coulomb repulsion will be the first to fuse as they can achieve the Gamow window at the lowest temperatures. As a result, hydrogen burning is the first stage that stars of all masses go through and where they spend the bulk of their lifetime. There are two main methods for burning hydrogen: the *pp*-chains and the CNO cycles. The *pp*-chain requires lower temperatures to initiate burning than the CNO cycle, but are much slower because the first step is *pp*-fusion ($p + p \rightarrow d + e^+ + \nu_e$), which is mediated by the weak interaction [22, p.336]. After *pp*-fusion, the next few steps of the *pp*-chain come in three different flavours, *pp*-I/II/III, with the dominant chain depending on the temperature [23, p.368]. The CNO cycles are a set of *catalytic* nuclear reactions involving C, N, O, and F isotopes that process hydrogen burning via a series of (p, γ) and (p, α) reactions, alongside weak decays, that form closed cycles. Whilst requiring a higher initial temperature, the CNO cycles are much more temperature sensitive than the *pp*-chains, so they dominate hydrogen burning for high mass stars with higher core temperatures. Because the CNO cycles require some CNO abundance, their efficiency scales directly with metallicity.[2]

As hydrogen burning proceeds, ^{4}He ashes accumulate in the core of the star forming an inert core surrounded by a hydrogen burning shell. This core is supported by the *electron degeneracy pressure*, which is the pressure produced by electrons when compressed into a small volume such that they are forced to occupy high momentum states by the Pauli exclusion principle [22, p.105]. For stars of $< 0.5 M_\odot$ ($M_\odot$ = solar mass), the electron degeneracy will support the star's mass as hydrogen burning ends and the star will cool into its white dwarf phase, although this takes trillions of years for such light stars.

For stars of mass $> 0.5 M_\odot$, the accumulation of helium ashes causes the core to contract until the temperature increases to $T > 100$ MK. At this temperature the triple-α (3α) process—the dominant reaction in *helium burning*—becomes possible as the high temperatures establish an $\alpha + \alpha \rightleftharpoons {}^8\text{Be}$ equilibrium for the highly radioactive ^{8}Be that allows a third α particle to be captured via $^8\text{Be}(\alpha, \gamma)^{12}\text{C}$. The 3α process then provides ^{12}C seeds for the next α-capture reaction $^{12}\text{C}(\alpha, \gamma)^{16}\text{O}$, that only partially consumes the produced ^{12}C. For stars of mass 0.5–$7 M_\odot$, hydrostatic helium burning will proceed until helium is exhausted in the core, leaving behind an electron-degenerate C-O core. After this, hydrogen and helium burning will still alternate in onion-layered shells around this core. Stars in this phase are called asymptotic giant branch (AGB) stars, and will be discussed in much more detail in Section 1.4.2 as an important site for the slow neutron capture process. Stars with mass 7–$10 M_\odot$ are hot enough ($T > 0.3$ GK) for the $^{16}\text{O}(\alpha, \gamma)^{20}\text{Ne}$ and $^{20}\text{Ne}(\alpha, \gamma)^{24}\text{Mg}$ reactions to also proceed, in addition to a final stage of carbon burning, leaving behind a degenerate O-Ne core [24]. The strong stellar winds during the AGB phase eventually

[2] Because the universe's mass is primarily dominated by H and He, astronomers refer to all other elements as *metals*. When we refer to the *metallicity* of an object, this describes the abundance proportion of metals. Low metallicity therefore refers to objects dominated by primordial H and He.

blow away the stellar envelope forming a planetary nebula and the degenerate core is left behind as a white dwarf.

1.2.2 Massive stars

Stars with mass $\gtrsim 10M_\odot$ will go through the same hydrogen and helium burning phases, but the pressure will be high enough that the contraction of the core will cause advanced burning stages that are ignited successively using the ashes of previous burning phases as fuel. The primary energy source for each phase will be the named reaction, e.g. ^{12}C fusion for carbon burning, but the phase features a complicated network of nuclear reactions across many species. As the fuel in the core is exhausted, burning will continue in a shell as the core contracts until the next phase is ignited, proceeding through carbon burning, neon burning, oxygen burning, and silicon burning, leaving behind an iron group core. Beyond the iron group, fusion can no longer provide a source of energy as these nuclei are the most tightly bound on the nuclear chart (specifically ^{56,58}Fe and ^{62}Ni). Thus, a massive star in its final stages forms a "stellar onion" where successive burning continues in many layered shells around a growing iron-group core.

Advanced burning will continue until the iron-group core accrues enough mass that the electron-degeneracy pressure can no longer support the gravitational attraction of the star. The mass at which this occurs is $\approx 1.4M_\odot$ and is called the *Chandrasekhar mass limit*. At this point the core will collapse and the matter free falls until the nucleons encounter the hard, repulsive component of the nuclear force. This repulsion acts like a stiff spring causing the matter to bounce back and generate a shock wave that propagates back outwards through the core, igniting a *core-collapse supernova* (CCSN) explosion that ejects the outer layers of the star back into the interstellar medium (ISM). Depending on the mass of the star, the core is left behind as either a neutron star or a black hole.

Understanding massive star structure and supernovae are essential to understanding the synthesis of elements around the iron peak because they not only provide a mechanism to eject the advanced burning products of massive stars back into the ISM, but the shock wave itself changes the composition of the burning ashes via explosive nucleosynthesis. In particular, as the shock wave moves through the layers of the star, it provides energy to initiate partial explosive burning that reprocesses the stellar material before it is ejected into the ISM [23, p.446].

Whilst core-collapse supernova of massive stars accounts for about half of iron-peak abundances, the other half originates from type-Ia supernovae [25, p.74], i.e., the explosion of C-O white dwarfs. As the white dwarf acquires mass—either from a companion star or via some stellar merger—and approaches the Chandrasekhar limit, the carbon ignites under degenerate conditions causing a thermonuclear runaway supernova. Despite identifying white dwarfs as the progenitors for type-Ia supernovae over 60 years ago [26], modelling and observations of type Ia supernovae is still a very active field [27].

1.3 Heavy element nucleosynthesis

Nuclear fusion is no longer exothermic beyond the iron group, and progressively larger Coulomb barriers prevents the charged-particle fusion of heavier elements, even in the most violent astrophysical scenarios. Neutrons, however, do not need to battle the Coulomb barrier, and thus neutron capture cross sections remain relatively constant along the valley of stability (within 2 orders of magnitude). As a result, the successive capture of neutrons on iron-group seeds provides the mechanism for producing elements beyond iron.[3] This thesis focuses on the measurement and impact of exotic β decay for heavy element nucleosynthesis, so this section provides a detailed review, focusing on the slow neutron capture process.

B^{2}FH [7] established the two, very different types of neutron capture processes that dominate heavy element production. In particular, they observed the accumulation of abundances around the stable neutron shell closures[4] with a distinct double peak feature, as labelled in Figure 1.1. Whilst the peaks directly at the neutron shell closures indicate a neutron capture process proceeds along the valley of stability, the peaks at ~ 10 mass units lower indicate that a neutron capture process must proceed through very neutron-rich nuclei that then β decayed back to stability. Such neutron-rich nuclei could only be sustained at very high neutron densities. The two processes were identified as the "slow" (s) and "rapid" (r) neutron capture process, where slow/rapid refers to the rate of neutron capture with respect to β decay. Through this comparison to β-decay rates across the nuclear chart, it was inferred that each process must have neutron densities of $n_n \approx 10^8$ cm^{-3} and 10^{21} cm^{-3}, respectively [23, p.504].

The s- and r-process paths are plotted in Figure 1.2, where the start of the s-process path is highlighted. The s process proceeds along the valley of stability via successive neutron captures until an unstable nucleus is reached, at which point it β decays back to stability. In a handful of isotopes, the neutron-capture rate is approximately equal to the β-decay rate, and these are called *branching points* because the s-process path splits as the two channels compete. The r process proceeds through neutron-rich nuclei, who then decay back to stability during *freeze out* after the neutron source is exhausted, so the β-decay chains arrive diagonally at the valley of stability. These characteristic paths mean that whilst most stable isotopes are produced by both the s and r processes, some isotopes are produced exclusively by the s or r process. In particular, s-only isotopes are shielded from r-process production by lower-Z isobars, whilst r-only isotopes are protected from the s-process path by breaks in the neutron capture chain.

[3] Note that unlike fusion reactions, neutron captures do not produce enough heat to sustain nuclear environments, and additionally free neutrons decay to protons with a half-life of $T_{1/2} = 10.16(1)$ minutes [28], so any neutron capture process requires a neutron source to proceed.

[4] The proton/neutron shell closures refer to specific nucleon numbers (2, 8, 20, 28...) associated with large energy gaps to the next nuclear state that make nuclei at or near these numbers much more bound than other nuclei.

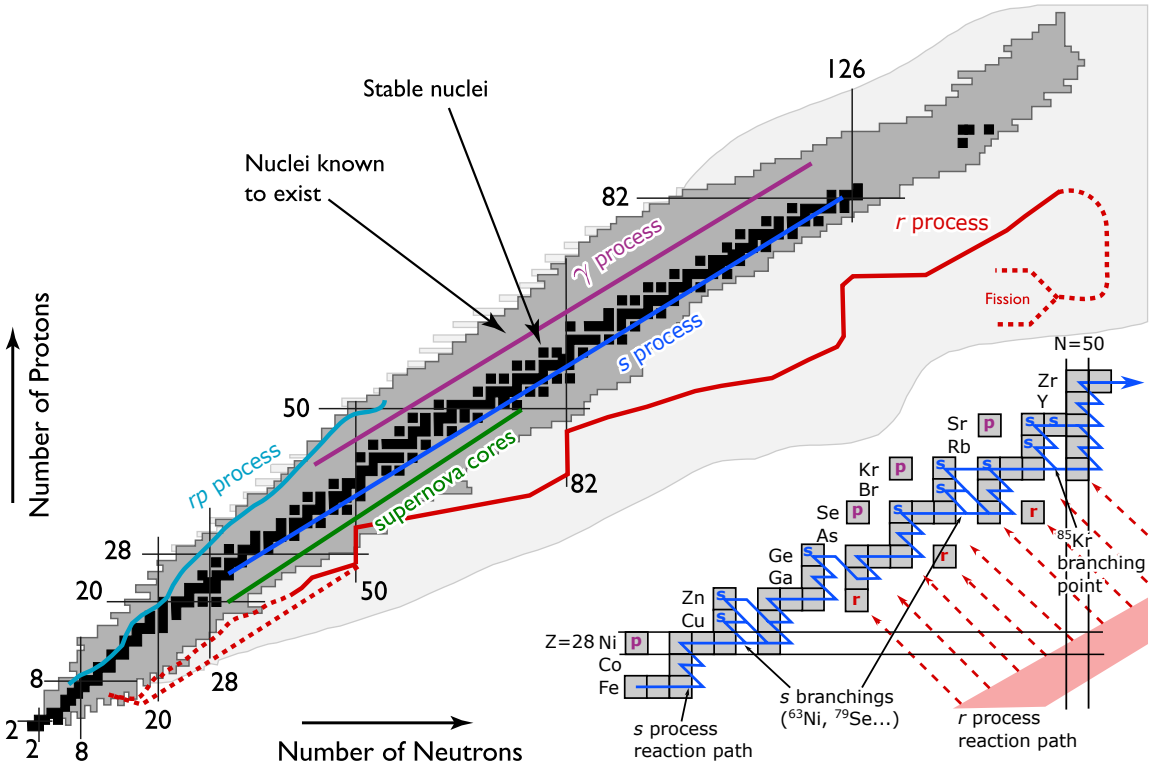

Figure 1.2: The heavy element nucleosynthesis process paths are plotted on the nuclear chart. The *s* process follows the valley of stability. The *r* process can start on a variety of seeds (dashed path), and then proceeds through very neutron rich nuclei before recycling through fission. The γ process starts on heavy seed nuclei and proceeds down the neutron-deficient side via photodissociation. The *rp* process occurs in explosive burning with rapid proton capture on light nuclei up the neutron deficient side of the chart. Figured reproduced from cococubed.com.
Inset: The *s*- and *r*-process' unique paths produce *s*- and *r*-only nuclei that are crucial in constraining the processes. The *p* nuclei are isolated from production by both neutron capture processes. Figure inspired by Käppeler (1999) [29].

These *s*- and *r*-only isotopes are crucial in constraining the separate contributions of each process to the overall abundance pattern, as well as the astrophysical sites where they can occur. Because the *s*-process abundances can be so well constrained due to the extensive nuclear data available around the valley of stability, the *r*-process contribution to the solar abundances can be derived by $N_r = N_\odot - N_s$ (shown in Figure 1.3). The fact that two processes as different as the *s* and *r* processes contribute roughly equally across the entire span of the heavy elements is quite remarkable. The *s* process is discussed in detail in the following Section 1.4.

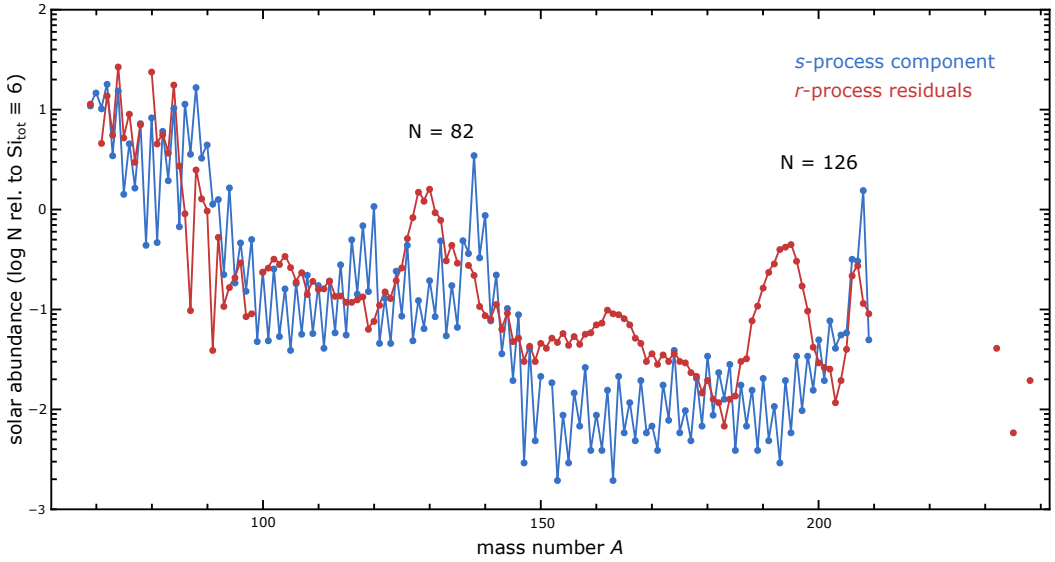

Figure 1.3: The decomposition of the heavy-element solar abundances by Sneden *et al.* (2008) [30].

1.3.1 The *r* process

Neutron capture in the r process proceeds very rapidly such that highly neutron-rich nuclei are produced. The Q value for neutron capture, which is equivalent to the *neutron separation energy* S_n, decreases along isotopic chains as the neutrons become less bound. Eventually, S_n drops to zero at which point additional neutrons are no longer bound, and this point defines the *neutron drip-line*. Rapid neutron capture is eventually counterbalanced before isotopic chains reach the neutron drip-line, although the specific mechanism depends on the temperature. In hot r processes, the inverse photodissociation reaction establishes an equilibrium with the neutron captures, whereas in cold r processes, the β decays directly compete with the neutron captures. Modern r-process simulations explicitly handle this competition by numerically solving large nuclear-reaction networks along temperature and density trajectories from astrophysical simulations [31, 32].

At the neutron shell closures, the neutron-capture cross-section beyond the shell closure is small as the extra neutron is weakly bound, so the abundance flow builds up along these neutron shell closures, as shown in Figure 1.2. This abundance accumulation at the shell closures generates the r process peaks clearly visible in Figure 1.3. If the r-process lasts sufficiently long, the r-process path will extend beyond the $N = 184$ neutron shell closure and a variety of fission channels will produce several fragments in the $A \sim 110$–170 region in what is called *fission recycling* [31, 33]. Finally, during the r-process freezeout when the neutron-rich nuclei decay back to stability, the β decay may populate states in the daughter nucleus that are above the neutron separation energy, causing a β-delayed neutron emission

that shifts the mass chain one step lower.

The astrophysical site of the r-process is still uncertain. Binary neutron star and neutron star-black hole mergers have long been suggested as a site for the r-process due to the high neutron densities available in the merger dynamics [34]. Both hot and cold r processes are achieved in different components of the merger. The first gravitational wave detection of a binary neutron star merger (GW170817) by the Advanced LIGO and Virgo collaborations [35], alongside the electromagnetic follow-up of the kilonova [36], confirmed that an r-process took place due to the presence of lanthanide emission in the kilonova lightcurve [37]. However, current Bayesian analyses of the rate of compact remnant mergers now favour a significant contribution from exotic types of supernova explosions, with multiple sources acting at different galactic times [38]. Whilst regular core-collapse and type Ia supernova seem unable to produce neutron-rich conditions, some exotic supernova featuring strong magnetic fields ($> 10^{15}$ G), rapid core rotation, or very high accretion rates ($\sim 0.1 M_{\odot}$ s^{-1}) may produce r-process conditions. Cowan *et al.* (2021) [34] provide a detailed a review of the current state of the r process.

1.3.2 The p processes

The roughly 1% of heavy nuclei that cannot be produced by either the s- or r-process are called "p-nuclei," since they lie on the proton-rich side of the nuclear chart [7, p.615]. Several processes are need to adequately explain the p-nuclei. The predominant mechanism for producing p-nuclei over the whole mass range is the photodisintegration of preexisting s- and r-nuclei in what is called the γ process [39]. The required temperatures to produce a bath of photons with enough energy to disintegrate stable nuclei via (γ, n), (γ, p), and (γ, α) reactions are achieved in supernova explosions, both in core-collapse and type Ia supernovae [40]. However, the γ process cannot produce the most abundant p-nuclides, in particular ^{92,94}Mo and ^{96,98}Ru, and so the νp process is also thought to contribute, where the highly proton-rich environment of the neutrino-driven wind in a CCSN drives rapid proton captures on seed nuclei produced in the explosion [41]. However, both of these processes still require more research to reach a satisfactory explanation of the p nuclei.

1.3.3 The i process

Whilst the s, r, and p processes are all required to explain the solar abundances, an "intermediate" neutron capture process (i process) has been suggested [42] to explain peculiar abundances in carbon-enhanced metal-poor (CEMP) stars that cannot be generated by combinations of the s or r process [43]. The i process would operate at intermediate neutron densities of $\sim 10^{13-15}$ cm^{-3}, which runs along a path a few mass units off the valley of stability. Proposed astrophysical sites for the i process include the He shell flashes in (i) rapidly accreting white dwarfs [44], (ii) low-mass, low-metallicity AGB stars [45], and (iii) super-AGB stars [46].

1.4 The slow neutron capture process

A detailed review of the *s*-process will now be provided in order to understand the mechanics involved in the production of ^{205}Pb, discussed in Chapter 4. The basic principles of the *s* process outlined in B^{2}FH [7] are still valid today, despite there being little knowledge at the time of the neutron source or astrophysical environment. This phenomenological model is now called the classical *s* process, and it aimed to extract information about the astrophysical conditions from a purely mathematical description of the abundances.

1.4.1 The classical *s* process

For the classical *s* process, it is assumed that for most isotopes, the β-decay rate λ_β is much faster than the neutron-capture rate $\lambda_{n,\gamma}$. Under this scenario, B^{2}FH [7] stated that the abundance flow for a given isotope on the *s*-process path depends only on the neutron capture rate and the present/neighbouring abundance:

$$\frac{dN_s(A)}{dt} = \lambda_{n,\gamma}(A-1)\,N_s(A-1) - \lambda_{n,\gamma}(A)\,N_s(A), \tag{1.1}$$

where $N_s(A)$ is the *s* abundance at a given mass number A and $\lambda_{n,\gamma}(A) = n_n\langle\sigma v\rangle_A$ is the neutron capture rate dependent on the neutron number density n_n and the capture rate per particle pair $\langle\sigma v\rangle_A$ for a given A. Note that in this simple model, the *s* process takes a single path along the valley of stability, starting on the seed nucleus ^{56}Fe, so each mass number is uniquely defined, even if the flow to that mass number requires a β decay.

If we additionally assume that the temperature throughout the *s* process is constant, and note that the neutrons are thermalised following a Maxwell-Boltzmann distribution, then the capture rate per particle pair can be expressed in terms of the Maxwellian-averaged cross section (MACS) such that $\langle\sigma v\rangle_A = \langle\sigma\rangle_A\, v_T$. Here the MACS is defined as [47]:

$$\langle\sigma\rangle_A = \frac{\langle\sigma v\rangle_A}{v_T} = \frac{2}{\sqrt{\pi}(kT)^2}\int \sigma(E)\,E\,e^{-\frac{E}{kT}}\,dE, \tag{1.2}$$

where v_T is the mean thermal energy $v_T = \sqrt{2kT/\mu}$, μ the reduced mass, k the Boltzmann constant, T the temperature, and E the energy of relative motion between the neutron and nucleus.

With the mean thermal energy separated from the cross section, we can define the neutron exposure τ of an *s*-process event by

$$\tau = v_T\int n_n(t)dt \quad \text{or} \quad d\tau = v_t\,n_n(t)\,dt, \tag{1.3}$$

which is essentially the time-integrated thermal neutron flux $\phi_n = \frac{2}{\sqrt{\pi}} n_n\,v_T$ [23, p.506]. With some rearranging, this simplifies equation (1.1) to

$$\frac{dN_s(A,\tau)}{d\tau} = N_s(A-1,\tau)\langle\sigma\rangle_{A-1} - N_s(A,\tau)\langle\sigma\rangle_A. \tag{1.4}$$

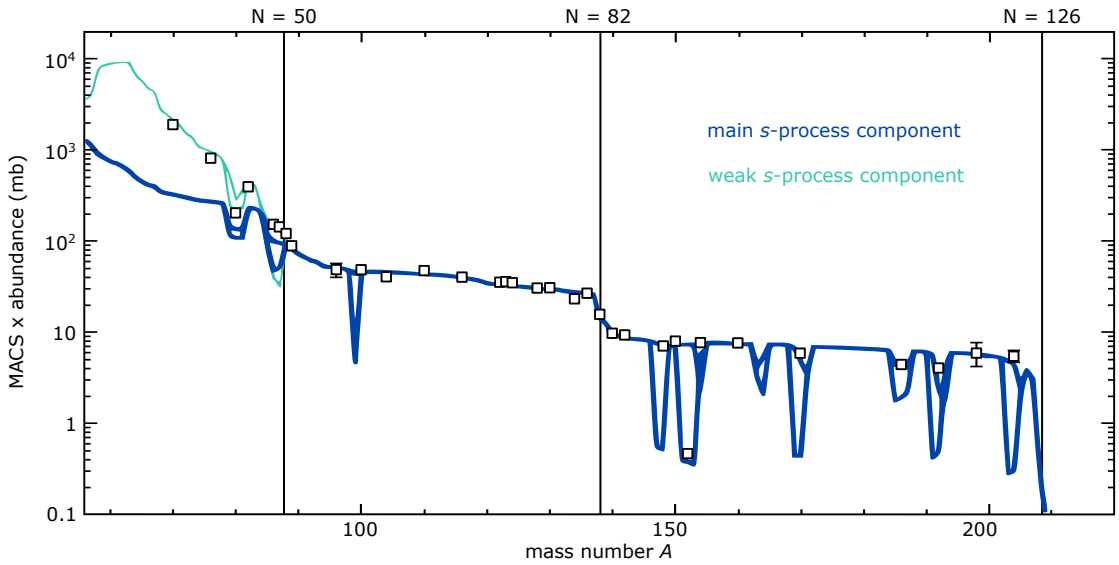

Figure 1.4: The characteristic product of the neutron capture cross section by the *s*-process abundance (normalised to a Si abundance of 10^6). The thick line shows the best fit of the main *s* process, whilst the thin line shows the weak *s* process. Splitting of the line represents the different branching points. The hollow squares are the *s*-only abundances to which the classical *s* process is fit. Figure reproduced from Käppeler (1999) [29].

These coupled differential equations are self-regulating in the sense that the abundance builds up until the destruction rate equals the production rate. For nuclei with similar MACS, which holds approximately for nuclei between the closed neutron shells, this results in a steady flow along the *s*-process path such that $N_s(A,\tau)\langle\sigma\rangle_A \approx$ constant. This observation was the key conclusion made in B^2FH [7], and as can be seen in Figure 1.4, it holds remarkably well for $A > 90$ between the neutron shell closures.

The fit in Figure 1.4 actually uses one minor adjustment; Clayton *et al.* (1961) [48] pointed out that a single neutron exposure does not accurately reproduce the solar abundances, so Seeger *et al.* (1965) [49] suggested an exponential distribution of neutron exposures, specifically of ^{56}Fe seeds having received a neutron exposure τ, that looks like

$$p(\tau) = \frac{G\,N_\odot(56)}{\tau_0}\,e^{-\frac{\tau}{\tau_0}}. \tag{1.5}$$

This seems physically reasonable for a set of abundances that has been processed through multiple events. Equation (1.5) contains just two parameters: the fraction G of seeds having experienced a non-zero neutron exposure and the mean neutron exposure τ_0. If we assume that the neutron density is constant across these exposures, then an analytic

solution for $\langle\sigma\rangle_A N_s(A)$ can be determined [50]:

$$\langle\sigma\rangle_A N_s(A) = \frac{G N_\odot(56)}{\tau_0} \prod_{i=56}^{A} \left(1 + \frac{1}{\tau_0 \langle\sigma\rangle_i}\right)^{-1}. \tag{1.6}$$

The fit in Figure 1.4 uses equation (1.6). If we ignore $A < 90$ and the branching point isotopes, it is able to reproduce the s-only abundances with a mean-square error of just 3% [51]. This is remarkably good for an analytic model that encodes the entire astrophysical history of the predicted abundances in just two parameters.

For the classical s-process, the success of equation (1.6) between $A = 90$–209 describes the so-called "main" s-process component. The best fit parameters are $G = 0.057(4)\%$ and $\tau_0 = 0.295(9)$ mb^{-1} for $kT = 29$ keV [51], and this suggests the main s process only irradiates 0.06% of the ^{56}Fe seeds we see in the solar abundances with an average number of neutron captures per seed at $n_c = 10.7(7)$.

Where this regime clearly fails is for $A < 90$, and B^{2}FH [7] actually predicted that this divergence indicated "that the abundances in the Solar System of s-process isotopes have been produced in more than one stellar synthesis process." This second component is called the "weak" s process, and can be described by a second fit to equation (1.6) with best fit parameters of $G = 1.6\%$ and $\tau_0 = 0.07$ mb^{-1} resulting in $n_c = 3$ [23, p.511]. This indicates a lower mean neutron exposure but a much higher number of seeds irradiated, when compared to the main s process.

Together, the main and weak s-process components describe the solar abundances quite well. However, whilst the total neutron exposure can be derived from this method, the overall fit to $\langle\sigma\rangle_A N_s(A)$ is not sensitive to the conditions of the s process. Instead, the branching points of the s process can be used to constrain the temperature and density. If we consider just a simple branching involving one isotope A, similar to ^{85}Kr in Figure 1.2, then the branching fraction is:

$$f_\beta \equiv \frac{N_s(A,\tau)\langle\sigma\rangle_A}{N_s(A+1,\tau)\langle\sigma\rangle_{A+1}} = \frac{\lambda_\beta}{\lambda_\beta + \lambda_{n,\gamma}} = \frac{\ln 2/T_{1/2}(A)}{\ln 2/T_{1/2}(A) + n_n \langle\sigma\rangle_A v_T}. \tag{1.7}$$

Rearranging gives the neutron density as

$$n_n = \frac{1 - f_\beta}{f_\beta} \frac{1}{\langle\sigma\rangle_A v_T} \frac{\ln 2}{T_{1/2}(A)}. \tag{1.8}$$

Thus with accurate abundance ratios, cross sections, and half-lives, a neutron density can be predicted for each branching ratio. Whilst the analytic solution gets slightly more complicated to handle multiple branchings, the triple branching of ^{147}Nd and ^{147,148}Pm was often used to extract the neutron density of the main s process [29, 52].

However, both the β-decay rate and the neutron-capture rate of some branching point nuclei can be temperature dependent. Low-lying nuclear excited states that have significantly different spin and parity to the ground state can be thermally populated in the

stellar plasma and alter the nucleus' properties. An interesting example is ^{79}Se, which has a $J^\pi = 7/2^+$ ground state with a half-life of 327(28) kyr, but a 96 keV, $1/2^-$ excited state with a half-life of just 3.9 minutes [53]. Thermal population of this state determines the overall half-life, so if the neutron density is constrained by another branching point (e.g. ^{85}Kr), then the ratio of s-only isotopes ^{80,82}Kr can constrain the temperature of the s process [54] (see Figure 1.2 for this case). Thus, by building up a set of branching points, a systematic study can constrain the allowed values of the neutron density and temperature at which the classical s process took place (both assumed to be constant). The values provided by Käppeler *et al.* (1999) [29] are $n_n = 4.1(6) \times 10^8$ cm^{-3} and $T = 350(40)$ MK.

Throughout the 1990's, however, as experimental uncertainties improved, it became evident that a consistent pairing of neutron density and temperature was not possible. In particular, a new neutron capture cross section for the s-only isotope ^{142}Nd [55], which is not even a branching point nucleus, unveiled a 5σ overproduction by the classical model. Further data showed that neither temperature nor neutron density were consistent across branching points [23, p.514]. This coincided with the rising success of AGB stellar models to describe the main s process based on realistic and dynamic astrophysical environments, which did not suffer the same issues [56]. Modern efforts to describe the s-process do so with self-consistent astrophysical models. Nevertheless, the classical s process aided this theoretical development in times of low computing power.

1.4.2 The main s process in AGB stars

The main s process occurs in the intershell region of Asymptotic Giant Branch (AGB) stars [24, 56–58].[5] The most striking evidence for this came when technetium was observed in the atmospheres of red-giant stars [59]. Since Tc has no stable isotopes, ^{97,98}Tc being the longest lived with both having half-lives of 4.2 Myr, this was direct evidence that a process was actively producing heavy nuclei inside stars. As mentioned in Section 1.2, the AGB phase occurs in stars after the exhaustion of He burning in the core, where the C-O core is supported by electron degeneracy and H and He burning alternate in shells around the core (shown in Figure 1.5). In particular, after core He burning ends and shell He burning proceeds, the He shell thins until it becomes thermally unstable. At this point, the He shell has been mostly extinguished until enough helium ashes accumulate under compressive heating such that the He ashes ignite and burn fiercely in a so-called *thermal pulse* (TP). The thermal pulse drives core luminosities of $\gtrsim 10^8 L_\odot$ [24, p.21] before the He fuel is exhausted, the pulse subsides, and shell H burning resumes. The thermal pulse cycle can repeat up to hundreds of times [58] giving stars in this phase the name thermally-pulsing-AGB (TP-AGB) stars.

[5] The name originates from the fact that AGB stars trace a track on the luminosity-vs-temperature graph (i.e. the Hertzsprung-Russell diagram) that is asymptotic to the red giant branch, the track taken by stars undergoing core helium burning.

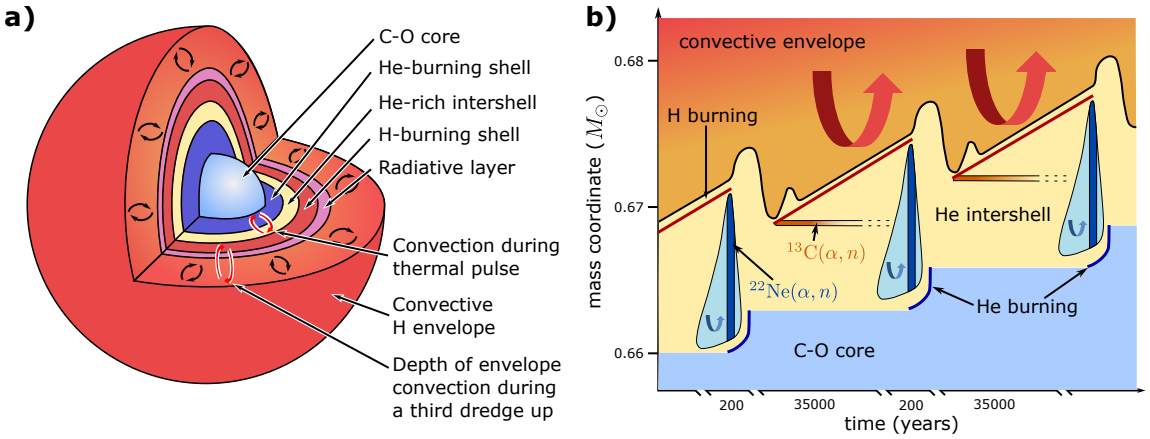

Figure 1.5: a) The onion-layer structure of a TP-AGB star (not to scale). The H-rich envelope contains most of the mass of the star, and recurrent thermal pulses drive spikes in the star's luminosity. Figure adapted from Lugaro *et al.* (2023) [58]. **b)** A simplied "Kippenhahn diagram" that shows the different shells (mass coordinate is mass enclosed) against time (not to scale). H and He burning occur in alternating thin shells. The $^{13}C(\alpha, n)$ reaction starts after the third dredge-up and then gradually weakens. The $^{22}Ne(\alpha, n)$ reaction is activated at the peak of the thermal pulse. Diagram reproduced from Wallner *et al.* (2016) [60].

The thermal pulse cycle can be described in four phases [24, p.22]:

1. **Thermal pulse:** H shell ashes accumulate until He ignition, where the thermal pulse drives a convective region in the He-rich intershell that almost reaches the H burning shell, homogenising the abundances within the intershell. One TP phase lasts approx 100 years [58].
2. **Power down phase:** As the energy ouput from the TP expires, the convective region recedes to the bottom of the intershell and a temperature gradient is restored radiatively. The energy released during the TP goes into expanding the core, and associated cooling extinguishes the H burning shell.
3. **Third dredge-up:** The expansion and extinguishing of the H burning shell allows the convective envelope to penetrate through the dormant H burning shell into the He-rich intershell, where the composition of the intershell is dredged up to the surface in the *third dredge-up* (TDU). The efficiency of the TDU is dependent on the treatment of the convective border [56].
4. **Interpulse phase:** At the deepest point of the TDU, shell H burning starts again as H is exposed to the intershell temperature gradient, and lasts for roughly 10^3–10^5 years [58]. The H burning reestablishes the H burning shell and the convective envelope is once again expelled from the core.

The main s process in AGB stars occurs via two neutron sources that are activated by different components of the thermal pulse cycle. The bulk of the neutrons in TP-AGB stars come from the $^{13}\mathrm{C}(\alpha, n)^{16}\mathrm{O}$ reaction, which is activated at $T \gtrsim 90$ MK during the interpulse phase. Some $^{13}\mathrm{C}$ exists in the intershell region after the CNO cycles, but not enough to account for the observed s-process enrichment in AGB stars [24, p.36]. Thus, it is hypothesised that at the deepest extent of the TDU, the sharp chemical discontinuity between the convective H-rich envelope and the radiative He/C-rich intershell creates a *partial mixing zone* (PMZ) where protons are mixed with abundant $^{12}\mathrm{C}$. After the re-ignition of H burning, these react via $^{12}\mathrm{C}(p, \gamma)^{13}\mathrm{N}(\beta^+\nu)^{13}\mathrm{C}$ to create a thin layer rich in $^{13}\mathrm{C}$ and $^{14}\mathrm{N}$, which is called the *^{13}C pocket*. Neutrons are then released via the $^{13}\mathrm{C}(\alpha, n)^{16}\mathrm{O}$ reaction, and this produces a neutron exposure of up to 1 mb^{-1} that lasts over the majority of interpulse period (10^3–10^5 years) at relatively low neutron densities of $\sim 10^7$ cm^{-3} [58]. The s-process products of the $^{13}\mathrm{C}$ pocket are then engulfed and homogenised by the next thermal pulse.

The exact formation mechanism of the $^{13}\mathrm{C}$ pocket is still an open question, although the general idea is quite robust to predictions. The mechanism needs to produce an appropriate amount of mixing to build up $^{13}\mathrm{C}$, but cannot provide too many protons otherwise the CNO-I cycle moves toward completion producing $^{14}\mathrm{N}$. This isotope is an efficient absorber of neutrons and thus acts as a neutron poison via the $^{14}\mathrm{N}(n, p)^{14}\mathrm{C}$ reaction, so the $^{14}\mathrm{N}/^{13}\mathrm{C}$ ratio cannot exceed unity otherwise no neutron flux is produced [24, p.36]. Given this complexity, the behaviour of the $^{13}\mathrm{C}$ pocket is often parametrised phenomenologically and then tuned to match observations. More details on current models are given in Section 4.3.

The other neutron source activated in TP-AGB stars is the $^{22}\mathrm{Ne}(\alpha, n)^{25}\mathrm{Mg}$ reaction, which provides a minor neutron exposure compared to $^{13}\mathrm{C}(\alpha, n)^{16}\mathrm{O}$. $^{22}\mathrm{Ne}$ is produced during He burning in the thermal pulse via the $^{14}\mathrm{N}(\alpha, \gamma)^{18}\mathrm{F}(\beta^+\nu)^{18}\mathrm{O}(\alpha, \gamma)^{22}\mathrm{Ne}$ chain, and if the temperature exceeds roughly 300 MK then neutrons are released via the $^{22}\mathrm{Ne}(\alpha, n)^{25}\mathrm{Mg}$ source. These high temperatures are typically only achieved in AGB stars of mass $\gtrsim 3M_\odot$, and whilst only a few percent of the $^{22}\mathrm{Ne}$ are burnt, it provides high neutron densities of $\sim 10^{13}$ cm^{-3} for just a few years [58]. This typically totals to around 0.1 mb^{-1} and thus does not provide the bulk of the s-process abundance observed, but because the intershell is convectively mixed during the thermal pulse, the $^{22}\mathrm{Ne}$ neutrons can cause reprocessing of the $^{13}\mathrm{C}$ distribution by activating high-neutron-density branching points. It is interesting to note that substantial neutron exposure via $^{22}\mathrm{Ne}(\alpha, n)^{25}\mathrm{Mg}$ is achieved in intermediate-mass AGB stars of $\gtrsim 4M_\odot$ due to higher temperatures at the base of the convective intershell. However, the mass of the intershell and the TDU efficiency are considerably smaller for these high-mass AGB stars, and thus they do not contribute much to galactic chemical evolution [56].

Models of both individual AGB stars and full galactic chemical evolution simulations [61] reproduce the main s-process abundances quite well, as seen in Figure 1.6a. The abundances of $A = 60$–90 are still underproduced, however, and so the weak s process is still required to explain the solar distribution.

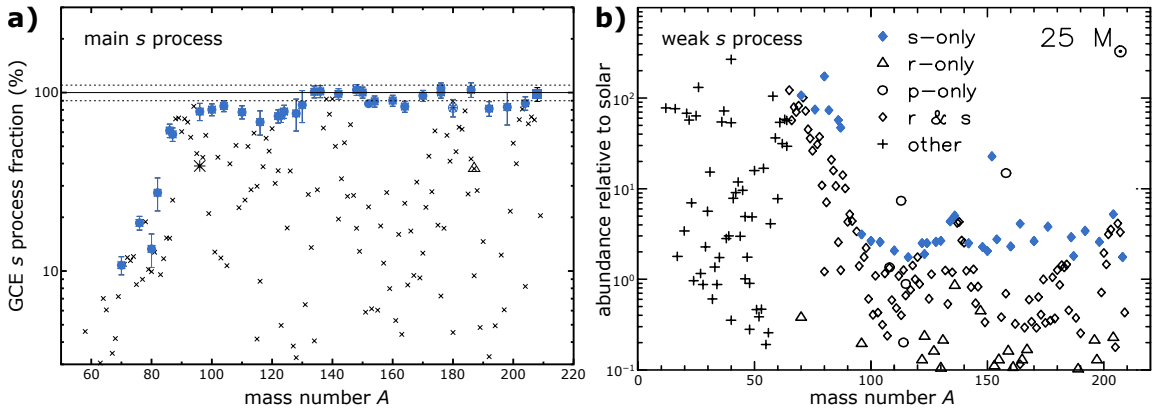

Figure 1.6: a) The contribution to the solar *s*-process abundances from a full galactic chemical evolution calculation of the main *s* process in AGB stars from Bisterzo *et al.* (2014) [61]. **b)** The abundance distribution of the weak *s* process in a $25M_{\odot}$ star of solar metallicity after core He burning and shell C burning from The *et al.* (2007) [62]. It is clear that the distributions are complementary to reproduce the solar abundances. Abundances are represented as overproduction factors of the solar abundance pattern. *s*-only isotopes are highlighted in blue.

1.4.3 The weak *s* process in massive stars

The weak *s* process occurs during core He burning and shell C burning in stars of mass $\gtrsim 10M_{\odot}$, powered by the $^{22}\mathrm{Ne}(\alpha,n)^{25}\mathrm{Mg}$ neutron source [56, 58, 62–65]. The ^{22}Ne is built via the $^{14}\mathrm{N}(\alpha,\gamma)^{18}\mathrm{F}(\beta^{+}\nu)^{18}\mathrm{O}(\alpha,\gamma)^{22}\mathrm{Ne}$ chain during the convective core He burning, where the ^{14}N is provided by the CNO cycle from the previous H burning phase. Once the core temperature reaches roughly 300 MK, the $^{22}\mathrm{Ne}(\alpha,n)^{25}\mathrm{Mg}$ source is activated and neutron densities steadily increase to a peak of roughly 10^{7} cm^{-3} over $\sim 10^{5}$ years for a total exposure of $\tau \approx 0.2$ mb^{-1} [62, 65]. Not all of the ^{22}Ne is burnt though, so the $^{22}\mathrm{Ne}(\alpha,n)^{25}\mathrm{Mg}$ source is reactivated during shell C burning, where the α particles are supplied by $^{12}\mathrm{C}(^{12}\mathrm{C},\alpha)^{20}\mathrm{Ne}$ reaction. Shell C burning occurs at ~ 1 GK, so the initial neutron flux is high at roughly 10^{11} cm^{-3} with a neutron exposure of $\tau \approx 0.1$ mb^{-1} [65].

The distribution at the end of shell C burning for a $25M_{\odot}$ star at solar metallicity [62] is shown in Figure 1.6b, and the drop in efficiency of the weak *s* process beyond $A = 90$ is obvious. This abundance pattern can only be ejected into the interstellar medium via the ensuing core-collapse supernova of the star. The chemical composition of the outer core containing the advanced burning layers—up to $3.5M_{\odot}$ for such a $25M_{\odot}$ star—is reprocessed by the explosive nucleosynthesis, erasing the *s*-process abundance pattern. Despite this, a significant fraction of the ejecta—roughly $2.5M_{\odot}$—remain unprocessed by the explosion and thus preserve the weak *s*-process abundances [56].

Because the overall neutron exposure for massive stars is considerably lower than in TP-AGB stars, the *s*-process path does not achieve equilibrium, and thus a particular MACS

does not only define its own abundance, but also impacts the abundances of all heavier isotopes [65, 66]. This compounding uncertainty makes the weak s process much more sensitive to experimental uncertainties in the MACS. Additionally, the weak s process also features strong competition of neutron capture onto lighter elements, like $^{25}\mathrm{Mg}(n,\gamma)^{26}\mathrm{Mg}$, that act like neutron poisons, which also provide their own set of uncertainties [66]. Thus, there are still many sources of uncertainty surrounding the weak s process, but galactic chemical evolution models are still currently capable of reproducing the solar s abundances quite well [17]. Continued progress in massive star structure will also improve our understanding of the weak s process.

1.5 Nuclear β decay

Given the critical role that nuclear β decay plays in every heavy-element nucleosynthesis process, understanding β-decay pathways and β-decay rates are essential in predicting accurate abundance yields. In particular, β-decay properties of highly-charged ions are some of the most impactful measurements done at heavy-ion storage rings, and this thesis focuses on such β-decay measurements, so we will take this section to introduce the foundations of nuclear β decay.

Nuclear β decay describes the process by which a proton transmutes into a neutron, and vice versa:

$$\begin{aligned} \beta^+ \text{ decay:} \quad & p \rightarrow n + e^+ + \nu_e, \\ \beta^- \text{ decay:} \quad & n \rightarrow p + e^- + \overline{\nu}_e. \end{aligned} \tag{1.9}$$

For the two aforementioned 'normal' modes of β decay, the electron/positron and antineutrino/neutrino (i.e. the lepton pair) are created in continuum states and so the β decay is a three-body decay and as such the lepton pair are emitted with a continuous spectrum of energy. Note that because of the atomic mass differences, β^+ decay is only possible where $Q_\beta \geq 1.022$ MeV. Nuclei with Q_β values less than this threshold can only decay by the third channel, electron capture (EC), where an atomic electron is captured by the nucleus and a monochromatic neutrino is emitted:

$$e^- \text{ capture:} \quad p + e^- \rightarrow n + \nu_e. \tag{1.10}$$

In addition to these modes, the special case where the β^- is created in a bound atomic state, known as bound-state β decay, is discussed in detail in Section 1.5.3.

The first complete formalism of β decay was proposed by Enrico Fermi in 1933 [67], where he assumed that the β-decay interaction was weak compared with the nuclear interaction that forms the quasi-stationary states of the nucleus. This allows β decay to be described as a weak perturbation, where the transition rate is governed by Fermi's golden rule such that the probability $N(p)dp$ per unit time of emitting an electron with momentum

in the range $p + dp$ is [23, p.61][68, p.277]:

$$d\lambda = N(p)dp = \frac{2\pi}{\hbar}|H_{fi}|^2\rho(E_f). \tag{1.11}$$

Here, $|H_{fi}|$ is the *matrix element* of the transition between quasi-stationary initial and final states Ψ integrated over the interaction operator O such that

$$|H_{fi}| = g\int \Psi_f^* O \Psi_i dV, \tag{1.12}$$

where V is a bounding volume to normalise the wavefunction and $\rho(E_f) = dn/dE_0$ is the *density of states* for the final state per unit energy. The final-state wavefunction can be decomposed into its nuclear, electron, and neutrino components: $\Psi_f^* = \psi_f^*\phi_e^*\phi_\nu^*$.

The emitted electron and neutrino can be approximated as free particles, and thus have wavefunctions of the form [23, p.62][68, p.279]:

$$\begin{aligned}\phi_e(\vec{r}) &= \frac{1}{\sqrt{V}}e^{-i\vec{p}\cdot\vec{r}/\hbar} \approx \frac{1}{\sqrt{V}}\left(1 + i\frac{\vec{p}\cdot\vec{r}}{\hbar} + \cdots\right),\\ \phi_\nu(\vec{r}) &= \frac{1}{\sqrt{V}}e^{-i\vec{q}\cdot\vec{r}/\hbar} \approx \frac{1}{\sqrt{V}}\left(1 + i\frac{\vec{q}\cdot\vec{r}}{\hbar} + \cdots\right),\end{aligned} \tag{1.13}$$

where $\vec{p}$ and $\vec{q}$ are the linear momentum of the electron and neutrino, respectively. Because the electron/neutrino wavelength is much larger than the nucleus, we can consider only the first term in the Taylor expansion, which is called the *allowed approximation*. In this case, the matrix element simplifies to

$$|H_{fi}| = \frac{1}{V^2}\left|g\int \psi_f^* O \psi_i dV\right| = \frac{g^2|M_{fi}|^2}{V^2}, \tag{1.14}$$

where $|M_{fi}|$ is just the *nuclear matrix element*.

Even in his initial theory, Fermi realised that a plane wave was not a good approximation for the electron wavefunction because of the Coulomb forces on the outgoing electron. To describe the distorted wave, a correction is applied called the *Fermi function* $F(Z, p)$ that depends on the product's nuclear charge Z and the electron momentum p. By manipulating the expression for the density of states (for details, see refs. [23, 68]), one can derive that in the allowed approximation, the total β-decay rate is

$$d\lambda = \frac{g^2|M_{fi}|^2}{2\pi^2\hbar^7c^3}\, p^2\,(E_0 - K_e^2)\, F(Z,p)\, dp \tag{1.15}$$

$$= \frac{m_e^5c^4}{2\pi^3\hbar^7}\, g^2|M_{fi}|^2\, f(Z, E_e^{\max}), \tag{1.16}$$

where E_0 is the available energy (equivalent to the Q value of the decay), K_e is the kinetic energy of the electron, and $f(Z, E_e^{\max})$ is a dimensionless quantity called the *Fermi integral* that is tabulated numerically.

We can rearrange equation (1.15) such that

$$f(Z, E_e^{\max})\, t_{1/2} = \frac{2\pi^3\hbar^7}{m_e^5 c^4} \frac{\ln 2}{g^2 |M_{fi}|^2}. \tag{1.17}$$

This quantity $f(Z, E_e^{\max})\, t_{1/2}$ is called the ft-value or the comparative half-life because it isolates the nuclear matrix element of the β decay without the kinematic factors. Because of the large variation in ft-values, the $\log(ft)$ is often compared instead.

1.5.1 β selection rules

To be consistent with special relativity, the weak Hamiltonian can be composed of five base operators O_X: a scalar S, a pseudoscalar P, a vector V, an axial-vector A, or a tensor T operator. Through careful experiments of the parity violation in β decay, it was determined that only the vector and axial-vector operators contribute, and the so-called universal $V - A$ theory of β decay was developed. As a result, the weak matrix element is properly decomposed into its vector and axial-vector components, which are referred to as the *Fermi* and *Gamow-Teller* components [23, p.62]:

$$|H_{fi}| = \frac{1}{V^2} \left(G_V^2 M_F^2 + G_A^2 M_{GT}^2 \right), \tag{1.18}$$

where G_X are the respective coupling constants and M_X are the nuclear matrix elements.

The details of the vector operator results in the fact that Fermi transitions produce an electron/(anti)neutrino pair with anti-parallel spins such that $S = 0$. Similarly, the axial-vector operator results in Gamow-Teller transitions producing a parallel lepton pair with $S = 1$. This angular momentum coupling results in selection rules for β transitions. In the allowed case, Fermi transitions have $\Delta J = 0$ so $0 \to 0$ transitions are pure Fermi, whilst Gamow-Teller transitions can have $\Delta J = 0, 1$ (but can't be $0 \to 0$) so $\Delta J = 1$ are pure Gamow-Teller. Parity is conserved for allowed transitions.

So far, we have only considered the allowed approximation, but sometimes the nuclear matrix element may be zero for allowed transitions (i.e. no final states of the right spin available). In this case, we must consider the next term in the plane wave expansion, and this is called *forbidden decay*. The transition is not actually forbidden, but rather suppressed by the fact that the second term in the expansion (that can carry away angular momentum) has a much smaller amplitude than the allowed component. In forbidden transitions, the lepton pair can carry away angular momentum, so the nuclear spin change can be larger. $\ell = 1$ is called first-forbidden, $\ell = 2$ second-forbidden, and so on. The odd/evenness of the angular momentum determines whether parity changes, so first-forbidden transitions are often encountered when a parity change is required.

1.5.2 Modern β-decay theory

The low-energy formulation of weak decay was crucial in constructing the gauge theory that lead to the electroweak formulation of the Standard Model, which comprehensively describes weak decay [69]. For low-energy nuclear β decay, modern $V - A$ theory has two popular formulations that are equivalent, that proposed by Behrens and Bühring (1982) [70] and that by Holstein (1974) [71]. In these formalisms, all the extra corrections are summarised in a function called the *shape factor* $C(Z, W)$ such that [72]

$$N(W)dW \propto pW\,(W_0 - W)^2\,F(Z, W)\,C(Z, W), \tag{1.19}$$

where $W = E/m_e c^2 + 1$ is the β energy in terms of the electron rest mass, and $F(Z, W)$ is still the same Fermi function described above. Note that this shape factor does not refer to the nuclear shape (as in deformation), although the effects of a finite nucleus are included as a correction. Astrophysical weak decay rates for ^{205}Pb and ^{205}Tl calculated in the Behrens and Bühring formalism are discussed in Section 4.2, however, further details are left to the references as this work was not done for this thesis.

1.5.3 Bound-state β decay

Bound-state β decay (β_b decay) is an exotic type of β decay where the β electron is created directly in a bound state of the daughter atom, as shown in Figure 1.7a. Because the electron is not ejected, β_b decay is a two body decay and thus produces a monochromatic antineutrino. β_b decay was first theoretically described by Daudel *et al.* (1947) [73] and fully formalised by Bahcall (1961) [74]. The description is a modification of the standard β decay we have just discussed that correctly handles the phase space of the leptons involved.

Whilst β_b decay is technically possible for any empty atomic orbital, it is most impactful in highly-charged ions where the K shell is unoccupied. This is because the binding energy of the bound state becomes available for the Q value of the decay, and the large K-shell binding energy in heavy ions can have dramatic changes on the decay rate.

In some nuclei whose β-decay Q value is only slightly negative, the extra energy available by creating the electron in a bound state can make the β_b decay Q value positive, thus turning a stable nucleus radioactive by stripping off its electrons. It is quite a remarkable phenomena that by just changing the ionisation state of an ion, its nuclear stability can be altered. This is the case for just three stable nuclei: ^{163}Dy, ^{193}Ir, and ^{205}Tl, although Takahashi *et al.* (1987) [76] catalogued 22 additional isotopes for which β_b decay could make a significant contribution to the overall decay rate.

The first case of β_b decay measured experimentally was $^{163}\mathrm{Dy}^{66+}$ in the Experimental Storage Ring (ESR) at GSI, Darmstadt, where a β_b-decay half-life of 47^{+5}_{-4} days was observed [77]. The ESR is presently the only facility where β_b decay can be measured, as it is the only facility that can store millions of fully stripped ions for several hours. Following ^{163}Dy, the β_b-decay rate of $^{187}\mathrm{Re}^{75+}$ was measured in 1996 [78], which demonstrated that

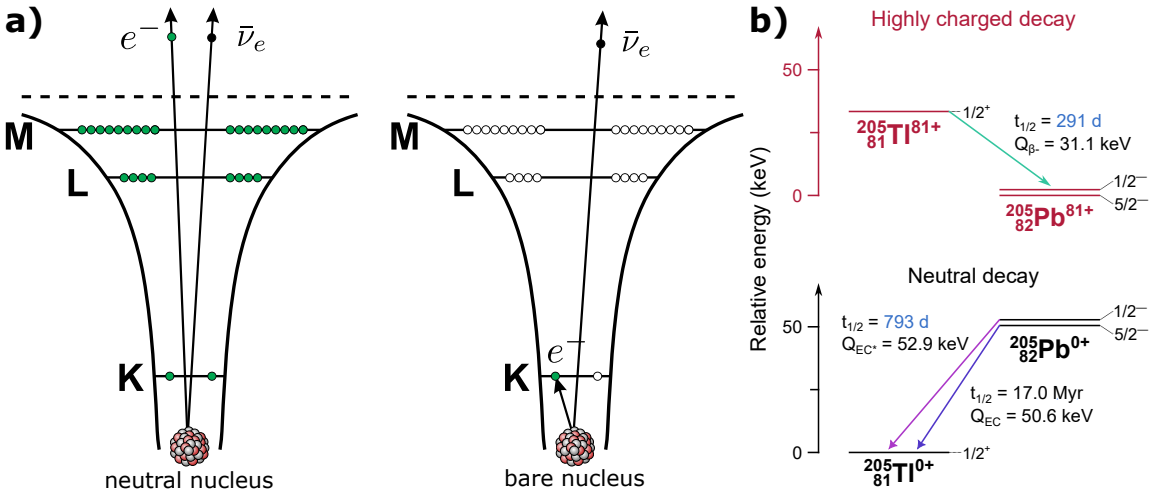

Figure 1.7: a) For a neutral nucleus, nearly all atomic orbitals are filled, so the β electron is created in a continuum state. If the nucleus is highly charged, then the β electron can be created in a bound atomic state, conserving the binding energy of the bound state and increasing the Q value of the decay. Figure reproduced from Litvinov & Bosch (2011) [75]. **b)** The low-lying nuclear levels of the ^{205}Tl–^{205}Pb pair. In the neutral case, ^{205}Pb decays to ^{205}Tl by electron capture, but in the highly-charged case, the energetics are such that β_b decay of ^{205}Tl^{81+} to ^{205}Pb^{81+} occurs. The half-lives in blue are the partial β half-lives based on the measurement described in Chapter 3.

the half-life of ^{187}Re was shortened by nine orders of magnitude at the highest charge states, raising questions about its utility as cosmochronometer to determine the age of the galaxy. The β_b-decay rate of ^{207}Tl^{81+} was measured in 2005 [79] and was the first experiment to observe the competition of bound and continuum β decay.

The nucleus of interest in this thesis, ^{205}Tl, is stable as a neutral atom. The isobar ^{205}Pb decays by electron capture (EC) to ^{205}Tl with a half-life of 17.0(9) Myr [53]. The Q value of this EC decay was historically conflicting [80–82], but has now been settled at $Q_{EC} = 50.6(5)$ keV [83]. Given that Q_{EC} is the mass difference between ^{205}Pb^{0+} and ^{205}Tl^{0+}, the β_b-decay Q value is calculated by

$$Q_{\beta_b}^{K,L,\ldots} = -Q_{EC} - E^* - |\Delta B_e| + B_{K,L,\ldots}, \tag{1.20}$$

where E^* is the nuclear excitation energy of the final state in the daughter nucleus, ΔB_e is the difference in total atomic binding energies of the two nuclei, and $B_{K,L,\ldots}$ is the binding energy of the atomic shell that the β electron is created in. Using values of $E^* = 2.329(7)$ keV [84], $\Delta B_e = 17.338(1)$ keV, and $B_K = 101.336(1)$ keV [85–88], the Q value for the first-forbidden β_b decay of ^{205}Tl^{81+} to the first excited state of ^{205}Pb^{81+} is

$$Q_{\beta_b}^{K}(^{205}\mathrm{Tl}^{81+}) = 31.1(5) \text{ keV}. \tag{1.21}$$

This positive Q value means that $^{205}\mathrm{Tl}^{80/81+}$ β_b decays with a predicted half-life of a few hundred days. β_b decay to the L shell is energetically forbidden as $Q^L_{\beta_b} = -45.3(5)$ keV. Thus, ^{205}Tl is stable all the way up to and including the 79+ charge state.

Note that for $^{205}\mathrm{Tl}^{81+}$, decay from the $J^\pi = 1/2^+$ state to the $5/2^-$ ground state of $^{205}\mathrm{Pb}^{81+}$ is negligible compared to the $1/2^-$ low-lying excited state due to suppression of the decay rate as a result of the large nuclear structure differences between the two states (Takahashi *et al.* (1987) [76] predicted the ratio of rates as $\lambda_{E^*}/\lambda_{GS} \approx 10^9$).

1.6 Astrophysical motivation for studying ^{205}Tl

The measurement of the bound-state β decay of $^{205}\mathrm{Tl}^{81+}$ is interesting because of its ability to constrain the nuclear matrix element (NME) $|M_{fi}|^2$ between the two spin-1/2 states of $^{205}\mathrm{Tl}^{81+}$ and $^{205}\mathrm{Pb}^{81+}$ (see Figure 1.7b). Following equation (1.15), if the decay rate of a transition can be measured, then the nuclear matrix element can be extracted because the other components that affect the weak decay rate are easily determined (e.g. energy of the transition, etc.). The 2.3 keV excited state of ^{205}Pb decays by internal conversion with a half-life of 24.2(4) μs [89], so it is impossible to measure the partial electron capture rate from this excited state due to the dominance of the internal conversion channel. As a result, measuring the β_b-decay rate of $^{205}\mathrm{Tl}^{81+}$ is the only way to determine the nuclear matrix element of the two spin-1/2 states of ^{205}Tl and ^{205}Pb.

The spin-1/2 Tl–Pb nuclear matrix element (Tl-Pb NME) helps us constrain other reactions involving these states. One example is the neutrino capture on ^{205}Tl, which Freedman *et al.* (1976) [90] identified has the lowest threshold of any known neutrino capture process, making it dominantly sensitive to solar *pp* neutrinos. For this reason, Freedman and collaborators hoped that this reaction could help solve the solar neutrino problem, where the intensity of the solar neutrino flux was observed (by several geochemical activation experiments [91–94]) to be a third of the value expected from predicted hydrogen burning rates in the core of the Sun [95, 96]. Freedman (1988) [97], inspired by Kienle's original idea [98], laid out exactly how the β_b decay of $^{205}\mathrm{Tl}^{81+}$ would need to be measured before ^{205}Tl could be used as a solar neutrino probe.

Freedman *et al.* (1976) [90] also identified a deposit of the Tl-bearing mineral lorandite ($\mathrm{TlAsS_2}$) in the Allchar mine in North Macedonia that could be used as long-time-averaged dosimeter. If the deposit was deep enough to protect it from cosmic rays, then the lorandite would be exposed to only the solar neutrino flux and accumulate ^{205}Pb reaction products that could be counted. This so-called "LORandite EXperiment" (LOREX) has been developed by Pavićević [99–101] by characterising the ore depth, age, background channels, and most recently by collecting 400 g of lorandite out of 10.5 tons of ore. However, the LOREX project has, until now, been stymied by the lack of an accurately predicted neutrino capture rate. The impact of our measurement on the LOREX project has been published in Sidhu *et al.* (2024) [102] and is briefly summarised in Section 3.5, but this has not been

the focus of this thesis.

The other case where the Tl-Pb NME is needed is in the behaviour of ^{205}Pb in stellar interiors. ^{205}Pb has the potential to be a very powerful cosmic chronometer, having a lifetime useful for timing processes in the early Solar System. However, the 2.3 keV state of ^{205}Pb can be thermally populated at stellar temperatures, significantly reducing the astrophysical half-life of the isotope. At even higher temperatures, ^{205}Tl can be fully stripped allowing β_b decay to occur. The Tl-Pb NME determines both of these decay rates in stars, and is thus crucial to understanding the production of ^{205}Pb. The impact of the ^{205}Tl^{81+} β_b-decay measurement on ^{205}Pb as a cosmochronometer has been a significant component of this thesis work, and is described in Chapter 4.

1.7 Thesis structure

The broad strokes of how the chemical elements were created have now been outlined, but many details of the individual processes are still uncertain. Uncovering these details provides a rich opportunity for interdisciplinary discovery that deepens our understanding in other areas of nuclear phyiscs and astrophysics.

The *s* process is well understood from a nuclear physics perspective, in part due to a comprehensive effort to measure most of the relevant neutron-capture cross sections in the astrophysically relevant energy range [103]. However, in some cases, unknown nuclear matrix elements may impact key stellar weak decay rates, which can be crucial for predicting specific key isotopic abundances accurately. The case of the bound-state β decay of ^{205}Tl^{81+} is a particularly impactful example, and the analysis of this experiment at the Experimental Storage Ring (ESR) at the GSI Helmholtz Centre, Darmstadt, is described in Chapter 3. In addition, uncertainties associated with stellar modelling still persist. The handling of mixing and the formation of the ^{13}C pocket remain open questions [24]. Recent advances in analysing the isotopic composition of pre-solar grains from AGB stars has provided a wealth of new data with which to test *s*-process models [104, 105].

Our relatively good understanding of the *s* process can also be used to make powerful predictions for other open questions. Understanding the timing of processes in the early Solar System is one example, where the regular enrichment of the interstellar medium with *s*-process material can allow us to extract the time it took for the Solar System to isolate itself from further enrichment and then collapse to form the first solids [106]. In particular, the calculation of this isolation time using the isotope ^{205}Pb is described in Chapter 4.

For the *r* process, immense amounts of nuclear data are still needed for radioactive species to help constrain the theoretical models that are used to predict the properties of the nuclei along the *r*-process path. Heavy-ion storage rings provide unique capabilities in measuring the masses and half-lives of large swathes of neutron-rich nuclei simultaneously, with potential for detecting β-delayed neutron emission in the future [107, 108]. Realising these measurements is the goal of the Isomeric states, LIfetimes, and MAsses (ILIMA)

collaboration, under which this thesis work was done. The operational features of storage rings are introduced in Chapter 2, with a focus on the ESR. For these measurements, particle detectors in steel pockets extending into the ultra-high vacuum of the storage ring are required to detect ions that have decayed and left the momentum acceptance of the storage ring. The construction and commissioning of a new particle detector called PLEIADES is described in Chapter 5, which will be used in future experiments.

To conclude, some perspectives on future work at the ESR are provided in Chapter 6, with a focus on how PLEIADES can be used for future measurements in exotic decay studies.

Chapter 2

Heavy-Ion Storage Rings

Whilst a vast array of techniques are necessary to measure the nuclear properties required for astrophysical applications, heavy-ion storage rings combine several cutting-edge features that enable unique nuclear physics measurements. In this chapter, we will review the operation of storage rings in order to understand the experimental methods presented in Chapter 3 and the design choices in Chapter 5.

Storage rings became popular in the 1980s due to advances in beam cooling made in the prior decade, primarily motivated by the need for high-energy collisions in particle physics [109]. Several test facilities at CERN and Fermilab developed the key techniques of electron [110, 111] and stochastic cooling [112, 113] that culminated in the Low Energy Antiproton Ring (LEAR) at CERN, where advanced storage ring technologies and beam manipulation techniques were pioneered [108]. Almost all of the storage rings built throughout the 1980s were prompted by the success of LEAR, with a list of facilities catalogued in refs. [109, 114]. These facilities were used for high-energy particle physics or precision atomic physics by providing high charge states of heavy ions. However, most of these facilities were stable beam facilities, which limited their utility for nuclear physics. In recent years, heavy-ion storage rings connected to radioactive beam facilities are becoming increasingly popular due to their unique capabilities.

Currently, there are four heavy-ion storage rings in the world, listed with characteristic properties in Table 2.1. The Experimental Storage Ring (ESR) [115] at the GSI Helmholtz Centre, Darmstadt, shown in Figure 2.1, is the oldest and hence most technically advanced and versatile. The CRYRING[6] [116, 117], originally operated at Stockholm, was repurposed by moving it to Darmstadt and connecting it to the ESR. It is a low-energy ring, where the lowest energy is limited only by beam losses due to charge exchange, and with a transfer line to the ESR can offer radioactive isotopes at very low energies. The Cooler-Storage Ring at the Heavy Ion Research Facility, Lanzhou (HIRFL) [118] was built in 2007 and operates two rings, a main ring (CSRm) for acceleration and initial cooling/bunching, and an experimental ring (CSRe) for measurement. The CSRe is essentially a reproduction of the ESR, with lots of collaboration between the two facilities. Finally, The RIKEN Rare-Ion Ring (R3) [119] at the RIKEN Nishina Centre, Wakō specialises in isochronous mass spectrometry (see Section 2.5.2). The R3 ring is a very unique ring that operates as a cyclotron, rather than a synchrotron like the other rings, and requires no beam cooling

[6]CRYRING stands for the CRYsis-synchrotron-RING, where CRYSIS was the CRYogenic Stockholm Ion Source.

Table 2.1: Properties of active heavy-ion storage rings. Data from Steck *et al.* (2020) [108].

	ESR	CRYRING	CSRe	R3
Circumference	108.4 m	54.2 m	128.8 m	60.4 m
Max $B\rho$	10 Tm	1.4 Tm	9.4 Tm	6.0 Tm
Max energy	550 MeV/u	14.8 MeV/u	500 MeV/u	230 MeV/u
Min energy	3 MeV/u	charge exch. limited	5 MeV/u	-
Beam cooling	stochastic, electron	electron	electron	none
Internal target	gas jet	gas jet	gas jet	none
Vacuum pressure	10^{-11} mbar	10^{-12} mbar	10^{-11} mbar	10^{-10} mbar
Isochronous γ_t	1.41	n/a	1.40	1.18

since it operates exclusively in an isochronous mode.

The following explanation of storage ring principles will focus on the ESR as the primary example because of its relevance to this thesis. However, almost all the techniques and mechanisms described here are applicable to the CRYRING and the CSRe as well. As already noted the R3 ring operates quite uniquely and will not be discussed further.

2.1 Beam dynamics

To control high-energy ions, magnetic fields are used because the Lorentz force is proportional to velocity, which makes it feasible to provide the forces required for steering. Storage rings are synchrotron accelerator systems[7] that use dipole magnets for bending, quadrupoles for beam focusing, and sextupoles for correcting the energy-dependent focusing of the quadrupoles (details in Section 2.1.4). Together, these magnets make up the *lattice* of the storage ring. The position and momentum of beam particles is formulated in relation to the trajectory of an ideal reference particle that traces the *design orbit* of the lattice. This longitudinal reference orbit is parameterised by s (for the German word "Sollbahn"). The transverse dimensions are denoted x and y, with the rate of change denoted by $x' = dx/ds$. Because the longitudinal velocity of the beam is much greater than the transverse components, the small angle approximation holds such that the rate of change x' is equivalent to the angular deviation from the ideal path, and is most commonly expressed in milliradians.

Dipole magnets provide a constant magnetic field to bend the ion trajectory. In this field, ions experience a cyclotron motion with a constant radius of curvature ρ that is proportional to the magnetic field strength B. The product of these two, $B\rho$, is called the

[7] The R3 ring being an obvious exception, which operates in a cyclotron mode.

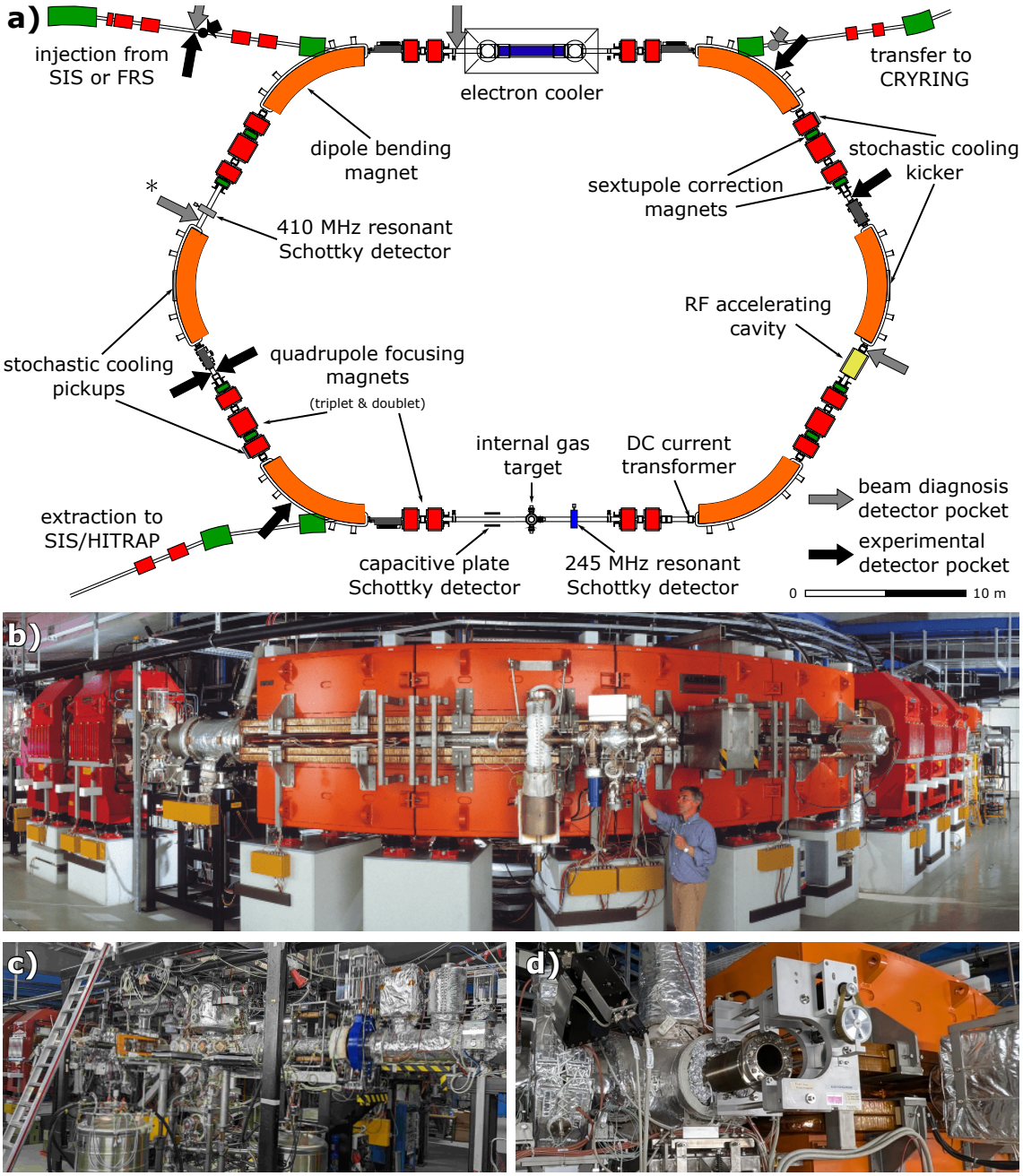

Figure 2.1: **a)** The ESR is shown schematically, reproduced from Beckert *et al.* (1998) [120]. The ring lattice is symmetric resulting in 2 periodic segments per revolution. **b)** The bottom-right corner of the ring is pictured (© J. Mai, GSI, Darmstadt). **c)** The target area is shown, alongside the 245 MHz Schottky detector in blue. **d)** A detector pocket (marked with $*$ on diagram) is shown.

magnetic rigidity and is related the momentum of a particle:

$$B\rho = \frac{p}{q}, \tag{2.1}$$

where p is the momentum and q is the charge of the ion. The magnetic rigidity defines the momentum of particles accepted by the design orbit of the ring.

2.1.1 Orbital frequency

In reality, there are no such ideal particles, so we have to consider deviations from the ideal orbit. As described by Edwards & Syphers [121], a particle's orbital period is given by $T = L/v$, where L is the path length through the storage ring and v is the velocity. The change in the revolution period ΔT is then described by

$$\frac{\Delta T}{T} = \frac{\Delta L}{L} - \frac{\Delta v}{v}. \tag{2.2}$$

In other words, a particle moving at a greater speed will take less time to orbit, whilst a particle taking a longer path with take more time to orbit. The change in the velocity can be expressed in terms of momentum:

$$\frac{\Delta v}{v} = \frac{1}{\gamma^2}\frac{\Delta p}{p}, \tag{2.3}$$

where $\gamma = \sqrt{1 - v^2/c^2}$ is the Lorentz factor. The change in path length can also be related to the momentum, since a higher momentum particle will take a wider path through the dipole. This relation is not simple and depends on the specific optics of the storage ring, so the so-called *transition energy* γ_t is introduced such that

$$\frac{\Delta L}{L} = \frac{1}{\gamma_t^2}\frac{\Delta p}{p}. \tag{2.4}$$

The change in the period thus simplifies to

$$\frac{\Delta T}{T} = \left(\frac{1}{\gamma_t^2} - \frac{1}{\gamma^2}\right)\frac{\Delta p}{p} = -\eta\frac{\Delta p}{p}, \tag{2.5}$$

where $\eta \equiv \gamma^{-2} - \gamma_t^{-2}$ is called the *slip factor*. The slip factor determines how much particles that are ahead or behind in phase will slip back to the synchronous orbit.

If we consider also the change in momentum due to difference in mass-to-charge ratios, m/q, then we have

$$\frac{\Delta p}{p} = \frac{\Delta(m/q)}{m/q} + \gamma^2\frac{\Delta v}{v}. \tag{2.6}$$

The change in period, or alternatively orbital frequency, is thus given by [107]

$$\frac{\Delta f}{f} = -\frac{\Delta T}{T} = -\frac{1}{\gamma_t^2}\frac{\Delta(m/q)}{m/q} + \left(1 - \frac{\gamma^2}{\gamma_t^2}\right)\frac{\Delta v}{v}. \tag{2.7}$$

This equation describes the resolution of orbital frequencies in storage rings. Further details on sychrotron oscillations and their use in beam manipulation can be found in Appendix A.

2.1.2 Betatron oscillations

In the previous section, longitudinal deviations of the beam compared to the reference particle were discussed, but beam particles will also deviate in the transverse dimensions. Whilst alternatives were considered, almost every accelerator system uses quadrupole magnetic fields to provide *strong focusing* to the transverse spread of the beam. The focusing of beam particles is directly analogous to photon-based optics, so focusing elements are often referred to as lenses.

Due to the requirement that $\vec{\nabla} \times \vec{B} = 0$, quadrupoles can only focus the beam along one transverse axis at a time, whilst the other axis experiences a defocusing. However, combining an appropriately placed set of focusing and defocusing lenses can still create an overall focus, provided the drift length between lenses is chosen appropriately. This is why quadrupole magnets are often found in sets of 2 or 3.

The strong focusing of quadrupoles (and other beam optics) results in an oscillatory motion around the design orbit of the storage ring. These transverse oscillations are called *betatron oscillations*, and the amplitude is given by $\beta(s)$. In particular, given the quadrupole sets can provide a focusing effect and the fact that storage ring lattices are periodic, the betatron oscillations are also periodic. The exact form of the oscillation depends on the specific ring lattice. A storage ring must be operated such that the number of betatron oscillations per revolution *is not* an integer, otherwise the resonance in betatron oscillations will cause beam losses. This applies to both vertical and horizontal oscillations, where planar coupling should be avoided.

2.1.3 Emittance and Louisville's theorem

So far, individual particles have been described with deterministic orbits. This orbit can be tracked in positional and angular phase space, where the trajectory of a particle's orbit is determined by the phase $\psi(s)$ of the betatron oscillation. Any individual particle will trace out an ellipse in phase space as it traverses the betatron oscillation. The area of this ellipse, ε, is called the *emittance* of the particle.

For a beam made of finite particles, the beam is created with some random phase space distribution that is then shaped by acceleration, optics, or straggling in the system. Even if the initial phase distribution of an injected beam is not ellipsoidal, field imperfections will cause the phase distribution to smear out and match the characteristic phase ellipse of the

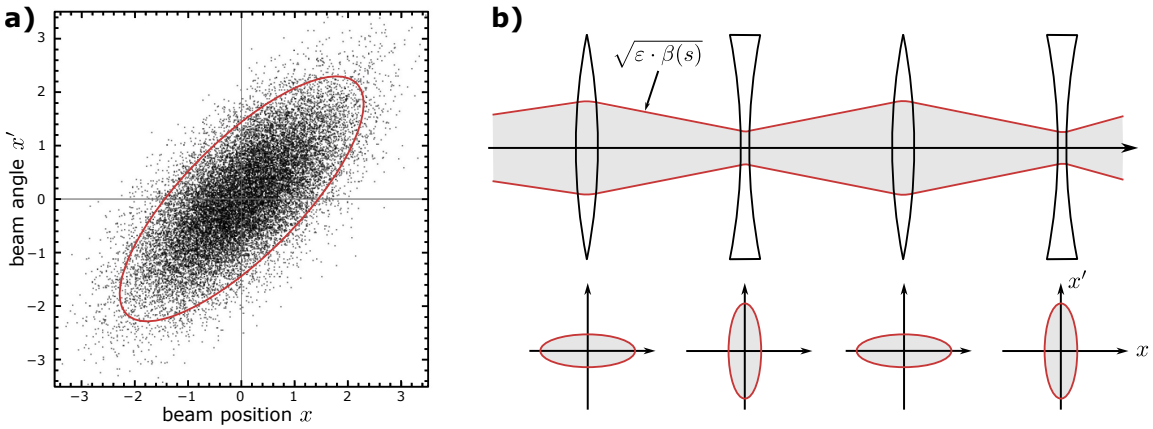

Figure 2.2: **a)** The idealised bivariate Gaussian emittance is shown alongside an emittance of enclosing 90% of the beam. **b)** The emittance alongside a sequence of focusing and defocusing lenses demonstrates the creation of waists by squeezing the emittance, whilst the overall area is conserved.

ring lattice [121, p.81]. Thus, most beams will take on a bivariate Gaussian distribution in phase space that is bounded by another ellipse called the beam emittance.

Louisville's theorem from Hamiltonian mechanics tells us that under conservative forces, the emittance of a beam is conserved and the particle density is constant [122]. Thus, whilst travelling around a storage ring, the beam cannot be condensed in phase space by electromagnetic steering alone. Instead only 'waists' in the emittance can be achieved, as shown in Figure 2.2.

2.1.4 Momentum dispersion

When introducing the transition energy in the above discussion of the longitudinal spread of the beam, it was mentioned that this momentum spread causes transverse deviations from the design orbit because higher momentum particles are bent less by the dipole bending magnets, and vice versa. This effect is shown in Figure 2.3a. On top of this, the focusing strength of quadrupoles is proportional to the beam momentum, so higher momentum particles are less defocused and then correspondingly less refocused, resulting in longer focal lengths. This is shown in Figure 2.3b, with the reverse being true for lower momentum particles. Thus, momentum spread in the beam will also cause additional betatron oscillations, on top of those induced by the emittance of the beam.

Further details and a more formal mathematical derivation of the beam dynamics in storage rings is provided in Appendix A.

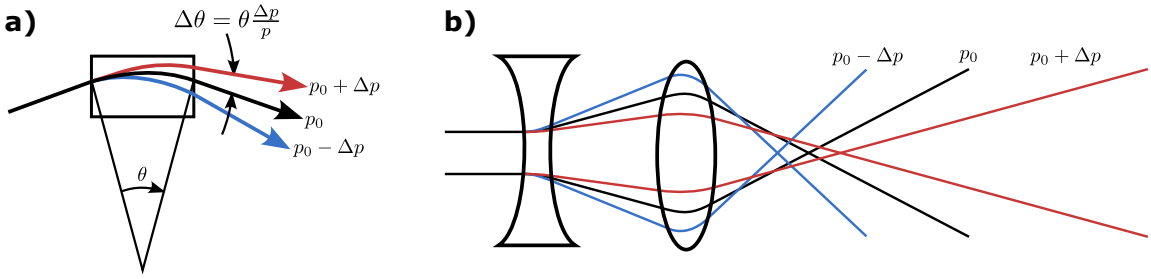

Figure 2.3: **a)** Dipole magnets will impart angular deviations to particles whose momentum deviates from the design orbit. **b)** A defocusing-focusing quadrupole pair will also impart angular deviations. Figure inspired by Steinhagen (2016) [123].

2.2 Beam cooling

The momentum spread and transverse emittance of the beam can be equivalently described as the temperature of the beam. Since the two ion motions are only weakly coupled, the longitudinal and transverse temperatures are different, i.e. $T_\parallel \neq T_\perp$. In particular, the beam temperature is defined by [124]:

$$\begin{aligned} \tfrac{1}{2}kT_\parallel &= \tfrac{1}{2}mv_\parallel^2 = E_0\left(\frac{\Delta p}{p}\right)^2, \\ \tfrac{1}{2}kT_\perp &= \tfrac{1}{2}mv_\perp^2 = E_0\frac{\varepsilon}{\langle\beta(s)\rangle}, \end{aligned} \tag{2.8}$$

where $\Delta p/p$ is the momentum spread, ε is the beam emittance, and $\beta(s)$ is the betatron amplitude.

Beam cooling is essential to enabling the precision research campaigns of storage rings, since the beam spread determines both the energy/mass resolution of ions inside the storage ring and their interaction luminosity. Cooling is especially crucial for secondary beams produced by nuclear reactions, as these will have large emittance due to the straggling during the production and separation process.

Whilst Louisville's theorem states that the emittance is conserved by the electromagnetic optics of a storage ring, there are several ways in which the emittance can be reduced. The two primary ways to reduce the emittance and momentum spread of a heavy-ion beam are stochastic and electron cooling. Acceleration of the beam and synchrotron radiation also reduce the beam temperature, but since storage rings are not for acceleration and synchrotron radiation is negligible for heavy ions, we will not consider them here.

2.2.1 Stochastic cooling

Fluctuations in the current distribution caused by the random phase distribution of a finite number of ions are called *Schottky noise*, after Walter Schottky who first observed the fluctuation in the DC current of an electron beam [125]. These fluctuations can be measured and corrected for using electromagnetic pickups in a method called *stochastic cooling*. The Schottky noise is recorded by a pickup electrode, and the feedback is then used as a correction signal that is sent to the kicker electrode further around the ring. In the simplest example, the electrodes are just parallel plates, so for the pickup electrode, particles closer to one plate will induce a larger signal making the difference of the two plates proportional to the position deviation from the design orbit. The pickup signal is amplified and provided to the kicker electrode, creating a transverse electric field that deflects the particle. Thus, to be most effective, the pickup should be located where the position spread is maximised and the kicker electrode where the angular spread is maximised. This corresponds to a phase advance of $\pi/2$, so the pickup and kicker should be separated by $\Delta\psi(s) = (n + \frac{1}{2})\pi$ in the betatron oscillation [126]. This constraint also means that stochastic cooling needs to be designed for a specific energy and ring optics, and thus must be considered when designing the storage ring. The ESR stochastic cooling system can operate from 400–550 MeV/u.

As already discussed, both transverse emittance ε and momentum spread $\Delta p/p$ result in betatron oscillations; stochastic cooling can correct both longitudinal and transverse spread via the same basic mechanism. The cooling time of stochastic cooling is proportional to $\tau \propto N/2W$, where N is the number of particles and W the bandwidth [126, p.12]. The bandwidth chosen for the ESR was 0.9–1.7 GHz [127]. The performance of stochastic cooling is ultimately limited by electronic noise induced in the amplification stage.

2.2.2 Electron cooling

Electron cooling works by overlaying the ion beam with a cold electron beam such that Coulomb interactions with the electrons thermalise the ions and reduce their temperature in both longitudinal and transverse directions. The electron beam is merged at the same speed as the ions so they co-propagate and the average relative velocity between ions and electrons is zero. This results in the situation depicted in Figure 2.4a, where hot ions scatter off cold electrons and eventually thermalise at the same temperature as the electron beam.

The electron beam is created by the electron gun, which features a hot cathode at high electric potential. The transverse electron temperature is directly determined by the cathode temperature, $T_\perp = T_{\text{cat}}$, which in the ESR operates at ~ 1000 K. The longitudinal temperature is more complicated because of the emittance compression during acceleration away from the cathode, and is given by $T_\parallel = kT_{\text{cat}}^2/4E_0$, where E_0 is the average kinetic energy of the electron beam. Typical electron temperature values are thus $kT_\perp \approx 0.1$ eV and $kT_\parallel = 0.1$–1 meV [124]. The electron beam is then guided onto the ion beam via

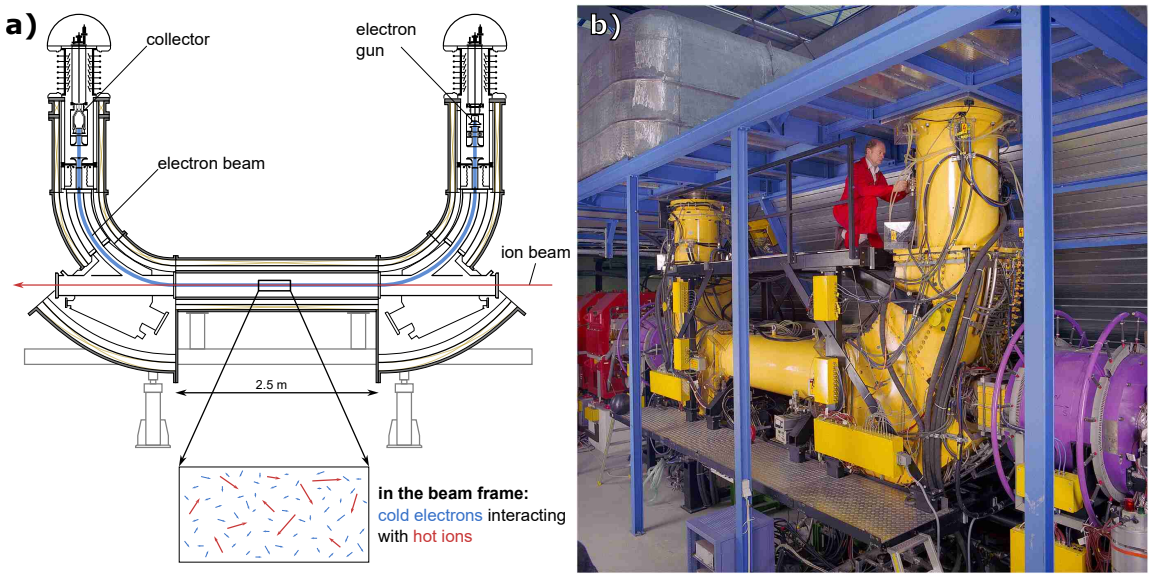

Figure 2.4: a) A schematic of the ESR electron cooler, reproduced from Fanzke *et al.* (1987) [115]. The zoom-in shows the beam interactions with the cool electrons. **b)** A photo of the ESR electron cooler (© A. Zschau, GSI, Darmstadt).

solenoidal and toroidal magnetic fields, as the electrons follow cyclotron orbits around the magnetic field lines.

The cooling time of electron cooling depends on the charge Q and mass A of the ions, the electron density n_e, the fraction of the ring used for cooling η_n, and most sensitively the relative velocity δv of the ions [108]:

$$\tau \propto \frac{A\,(\delta v)^3}{n_e\,\eta_n\,Q^2}. \tag{2.9}$$

In particular, the electron cooling force is small for large relative velocities, and becomes most efficient at the effective electron temperature. Thus, electron cooling is most effective if the beam is pre-cooled via stochastic cooling. In addition to the above properties, a large amplitude function $\beta(s)$ at the location of cooling reduces the transverse velocities of the ion beam, making electron cooling faster. However, this needs to be balanced against ensuring that the ion beam is not larger than the electron beam. The value of the dispersion function also affects the rate of beam cooling [108].

To minimise the cooling time, the ESR combines stochastic cooling followed by electron cooling. The ESR can accept hot fragment beams with $\Delta p/p = 3.5 \times 10^{-3}$ and $\varepsilon = 10$ mrad mm and stochastic cooling can quickly cool the beam to values of $\Delta p/p = 10^{-4}$ and $\varepsilon = 2$ mrad mm [124]. Then electron cooling takes over, where the resolution achievable

depends on the beam properties such as charge and number of ions. Values down to $\Delta p/p = 10^{-6}$ and $\varepsilon = 10^{-4}$ mrad mm are achievable for most ions [128]. Electron cooling at the ESR is typically operated with currents on the order of 10–300 μA. The strength of the cooler current mainly depends on beam lifetime considerations, which are discussed in Section 2.3.1.

Electron cooling is ultimately limited by intrabeam scattering and space charge effects. Intrabeam scattering results from Coulomb repulsive scattering of ions in the beam, and is proportional to the number of stored ions whilst inversely proportional to the phase space volume [108]. This scattering causes a beam heating effect. Space charge effects result from the electromagnetic fields created by the charge distribution of the beam itself. Finally, interactions with the residual gas or the internal target will also cause beam heating through scattering. The cooling of the beam will reach the best achievable resolution when heating from these three processes equals the cooling rate.

2.3 Beam manipulation

In addition to the orbital behaviour and cooling of the beam, the ESR has several other features that enhance its uniqueness and flexibility. Storage rings excel at storing hundreds of thousands of highly-charged ions for several hours. Whilst longer storage times and high charge-state breeding has been demonstrated by other traps, e.g. Morgner *et al.* (2023) [129], no other ion trap can store millions of fully-stripped ions for several hours.

2.3.1 Beam lifetime

The beam lifetime in a storage ring depends on three loss mechanisms: charge-changing reactions (i) in the electron cooler, (ii) with the residual gas in the storage ring, or (iii) with the gas of the internal target (if in use).

In the electron cooler, the main channel is capture of a free electron via radiative electron capture (REC), although dielectronic recombination (DRC) can become significant for well-cooled beams [130]. REC is where the atomic electron capture is accompanied by the emission of a photon. It is dominant at large velocity differences (electron temperature $> 0.1\ eV$) because the photon provides the momentum boost required for the continuum electron to transition to the bound-state of the fast moving ion [131]. DRC is where the continuum electron transfers energy by exciting a bound electron so it can be captured, thus proceeding via a double electronic excited state [132]. The recombination with free electrons is proportional to the electron current in the cooler, and thus losses in the cooler directly correlate with the cooling speed. For most ions, the beam lifetime is several times longer than the cooling time, so these losses are not problematic. Where experiments require long lifetimes, the cooler must be operated at low currents (< 50 μA) [108].

For the rest gas and the internal target, REC is the dominant capture mechanism, but ionisation can also occur if the stored ions are not fully ionised. Losses with the rest gas

and leakage from the gas target are minimised by operating the entire storage ring at ultra-high vacuum (UHV) conditions of a few 10^{-11} mbar. To reach these pressures, the entire ring needs to be baked at 300 °C, so all components exposed to the baking temperatures need to be chosen carefully.

2.3.2 Accumulation

Methods for stacking multiple injections in a storage ring have been developed to increase the intensity of stored ions. Two main methods are used, with the choice depending on the specific beam. The first method is called a *multiturn injection* where the transverse acceptance of the storage ring is filled across multiple turns of the beam as the betatron oscillation shifts the bunches around the transverse phase space. This process works well if the injected beam already has a low emittance compared to the storage ring acceptance.

An alternative method is used to fill the longitudinal phase space of the storage ring. The beam is condensed into bunches with an applied radiofrequency (RF) field, which leaves unstable space around the circumference of the ring where fresh beam can be injected. This stacking method is used in the ESR, where hot fragments have too large emittance for a multiturn injection, so the injected beam is stacked and cooled into RF bunches by stochastic and electron cooling [133, 134]. Longitudinal stacking plateaus in beam intensity when the loss mechanisms counterbalance the injection of new beams.

The accumulation of beams in storage rings is a crucial feature when using secondary, low-intensity, radioactive beams that are produced by a nuclear reaction. In this case, accumulation may be required to achieve intensities sufficient for the experimental goals. The stacking of radioactive beams is a recent development in the capability of the ESR [135].

2.3.3 Deceleration

Most storage rings are equipped with a radiofrequency cavity that allows them to be operated as synchrotrons. Usually this is done for acceleration, but the synchronous ramping of the magnetic rigidity with RF acceleration can be applied in reverse to reduce the stored beam energy. In the ESR, this is done to provide low energy beams ($\sim$ 4 MeV/u) to the GSI Penning trap, HITRAP [136], to transfer beams to the low-energy CRYRING, or for astrophysical reaction studies at low energies in the ESR itself.

During deceleration, the beam emittance grows. Electron cooling can keep the emittance from expanding, although the equilibrium cooling is less effective due to increased intrabeam scattering at low energies. Beam losses at low energies are dominated by reactions with the residual gas, so electron cooling losses can be neglected. A typical deceleration cycle in the ESR takes about 30 s, where the beam starts at 400 MeV/u to match the stochastic cooling range, and then is ramped down to 30 MeV/u where electron cooling is turned on and can be further decelerated to as low as 3 MeV/u. Beam losses during this cycle are at least 50%, and the lifetime is just a few seconds at these low energies [108].

2.4 Internal gas target

The gas target in a storage ring has several advantages whilst simultaneously generating some challenging constraints. The revolution frequency in the ring, which is on the order of MHz depending on the energy of the beam, boosts the luminosity L of reactions with the beam:

$$L = f_{\text{rev}}\, N_{\text{ion}}\, \rho_t\, l_t, \tag{2.10}$$

where f_{rev} is the revolution frequency, N_{ion} the number of ions stored, ρ_t the gas target density, and l_t the length of the target. This permits the use of thin targets—thin describing the amount of matter the beam passes through—which reduces the energy straggling in the beam for a single pass. Furthermore, after a pass through the target, the energy resolution of the beam is restored by cooling. This is both an advantage and a requirement; the target must be thin enough so that beam cooling can restore the beam integrity to maintain storage. The low energy straggling in the target and the restoration by beam cooling means that all reaction measurements in storage rings achieve a high energy resolution.

Since very thin foils would be burned by stored beam and ion beams are space-charge limited, molecular gas jet targets are the most successful realisations of an internal target [137]. However, the target must also not overly affect the ultra-high vacuum (UHV) at which the storage ring operates. Thus, the pressure of the gas jet has to be reduced to almost match the UHV. In *cluster jet targets*, this is achieved through the combination of a Laval nozzle followed by several collimating apertures called skimmers that create a supersonic gas jet with a low temperature.

The ESR target can provide target densities of 10^{10}–10^{15} atoms cm^{-3} for species including hydrogen, nitrogen, and a range of noble gases [138]. The highest densities are easily achieved for the noble gases, and the target density is instead limited by the cooling available from the electron cooler. For lighter gases like hydrogen and helium, high target densities at acceptable pressure is much more challenging. Thus, the ESR also features a *liquid droplet beam* that enables high densities for lighter gases. This droplet target uses a cryogenically cooled nozzle such that the target gas liquefies before being injected into the ring, where it breaks up into a stream of droplets [139]. These liquid droplets have a much higher density, boosting the overall density of the target. However, the vaporisation of the droplets by the beam degrades the UHV more than the cluster jet target.

Other target options are available, but less commonly used. Laser overlap throughout the storage ring has been used in a target-like way to excite atomic transitions in stored ions. Electron coolers have also been used as electron targets by deliberately detuning the electron beam velocity. Recently, free neutron sources have also been proposed as a target for storage rings [140–142]. Because neutrons are also radioactive, the multiple passes of a revolving beam through the free neutron target that is only possible in a storage ring is crucial in achieving the luminosities required for direct capture measurements on radioactive beams. However, due to the extreme technical challenges of dealing with a radioactive beam and radioactive target, these projects are still at very preliminary stages.

2.5 Schottky beam monitoring

In a storage ring, non-destructive beam monitoring is ideal to preserve the storage of ions. Simple diagnostic monitoring can be achieved by *current comparator* devices, that detect the electromagnetic fields produced by the beam. The ESR uses a DC Current Transformer (DCCT), which is a device that detects magnetising forces induced by the beam in a toroidal core surrounding the beam. An electronic system balances magnetic flux through the core with a feedback current, and that current is proportional to the ion beam current [143]. The DCCT can thus measure the total current of the beam in the range of μA to A [108]. The simple capacitive pickups, described in Section 2.2.1 that use the beam fluctuations to stochastically cool the beam, can also be used as position sensitive detectors to measure and adjust the bulk beam orbit.

These simple beam monitoring devices do not have enough precision to analyse the composition of the beam. However, the fluctuations in the beam current, introduced earlier as Schottky noise, carry a lot of information about the individual components of the beam. This information is detected in Schottky noise spectrometry, and the detectors that measure the Schottky noise are called Schottky detectors.

2.5.1 Schottky noise principles

Individual ions in the storage ring are relativistic, and thus induce δ-function pulsed signals in the electromagnetic Schottky pickups. In particular, the pickups record the 'self-fields' produced by the image charges of an ion. If we consider the longitudinal domain of the ion's motion, a single ion will produce an infinite train of pulses in the time domain, and this will correspond to an infinite set of harmonics in the frequency domain after the Fourier transform is applied [144]. The beam, of course, does not consist of a single particle but rather a finite number of particles with a momentum spread. For a set of N particles, the total beam current is then given by [145]

$$\begin{aligned} I(t) &= qe \sum_{i=1}^{N} \sum_{k=-\infty}^{\infty} \delta\big(t - (t_i + kT_i)\big) \\ \tilde{I}(\omega) &= qe \sum_{i=1}^{N} \omega_i \sum_{k=-\infty}^{\infty} \delta\big(\omega - k\omega_i\big) \exp\big(-i\omega t_i\big), \end{aligned} \tag{2.11}$$

summed over the i^{th} particle and the k^{th} harmonic where qe is the ion's charge, T_i is the orbital period, t_i the time offset, $\omega_i = 2\pi/T_i$, and $\tilde{I}$ represents the frequency domain of the Fourier transform. In the time domain, this describes a constant mean current $I_b = \langle I(t) \rangle$ with a stochastic variation produced by the random distribution of the beam in phase space I_S, where $I(t) = I_b + I_S$. In the frequency domain, whilst the expectation value of $\tilde{I}(\omega)$ is zero by the cancellation of phases, the cancellation is never complete due to the

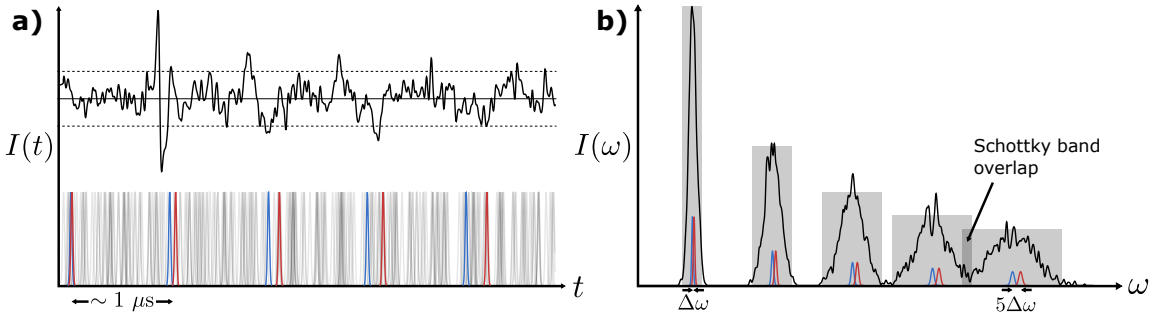

Figure 2.5: a) The individual ion pulses in the time domain add to give the total beam current. The signal from a fast/slow ion has been highlighted in red/blue, respectively. **b)** The frequency domain reveals the frequency spread caused by the non-zero momentum spread. The Schottky noise power for each harmonic is conserved, so as the harmonics increase and spread out, eventually there is overlap in the Schottky bands. Note that the resolution is typically much better than shown here schematically.

finite number of beam particles. This means the stochastic signal I_S is detectable and will depend on the frequency of the orbiting ions. This situation is represented visually in Figure 2.5.

The width of the Schottky frequency peaks is determined by the momentum spread. We have already seen this effect in Section 2.1.1 and equation (2.5):

$$\frac{\Delta f}{f} = \eta \frac{\Delta p}{p}, \tag{2.12}$$

where $\eta \equiv \gamma_t^{-2} - \gamma^{-2}$ is the slip factor. The fact that the width of the Schottky signal in frequency space is directly related to the momentum spread is one way Schottky detectors are used to determine the momentum spread of the beam.

Continuing from equation (2.11), the power in the Schottky spectrum, including dependence on the sensitivity of the detector S and the impedance of the analysing circuit Z, is given by [145]:

$$P(\omega) = \frac{NZ(qe\omega_0)^2}{4} \left|\tilde{S}(\omega)\right|^2 \frac{\Psi(\Delta p/p)}{|\eta k|}, \tag{2.13}$$

where $\Psi(\Delta p/p)$ is the power density function. For a peak associated with just one species, the power density function is given by $\Psi(\Delta p/p) = k\omega_0(1 + \eta \Delta p/p)$. A beam of multiple species will feature multiple peaks, each associated with the revolution frequency of that species. It should be noted that the Schottky power in equation (2.13) is proportional to q^2, so highly-charged heavy ions produce large Schottky signals, making it possible to observe single ions. Furthermore, the power density of a Schottky peak is directly proportional to the number of ions in the peak, meaning that the integrated Schottky peak can be used to determine the number of ions in the beam.

As is evident from equation (2.11) and Figure 2.5b, the non-zero frequency spread is compounded with each harmonic such that the width of the harmonic band grows proportional to the harmonic number k. The Schottky noise power in each harmonic band is constant, as demonstrated by the fact that equation (2.13) does not depend on k. This means that as the width of each harmonic grows, the noise power amplitude decreases by $1/k$, as shown in Figure 2.5b. For a high enough harmonic, the Schottky bands will overlap and the signals from different harmonics will mix.

From the discussion so far, we can see how Schottky signals from the longitudinal momentum spread can be used to measure the beam's mean revolution frequency, frequency spread (and thus momentum spread), and the number of particles (from the beam current). Schottky signals of sufficiently high resolution will also be able to separate different species. In addition to these parameters, the transverse Schottky signal of the beam can also be used to infer the fractional component of the tune, the linear component of the chromaticity, and the emittance of the beam [145]. Longitudinal signals are collected from the sum of the Schottky plates, whilst transverse signals are from the difference. We will not discuss the transverse methodology because we are primarily concerned with the longitudinal frequency analysis to extract that revolution frequency of the ions.

2.5.2 Schottky mass spectrometry

Whilst Schottky analysis was primarily implemented in the ESR to understand the beam parameters and behaviour of the storage ring, Schottky detectors are now mostly used for Schottky mass spectrometry (SMS). Schottky mass spectrometry utilises the fact that the revolution frequency in the storage ring is proportional to the p/q of an ion, as a result of the constant magnetic rigidity of the storage ring. The expression for the frequency relation in storage rings has already been derived in equation (2.7):

$$\frac{\Delta f}{f} = -\frac{1}{\gamma_t^2}\frac{\Delta(m/q)}{m/q} + \left(1 - \frac{\gamma^2}{\gamma_t^2}\right)\frac{\Delta v}{v}. \tag{2.14}$$

The non-zero momentum spread limits the frequency resolution of the ions as a result of the second term. Two operating modes are used to minimise this term: the *standard mode* where the velocity spread is suppressed via beam cooling, and the *isochronous mode* where the ring optics are tuned such that $\gamma_t = \gamma$ [146, 147]. Each mode has its advantages and disadvantages.

The standard ion optical mode has many advantages that, as the name suggests, makes it the primary operating mode for most experiments at the ESR. The standard mode features a large momentum acceptance of $\pm 2\%$ and large horizontal and vertical emittance acceptances of 450 and 150 mm mrad respectively [146]. These large acceptances mean many species can be analysed at once, which is crucial to ensure reference masses are available to minimise systematics. Additionally, the momentum dispersion in the straight sections of the ring is zero to first order in the standard mode, which is important for

focusing the beam on the internal target in other experiments. The lifetime of beams in the standard mode is also much longer, which is crucial for precision β decay studies of highly-charged ions [75, 147, 148]. Even when the primary goal of the experiment is not mass spectrometry, the SMS method is often applied to analyse the composition of the beam. However, the electron cooling required in the standard mode takes $\sim$ 1 s, which puts a lower limit on the half-life of ions that can be studied.

In the isochronous mode, the isochronous condition $\gamma_t = \gamma$ means that all orbits in the ring have the same revolution time (are isochronic). This produces the desired frequency resolution by cancelling out the velocity dependent term in equation (2.14). As a result, the beam does not need to be cooled so isotopes with much shorter lifetimes down to $\sim$ 10 ms can be measured, where the limiting factor is the measurement time of the Schottky detector [147, p.101]. The challenge for isochronous mass spectrometry (IMS) is that the isochronous condition $\gamma_t = \gamma$ needs to be established for a range of momenta such that multiple species can be measured [146, 147]. Since this mode needs to be established for each new magnetic rigidity, tuning the ring can be difficult and time consuming.

2.5.3 Schottky detectors at the ESR

From the earliest stages of the ESR's development, an electromagnetic pickup dedicated to Schottky analysis was implemented [149]. The parallel-plate Schottky detector, pictured in Figure 2.6a, uses two pairs of parallel plates connected capacitively in both the vertical and horizontal planes for longitudinal and transverse Schottky signals. The plates themselves are broad-band pickups, allowing for full beam diagnostics, but can be connected to a resonant circuit when sensitivity is required for Schottky mass spectrometry. The Schottky spectrum is typically observed at the 30^{th} harmonic for this detector, corresponding to roughly 60 MHz.

In 2011, a resonant-cavity Schottky detector was built, pictured in Figure 2.6b, to enhance the sensitivity for Schottky mass spectrometry [151]. The detector features a resonant pillbox cavity that is resonant at 245 MHz corresponding to roughly the 125^{th} harmonic. The larger harmonic means that Schottky peaks are better separated, which reduces the time required to capture a Schottky spectrum by a factor of four giving the detector a much better time resolution. The cavity is separated from the UHV by using a ceramic gap in the beam pipe, which was intended to protect the beam from the high impedance of the cavity whilst also allowing the detector to be pulled back if sensitive beams need to be stored. The walls of the cavity are electrically connected to the beam pipe with copper springs. The resonant response of the cavity can be adjusted by two plungers, which can alter the frequency response by over 2 MHz.

In 2020, a new 410 MHz resonant-cavity Schottky detector was built that improved many of the design features of the old resonant detector [152]. It was determined that the high impedance of the resonant cavity was not too detrimental to most beams used in the ESR, so to improve production efficiency and lower the price, the ceramic gap and copper

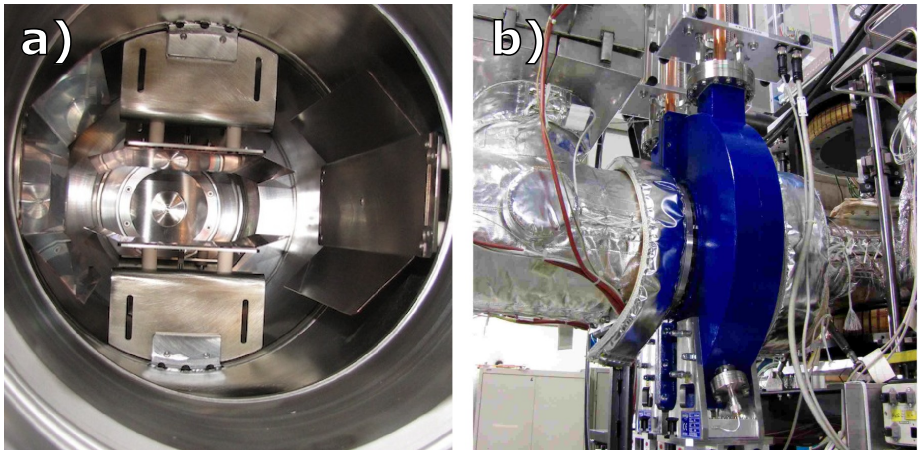

Figure 2.6: a) A photo of the broad-band parallel-plate Schottky detector, with plates for vertical and horizontal analysis. Reproduced from Sanjari (2013) [150] (© P. Petri, GSI, Darmstadt). **b)** A photo of the 245 MHz resonant-cavity Schottky detector. Reproduced from Steck & Litvinov (2020) [108] (© S. Sanjari, GSI, Darmstadt).

lining were removed and the detector was machined as one piece.

The resonant Schottky detectors are sampled by the new time capture Schottky data acquisition (NTCAP-DAQ) [153]. The spectrum analyser samples the waveform by recording the in-phase (I) and quadrature (Q) components, corresponding to an in-phase and quarter-cycle phase shift amplitude measurement that can be expressed as

$$x(t) = I\cos(\omega t) + Q\sin(\omega t). \tag{2.15}$$

The maximum sampling rate of the NTCAP-DAQ is 75 MSamples s^{-1}. For a given experiment, it is possible to choose how many IQ-samples are used in each Fourier transform, thus determining the time window of each spectrum. However, the frequency resolution is is inversely correlated to the time resolution of the detector.

2.6 Particle detectors

Whilst the ESR has a relatively large acceptance, there are many processes that will cause ions to leave the acceptance of the storage ring. These may be beam losses associated with charge-changing reactions, or they may originate from physical processes like β decay or reactions in the target. As a result, particle detectors are required to identify ions that leave the acceptance of the storage ring, both for experimental measurements and beam loss monitoring.

These particle detectors are housed in steel pockets that are 37 mm wide and 57 mm high, with a 25 μm thick stainless steel window where particles can enter [154]. Separating

the detectors from the ultra-high vacuum (UHV) of the storage ring has two distinct advantages. First, since everything inside the UHV needs to be baked at 300 °C, the detectors are not required to be made of UHV compatible material, which simplifies many design considerations. Secondly, different particle detectors can be easily swapped in and out between experiments without breaking the UHV. The ESR now features 12 pocket positions, shown as arrows in Figure 2.1, of which four are used for beam diagnosis, whilst eight are available for experimental use [155]. The experimental positions are chosen to intercept the orbits of ions whose charge state changed in the straight arms of the ring.

If only timing is required, fast scintillator detectors can be used. The incident ions excite a fluorescence response in the scintillator, whose light signal is collected by a photo-multiplier tube. Scintillators are known to have a much faster signal collection than most other detectors, and thus can handle much higher rates.

2.6.1 Multi-wire proportional chambers

The most popular type of particle detector used in the ESR is the gas-filled multi-wire proportional chamber (MWPC), which is pictured alongside the detector pocket in Figure 2.7a [154]. These detectors feature a stack of vertical cathode wires for horizontal position, anode wires in the middle, and cathode strips at the back, as depicted in Figure 2.7b. The detector is filled with a gas, typically isobutane, and the incident ion creates a path of electron-ion pairs where the electrons are collected on the anode wires generating a signal. The anode wires are all connected to create a fast signal that is used for timing, whilst the cathode wires/strips are connected by a 4 ns time delay chip to form a delay chain such that the timing difference between the two ends gives the position [156, 157]. These detectors can typically handle a rate of ~ 1 MHz [154].

If the beam is relatively simple and the number of detected ions high, then the MWPC spectrum can be used to identify isotopes based on their magnetic rigidity. These detectors are still the most widely used detectors in the ESR due to their flexibility and radiation durability. However, when there are many radioactive isotopes in the ring, more information is needed for particle identification.

2.6.2 δE particle detectors

Because the energy loss of a particle is proportional to Z^2 (at least at MeV energies, more details in Section 5.2.1), δE detectors provide elemental resolving power. The first δE particle detector for the ESR was designed at the TU Munich for the measurement of the bound and continuum β-decay rates of $^{207}Tl^{81+}$ [158]. This detector featured a stack of 14 Si PIN-diodes, shown in Figure 2.8a, with which energy loss could be measured with a δZ resolution of 0.55. This allowed for the identification of different species, crucial for separating $^{207}Pb^{80+}$ and $^{207}Tl^{80+}$ ions that have the same magnetic rigidity and left the ring due to electron capture during the experiment. However, this first-generation δE

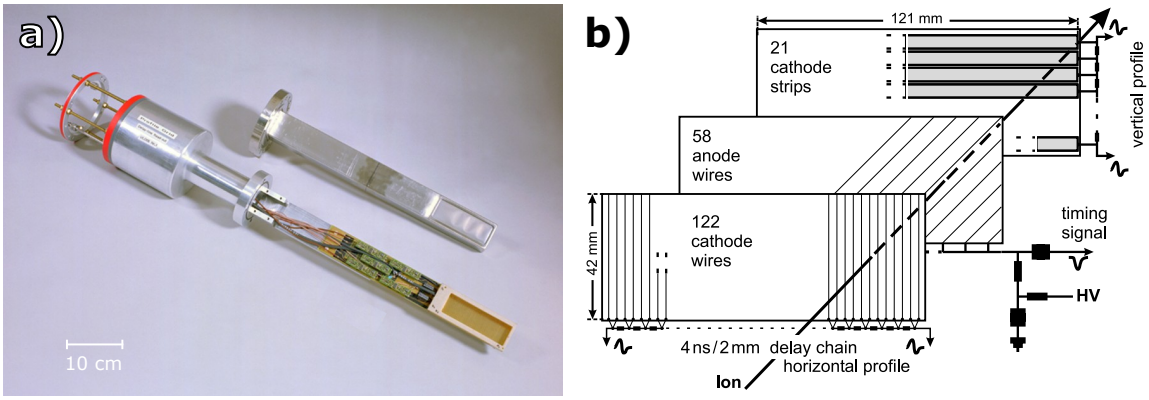

Figure 2.7: a) A photo of the MWPC detector alongside the ESR detector pocket (© O. Klepper, GSI, Darmstadt). The detector aperture is 121 mm × 42 mm. **b)** A schematic of the wire layout of the MWPC. The wire spacing gives 1 mm horizontal resolution. Reproduced from Klepper *et al.* (2003) [156].

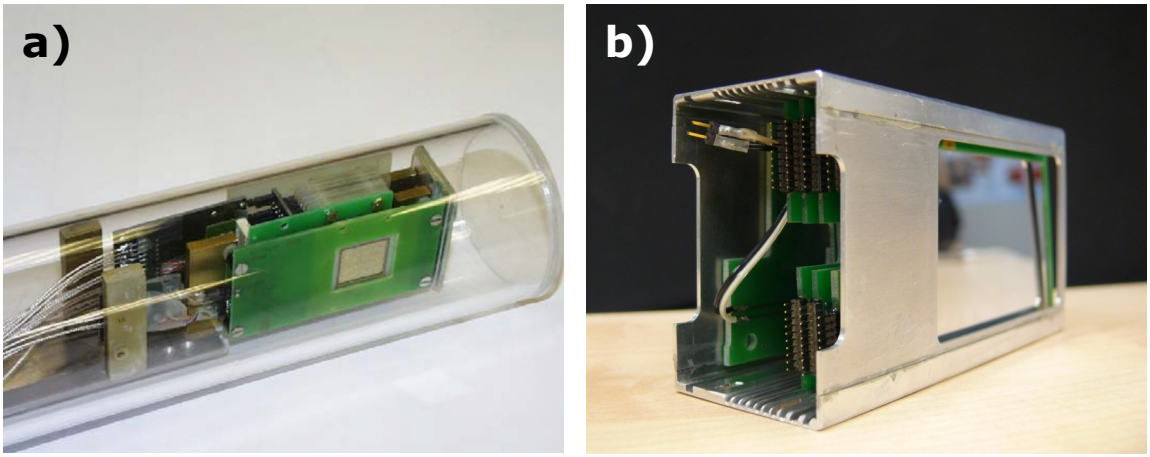

Figure 2.8: a) The TU Munich particle detector was the first δE detector for elemental identification of decay products. The Si active area is 21 mm × 21 mm. Reproduced from Maier (2007) [158]. **b)** The newer detector (CsISiPHOS) is pictured, which is a δE–E telescope detector for isotopic identification of decay products. It has a larger area Si detectors than the previous detector with an active area of 60 mm × 40 mm, and features a CsI scintillator stopper.

detector still cannot analyse complex beams with many species decaying because it cannot separate isotopes of the same element.

To achieve isotopic separation for heavy ions, a δE–E detector is required. The principle behind δE–E analysis is that the energy loss δE determines the Z of the particle whilst the total energy E determines the mass. The total energy of the particle is proportional to the mass A because each ion is kept at the same velocity in the storage ring by the electron cooler.

The CsI–Silicon Particle detector for Heavy ions Orbiting in Storage rings (CsISiPHOS) was the first prototype δE–E telescopic detector for the ESR, and was also built at the TU Munich [159]. The detector iterates on the previous design and also uses a stack of silicon detectors for energy loss, albeit with a much wider area allowing for complete coverage of the pocket window. To record the total energy of the particle, a CsI scintillator was added behind the silicon stack.

CsISiPHOS was commissioned during the precision measurement of H-like $^{142}Pm^{60+}$ and $^{140}Pr^{58+}$ ions [160]. It was able to fully separate the decay daughter and electron recombination product of $^{142}Pm^{60+}$, $^{142}Nd^{59+}$ and $^{142}Pm^{59+}$, respectively. This demonstrated successfully the isotopic separation ability of the detector. CsISiPHOS was also used for the measurement of the bound-state β decay of $^{205}Tl^{81+}$, which is described in Chapter 3.

CsISiPHOS was built as a prototype detector for a series of δE–E telescope detectors that were to be used in the Collector Ring (CR) at FAIR, Darmstadt. However, the construction of the CR has been postponed indefinitely, and so the detector design has been refocused for the ESR. A new detector called the ParticLE sIlicon-scintillAtor DEtector for Storage rings (PLEIADES) has been built with several improvements on the CsISiPHOS design. The construction and commissioning of PLEIADES is a major component of this thesis work, and is described in Chapter 5.

Chapter 3

Bound-State β Decay of $^{205}Tl^{81+}$

The experiment to measure the bound-state β decay of $^{205}Tl^{81+}$ exemplifies the type of unique measurements that can be achieved with heavy-ion storage rings. This experiment has a long history. It was one of the motivating experiments for the construction of the Experimental Storage Ring (ESR) [98] and was first proposed in the 1980s. Difficulties with the toxicity of Tl sources meant that the Tl beam had to be created via projectile fragmentation, which delayed the experiment until GSI had developed the technical capabilities of stacking multiple, secondary beams in the ESR. The realisation of this experiment has been the result of 40 years of hard work by many individuals.

The experiment was conducted in March/April 2020 during the opening weeks of the COVID-19 pandemic. Because only two people were allowed in a single room and international collaborators could not travel, some detectors were not set up optimally. This resulted in an analysis that was quite challenging, the conclusions of which are summarised in this chapter.

3.1 Experimental methods

To measure bound-state β^- decay (β_b decay), it is necessary to store ions in a highly-charged state, in the case of ^{205}Tl, the 80+ or 81+ state. In addition, to record a significant number of decays for isotopes with half-lives on the order of months to years, millions of ions need to be stored for several hours. Currently, heavy-ion storage rings are the only devices capable of meeting all three requirements, which is why the ESR is still the only facility that has experimentally measured β_b decay.

The GSI accelerator complex features a two stage acceleration system, with initial acceleration in the UNIversal Linear ACcelerator (UNILAC) [161] up to 20 MeV/u, followed by injection into the SIS-18 synchrotron [162] for further acceleration up to 1–2 GeV/u, depending on the beam. The UNILAC-SIS combination is capable of accelerating any beam from protons to ^{238}U, and the maximum energy is limited by the maximum magnetic rigidity of the SIS-18 at 18 Tm. Secondary beams can be created by projectile fragmentation, where a heavy beam is impinged on a light target creating a cocktail of collision products, typically dominated by several nucleon knockout products. These cocktail beams are then filtered with the Fragment Separator (FRS), which uses magnetic rigidity and energy loss separation, known as the $B\rho$–ΔE–$B\rho$ method, to isolate the secondary beam of interest from unwanted ions. All components in the FRS, such as the production target and energy

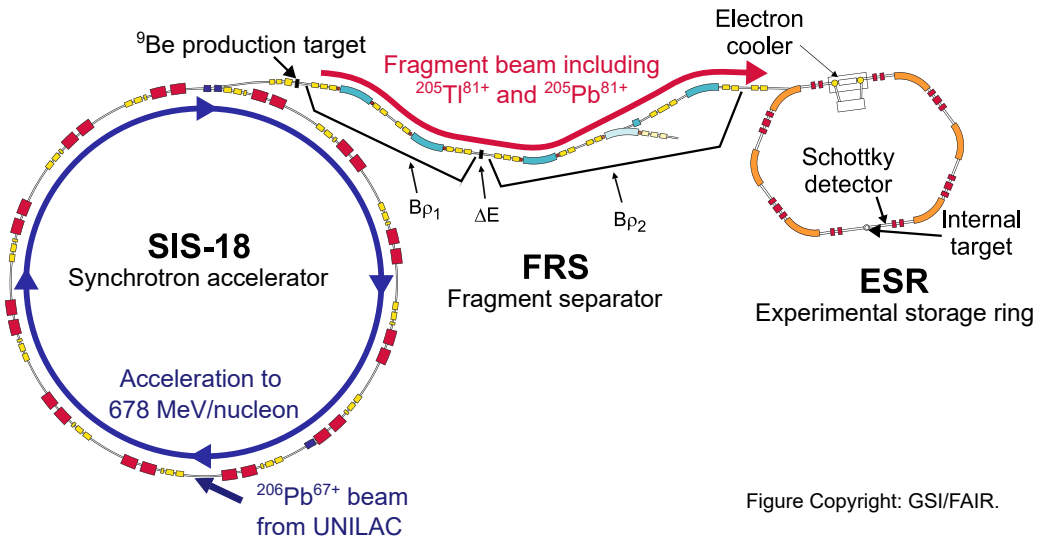

Figure 3.1: The layout of the GSI accelerator complex is shown. Low energy beams ($0.17c$) are delivered by the UNILAC and then accelerated to high energies ($0.82c$) by the SIS-18. Beams can be directly injected into the ESR, or secondary beams can be produced by projectile fragmentation and filtered with the FRS before being delivered to the ESR (details in text). Figure reproduced from Leckenby *et al.* (2024) [164].

degrader, are thick enough such that the emerging ions are in equilibrium charge-state distributions and do not depend on their initial charge [163]. This distribution is dominated by fully stripped ions at 400 MeV/u, which is the energy required to match the acceptance of the stochastic cooler. The beams (primary or secondary) are then injected into the ESR, where longitudinal stacking can be used to build up the beam intensity. The GSI accelerator complex is depicted in Figure 3.1.

The first β_b decay experiments [77, 78] used purpose-built ion sources made from the desired isotope to create an intense primary beam, since ^{163}Dy and ^{187}Re were stable. With longitudinal stacking in the ESR, it was possible to achieve up to 10^8 ions circulating in the storage ring. Unfortunately, thallium vapours are highly toxic, and hence the use of Tl as a source material was prohibited by GSI. Other options were investigated and found to be impractical, so it was concluded that ^{205}Tl had to be produced by projectile fragmentation. This method was pioneered in the ^{207}Tl measurement [79], where ^{207}Tl was created via one-proton knockout from a ^{208}Pb beam. However, since the neutral half-life of ^{207}Tl is 4.77 minutes, it was possible to observe sufficient decay products with just 10^3 parent ions.

Since the half-life of $^{205}Tl^{81+}$ was conservatively estimated to be up to a year, it was necessary to accumulate at least 10^6 parent ions to guarantee the detection of the decay, so much higher beam intensities had to be used for this experiment. As a result, whilst the

$^{205}Tl^{81+}$ β_b measurement was proposed in 1992, it wasn't until 2020 that the GSI accelerator facility had sufficiently improved technical capabilities across all accelerator systems that the measurement became feasible. The following discussion of the experimental method summarises many of the details provided in the thesis of R.S. Sidhu [165].

3.1.1 Production of $^{205}Tl^{81+}$ beams

For the ^{205}Tl measurement, an enriched ^{206}Pb source was used to create a $^{206}Pb^{67+}$ beam. The $^{206}Pb^{67+}$ beam was accelerated to 11.4 MeV/u in the UNILAC and was then injected into the SIS-18 where it was further accelerated to 592 MeV/u. $^{206}Pb^{67+}$ particles were accumulated in the SIS-18 via a multi-turn injection until $\sim 10^9$ particles per bunch were stored. These bunches were then fast-extracted within a single revolution and directed to the FRS for secondary beam production.

The production target at the entrance of the FRS was composed of beryllium with a niobium backing to facilitate fully-stripped ions that each had an effective thickness of 1607 mg cm^{-2} and 223 mg cm^{-2} respectively. The fragment beam produced was completely mixed due to energy and angular straggling in the target [166, 167]. The cross sections for fragment production via nucleon knockout decrease rapidly with the number of nucleons removed [168]. Most fragments were easily separated in the FRS or well resolved in the ESR. The exception was the isobaric contaminant $^{205}Pb^{81+}$, which is also the β_b-decay daughter. To separate this contaminant, a wedge-shaped Al degrader (effective thickness 735 mg cm^{-2}) was used at the central focal plane (S2), since energy loss is roughly proportional to the Z^2 of the ion [169]. This energy loss at S2 produced a spatial separation at the exit of the FRS (S6), as shown in Figure 3.2. Using a thicker degrader produced better separation, but at the cost of reduced transmission of the $^{205}Tl^{81+}$ beam. Roughly 10^4 $^{205}Tl^{81+}$ ions per bunch were injected into the ESR at 400 MeV/u, with $\sim$ 0.1% contamination from $^{205}Pb^{81+}$ ions.

The slits in the FRS are thick enough that they completely stop the beam. They are moved in with precise stepper motors, and the sharp edge can cut away the beam at different points in the FRS trajectory. During the setup of the experiment, many combinations of the slits S2 and S6 were tested to determine the optimum contamination suppression whilst not sacrificing transmission of the $^{205}Tl^{81+}$ beam. Two slit settings were used to take the bulk of the measurements (slit locations left/right in the horizontal plane):

1. **Setting 1:** 10 storage periods with slits S2 at 0/35 mm and S6 removed, and
2. **Setting 2:** 17 storage periods with slits S2 at 0/35 mm and S6 at −20/7 mm.

Whilst the slits at S6 were open in the first setting, the ESR has a finite acceptance so most $^{205}Pb^{81+}$ contamination was blocked by the ESR injection acceptance.

To achieve the desired 10^6 ions stored in the ring, roughly 100 injections were longitudinally stacked in the ESR. As described in Section 2.3.2, stochastic and electron cooling ($I_e = 200$ mA) were applied during this accumulation phase. The stacking was done on an

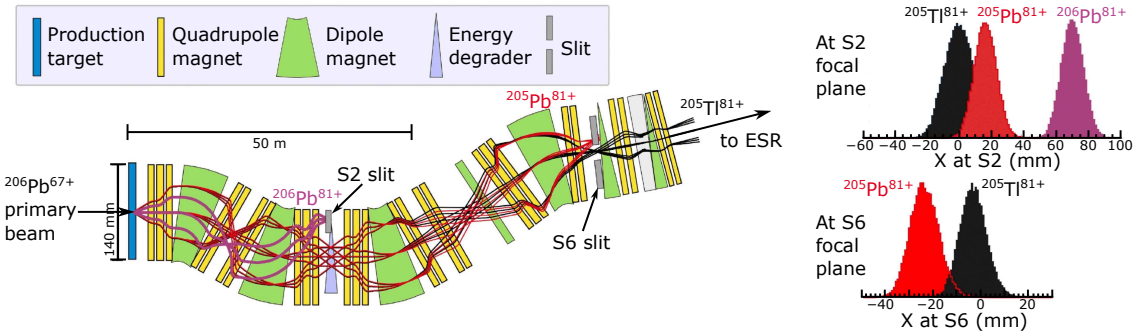

Figure 3.2: An ion-optical simulation of the expected $B\rho$–ΔE–$B\rho$ separation of $^{205}\mathrm{Tl}^{81+}$ and contaminant $^{205}\mathrm{Pb}^{81+}$ ions in the FRS. Note that the experimental separation achieved was larger than simulated here. Figure reproduced from Sidhu (2021) [165].

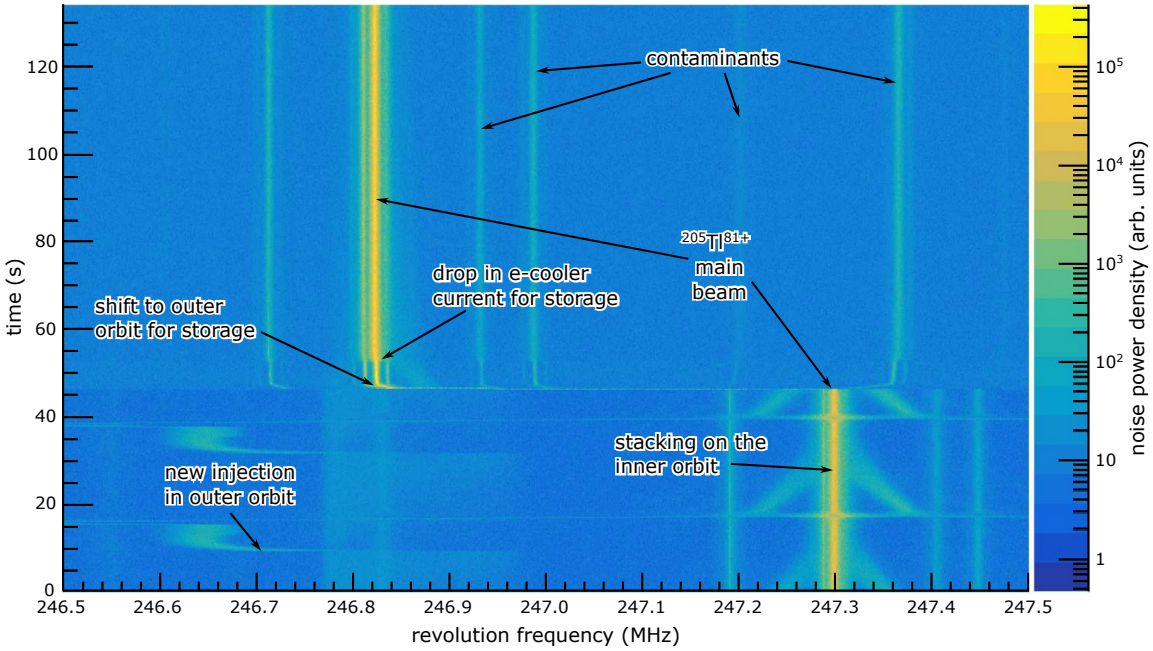

Figure 3.3: The Schottky noise power spectrum for 120 s showing the end of $^{205}\mathrm{Tl}^{81+}$ stacking, the orbit shift, and the start of storage. Figure reproduced from Sidhu (2021) [165].

inner orbit of the ESR and at the end of stacking the dipole magnets were simultaneously ramped down to move the $^{205}Tl^{81+}$ beam to an outer orbit in the ring. At this point the electron cooling current was lowered to $I_e = 20$ mA to reduce the radiative electron capture (REC) rate and facilitate the long lifetimes required for storage. This accumulation phase is shown in the Schottky spectrum in Figure 3.3.

3.1.2 Measurement protocol

During storage, the $^{205}Tl^{81+}$ parent ions decayed via β_b decay to $^{205}Pb^{81+}$ daughter ions. Because the β_b daughters have the same charge state as the parent ions (due to the bound β electron), the m/q only changes by the Q value of the decay, which in our case is very small ($Q^K_{\beta_b}(^{205}Tl^{81+}) = 31.1(5)$ keV). Consequently, the longitudinal orbits of the two species are so similar that intrabeam scattering disrupts the momentum resolving power of the electron cooler and the $^{205}Pb^{81+}$ orbit is mixed into the $^{205}Tl^{81+}$ beam. Thus, the $^{205}Pb^{81+}$ ions are completely indistinguishable from the $^{205}Tl^{81+}$ ions in the Schottky detector spectrum.

To count the number of β_b-decay daughters, the bound electron was stripped off by interacting the beam with an Ar gas jet target with densities between $(2\text{–}4)\times10^{12}$ atoms cm^{-2}. This revealed the ^{205}Pb ions in the 82+ charge state, where they had a substantially different m/q from the $^{205}Tl^{81+}$ ions ($^{205}Tl^{81+}$ is already fully stripped). During this phase, the electron cooler was set to $I_e = 200$ mA to keep the beam stored. After 10 minutes of stripping, the gas target was turned off and the Schottky peaks became well resolved due to the high electron cooler current. At this point, the Schottky areas of both $^{205}Tl^{81+}$ and $^{205}Pb^{82+}$ ions were measured.

The measurement protocol can be broken down into four phases:

1. **Accumulation:** where 100 injections from the FRS are stacked in the ESR,
2. **Storage:** where the $\sim 10^6$ $^{205}Tl^{81+}$ ions are decaying in the ESR,
3. **Gas stripping:** where the β_b daughters are stripped to $^{205}Pb^{82+}$ ions, and
4. **Measurement:** where the cooled and resolved Schottky intensities are recorded.

This breakdown is shown in Figure 3.4 where the integrated Schottky noise power intensities for the $^{205}Tl^{81+}$ and $^{205}Pb^{82+}$ peaks are plotted for a 3 hour storage cycle.

Recording of the final Schottky intensities happens during phase 4, but the number of ions needed to extract the half-life is at the end of phase 2. This is because the daughter-to-parent ratio before the gas stripping is required, since the differential loss rates during the interaction with the gas target will greatly alter the ratio. To go from the number of ions (proportional to the Schottky noise power area) measured during phase 4 to the end

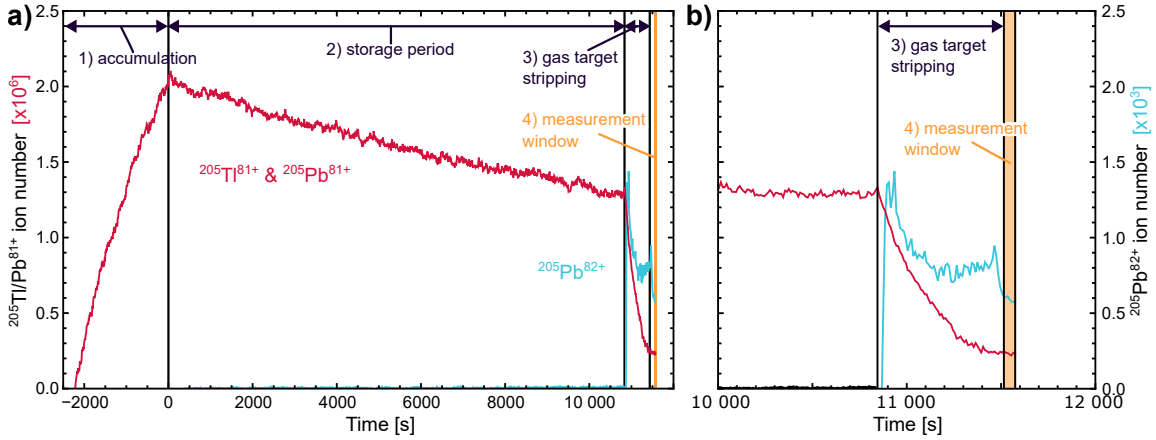

Figure 3.4: a) The measurement protocol is shown for a 3 hour storage, demonstrating the four key phases and highlighting how $^{205}Pb^{82+}$ ions are revealed during gas target stripping. **b)** The end of the measurement is shown. The $^{205}Pb^{81+}$ intensity plateaus once all ions are stripped. Figure reproduced from Leckenby *et al.* (2024) [164].

of phase 2, the following corrections need to be applied:

$$N^2_{\mathrm{Pb}^{81+}}(t_s) = N^4_{\mathrm{Pb}^{82+}}(t_s) \cdot \frac{1}{R_C} \cdot \frac{\sigma_{\mathrm{Pb,str}} + \sigma_{\mathrm{Pb,rec}}}{\sigma_{\mathrm{Pb,str}}} \cdot \frac{1}{1 - e^{-\lambda_{\mathrm{Pb,str}} \Delta t_{\mathrm{str}}}} \tag{3.1}$$

$$N^2_{\mathrm{Tl}^{81+}}(t_s) = N^4_{\mathrm{Tl}^{81+}}(t_s) \cdot S_C(t_s) \cdot \frac{1}{e^{-\lambda_{\mathrm{Tl,str}} \Delta t_{\mathrm{str}}}}, \tag{3.2}$$

where t_s indicates dependence on storage time, N^m_X is the number of X ions at phase m of the measurement, R_C is the resonance correction that accounts for the resonance response of the Schottky detector, $\sigma_{\mathrm{Pb,str/rec}}$ are the stripping and recombination cross sections in the gas target, $\lambda_{X,str}$ is the decay rate of ions interacting with the gas target, Δt_{str} is the stripping time, and S_C is the saturation correction to handle the observed saturation of the Schottky noise power areas. All these corrections, and the physical processes behind them, will be described in Section 3.2.

3.1.3 Particle detection

Throughout the measurement, both stored ions and ions leaving the acceptance of the storage ring were monitored with a variety of particle detectors. Beam monitoring was primarily done with the Schottky detectors, which continuously monitored the revolution frequencies of ions in the ring. In complement to the Schottky detectors, the beam was monitored by a DC beam Current Transformer (DCCT) that measures the total ion current in the ring. The DCCT was recorded with a scaler counter, where higher count rates

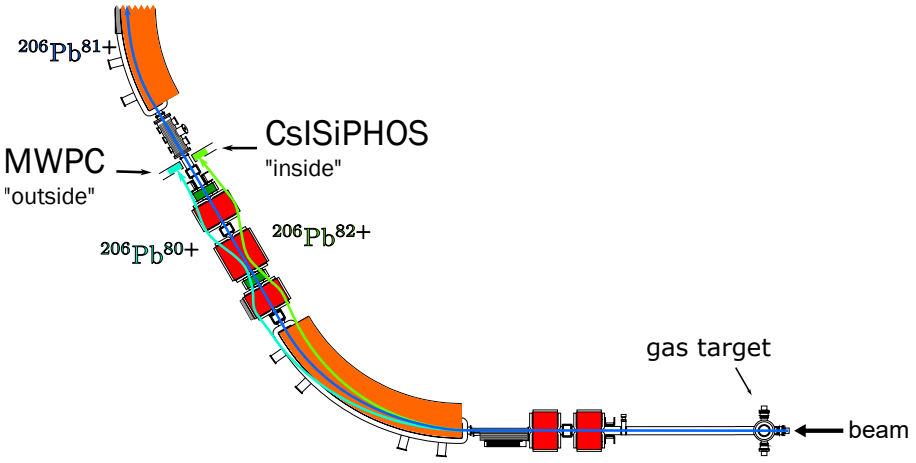

Figure 3.5: The inner and outer pockets were used to house the CsISiPHOS and MWPC detectors to measure the charge-changing cross-section ratio of H-like $^{206}Pb^{81+}$ ions (H-like means to have 1 electron, with an atomic electron configuration like H). Note that ion trajectories are schematic only.

indicated larger currents with some non-zero offset. It should be noted that the DCCT is a beam diagnostic tool, and was not intended for precision measurements.

Ions leaving the ring after the gas target were captured by the CsISiPHOS detector on the inside of the ring or an MWPC detector on the outside of the ring, as shown in Figure 3.5. CsISiPHOS is a *dE–E* telescope detector capable of separating individual isotopes. The MWPC detectors only have position sensitivity, but have proven to be very robust ion counters. Both detectors were introduced in Section 2.6. CsISiPHOS was used to detect stripping products from the gas target, whilst the MWPC detected recombination products. These particle detectors were used to determine several correction factors, and also used for redundant measurements of the beam lifetime during the gas stripping phase.

3.1.4 Growth equation

Because the stored ions are depleted by loss mechanisms (details in Section 3.2.6), the equation to describe the growth of decay-daughter products is non-trivial. The differential equations for $^{205}Pb^{81+}$ and $^{205}Tl^{81+}$ ions are given by

$$\frac{dN_{\mathrm{Tl}}(t_s)}{dt_s} = -\left(\lambda_{\mathrm{Tl}}^{\mathrm{loss}} + \frac{\lambda_{\beta_b}}{\gamma}\right) N_{\mathrm{Tl}}(t_s) \quad \text{and} \tag{3.3}$$

$$\frac{dN_{\mathrm{Pb}}(t_s)}{dt_s} = -\lambda_{\mathrm{Pb}}^{\mathrm{loss}} N_{\mathrm{Pb}}(t_s) + \frac{\lambda_{\beta_b}}{\gamma} N_{\mathrm{Tl}}(t_s), \tag{3.4}$$

where $\lambda_X^{\mathrm{loss}}$ is the loss rate for species X in the storage ring, and λ_{β_b} is the bound-state β-decay rate that needs to be converted to the laboratory reference frame by dividing by

the Lorentz factor γ. Whilst the solution to these equations is non-linear in its full form, Sidhu (2021) [165, p.45] showed that the solution is well approximated[8] by

$$\frac{N_{\mathrm{Pb}}(t_s)}{N_{\mathrm{Tl}}(t_s)} = \frac{\lambda_{\beta_b}}{\gamma} t_s \left[1 + \tfrac{1}{2}(\lambda_{\mathrm{Tl}}^{\mathrm{loss}} - \lambda_{\mathrm{Pb}}^{\mathrm{loss}}) t_s + \mathcal{O}(t_s^2)\right] + \frac{N_{\mathrm{Pb}}(0)}{N_{\mathrm{Tl}}(0)} \exp\left[(\lambda_{\mathrm{Tl}}^{\mathrm{loss}} - \lambda_{\mathrm{Pb}}^{\mathrm{loss}}) t_s\right], \quad (3.5)$$

which is linear with respect to λ_{β_b}. Note that the initial ratio $N_{\mathrm{Pb}}(0)/N_{\mathrm{Tl}}(0)$, which will be referred to as R_0 going forward, gets larger with storage due to the differential loss rates between $^{205}\mathrm{Pb}^{81+}$ and $^{205}\mathrm{Tl}^{81+}$ ions.

Across the two slit settings, 27 storage cycles were completed. The raw data for each of these measurement cycles is given in Table 3.1. Note that only parameters that vary with each storage cycle are given in Table 3.1, global corrections are provided in the following section. This result data, alongside further intermediate data from the Schottky and DCCT detectors, has been made publicly available on the data sharing platform Zenodo [170].

3.2 Analysis corrections

To determine the intensities of $^{205}\mathrm{Pb}^{81+}$ and $^{205}\mathrm{Tl}^{81+}$ ions at the end of the storage time, six analysis steps need to be conducted, as detailed in equations (3.1) and (3.2). These six steps include the measurement of the Schottky peak areas, four corrections to these Schottky values, and the determination of the respective storage loss rates.

3.2.1 Schottky integration

As discussed in Section 2.5.1, the noise power signal from a Schottky detector is proportional to the number of ions in the storage ring. Hence, the ratio of the integrated Schottky areas for the peaks in the spectrum associated with $^{205}\mathrm{Tl}^{81+}$ and $^{205}\mathrm{Pb}^{82+}$ is equal to the ratio of the numbers of those ions. For this analysis, the 245 MHz resonant Schottky detector was used as the 410 MHz detector had not yet been commissioned at the time of the experiment. At 245 MHz, the Schottky detector spanned three harmonics (124^{th}, 125^{th}, & 126^{th}), as shown in Figure 3.6. As a result of the saturation effect discussed in the following section, the 126^{th} harmonic was used to determine the ion intensity.

When constructing a Schottky spectrum, the number of IQ samples used to create a spectrum is a competition between time and frequency resolution. As high time resolution was not important, 2^{18} IQ samples were used to create 1 frame, and then 128 frames were averaged to get 1 histogram. Since the NTCAP DAQ [153] took 8 million samples per second for this experiment, the time width for each FFT frame was 32.8 ms making each histogram 4.19 s wide.

[8] Specifically, equation (3.5) differs by 0.15% for $t_s = 10$ hours, which is the largest deviation for our storage times.

Table 3.1: Result data for the measurement of the β_b decay of $^{205}Tl^{81+}$. 'Strg' refers to phase 2: storage, whilst 'strp' refers to phase 3: stripping. For the ratio, both raw errors and errors including the estimated contamination variation (CV) are given.

ID Tag	t_{strg} (hr)	SA_{Tl}	SA_{Pb}	SC	t_{strp} (s)	$\lambda_{\mathrm{Tl,strp}}$ (s^{-1})	$\lambda_{\mathrm{Pb,strp}}$ (s^{-1})	Ratio	$\mathrm{Err}_{\mathrm{raw}}$	$\mathrm{Err}_{\mathrm{CV}}$
Slit Setting 1 (S2: 0/35 mm, S6: removed)										
0hr_0403_02	0.01	3.966(17)e5	754(5)	1.254	609	2.739(5)e-3	6.05(26)e-3	1.19e-3	2.2e-5	9.6e-5
0hr_0403_12	0.01	3.769(25)e5	652(3)	1.219	610	2.795(5)e-3	6.07(26)e-3	1.07e-3	2.0e-5	9.6e-5
0.5hr_0403_00	0.51	6.707(55)e5	158(2)	1	607	2.711(15)e-3	5.94(28)e-3	1.87e-3	4.3e-5	1.0e-4
0.5hr_0403_03	0.51	3.677(18)e5	3,471(62)	1.210	618	2.756(6)e-3	6.04(27)e-3	5.89e-3	1.5e-4	1.8e-4
0.5hr_0403_11	0.51	4.355(14)e5	814(8)	1.307	601	2.870(5)e-3	6.04(23)e-3	1.05e-3	2.7e-5	9.8e-5
1hr_0403_01	1.01	3.467(13)e5	654(4)	1.181	610	2.784(6)e-3	6.03(27)e-3	1.21e-3	2.3e-5	9.8e-5
2hr_0403_04	2.01	2.594(10)e5	595(4)	1.091	609	2.828(7)e-3	6.33(22)e-3	1.56e-3	3.2e-5	1.0e-4
3hr_0402_20	3.02	2.439(16)e5	440(2)	1.078	609	2.728(8)e-3	5.91(29)e-3	1.32e-3	2.9e-5	1.0e-4
4hr_0403_06	3.99	2.370(10)e5	538(5)	1.071	609	2.694(8)e-3	5.75(31)e-3	1.72e-3	3.8e-5	1.1e-4
8hr_0403_12	8.00	1.551(6)e5	452(5)	1	610	3.002(9)e-3	6.70(16)e-3	1.89e-3	4.5e-5	1.1e-4
Slit Setting 2 (S2: 0/35 mm, S6: -20/7 mm)										
0hr_0403_23	0.01	3.818(39)e5	476(6)	1.223(6)	609	3.065(5)e-3	6.85(13)e-3	6.48e-4	1.1e-5	7.3e-5
0hr_0404_02	0.00	2.858(11)e5	575(6)	1.113(4)	609	3.063(6)e-3	6.85(13)e-3	1.15e-3	1.3e-5	7.2e-5
0hr_0404_17	0.01	1.871(8)e5	340(4)	1.033(4)	609	3.100(8)e-3	6.92(11)e-3	1.09e-3	1.4e-5	7.2e-5
0hr_0406_04	0.00	2.810(15)e5	620(4)	1.110(4)	607	3.368(18)e-3	7.60(5)e-3	1.05e-3	1.5e-5	7.3e-5
0.5hr_0404_00	0.42	2.791(11)e5	581(3)	1.106(4)	609	3.110(7)e-3	6.98(11)e-3	1.16e-3	8.4e-6	7.2e-5
0.5hr_0404_16	0.51	2.591(12)e5	548(3)	1.089(4)	609	3.231(6)e-3	7.12(8)e-3	1.11e-3	9.4e-6	7.2e-5
0.5hr_0405_21	0.52	2.869(10)e5	574(6)	1.115(4)	609	3.256(6)e-3	7.22(7)e-3	1.01e-3	1.1e-5	7.2e-5
0.5hr_0405_22	0.52	2.827(20)e5	579(5)	1.113(4)	608	3.084(6)e-3	6.93(15)e-3	1.16e-3	1.3e-5	7.3e-5
1hr_0405_23	1.01	2.669(10)e5	605(5)	1.096(4)	609	3.231(6)e-3	7.27(6)e-3	1.18e-3	1.2e-5	7.3e-5
1.5hr_0406_05	1.52	2.536(14)e5	566(4)	1.084(4)	607	3.322(11)e-3	7.48(3)e-3	1.12e-3	1.2e-5	7.4e-5
2hr_0405_09	2.02	2.373(11)e5	534(7)	1.070(4)	609	3.170(7)e-3	7.12(8)e-3	1.25e-3	1.8e-5	7.5e-5
3hr_0406_00	3.01	2.131(11)e5	534(4)	1.051(4)	608	3.284(8)e-3	7.38(4)e-3	1.32e-3	1.4e-5	7.5e-5
4hr_0405_15	4.02	1.816(12)e5	392(5)	1.027(4)	609	3.046(8)e-3	6.74(15)e-3	1.35e-3	2.0e-5	7.8e-5
5hr_0404_09	5.01	1.578(8)e5	400(3)	1	607	3.064(9)e-3	6.65(16)e-3	1.62e-3	1.8e-5	7.8e-5
6hr_0404_02	6.00	1.084(5)e5	289(3)	1	603	3.230(10)e-3	7.31(6)e-3	1.56e-3	1.9e-5	7.9e-5
10hr_0404_23	10.05	6.77(5)e4	221(3)	1	608	3.236(12)e-3	7.36(5)e-3	1.87e-3	3.1e-5	8.6e-5
10hr_0406_08	10.02	1.179(10)e5	402(6)	1	606	3.141(21)e-3	7.01(11)e-3	2.08e-3	4.5e-5	9.3e-5

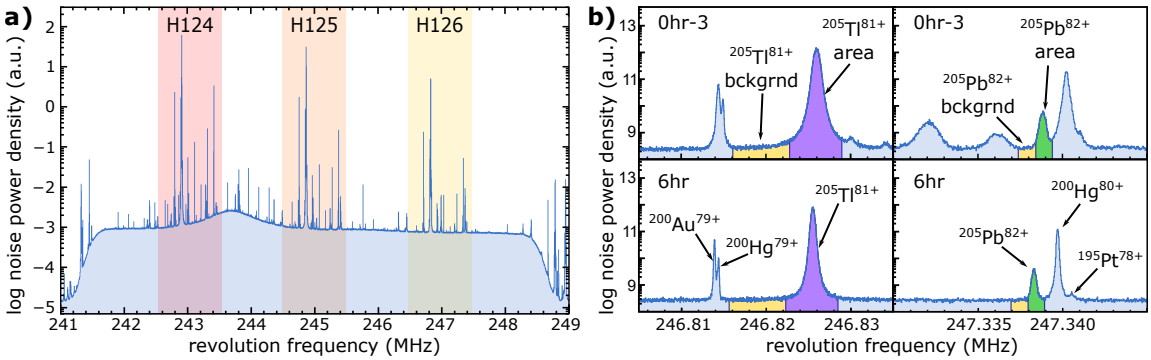

Figure 3.6: a) A Schottky spectrum showing all three harmonics recorded. The resonance effect of the cavity can be seen in the bump of the thermal noise at 243.8 MHz. The shoulders of the background are generated from the windowing in the Fourier transform. **b)** To determine the peak area, the spectrum was integrated (purple/green for $^{205}Tl^{81+}/^{205}Pb^{81+}$, respectively) and the neighbouring constant background (yellow) was subtracted.

To determine the peak area for a given histogram, a direct integration was done across the peak width, and a background integration of identical width was subtracted. This simple integration method was chosen because a) the peaks were well separated even on a log scale as shown in Figure 3.6b, and b) the $^{205}Tl^{81+}$ peak shape was neither Gaussian nor Lorentzian, so would have been challenging to fit. The measurement period (phase 4) occurred 100–140 s after the gas target was turned off and the beam was cooled. Thus 9 histograms from this time period were averaged to get a mean peak area with an error in the mean calculated by $\sigma/\sqrt{N}$.

3.2.2 Schottky saturation correction

The first correction that needs to be applied to the Schottky peak areas is the Saturation Correction (SC), which accounts for a saturation effect observed in the recorded Schottky data. The Schottky signals are transported to the NTCAP DAQ with the assistance of several amplifiers. One of these amplifiers was mistakenly switched on by default in an unexpected interaction with the updated accelerator control systems. This caused the NTCAP DAQ to clip the incoming waveforms as the signal exceeded the dynamic range of the NTCAP DAQ, which generated a saturation effect resulting in the Schottky noise power density no longer being proportional to ion number. Consequently, the integrated Schottky peaks decay non-exponentially, as seen in Figure 3.7c. The effect was independently confirmed with a follow up test using $^{238}U^{73+}$ beam and a Tektronix spectrum analyser, where the saturation of the NTCAP DAQ was clearly reproducible, as demonstrated in Figure 3.7b. To identify the intensity threshold at which saturation set in for our data, the decay constant of the beam measured by the MWPC was used in a fit to the Schottky noise power data such that the only free parameter was the final intensity at the end of

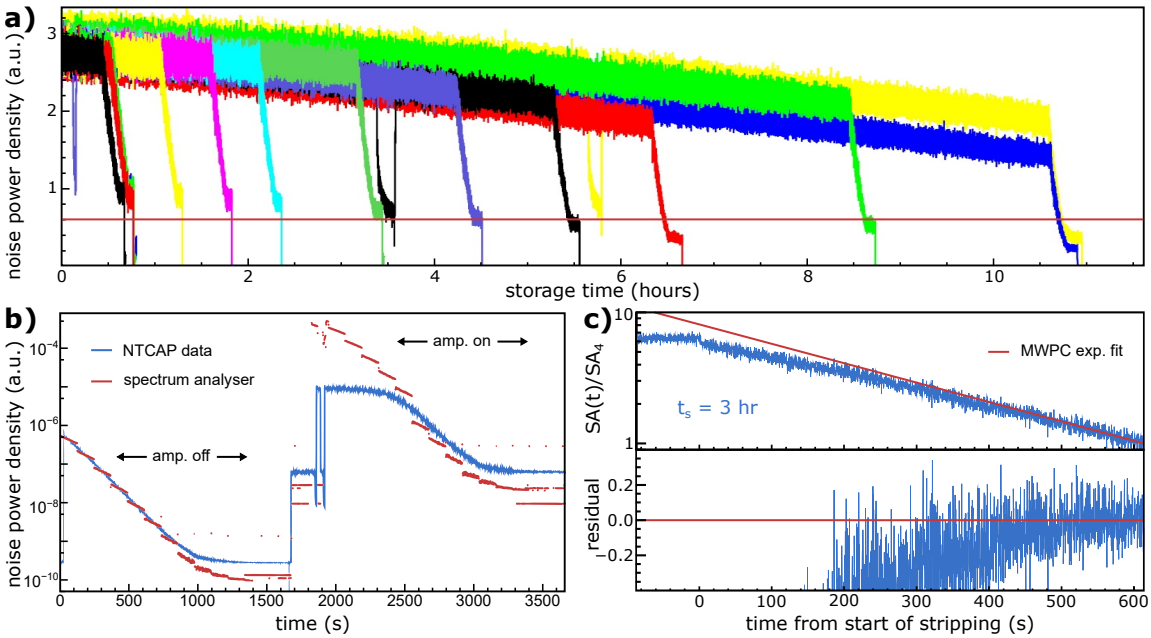

Figure 3.7: a) The saturation threshold is compared to the $^{205}Tl^{81+}$ intensity for all storage times (colours are different storage time measurements). Almost all $^{205}Tl^{81+}$ peaks were saturated at the time of measurement. **b)** A beam test with $^{238}U^{73+}$ confirmed that the NTCAP DAQ adaptive amplifier caused the saturation effect when compared to a spectrum analyser. **c)** The intense Schottky peaks did not follow the exponential decrease measured by the MWPC detector. Here the Schottky area (SA) is normalised to the value at measurement (SA_4). The onset of saturation was determined by the departure from the measured MWPC exponential decay.

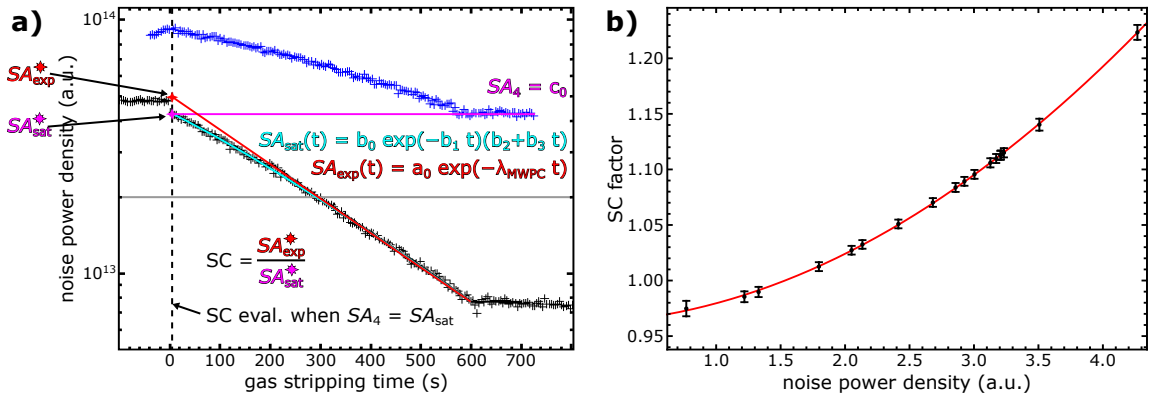

Figure 3.8: a) The algorithm where the expected exponential growth (SA_{exp}) for the 10hr-1 storage time is compared with the actual saturated growth (SA_{sat}), and the saturation correction (SC) is then evaluated at the intensity for measurement (SA_4 for this example of 0hr-1). **b)** The trend of the SC values with respect to the Schottky area is shown, demonstrating that the correction is dominated by the systematic error of fitting the 10hr-1 reference.

gas stripping (phase 3). This fit is shown in Figure 3.7c. The departure from exponential behaviour was observed at 400 s, which corresponded to noise power intensities over 0.6 (arbitrary units for the $^{205}Tl^{81+}$ peak). This was chosen to mark the saturated and non-saturated regions shown in Figure 3.7a.

This analysis revealed that for 12 shortest storage times, the Schottky noise power data was saturated for the $^{205}Tl^{81+}$ peak at the measurement phase (the $^{205}Pb^{82+}$ peak had a much smaller intensity, well below the saturation threshold). The $^{205}Tl^{81+}$ peak intensity during phase 2 (stripping) spans all values of the Tl peak at phase 4 (measurement). The first 10-hour storage cycle (10hr-1) was best suited as a calibrant as it had the lowest final intensity and thus the largest portion of phase 2 in the non-saturated region. Two models were applied to the 10hr-1 data:

$$SA_{\text{exp}}(t) = a_0 \exp(-\lambda_{MWPC} t) \tag{3.6}$$

$$SA_{\text{sat}}(t) = b_0 \exp(-b_1 t)(b_2 + b_3 t) \tag{3.7}$$

where $SA_{\text{exp}}(t)$ was the expected behaviour using the MWPC decay rate whilst $SA_{\text{sat}}(t)$ was a phenomenological model that replicated the saturation effect, as shown in Figure 3.8a. The ratio between these two models at the measurement intensity defined a Saturation Correction factor $SC = SA_{\text{exp}}/SA_{\text{sat}} > 1$ for any given noise power density at phase 4.

To quantify the error in the SC algorithm, a Monte Carlo calculation was used to propagate the fit errors to the SC values. To do this correctly, the four fit parameters for SA_{sat} had to be sampled from a Multi-Normal distribution to handle the correlations between the variables correctly. Examining the contributions of each fit parameter, the main source of error in the SC algorithm was the fitting of the 10hr-1 calibrant equations. If SA_{sat} and SA_{exp} had been fit simultaneously such that $a_0 = b_0$ was the same fit parameter, most of this systematic error would have cancelled out, but the algorithm was not designed with that in mind. Ultimately the SC value contributes only 0.5% of the total error.

Finally, as evident in Figure 3.8b, the saturation correction function produces SC values that are < 1 for the three longest storage times, which is not physical. This is possible because SA_{sat} and SA_{exp} have different parameters, and are thus slightly different. In hindsight, this was a poor analysis choice and $SA_{\text{exp}}/SA_{\text{sat}}$ should have been made to converge below the saturation threshold. Instead, all SC values below the saturation threshold (i.e. for storage times 5 hours and longer) had no saturation correction applied.

3.2.3 Resonance correction

The second correction to the Schottky area ratio is the resonance correction (RC), which accounts for the resonant response of the Schottky detector. Whilst the detector was sensitive between 241.6–248.4 MHz, a strong resonance response was centred at 243.8 MHz associated with the fundamental resonance frequency of the cavity. This amplified the Schottky power of species closer to the resonance peak, and the amplification needed to be corrected in order to compare the intensities of the $^{205}Tl^{81+}$ and $^{205}Pb^{82+}$ peaks.

Ideally, the resonance curve would have been mapped out by moving ions from a normalisation orbit to a variety of orbits so a functional form could be fit throughout the entire detector. Unfortunately, only the coincidental mapping associated with moving the $^{205}Tl^{81+}$ beam from an inner orbit for stacking to the outer orbit for storage was available, as a full characterisation was not planned. During this period, the beam was cooled and the magnets were simply ramped, so beam loss was negligible and the Schottky intensity of peaks can be compared directly before and after the orbit shift. Fortunately the $^{205}Pb^{82+}$ orbit was quite close to the inner stacking orbit, so this shift characterised the resonance curve at roughly the correct frequencies.

The resonance response of the detector is shown in Figure 3.9a. The zero-current noise is plotted in blue, showing the characteristic Schottky background shape featuring:

- the intensity shoulders associated with windowing[9] in the Fourier transform,
- the resonance peak from resonant amplification of thermal noise in the detector, and
- the flat background originating from the amplification of thermal noise in the electronic components of the detector.

The background plot has a fundamentally different shape than the function that describes the resonance response for integrated noise density peaks, plotted in red in Figure 3.9a. This is because thermal noise is additive after the amplifier but our signal is multiplicative after the amplifier, so the shape of the resonance curve does not scale with the increased signal. The green and purple data points are the integrated $^{205}Tl^{81+}$ noise density before and after the orbit shift associated with the 124^{th}, 125^{th}, and 126^{th} harmonics respectively. If these were accurate intensities, they could have been used to fit the resonance function in red. However, these peaks are saturated so the absolute intensity is not accurate. In Figure 3.9a, the resonance correction would be given by the ratio of the green and purple intensities, as these are the same ions.

Due to the saturation of the Schottky data, only the 126^{th} harmonic could be used for our data analysis so the resonance corrections need to be determined for this harmonic. The $^{205}Tl^{81+}$ intensities at the 126^{th} harmonic were saturated, so contaminant species had to be used to map out the resonance correction. Two candidates were identified that were close to the desired orbits, the mixed $^{203}Tl/Hg^{80+}$ peak and the mixed $^{200}Hg/Au^{79+}$ peak. These contaminant species are resolvable but overlapping in the Schottky spectrum (see Figure 3.6b), so for simplicity the whole double-peak area was used.

Figure 3.9b shows the before/after orbit shift intensities for these contaminants against their frequency. Because the intensity for each measurement is different, only two data points are available for each measurement, so the intensity values in Figure 3.9b have been normalised to 1 at 247 MHz. Over the scale of this 0.8 MHz range, the resonant response of the detector is assumed to be approximately linear, so a line was drawn through

[9] Windowing is a technique used in spectral analysis to reduce the impact of discontinuities in the signal due to the finite sample used in the fast Fourier transform algorithm.

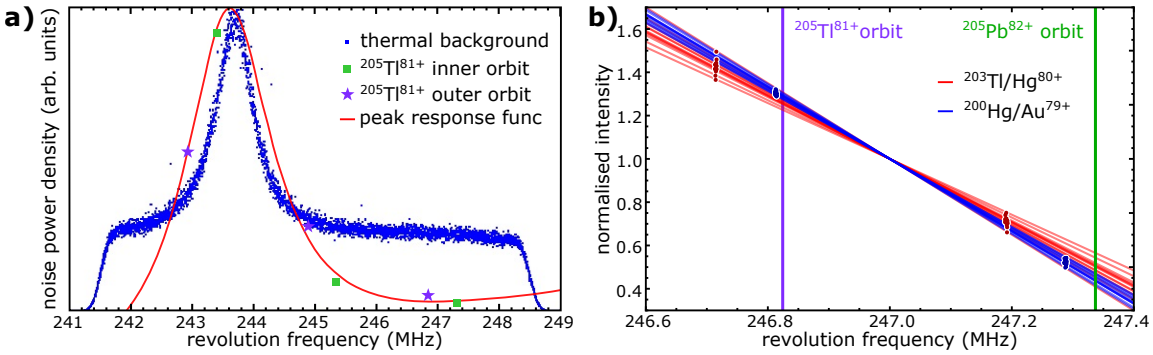

Figure 3.9: a) The zero-current response of the Schottky detector is shown in blue, demonstrating the resonance peak in response to thermal noise. In green/purple, the intensity of the $^{205}Tl^{81+}$ peak before/after the orbit shift is overlayed for the three harmonics. **b)** The before/after intensities (normalised to 1 at 247 MHz) are plotted for the 126th harmonic for the contaminants $^{203}Tl/Hg^{80+}$ and $^{200}Hg/Au^{79+}$. The frequency of the desired $^{205}Tl^{81+}$ and $^{205}Pb^{82+}$ peaks are shown in cyan and green respectively.

the two data points to approximate the resonance curve for each measurement. This allowed us to calculate the resonance correction for each measurement at the $^{205}Tl^{81+}$ and $^{205}Pb^{82+}$ frequencies of 246.8244 MHz and 247.3371 MHz respectively (see vertical lines in Figure 3.9b).

A statistical scatter was observed amongst the calculated RC values, as seen in the fitted lines in Figure 3.9b. It was hypothesised that such a scatter could be generated from the frequency shifts between experiments. However, Figure 3.9b shows just how small the frequency shift was compared to the scatter in the slope (equivalent to RC value). In addition, the correlations between contaminant ions and harmonics were analysed to determine if this scatter was correlated to the storage measurements, which would indicate the scatter was systematic. No significant correlations were observed, even in self-correlations across different harmonics, so it was concluded that the scatter in the RC values was statistical. Thus, the mean values for each contaminant, with errors derived from bootstrapping, were $RC_{\mathrm{Tl/Hg}} = 0.394(11)$ and $RC_{\mathrm{Hg/Au}} = 0.345(4)$. It is unsurprising that the $^{200}Hg/Au^{79+}$ values were more precise as the before/after frequencies are closer to the $^{205}Tl^{81+}$ and $^{205}Pb^{82+}$ frequencies. Because of this a weighted average of $RC = 0.352(4)_{\mathrm{stat}}$ was taken as the final statistical value despite the fact that the values are not in statistical agreement.

Because the values are not in statistical agreement with each other, and because the linear scaling from both contaminants are equally valid, albeit with the $^{200}Hg/Au^{79+}$ being more accurate, a systematic error equal to the standard deviation of a uniform distribution (i.e. $\Delta RC/\sqrt{12}$) was adopted to represent the tension between the two measurements. Thus, the adopted value for the resonance correction was

$$RC = 0.352(4)_{\mathrm{stat}}(14)_{\mathrm{syst}}. \tag{3.8}$$

This correction is a systematic error common to all measurements as the resonance response is a property of the detector.

3.2.4 Charge-changing cross-section ratio

The third correction factor has been termed the "cross-section ratio correction" (CSRC). This correction accounts for the fact that whilst $^{205}Pb^{82+}$ ions stripped by the gas target were recorded, $^{205}Pb^{80+}$ ions created by electron recombination left the acceptance of the ring. Since the beam and target are identical for these two reaction channels, the correction factor is the ratio of the charge-changing reaction cross-sections:

$$\frac{\sigma_{\mathrm{Pb,str}} + \sigma_{\mathrm{Pb,rec}}}{\sigma_{\mathrm{Pb,str}}} = \frac{N_{\mathrm{CsISi}} + N_{\mathrm{MWPC}}}{N_{\mathrm{CsISi}}} = \frac{R_{\mathrm{DCCT}}}{R_{\mathrm{DCCT}} - R_{\mathrm{MWPC}}}, \tag{3.9}$$

where N_X is the number of ions counted in a detector X and R_X is the rate in that detector.

To measure this cross-section ratio, a measurement was conducted with primary ^{206}Pb beam where H-like $^{206}Pb^{81+}$ ions were reacted with the gas target, and the CsISiPHOS and MWPC particle detectors captured the stripping and recombination products respectively. By counting the number of counts in the stripping vs recombination channels, the cross-section ratio could be determined. A DC beam Current Transformer (DCCT) was also used to measure the total ion current in the ring

Particle detectors

Unfortunately, simple ion counting with the particle detectors turned out to be impossible as issues with the energy signatures of events meant that the total number of particles could not be determined reliably. For CsISiPHOS, the main problematic feature was a 'lower band' of events that were recorded with a lower energy, despite having only mono-energetic $^{206}Pb^{81+}$ ions in the ring. This lower band is shown in Figure 3.10a on the n-side of the last silicon detector. Whilst several explanations regarding potential shaper or preamp undershoot were proposed, they were ultimately rejected because the timing distributions of the lower band events looked completely normal. In addition, the saturation of the CsISiPHOS deadtime[10] at $\sim 60\%$ could not be explained, despite being clearly correlated to the appearance of the lower band. Thus, it was concluded that a satisfactory explanation of the CsISiPHOS data could not be provided.

The MWPC also showed some peculiar features, shown in Figure 3.11. For the Y-axis channels, two anomalous peaks appeared around the main event spot, which appeared outside the physical limits of the detector when the position signal was calibrated. These were probably the result of electronic reflections where the DAQ did not trigger on the first

[10]Deadtime refers to the amount of time for which the DAQ is unable to accept new triggers due to it being busy reading out the previous event. It is often expressed as a percentage to indicate the extent to which the DAQ is unavailable to process new events.

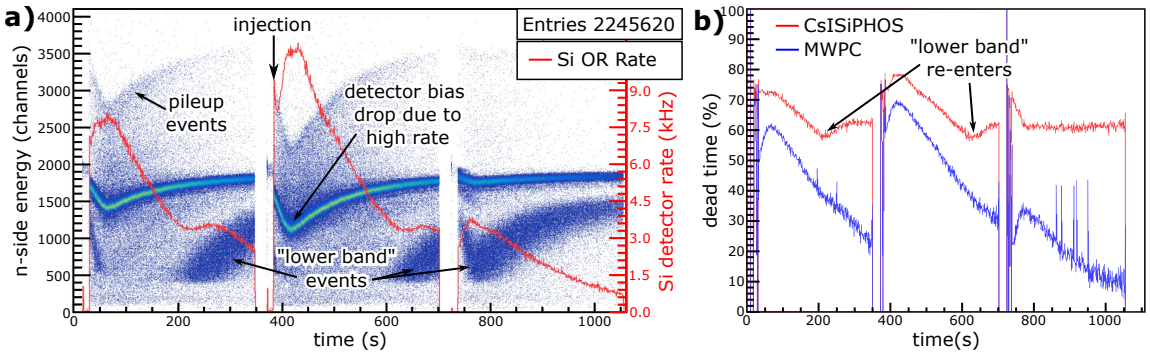

Figure 3.10: a) The CsISiPHOS n-side spectra shows a dE measurement of the ions. A depression in the energy is correlated with rate due to the voltage depletion caused by the high rate. An unknown 'lower band' of events, which is much more strongly affected by the voltage depletion, is also present; see text for hypotheses. **b)** The deadtime for the CsISiPHOS & MWPC detectors is shown for 3 injections. Whilst the deadtime of the MWPC decreases exponentially with rate, the CsISiPHOS deadtime plateaus, which coincides with the "re-entry" of the unknown lower band.

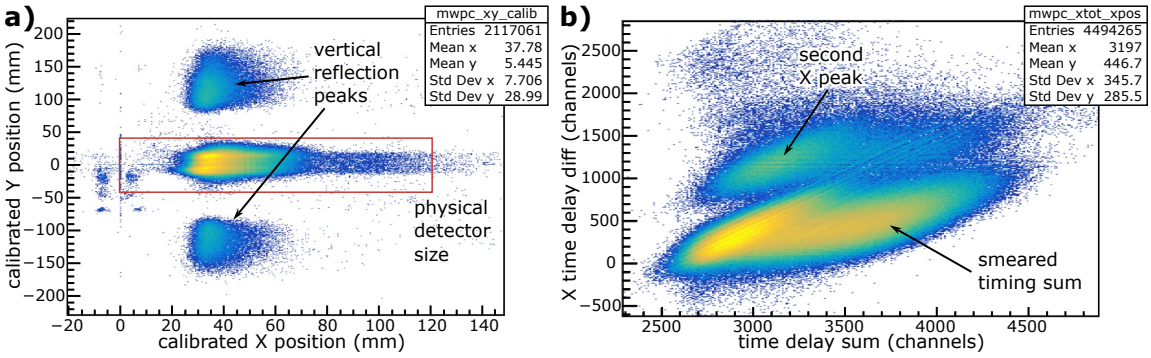

Figure 3.11: a) The calibrated MWPC position spectra is shown. Given the detector dimensions are 121×42 mm, the Y-resolution is quite bad and the secondary Y-peaks are unphysical (see text for details). **b)** The X-time delay (constant for all events) vs the X-position reveals two peaks in X from under the time delay smearing, despite there being only one species in the ring.

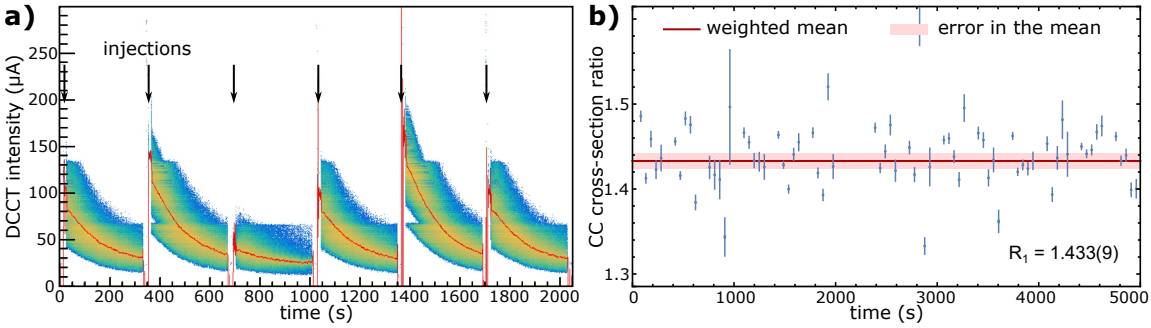

Figure 3.12: a) The DCCT intensity is plotted for individual events, with the 1s average superimposed in red. This variation is due to the high rate compared to the scaler count rate. **b)** The CCCS ratio calculated using the derivative from 50 s averaged DCCT intensity points, with the final value for this method plotted in red.

timing signal, but this was not confirmed. The X-axis channels also showed a second peak, indicating events were arriving from two slightly different trajectories. However given there were so many issues with the position channels on the MWPC, it was ultimately decided to just trust the anode signals, which counted the total number of events.

"Ions reacted" method

Because of the difficulties with CsISiPHOS, the CSRC was instead determined from the total ion loss rate, with ionisation to bare Pb being determined by the subtraction of the recombination rate from the total loss rate, as in the last expression of equation (3.9). Because the Schottky data was saturated, the DCCT was used. The DCCT was recorded with a scaler counter, and the high event rate meant that the scaler counter did not accrue many counts per event, so a stable time derivative to calculate the rate was very challenging. In particular, the derivative did not stabilise until a window of 50 seconds was used. Figure 3.12a shows the DCCT intensity for individual events, demonstrating the large scatter. The DCCT also has a zero-current offset to ensure non-zero scaler counting even if the ring is empty. This offset was determined in two ways, from 124 'stray' events when the ring was empty yielding a value of 23.44(23) μA, and from the offset of exponential + constant fits from the 14 injections of primary beam yielding a value of 22.86(23) μA. Both measurement distributions overlapped, so the 'stray events' method was chosen as it featured more events. Note that this DCCT offset was determined from the particle detector DAQ. A different offset was determined for the NTCAP DAQ, as will be discussed in Section 3.2.6.

In the first and most direct approach for calculating the cross-section ratio, the ions reacted (measured by the DCCT) over a 50 s recording window were used to calculate 70 independent values for cross-section ratio, shown in Figure 3.12b, each with uncer-

tainty values from the underlying counting statistics from the scaler and MWPC events and the DCCT offset calibration. The correlation in the DCCT offset was handled by propagating errors using a Monte Carlo calculation, which ensured the statistical errors were not correlated. However, the resulting normalised residuals indicated the raw error bars underestimated the statistical spread around the mean. Given the statistical errors only included counting errors, it was concluded that there was some unquantified missing statistical uncertainty since the DCCT was not intended for precision measurements. A Bayesian analysis was used to allow the data to constrain this missing uncertainty, which was assumed to be Gaussian from the Central Limit Theorem with a Jeffrey's prior. Integrating out the missing-uncertainty nuisance parameter lead to a Gaussian posterior distribution for the cross-section ratio of $R_1 = 1.433(9)$.

In the second approach, the DCCT data was fit with an exponential decay function, circumventing the problem of an uncertain local derivative with a global fit. However, the decay rates determined from the DCCT were systematically lower than from the MWPC, despite measuring the same interaction with the gas target, as shown in Figure 3.13a. A potential explanation was found in the Schottky spectrum where broad peaks next to the main peak were observed that grew over time, despite only having primary $^{206}\mathrm{Pb}^{81+}$ in the ring. Throughout this part of the experiment, the stochastic cooler could not be turned off due to a technical issue, so it was proposed that the stochastic cooler was providing a RF-kick to ions throughout the storage, building a "side band" over time which would reduce the measured decay constant of the DCCT rate. This could be modelled as two populations, the Main Beam (MB) and the Side Band (SB):

$$N'_{MB}(t) = -(\lambda + k)N_{MB}(t) \qquad N'_{SB}(t) = kN_{MB}(t), \tag{3.10}$$

where λ was the gas target decay rate and k was the stochastic cooler kick-out rate. This differential equation has the solutions

$$N_{MB}(t) = N_0 e^{-(\lambda+k)t} \qquad N_{SB}(t) = \frac{N_0 k}{\lambda + k}\left(1 - e^{-(\lambda+k)t}\right). \tag{3.11}$$

The total population $N_{MB} + N_{SB}$ was fit to the DCCT data using the MWPC value for λ, and the best fit was used to calculate the ions reacted with the gas target.

Whilst this theory was not able to be definitively proven, the decay rate from the MWPC was much more reliable as it comes from physical events and directly measured gas-target reactions. Thus, two values for the cross-section ratio were calculated: $R_2 = 1.425(3)$ from explicitly fitting a 'side band', and $R_3 = 1.418(2)$ from simple exponential decay also using the MPWC decay rate.

To combine the alternate methods, the spread in the three analysis models was accounted for with a modelling systematic uncertainty of 0.0043, taken from the variance of a uniform distribution ($\Delta R/\sqrt{12}$). The side band model was chosen as the most accurate analysis to be used as the central value. As mentioned when discussing the MWPC above,

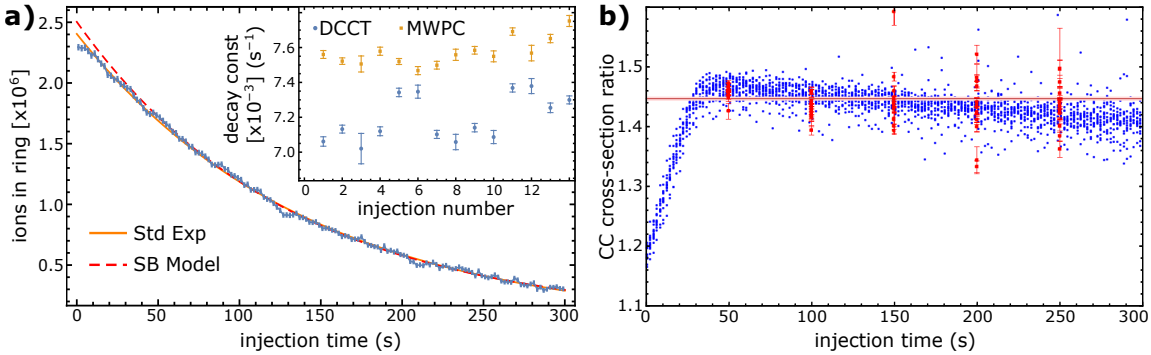

Figure 3.13: a) The global exponential fit to the DCCT data is shown. The inset shows the decay rates for the DCCT and the MWPC, with the MWPC showing systematically higher rates. **b)** The difference in decay rates causes the ratio to decrease with time. Note though that the spread of this method is well within the spread of the DCCT averaging method, plotted in red.

$\sim$ 5% of MWPC events demonstrated anomalous behaviour despite only primary beam being in the ring (i.e. the Y-reflection events and the 2nd X-peak). A systematic error of 0.0117 from the difference in including vs excluding these events was added, also using the variance of a uniform distribution. This resulted in a final value for the charge-changing cross-section ratio of

$$R = 1.4247(29)_{\text{stat}}(126)_{\text{syst}}. \tag{3.12}$$

Note that in a Bayesian analysis, you would ideally construct a probability distribution with these different values to represent your systematic error. Since we are conducting a Frequentist analysis, we decided to represent the magnitude of our systematic uncertainty using uniform distributions associated with the range between different model results, but ultimately use the value of the most reliable model as the central value.

3.2.5 Gas stripping efficiency

The fourth correction factor accounts for the interaction with the gas target. In particular, $^{205}\text{Tl}^{81+}$ ions are lost to electron recombination whilst $^{205}\text{Pb}^{82+}$ daughters are uncovered by stripping (recombination is already accounted for by the cross-section ratio correction), so the intensity of the two species throughout gas stripping is given by:

$$N_{\text{Tl}^{81+}}(t) = N_{\text{Tl},2}\, e^{-\lambda_{\text{Tl,str}} t} \tag{3.13}$$

$$N_{\text{Pb}^{82+}}(t) = N_{\text{Pb},2}\big(1 - e^{-\lambda_{\text{Pb,str}} t}\big) \tag{3.14}$$

where $N_{\text{X},2}$ is the ion number at the end of phase 2 (storage) and $\lambda_{\text{X,str}}$ is the stripping decay constant, which is specific to individual species.

The MWPC was inserted during most storage times, so individual values for $\lambda_{\text{Tl,str}}$ were determined for 24 of the 28 storage times by fitting an exponential to the event rate

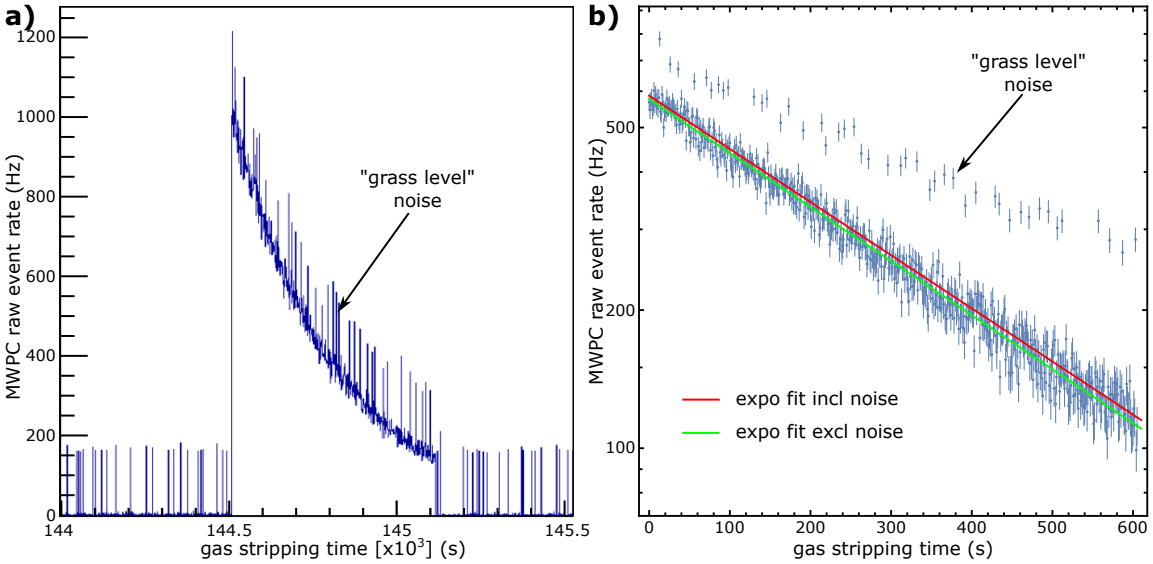

Figure 3.14: a) A "grass-level" noise was observed in the MWPC, even when the gas target was turned off. The high intensity spurts at 180Hz are quite puzzling, but easy enough to exclude from the fit, as demonstrated in **b)**.

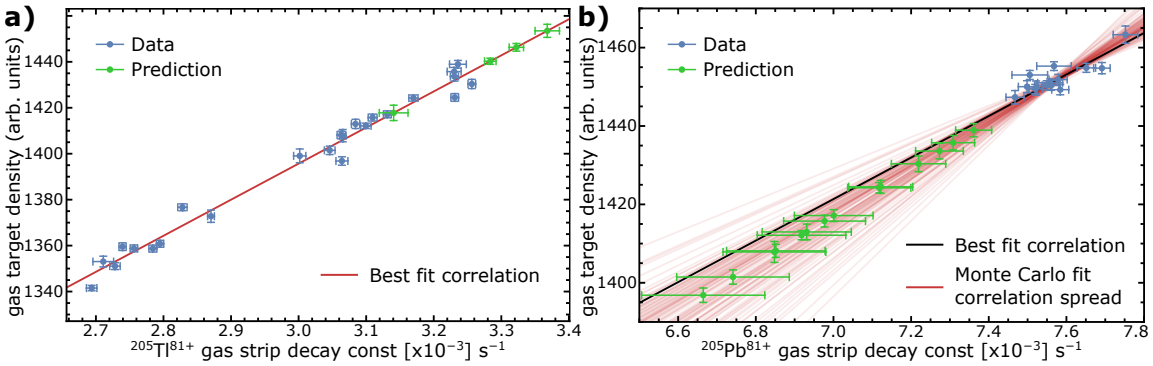

Figure 3.15: Variations in the stripping decay constants were very well described by a correlation with the gas target density. Panel **a)** shows the $^{205}Tl^{81+}$correlation, whilst **b)** shows the $^{206}Pb^{81+}$ rates, which cover considerably less range than the $^{205}Tl^{81+}$rates. Thus the extrapolation for the $^{206}Pb^{81+}$ rates is much more uncertain, but this ultimately has little impact on the percentage of ions stripped.

measured in the detector. A "grass-level" noise was observed on top of the MWPC rate signal, which featured a temporally stochastic $\sim$ 180 Hz background on top of the real signal, as shown in Figure 3.14a. Whilst the origin of this noise was not determined, it was stochastic enough to not be a binning error and constant enough to not be associated with the signal of interest. Thus, a fitting routine was developed to discard these points, shown in Figure 3.14b.

The fitted decay rates for $^{205}Tl^{81+}$ stripping showed considerable variation larger than their error bars. This variation was perfectly explained by correlation with the gas target density, which was measured by the scaler counter throughout the experiment, as shown in Figure 3.15a. This correlation was then used to estimate the $\lambda_{\mathrm{Tl,str}}$ value for the four measurements for which the MPWC was not inserted, with the uncertainties determined by the intercepts of the gas target error bars with the fitted correlation line.

The $^{205}Pb^{81+}$ stripping rates could not be measured directly, but they are identical to the $^{206}Pb^{81+}$ stripping rates that were measured for the charge-changing cross-section ratio. However, as shown in Figure 3.15b, the gas target density range covered by the 14 ^{206}Pb stripping runs was much smaller than the range that occurred during the storage measurements. Thus, the correlation fit is much less certain, as shown by the range of fits in red that were produced by doing a Monte Carlo calculation using the $^{206}Pb^{81+}$ errors. As a result, the extrapolation to the appropriate gas target values is also much less certain. However, these large uncertainties have surprisingly little impact on the final number because the calculated $^{205}Pb^{81+}$ stripping efficiencies are between 98.5-99.0% as the stripping time is quite long at $\sim$ 600 s.

3.2.6 Storage losses

The last parameter is the loss rate when storing the ions in the ring. Ideally, the storage decay constant would have been measured using the Schottky data for the $^{205}Tl^{81+}$ beam. However, this data was saturated, so the storage loss constant had to be determined from the DCCT data.

The DCCT was recorded by two data acquisition systems (DAQ). Because of the low event rate in the particle detectors during storage, the CsISiPHOS DAQ data was challenging to use, so only the NTCAP DAQ data was analysed. The DCCT is supposed to have a constant offset so the scaler signal can be recorded even at zero current. The offset was determined to be 28.20(1) μA from data where the ring was empty. However, when the storage loss data was fit with the offset as a free parameter, the offset varied between 27–33 μA. It was not confirmed whether the offset remains constant throughout different intensity regimes, but since this was how the detector was designed, it was assumed that it does.

With this offset, an exponential function was fitted to the DCCT storage loss data to determine the decay constant $\lambda_{\mathrm{Tl}}^{\mathrm{loss}}$ for the 12 non-0hr measurements from Setting 2 and 2 non-0hr measurements from Setting 1. Because the underlying statistical distribution of

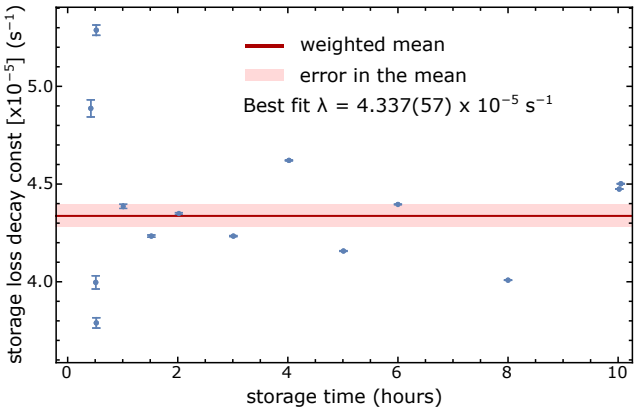

Figure 3.16: The NTCAP DCCT storage loss fits are plotted and the final λ_{Tl}^{cc} parameter is shown in red. Note that the size of the error bars are not calibrated (see text for details).

the NTCAP scaler counter was difficult to determine due to the consistent polling frequency (i.e. not a histogram so not simply Poissonian statistics), these fits were done without error bars using un-normalised least squares. As a result, the χ^2 was un-normalised and errors at $\chi^2_{\text{min}} \pm 1$ did not give parameter errors. In this case, the error on the parameters is essentially proportional to the number of data points in the fit, of which there were many due to the choice of binning. Thus, whilst the relative size of the error bars on the fits *is* meaningful, the absolute size *is not* calibrated.

Figure 3.16 shows the fit results. The error bars are miniscule compared to the variation because they are un-normalised errors. Given prior experimental experience, it was concluded that λ^{loss} was constant throughout the experiment. To extract the mean, a weighted bootstrapping was done, which successfully described the uncertainty resulting from the variation in the observed fits, whilst also using the inverse square errors as weights to reflect the accuracy of each fit (a 10hr storage constrains λ^{loss} better than a 0.5hr storage). The resulting value is $\lambda^{\text{loss}}_{\text{Tl}} = 4.337(57) \times 10^{-5}$ s^{-1}, which is also plotted in Figure 3.16 in red with 1σ shaded bands.

To derive $\lambda^{\text{loss}}_{\text{Pb}}$ in previous β_b experiments, the λ^{loss} value was measured for the H-like parent and a simple Z^2 scaling was applied. For this experiment, the $\lambda^{\text{loss}}_{\text{Pb}}$ value was intended to be measured directly with a 2-hour storage of the $^{206}\text{Pb}^{81+}$ beam. However, the stochastic cooler was unable to be turned off during this measurement, which resulted in the side-bands that grew with time, as mentioned in Section 3.2.4. Thus, $\lambda^{\text{loss}}_{\text{Pb}}$ could not be determined from this measurement.

Instead, a theory-based scaling factor had to be used to estimate the $\lambda^{\text{loss}}_{\text{Pb}}$ from the measured $\lambda^{\text{loss}}_{\text{Tl}}$ value. This theoretical calculation was done by Dr. Alex Gumberidze from GSI, who used non-relativistic quantum mechanical methods [171, 172] to estimate the radiative recombination (RR) rate of $^{205}\text{Tl}^{81+}$ and $^{205}\text{Pb}^{81+}$ ions bathed in a $I_e = 20$ mA

electron cooling current:

$$\mathrm{Tl}^{81+}:\ \text{RR rate } 9.0\times10^{-5}\ \mathrm{s}^{-1}, \qquad \mathrm{Pb}^{81+}:\ \text{RR rate } 8.3\times10^{-5}\ \mathrm{s}^{-1}. \tag{3.15}$$

There is a factor 2 disagreement with our measured value, but it is well known that theory and experiment deviate a lot at e-cooling conditions. Additionally, the electron current may have been slightly lower than 20 mA. This is not a problem as we use the ratio (0.92) for the scaling, and the theoretical calculation is usually reliable with respect to itself.

To complement the quantum estimate, a semi-classical approach (Kramer's formula) [173] was also done resulting in a ratio of $\mathrm{RR}_{Pb}/\mathrm{RR}_{Tl} = 0.90$. Each calculation used different approximations, so we believe the range of the two ratios (0.02) is reasonable estimate for the theoretical uncertainty. We chose to represent this uncertainty with a uniform distribution, but use the value of $\mathrm{RR_{Pb}}/\mathrm{RR_{Tl}} = 0.92$ to scale our result. This yields a $^{205}\mathrm{Pb}^{81+}$ loss rate of $\lambda^{\mathrm{loss}}_{\mathrm{Pb}} = 3.990(53)_{\mathrm{stat}}(23)_{\mathrm{syst}}\times10^{-5}\ \mathrm{s}^{-1}$ (theoretical uncertainty is the systematic).

Since the ultimate implementation of the λ^{loss} correction is used in the term $\frac{1}{2}(\lambda^{\mathrm{loss}}_{\mathrm{Tl}} - \lambda^{\mathrm{loss}}_{\mathrm{Pb}})t_s$ in equation (3.5), the difference between the two parameters is the most important. In the Monte Carlo half-life fit (see Section 3.3.2), the correlations involved in this scaling are handled so as not to overestimate the uncertainty from this $(\lambda^{\mathrm{loss}}_{\mathrm{Tl}} - \lambda^{\mathrm{loss}}_{\mathrm{Pb}})$ term. In particular, the $(\lambda^{\mathrm{loss}}_{\mathrm{Tl}} - \lambda^{\mathrm{loss}}_{\mathrm{Pb}})$ term can be written to more explicitly represent our scaling:

$$\begin{aligned}(\lambda^{\mathrm{loss}}_{\mathrm{Tl}} - \lambda^{\mathrm{loss}}_{\mathrm{Pb}}) = \lambda^{\mathrm{loss}}_{\mathrm{Tl}}\left(1 - \frac{\mathrm{RR}_{Pb}}{\mathrm{RR}_{Tl}}\right) &= \big(4.337(57)\times10^{-5}\big)\big(0.08(2)\big)\ \mathrm{s}^{-1},\\ &= 3.47(5)_{\mathrm{stat}}(87)_{\mathrm{syst}}\times10^{-6}\ \mathrm{s}^{-1}.\end{aligned} \tag{3.16}$$

This is the value that was used for the calculations.

3.2.7 Classification of errors

It is important to clarify our interpretation on the distinction between statistical and systematic errors in this analysis. Each analysis component that was measured individually for each storage period is a statistically independent measurement and will thus cause statistical scatter in the storage data points. This is what we call statistical errors. The analysis components that were measured and applied globally to every storage period are fully correlated and thus cannot cause statistical scatter in the data points. This is what we call systematic errors, even though their quoted uncertainty may have arisen from statistical effects. The classification of each source of error depends both on the underlying physics, and how each correction was observed to behave. In particular:

- **Schottky peak areas (§3.2.1):** The uncertainty arises from Poissonian counting statistics and thermal noise in the Schottky detectors, so clearly a source of statistical uncertainty.

- **Saturation correction (§3.2.2):** The uncertainty arises in the fitting of the calibration functions N_{exp} and N_{sat} for the 10hr-1 storage, and the final $^{205}\text{Tl}^{81+}$ intensity for the individual storages. Our Monte Carlo propagation showed that the calibration functions are the dominant source of uncertainty, making it a systematic uncertainty.
- **Resonance correction(§3.2.3):** The frequency shift between storages due to magnet fluctuation is too small to explain the variation in RC values, so our uncertainty is dominantly a systematic uncertainty.
- **Charge-changing cross-section ratio (§3.2.4):** This is a physical parameter, and thus clearly a systematic uncertainty.
- **Gas stripping efficiency (§3.2.5):** The $^{205}\text{Tl}^{81+}$ gas stripping losses originate from statistical uncertainties in fitting the MWPC rate, so they are statistical uncertainties. The $^{205}\text{Pb}^{81+}$ gas stripping efficiency arises from a linear interpolation based on the target density, and the uncertainty in these values is dominated by the uncertainty in the calibration fit, not the gas target density. Thus the $^{205}\text{Pb}^{81+}$ efficiency values are dominated by systematic uncertainties.
- **Storage losses (§3.2.6):** Based off previous experiments, and the fact that the DCCT was not the most reliable measuring device, it was concluded that the storage losses were not sensitive to individual variations in the cooler current. Thus, the dominant source of our uncertainty in the storage loss rates was measurement based, and the parameter was applied globally making this a systematic error.

The fractional contribution of each error is shown in Figure 3.17.

a)

Uncertainty Source	Type	Fraction	Legend
Schottky statistics	stat	6.5%	
Saturation correction	syst	0.47%	
Resonance correction	syst	17.1%	
CC cross-section ratio	syst	0.82%	
Tl gas stripping	stat	2.7%	
Pb gas stripping	syst	0.02%	
Tl storage losses	syst	0.12%	
Pb loss theory scaling	syst	3.5%	
γ factor	syst	0.005%	
Est. contam. variation	stat	68.7%	

b)

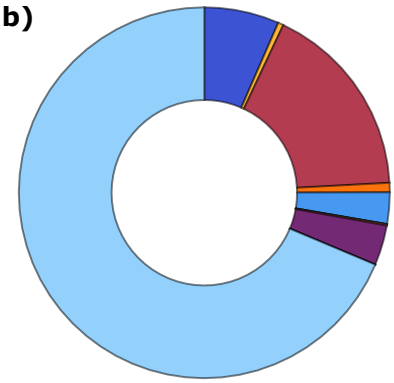

Figure 3.17: **a)** A table classifying the different sources of uncertainty and their fractional contribution to the total uncertainty. **b)** A pie chart of the uncertainty fractions. Statistical errors are shown in shades of blue, whilst systematic errors are shown in sunset shades.

3.3 $^{205}Tl^{81+}$ half-life fit

All the analysis steps that are required to get the $^{205}Pb^{81+}$ over $^{205}Tl^{81+}$ ratio at the end of storage have now been discussed, so the corrected ratios can now be plotted and the growth equation (3.5) can be fit. As discussed in Section 3.1.1, two slit settings were used and the two data sets are plotted in Figure 3.18, where the 1σ error bars are just the statistical errors.

The data is generally consistent but there are two obvious outliers: for Setting 1 the second 0.5-hr measurement is $5\times$ larger than the rest of the data, and in Setting 2 the first 0-hr measurement is half the value of the others. Both data points have been heavily examined for possible errors in the analysis, but the Schottky signals are unmistakable: there are simply more/less $^{205}Pb^{81+}$ ions in the ring for those measurements than in the other runs. Given the technical challenges of the measurement, these data points have been removed as unphysical for the analysis (see footnote in Section 3.3.3 for the impact of this choice on the final result).

The Setting 1 data presents other, slightly more challenging data points. For example, the first 0.5-hr measurement is also inconsistent with the rest of the data. This measurement had *much* lower statistics than the others, receiving only 9 stacks from the FRS (compared with the 30 stacks for other Setting 1 measurements, and 100 stacks for Setting 2 measurements). These statistics, however, should be encapsulated in the larger error bars and cannot explain a 60% larger value than nearby data. Nonetheless, this point was also excluded as an outlier for the analysis on the Setting 1 data, but this "threshold" is not particularly well motivated.

Looking at the raw data in Figure 3.18, the error bars are smaller for low storage times because the negligible effect of storage losses λ^{loss} resulted in better statistics that improved the determination of every component of the measurement.

3.3.1 Initial contamination variation

It is quite clear that for both sets of data, the error bars cannot account for the variation in the data (only 4 out of 16 of the 1σ error bars overlap). For the Setting 2, the χ^2 calculated from the best fit of Equation 3.5 is

$$\chi^2 = \sum_i \frac{(\text{data}_i - \text{model}_i)^2}{\sigma_{i\text{stat}}^2} = 302.7. \tag{3.17}$$

Given our 16 data points and two fit parameters λ_{β_b} and R_0, the 95% confidence interval for the χ^2 distribution with 14 degrees of freedom is $[6.57, 23.7]$. The value of 302.7 is clearly incompatible with this range. This means either:

1. our model does not describe the data well, or
2. our statistical errors do not fully account for the variation in the data.

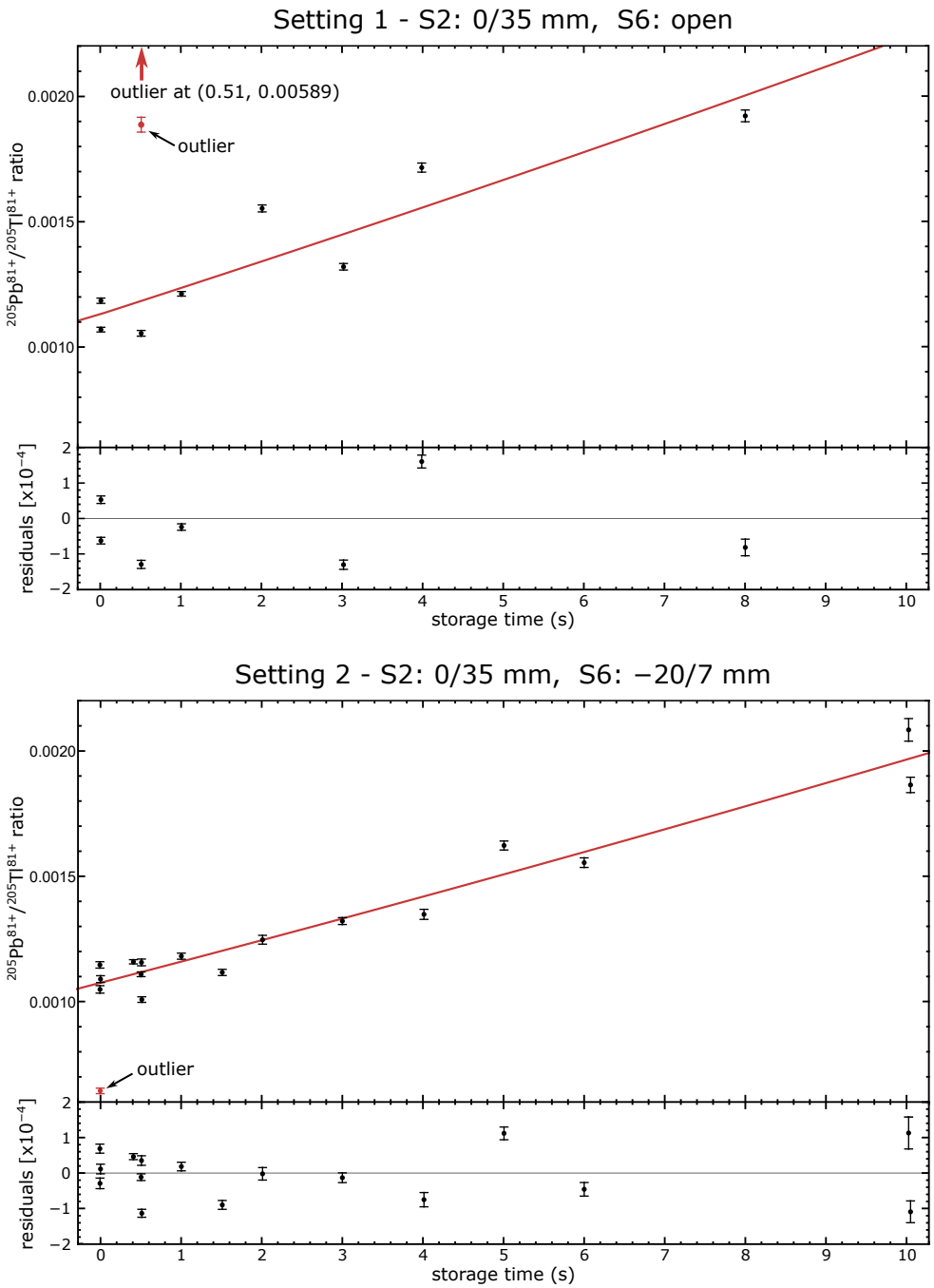

Figure 3.18: Both slit settings are plotted with only statistical errors. The best fit in this plot is a least-squares weighted fit *including* the estimated missing uncertainty. Note that the best fit excludes the outliers in red. The residuals show that the statistical errors cannot explain the scatter of the data.

The model cannot be wrong because it is a very simple construction based on the exponential nature of nuclear decay, and three previous experiments [77–79] have already validated it as an accurate description. Thus, it must be concluded that the plotted error bars do not capture all the stochastic uncertainty in our measurements.

After scouring for all other possible explanations, there is only one physical mechanism that could generate the missing stochastic variation: variation in the initial $^{205}Pb^{81+}$ contamination. It is important to keep in mind that whilst three possible sources for the contamination are considered, the contribution from projectile fragmentation forms the bulk of the contamination. For this section, we are specifically searching for *variation* in that contamination between storage runs.

Accumulation contamination

As Jung *et al.* (1992) [77] observed, β_b-decay daughters will accumulate during the stacking of beams before the storage time. Because they were working with primary beam, they achieved up to 10^8 ions during accumulation, and were thus able to purge β_b-decay daughters before storage whilst still maintaining enough ions to have sufficient decay statistics. With just 10^6 ions after accumulation, the loss of ions involved in purging the beam cannot be afforded. Fortunately, for most measurements in Setting 2, the accumulation cycle was identical and so contamination from accumulation should be constant. In addition, the magnitude of this contamination can be easily estimated if the half-life is known. Because the stacking was done on the inside orbit, minimal losses due to electron recombination occur so the differential equations during accumulation are:

$$\frac{dN_{\mathrm{Pb}}}{dt} = \frac{\lambda_{\beta_b}}{\gamma} N_{\mathrm{Tl}}, \qquad \text{with } N_{\mathrm{Pb}}(0) = 0, \tag{3.18}$$

$$\frac{dN_{\mathrm{Tl}}}{dt} = R_{\mathrm{accum}} - \frac{\lambda_{\beta_b}}{\gamma} N_{\mathrm{Tl}} \qquad \text{with } N_{\mathrm{Tl}}(0) = 0. \tag{3.19}$$

The solution to these equations is simple in the ratio form:

$$\frac{N_{\mathrm{Pb}}}{N_{\mathrm{Tl}}} = \frac{\left(1 - \frac{\lambda_{\beta_b}}{\gamma} t\right) \exp\left(\frac{\lambda_{\beta_b}}{\gamma} t\right) - 1}{1 - \exp\left(\frac{\lambda_{\beta_b}}{\gamma} t\right)}. \tag{3.20}$$

It is interesting to note that the rate of accumulation, if constant, does not appear in the ratio. This function monotonically increases with t. Using our best fit result of $\lambda_{\beta_b} = 2.76 \times 10^{-8}$ s^{-1}, $\gamma = 1.429$, and considering the typical and maximum accumulation times of 38 and 66 minutes, the $^{205}Pb^{81+}$ contamination accrued during accumulation was $R_0 = 2.2 \times 10^{-5}$ and 3.9×10^{-5}, respectively. Given the observed contamination, observable by the intercept of the best fit in Figure 3.18, accumulation only accounts for 2–3.5% of the observed contamination.

Thus, clearly accumulation was not the dominant form of $^{205}Pb^{81+}$ contamination. However, the variation in contamination from accumulation is possibly on a similar order of magnitude to the missing uncertainty. To see if this variation could explain the missing uncertainty, the accumulation time was plotted against the residual to the best fit, as shown in Figure 3.19a. Since the accumulation contamination is directly proportional to the accumulation time, the expected correlation should be very strong. With the exception of the the 10hr-1 storage, which had the largest accumulation time, no correlation is observed. For the 10hr-1 measurement, the magnitude of the estimated difference in contamination from the other data points accounts for only 13% of the observed residual. Thus, contamination from accumulation cannot account for the missing variation in the data.

Nuclear reactions in gas target

Jung *et al.* (1992) [77] also considered contamination created via nuclear reactions in the gas target. For $^{205}Tl^{81+}$, the relevant contamination reaction would be $^{205}Tl(^{40}Ar,^{40}Cl)^{205}Pb$. They determined that the contamination from nuclear reactions was $< 1\%$ for their experiment by performing stripping in the gas target with a neighbouring isotope ($^{161}Dy^{66+}$). Whilst the contamination levels are expected to be similarly small, no measurement was done to confirm this. If nuclear reactions contributed a significant amount of contamination, then it would be expected that the residuals would be correlated to the intensity of the $^{205}Tl^{81+}$ beam at stripping, as more ions would result in more reactions. This correlation is plotted in Figure 3.19b and again, no correlation is observed. Thus, nuclear reactions cannot account for our missing variation.

Production tails from fragmentation in the FRS

With the exception of the slits, the FRS settings were kept constant throughout the experiment. The expectation was that the contaminant $^{205}Pb^{81+}$ ions produced from the tails of the projectile fragmentation reaction would be constant across storage cycles. Given the contamination is at a 0.1% level, the most one would expect from counting statistics is approximately 3% ($1/\sqrt{10^3}$), but the missing uncertainty is on the order of 6%. Thus, further variation between runs is required.

The day-night temperature cycle can often affect the resistance of electromagnets, introducing a periodic shift in the magnetic field. However, when plotting the best-fit residual against the time of day and comparing to the outside temperature in Figure 3.19c, no correlation was observed. Another potential variation would be a long-term drift in the magnetic fields, causing a shifting contamination level with the experimental timeline. The fit residual against the time of accumulation is plotted in Figure 3.19d, but again, no correlation is observed.

The stability of the FRS is very challenging to ascertain given the complexity of the

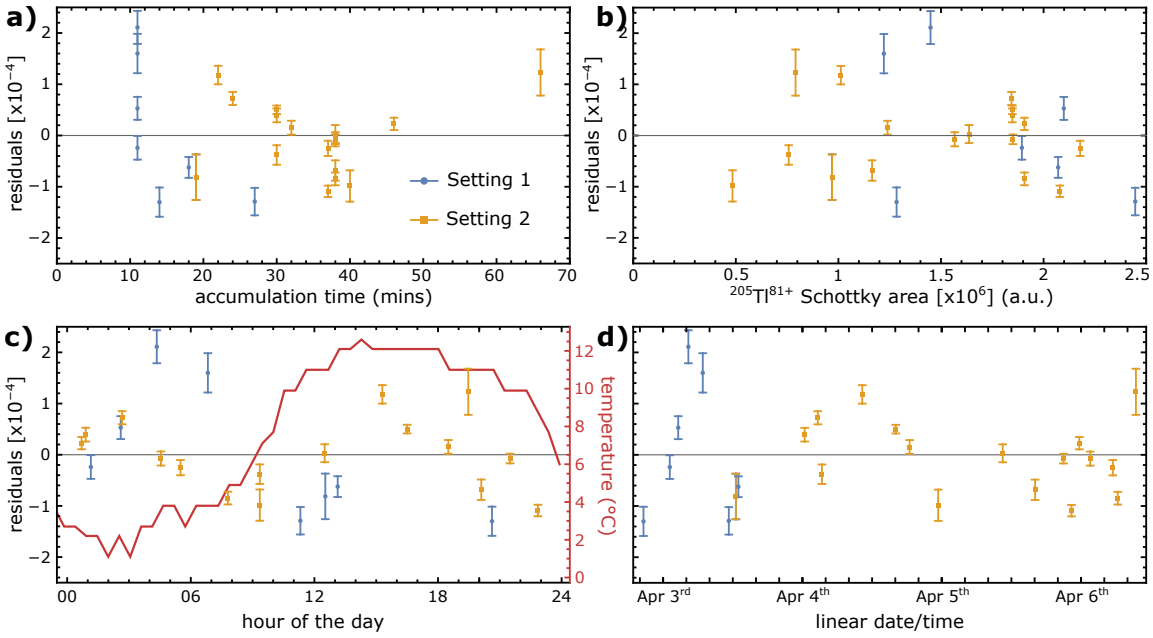

Figure 3.19: The best-fit residuals for both slit settings are plotted against: **a)** the accumulation time to check β_b decay during accumulation, **b)** the $^{205}Tl^{81+}$ Schottky area at the end of storage to check contamination via nuclear reactions in the gas target, **c)** the hour of the day in comparison to the temperature at that hour (as recorded by a weather station near to GSI), and **d)** the date + time of accumulation to test any long term trend. No correlations are observed.

machine. $^{205}Pb^{81+}$ ions are produced at a roughly 7× larger rate than $^{205}Tl^{81+}$ ions during projectile fragmentation [174]. So given the observed contamination is 0.1%, this corresponds to accepting the tail of the $^{205}Pb^{81+}$ distribution at $> 3.6\sigma$. Considering non-linear optics and energy/angular straggling in thin edges, it is unlikely that this tail is Gaussian at this point, so it is hard to predict how the tail would respond to instabilities in the magnet fields of the FRS. It was determined that the ESR magnets varied between runs at a level of $\delta B\rho/B\rho = 3.9 \times 10^{-5}$ from change in the revolution frequency between runs, so it was suggested that perhaps the FRS magnets also varied on this level. However, given the complexity of the tails and the fact that the FRS is a different machine, it could not be confirmed whether this effect could produce the observed variation.

Eventually, it was concluded that magnetic instabilities somewhere in the accelerator chain could produce the variation in the contamination observed. Since no systematic trend could be identified, the size of this variation had to be estimated from the scatter of the data. In ignorance of the exact mechanism for contamination variation, the Central Limit Theorem dictates that the contamination variation should be modelled as Gaussian noise added to each data point.

3.3.2 Monte Carlo uncertainty analysis

Whilst the model described in Equation 3.5 should be relatively simple to fit via linear regression, the correlation implicit in our systematic errors makes treating these errors consistently quite challenging. To handle this, a Monte Carlo error propagation was used. In a Monte Carlo uncertainty analysis, "the experiment is resampled n times". In an example i^{th} 'experiment', the statistical errors are individually sampled as they are independent measurements, whilst using a global i^{th} variate for our systematic errors. For the 16 data points of Setting 2, this will produce an $n \times 16$ array for the statistical values and a $n \times 1$ array for the systematic values, allowing us to do n fits and get n values for our final result λ_{β_b}. The distribution in the final result is the uncertainty in that parameter, as it consistently combines the individual 'experiments' through the use of the model, i.e. equation (3.5). More details can be found in, for example, ref. [175].

The calculation of the ratio values is straightforward, but valid handling of the contamination variation σ_{CV} is quite challenging. A χ^2 test is just a goodness-of-fit test, so adding missing uncertainty until $\chi^2 = 14$ (16 data points − 2 d.o.f.) is not an appropriate way of estimating the contamination variation. Instead, we constructed a mapping between σ_{CV} and the χ^2 of the data set, and randomly sample the $\chi^2(\nu = 14)$ distribution to determine the value of σ_{CV} for that Monte Carlo run; both functions are shown in Figure 3.20a. The mapping was done by globally minimising the χ^2 for a log-sampled range of missing uncertainty values, and the choice to globally minimise (i.e. over λ_{β_b} and R_0) was made because the fit function will minimise over these two parameters as well given the chosen missing uncertainty. By sampling the full χ^2 distribution, this marginalises over the possible values for σ_{CV} by sampling all possible values that are consistent with our data set.

Because the missing uncertainty is presumed to be a variation in $^{205}Pb^{81+}$ contamination, its contribution to the ratio will grow with storage time described by the R_0 growth factor $G = \exp\left((\lambda_{Tl}^{cc} - \lambda_{Pb}^{cc})t_s\right)$. Thus, the χ^2 that was used to create the missing uncertainty mapping is

$$\chi^2 = \sum_i \frac{(\text{data}_i - \text{model}_i)^2}{\sigma_{i\text{stat}}^2 + (G_i \cdot \sigma_{iCV})^2}. \tag{3.21}$$

This R_0 growth factor was also applied when the missing uncertainty was sampled for a given point.

Thus, in step 1 of the Monte Carlo analysis, the n Monte Carlo runs are combined to get the ratios as described by equation (3.1) and (3.2). Then the missing uncertainty for each n runs is sampled, and that value is used to sample a normal distribution with $\mu = 0$ and $\sigma = \sigma_{MU,i}$ to add variation to each data point[11]. Then those data sets are fitted with equation (3.5) (using the n values for λ^{loss}) to get a distribution of fit parameters λ_{β_b} and R_0, which is our final uncertainty distribution. The first 100 Monte Carlo fits are plotted in Figure 3.20b to illustrate the result.

[11] This is technically a Markov Chain link, making our analysis a Markov Chain Monte Carlo analysis.

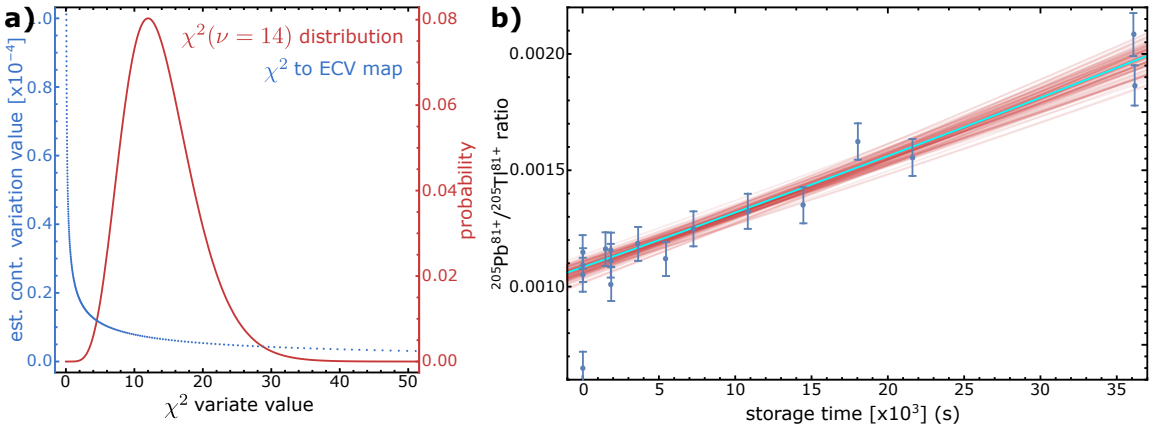

Figure 3.20: **a)** The mapping between the value of the missing uncertainty and the globally minimised χ^2 is plotted in blue, and compared to the $\chi^2(\nu = 14)$ probability distribution function. **b)** 100 Monte Carlo fits are plotted in red, with the final best fit parameters in cyan. Note that these fits are plotted without sampling of the systematic values to just compare statistical variation.

Slit results comparison

The results for the independent analysis of the two slit settings are given in Table 3.2. Figure 3.21 shows the uncertainty distributions. Note that only statistical errors, including the estimated missing uncertainty, are included for a fair comparison.

It is obvious that the result for Setting 1 is much less certain, which is caused by two effects: a) Setting 1 has half the data points of Setting 2 (8 vs 16), thus producing a less certain fit, and b) Setting 1 has greater scatter resulting in a larger estimated missing uncertainty, 12% compared to 6% respectively. It is also clear that the estimates for the two parameters are both larger for Setting 1. Comparing the two values via $(x_{S1} - x_{S2})/\sqrt{\sigma_{S1}^2 + \sigma_{S2}^2}$ yields a 1.28σ and 1.08σ difference for λ_{β_b} and R_0 respectively.

Our expectations are that the decay rate for each measurement should be the same, being a physical constant, whilst the initial contamination should be higher for Setting 1 as the S6 slit did not cut the $^{205}Pb^{81+}$ distribution. The uncertainty on both parameters are too large to meaningfully comment on this expectation. It should be noted that during the fit, the parameter correlation between λ_{β_b} and R_0 was -63%, so the larger contamination will partially cause a smaller decay rate. Hence, the larger half-life *and* larger contamination for Setting 1 is in slight tension with the expected correlation from just a contamination increase. However, Setting 1 had several data points with very large contamination values, so this data set is in general less trustworthy. As a result, only the Setting 2 data is reported for the final result.

Table 3.2: Results for slit settings with statistical errors only.

Slit setting	Runs	λ_{β_b} (s^{-1})	R_0
Setting 1	8	$3.56(56) \times 10^{-8}$	$1.113(46) \times 10^{-3}$
Setting 2	16	$2.76(25) \times 10^{-8}$	$1.075(24) \times 10^{-3}$

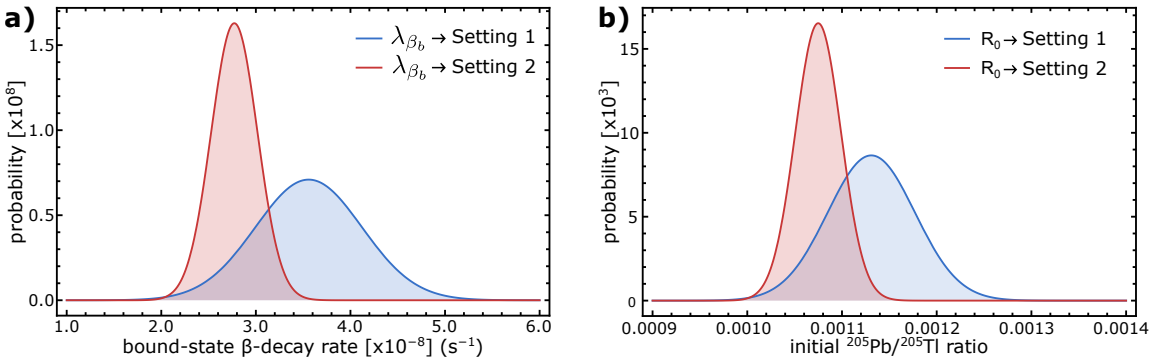

Figure 3.21: A comparison of the fit parameter uncertainty distributions for the two slit settings. **a)** shows the decay rate λ_{β_b} whilst **b)** shows the initial contamination ratio R_0.

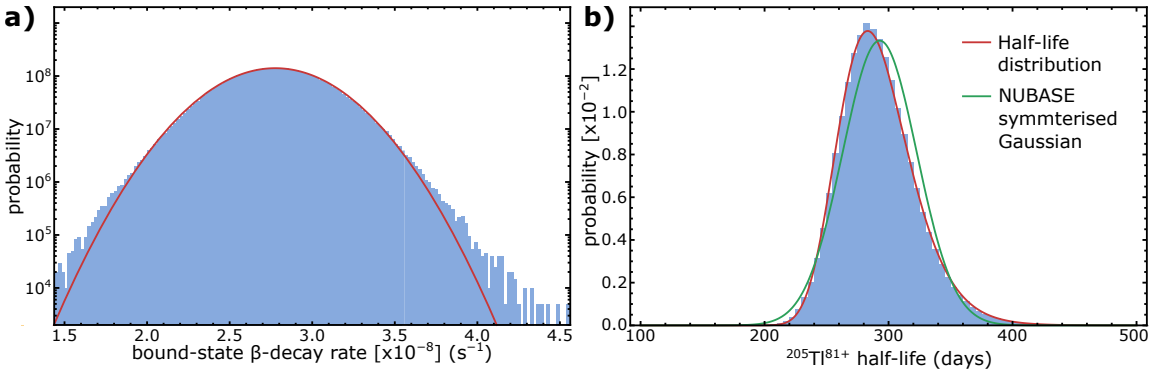

Figure 3.22: **a)** The final Monte Carlo distribution, along with the Gaussian fit. The distribution has a very Gaussian shape, except at the extreme tails. **b)** The Monte Carlo values shows that the half-life distribution is asymmetric. The NUBASE symmetrisation routine is plotted for comparison (details in text).

3.3.3 Final Result

The final result was determined from a Monte Carlo simulation with 10^6 runs resulting in $< 0.01\%$ Monte Carlo error in the final value. The determined decay rate was:[12]

$$\lambda_{\beta_b} = 2.76(25)_{\text{stat}}(13)_{\text{syst}} \times 10^{-8}\ \text{s}^{-1} = 2.76(28)_{\text{tot}} \times 10^{-8}\ \text{s}^{-1}. \tag{3.22}$$

Because the decay rate λ_{β_b} was a linear parameter in the fit, the errors are well approximated by a Gaussian, as demonstrated in Figure 3.22a.

By 'turning off' the Monte Carlo sampling for all other parameters, the contribution of each parameter to the final uncertainty can be understood. This is how the fractional contributions to the uncertainty in Figure 3.17 were calculated. Isolating the contributions shows us that our result features 78% statistical uncertainty and 22% systematic uncertainty, with the largest contribution being the initial contamination variation.

To get the half-life, the inverse of a Gaussian distribution must be taken, which is not a Gaussian itself, but rather an asymmetric distribution with a probability distribution function f of

$$f_{t_{1/2}}(x) = \frac{\alpha}{\sqrt{2\pi}\sigma\, x^2} \exp\left(-\frac{(\mu - \alpha/x^2)}{2\sigma^2}\right) \tag{3.23}$$

where $\alpha \to \frac{\ln 2}{3600*24}$ to get the half-life in days. This inverse distribution is plotted in Figure 3.22b. Taking the median and the 68% interval around the median to represent our '1σ' error bars, the corresponding half-life is

$$t_{1/2} = 291^{+33}_{-27}\ \text{days} \approx 294(30)\ \text{days}. \tag{3.24}$$

The approximation used by NUBASE to symmetrise asymmetric errors in their evaluation is also included for comparison [53].

Representation of systematic error

For each of the three main systematic error corrections, multiple values for the parameters were determined that did not agree within the statistical error. We wanted to use our best-motivated parameter estimate—as opposed to an average—but also wanted to represent the systematic uncertainty in our model choice. The action of choosing between models is not well defined in a Frequentist understanding of probability.

To represent the scale of the systematic uncertainty, we chose a uniform distribution between the min/max range of the estimates whilst keeping the median centred on our preferred parameter estimate. In this case, these systematic errors do not represent physical random distributions, but rather provided us a mechanism for comparing the size of our uncertainty on different parameters.

[12] The decay rate *including* the outlier is $\lambda_{\beta_b} = 3.13(47)_{\text{tot}} \times 10^{-8}\ \text{s}^{-1}$, which is compatible within error. The uncertainty is much larger when the outlier is included because the fit is very unstable as the range of the outlier is sampled.

3.3.4 Alternate analyses for confirmation

Because of the complexity and opaqueness of the analysis involved with the Monte Carlo error propagation and the initial contamination estimation, we felt it was important to try two completely different analysis methods to confirm the final result.

Direct calculation

To keep things as simple as possible, a direct calculation was done where the error propagation formula was used to propagate the statistical errors:

$$\sigma_f^2 = \left(\frac{df}{dx}\right)^2 \sigma_x^2 + \left(\frac{df}{dy}\right)^2 \sigma_y^2 + 2\left(\frac{df}{dx}\right)\left(\frac{df}{dy}\right)\rho_{xy}\sigma_x\sigma_y. \tag{3.25}$$

The function to fit, which included all the systematic corrections, was:

$$R(t_s) = \left[\frac{\lambda_{\beta_b}}{\gamma} t_s \left(1 + \tfrac{1}{2}(\lambda_{Tl}^{cc} - \lambda_{Pb}^{cc})t_s\right) + R_0 \exp\left((\lambda_{Tl}^{cc} - \lambda_{Pb}^{cc})t_s\right)\right] \cdot RC \cdot \frac{\sigma_{\text{str}}}{\sigma_{\text{str}} + \sigma_{\text{rec}}}. \tag{3.26}$$

For this fit, the (very small) statistical error bars were used as $1/\sigma_i^2$ weights. Mathematica has the option to define what "1σ" error means for the fit. By default, it will use the scatter of the data to determine the standard error, but the fit can be normalised as desired. In this case, we chose not to normalise the `VarianceEstimatorFunction`, because the statistical error bars clearly do not describe the data variation. Thus, Mathematica is essentially conducting its own determination of the 'missing uncertainty.' From this fit, the direct calculation gave statistical errors of $\lambda_{\beta_b} = 2.66(32)_{\text{stat}} \times 10^{-8}\ \text{s}^{-1}$.

Determining the error contribution of the systematic parameters is non-trivial because the λ^{loss} parameters in equation (3.26) are dependent on storage time. This problem is exactly why the Monte Carlo simulation was chosen to handle these errors. To get a rough idea of the contribution of the systematic parameters, the percentage errors were summed in quadrature, despite the fact that this does not really follow the error propagation formula. Regardless, this yielded a final result of $\lambda_{\beta_b} = 2.66(32)_{\text{stat}}(13)_{\text{syst}} \times 10^{-8}\ \text{s}^{-1} = 2.66(35)_{\text{tot}} \times 10^{-8}\ \text{s}^{-1}$. The smaller value is the consequence of the very small errors (high weights) on the low storage times causing the longer storage runs to have almost no impact on the fit. This method is in good agreement (within 4.5% or 0.5σ) with the Monte Carlo result.

Bayesian analysis

A full Bayesian analysis was also conducted, since the idea of randomly sampling the missing uncertainty somewhat borrows from this technique. To do this, the uncertainty on the systematic parameters were incorporated as priors. We chose a Gaussian likelihood for the data and incorporated the initial contamination variation as a nuisance parameter in an identical way to equation (3.21).

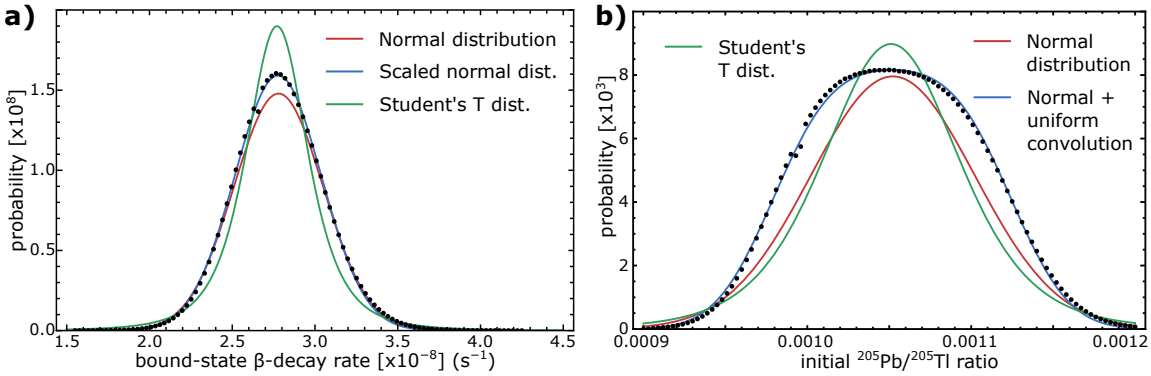

Figure 3.23: The Bayesian posterior distribution. **a)** The posterior as a function of λ_{β_b}, with all other nuisance parameters integrated out. Neither a normal distribution, nor a Student's T distribution fit the posterior well. Instead, a scaled normal distribution was required to account for the normalisation issue. **b)** The same posterior as a function of R_0. Only a convolution of a uniform and normal distribution approximated the R_0 posterior.

As a result, the posterior distribution was a function of λ_{β_b} and five nuisance parameters associated with the individual corrections described in Section 3.2. Integrating out the nuisance parameters produced the desired posterior distribution in λ_{β_b}, which can be seen in Figure 3.23a. This posterior distribution is unfortunately not normalised; integrating the distribution yields 1.049. This is obvious by the fact that a normal distribution with a scaling factor of 1.043 is the best fit, so the distribution parameters were determined by fitting this scaling parameter explicitly. This gives a final result from the Bayesian analysis of $\lambda_{\beta_b} = 2.78(26)_{\text{tot}} \times 10^{-8}$ s^{-1}, in perfect agreement with the Monte Carlo method. Note that for a Bayesian analysis, the statistical error cannot be separated from the systematic error.

It is not obvious why the distribution is not normalised. Mathematica does struggle with the tails of the integration as it runs into machine precision difficulties for these tiny numbers. However, extending the integral out further into this parameter space did not solve the problem. Given this method was just to check that the Monte Carlo method produced consistent numbers, the normalisation issue was not investigated further. This issue also points to the necessity of using a more robust Bayesian analysis framework.

We also looked at the R_0 posterior distribution, shown in Figure 3.23b. It produces a flat-topped distribution that can only be modelled by the convolution of a Gaussian and Uniform distribution. This will probably be linked to the convolution of the systematic priors, but it may also be indicating that a range of R_0 values work.

Table 3.3: Proposed $\log(ft)$ values for the $^{205}\mathrm{Tl}(\frac{1}{2}^+) \leftrightarrow {}^{205}\mathrm{Pb}(\frac{1}{2}^-)$ transition.

Systematic estimation	$\log(ft)$	Shell model calculation	$\log(ft)$
Freedman *et al.* (1976) [90]	5.3(1)	Ogawa & Arita (1988) [176]	5.90/6.03
Yokoi & Takahashi (1985) [177]	5.4	Warburton (1991) [178]	5.79
Braun & Talmi (1986) [179]	5.7	Xiao & Wang (2024) [180]	5.87
Liu *et al.* (2021) [181]	5.1		
This work: $\log(ft) = 5.91(5)$			

3.4 Comparison to theory

Comparing our experimental result to theoretical predictions can be problematic because the $^{205}\mathrm{Tl}(\frac{1}{2}^+) \leftrightarrow {}^{205}\mathrm{Pb}(\frac{1}{2}^-)$ transition is very hard to predict. As a result, the range of predictions across the decades spans almost an order of magnitude in half-life. Since the β_b-decay Q value has historically been uncertain (41.4(11) keV [80] vs 51.1(5) keV [81, 82]), it is easier to compare $\log(ft)$ values for the decay, which are independent of the Q value. A summary of literature values are provided in Table 3.3.

When Freedman *et al.* (1976) [90] first proposed the use of ^{205}Tl as a geochemical activation candidate to measure solar neutrinos, they estimated a $\log(ft) = 5.3(1)$ based on systematic trends with neighbouring single-particle transitions. However, Freedman [182] quickly acknowledged the point from Bahcall [183] that the $^{205}\mathrm{Tl}(\frac{1}{2}^+) \leftrightarrow {}^{205}\mathrm{Pb}(\frac{1}{2}^-)$ transition could not be a single-particle transition because the main single-particle state of the $^{205}\mathrm{Tl}(\frac{1}{2}^+)$ ground state does not have any particles in the $2p_{1/2}$ orbital. Rather, any decay from the $^{205}\mathrm{Tl}(\frac{1}{2}^+)$ state would have to come from the admixture[13] of a two neutron–two hole configuration, with the two neutrons occupying the $2p_{1/2}$ orbital rather than the $2f_{5/2}$ orbital as in the main configuration. This admixture percentage was completely unknown at the time. Noting this, Braun & Talmi (1986) [179] suggested $\log(ft) = 5.7$ based on estimates of the admixture percentage from several $^{205}\mathrm{Hg}(\frac{1}{2}^-) \rightarrow {}^{205}\mathrm{Tl}(\frac{1}{2}^+)$ transitions, which should probe the admixture of the $^{205}\mathrm{Tl}(\frac{1}{2}^+)$ state. Liu *et al.* (2021) [181] recently proposed $\log(ft) = 5.1$ based on an estimation from neighbouring transitions, but did not provide any details on their methodology.

Shell model calculations do better than systematic extrapolations because they predict realistic admixture percentages based on a self-consistent microscopic description of the nucleus. Ogawa & Arita (1988) [176] conducted the first shell model study, and calculated $\log(ft)$ values of 5.90 and 6.03 using different modelling choices. Warburton (1991) [178] followed up with another shell-model calculation in the lead region, which yielded $\log(ft) = 5.79$. Very recently, Xiao & Wang (2024) [180] published further shell-model calculations

[13] An admixture for a nuclear state refers to the mixing of different nuclear shell model configurations with the same spin and parity to form a given energy eigenstate of the nucleus.

with $\log(ft) = 5.87$. Given shell models are well calibrated for nuclei in this range, it is unsurprising that shell-model predictions match the experimental result much better than the systematic extrapolations.

In their study of stellar weak decay rates at the termination of the *s* process, Yokoi & Takahashi (1985) [177] proposed $\log(ft) = 5.4$, also from systematic extrapolation of nearby single-particle states. However, as already discussed, nearby single-particle states do a poor job of predicting this transition. Nonetheless, Takahashi & Yokoi's rates [184] are extensively used in the astrophysical modelling community to this day. The difference between the stellar weak decay rates calculated with our experimental result and those from Takahashi & Yokoi [184] are discussed in-depth in Section 4.2.

3.5 Impact on LOREX

Our experimental result also clarifies the solar neutrino capture rate on ^{205}Tl for the LOREX project, as discussed in Section 1.6. We conclude that the nuclear matrix element is smaller than predicted from systematics, reducing the overall neutrino capture rate and making a signal harder to detect. In particular, we estimate in Sidhu *et al.* (2024) [102] that 15(4) solar-neutrino-induced ^{205}Pb atoms per gram could be extracted from the Allchar lorandite crystals. This is lower than the value of 22(7) predicted by Pavićević before our measurement [101], who used calculations based on $\log(ft) = 5.7$ from Braun & Talmi (1986) [179].

Since one gram of lorandite contains 1.753×10^{21} atoms, this will be an extremely challenging measurement. A procedure for the chemical extraction of Pb from the lorandite has been devised by Pavićević & Brüchle and described briefly in ref. [185]. From the extracted Pb content, ^{205}Pb still needs to be separated. For such high masses, separation of the isobaric ^{205}Tl by accelerator mass spectrometry would be essentially impossible as the ^{205}Pb and ^{205}Tl energy loss distributions would largely overlap. However, analysis in the ESR can solve the isobaric contamination problem by using the fully-stripped charge state since ^{205}Tl^{81+} and ^{205}Pb^{82+} are well separated in the ESR. Given the best background estimates provided by Pavićević and Brüchle [185], our new result corresponds to a signal to background ratio of 3.7σ (assuming 100% efficiency). Unfortunately, this makes a statistically significant detection of ^{205}Pb ions unlikely. The neutrino capture rate on ^{205}Tl has been sought for 50 years and our results have recently been published in *Physical Review Letters* [102]. The details of the solar neutrino analysis can be found there, as those calculations were not done for this thesis.

Chapter 4

^{205}Pb in the Early Solar System

^{205}Pb is the decay daughter of ^{205}Tl and is a uniquely powerful case of a special class of nuclei called *short-lived radionculides* (SLRs) that are used as cosmic clocks to date processes occurring in the early Solar System (ESS). SLRs are short-lived in an astrophysical sense, with half-lives ranging from 0.1–100 Myr, which is on the same timescale as processes in the early Solar System. The timescale on which the solar material isolated itself from the interstellar medium (ISM) and then collapsed to form the first solids is called the *isolation time*, and this value can help determine what type of stellar nursery our Sun formed in [106]. Understanding this formation mechanism is crucial not only for understanding the structure and history of the Solar System, but also for understanding the conditions under which the solar abundances arose, given they play a pivotal role in nuclear astrophysics.

Trueman *et al.* (2022) [186] have shown that the three *s*-process SLRs that were available at the time—^{107}Pd, ^{182}Hf, and ^{135}Cs—predicted a self-consistent solution for the formation of the early Solar System. This solution posited that the SLRs had originated from standard galactic chemical evolution of the ISM and then the solar material was isolated for 9–26 Myr. This longer isolation time indicated that our Sun most likely formed inside a giant molecular cloud (GMC), like Scorpius-Centaurus OB2 [187] and the Orion molecular cloud complex [188]. However, these three *s*-process SLRs also have *r*-process contributions, and thus rely on the conclusion that the last *r*-process event occurred 100–200 Myr before the first solids in our Solar System formed. This situation is heavily implied by the abundances we measure for the *r*-only SLRs ^{129}I, ^{244}Pu, and ^{247}Cm [189, 190], and this long delay time would suppress any *r*-process contribution to ^{107}Pd, ^{182}Hf, and ^{135}Cs. ^{205}Pb offers a critical test for the self-consistency of this GMC theory because it is unique amongst the SLRs as the single *s*-only nuclide.

To use an SLR as a *cosmochronometer*, the isotopic abundance needs to be known in the interstellar medium at the Sun's birth and in the first meteorites that we can study today. In the case of ^{205}Pb, this means understanding its production site, which is dominantly the main *s* process in asymptotic giant branch (AGB) stars, as discussed in Section 1.4.2. Because the low-lying, first excited state in ^{205}Pb can be thermally populated in the stellar plasma, its astrophysical half-life is highly temperature dependent, and accurate determination of these rates requires the nuclear matrix element between the ^{205}Pb$^{*}(1/2^{-})$ and ^{205}Tl$(1/2^{+})$ states, as described in Chapter 3. This is especially true during the thermal pulse phase of an AGB cycle, where the temperature is high enough for enhanced ^{205}Pb EC decay and ^{205}Tl β_b decay to directly compete with each other.

This chapter describes the workflow of applying our new experimental nuclear matrix element to create accurate astrophysical rates, and then modelling AGB stars to derive the isolation time of the early Solar System as determined by ^{205}Pb. This effort was the result of a 2 year collaboration between the experimental team, our GSI theory colleagues, and several AGB modelling groups that culminated in the *Nature* publication Leckenby *et al.* (2024) [164].

4.1 ^{205}Pb as a short-lived radionuclide

Across the nuclear chart, there are 19 short-lived radionuclides (SLRs) that fit the required range of half-lives from 0.1–100 Myr. Their properties are summarised in Table 4.1. These SLRs are used in concert to provide timing information on the sequence of events taking place before and amidst the formation of the early Solar System, with each SLR constraining the picture in a unique way. As reviewed by Lugaro *et al.* (2018) [106] and others [191, 193, 194], this can inform the lifetime, or isolation time, of the stellar nursery in which the Sun was born. They can even shed light on the thermodynamic evolution of the planetesimals that can have important consequences for the habitability of the planets.

Each SLR is paired with a reference isotope, ideally of the same element to ensure identical chemistry, with which an abundance ratio can be recorded. The process by which this abundance ratio is extracted from the first solids to give the ESS ratio is described in Section 4.5. As shown in Table 4.1, the SLRs come from a variety of sources, with the bulk coming from processes that happen during core-collapse supernovae. The *s* and the *r* processes account for most of the remaining SLRs, with most *s*-process SLRs also featuring an *r*-process component. ^{205}Pb is a unique SLR as both itself and the reference isotope ^{204}Pb are *s*-only isotopes, as highlighted in Figure 4.1a. This makes ^{205}Pb uniquely positioned to constrain the 'live' *s*-process contribution to the early Solar System, as first reported by Blake *et al.* (1973) [195]. In addition, ^{205}Pb is a third-peak *s*-process isotope, which provides a separate constraint to the other main *s*-process SLRs, ^{107}Pd and ^{182}Hf, which are found much earlier in the *s*-process path.

Blake & Schramm (1975) [196] quickly retracted their optimism after S.E. Woosley pointed out that the 2.3 keV first excited state of ^{205}Pb (denoted hereafter as ^{205}Pb*) would be thermally populated as the stellar plasma approaches $kT = 2.3$ keV (~ 27 MK). The electron capture (EC) decay from this excited state is a $1/2^- \rightarrow 1/2^+$ transition, and this transition is not suppressed by the nuclear structure effects that inhibit the $5/2^- \rightarrow 1/2^+$ transition from the ground state.[14] As a result, the EC decay from this excited state has a partial half-life on the order of a few years, causing any ^{205}Pb that experiences these temperatures to decay immediately on an astrophysical timescale. Thus,

[14]It should be noted that in the ^{205}Pb case, the suppression of the unique transition is due to nuclear structure effects of the single-particle transition since mass-205 is near two closed shells. The suppression does not arise from weak selection rules [197].

Table 4.1: Properties of the 19 short-lived radionuclides (SLRs). The half-life refers to the SLR, since the reference isotope is stable (or very long-lived). The quality ranking (5$^{\text{th}}$ column), originally by Dauphas & Chaussidon [191] and updated in Lugaro *et al.* [106], takes into account confidence in the ESS ratio. The process/site listed is the dominant source only, minor contributions can come from other sources. The < symbol indicates only an upper bound is available.

SLR	Reference	$T_{1/2}$ (Myr)	ESS ratio	Quality	Process/Site
^{107}Pd	^{108}Pd	6.5(3)	$6.6(4) \times 10^{-5}$	⋆⋆⋆	$s+r$
^{182}Hf	^{180}Hf	8.90(9)	$1.02(4) \times 10^{-4}$	⋆⋆⋆	$s+r$
^{205}Pb	^{204}Pb	17.0(9)	$1.8(12) \times 10^{-3}$	⋆	s-only
^{135}Cs	^{133}Cs	1.33(19)	$< 2.8 \times 10^{-6}$	<	$s+r$
^{129}I	^{127}I	16.14(12)	$1.28(3) \times 10^{-4}$	⋆⋆⋆	r-only
^{247}Cm	^{235}U	15.6(5)	$5.6(3) \times 10^{-5}$	⋆⋆⋆	r-only
^{244}Pu	^{238}U	81.3(3)	$7(1) \times 10^{-3}$	⋆⋆	r-only
^{126}Sn	^{124}Sn	0.230(14)	$< 3 \times 10^{-6}$	<	r-only
^{26}Al	^{27}Al	0.72(2)	$5.23(13) \times 10^{-5}$	⋆⋆⋆	WR stars[1]/CCSNe
^{53}Mn	^{55}Mn	3.7(4)	$7(1) \times 10^{-6}$	⋆⋆⋆	CCSNe/SNIa
^{36}Cl	^{35}Cl	0.3013(15)	$2.4(7) \times 10^{-5}$	⋆⋆	CCSNe/WR stars
^{60}Fe	^{56}Fe	2.62(4)	$1.0(3) \times 10^{-8}$	⋆⋆	CCSNe
^{41}Ca	^{40}Ca	0.0994(15)	$4.6(19) \times 10^{-5}$	⋆	CCSNe/WR stars
^{92}Nb	^{93}Nb	35(2)	$1.57(9) \times 10^{-5}$	⋆⋆⋆	γ
	^{92}Mo		$3.2(3) \times 10^{-5}$	⋆⋆⋆	
^{146}Sm	^{144}Sm	92.0(26)[2]	$8.3(4) \times 10^{-3}$	⋆⋆⋆	γ
^{97}Tc	^{92}Mo	4.21(16)	$< 1 \times 10^{-6}$	<	γ
	^{98}Ru		$< 1.1 \times 10^{-5}$	<	
^{98}Tc	^{96}Ru	4.2(3)	$< 2 \times 10^{-5}$	<	γ
	^{98}Ru		$< 6 \times 10^{-5}$	<	
^{10}Be	^{9}Be	1.387(12)	(3–9)$\times 10^{-4}$	⋆⋆⋆	cosmic rays
^{7}Be	^{9}Be	53.22(6) d	$6.1(13) \times 10^{-3}$	⋆	cosmic rays

Data sourced from Table 1 & 3 of Lugaro *et al.* (2018) [106]. ESS ratios are quoted with 2σ errors, as is customary in meteoritics, ESS references given in ref. [106]. Half-lives have 1σ errors and are taken from NUBASE2020 [53].

[1] Wolf-Rayet stars are a rare type of massive star that has such strong stellar winds that the hydrogen envelope has been entirely blown away, leaving an exposed core that is still burning He or heavier elements.

[2] Updated half-life from Chiera *et al.* (2024) [192].

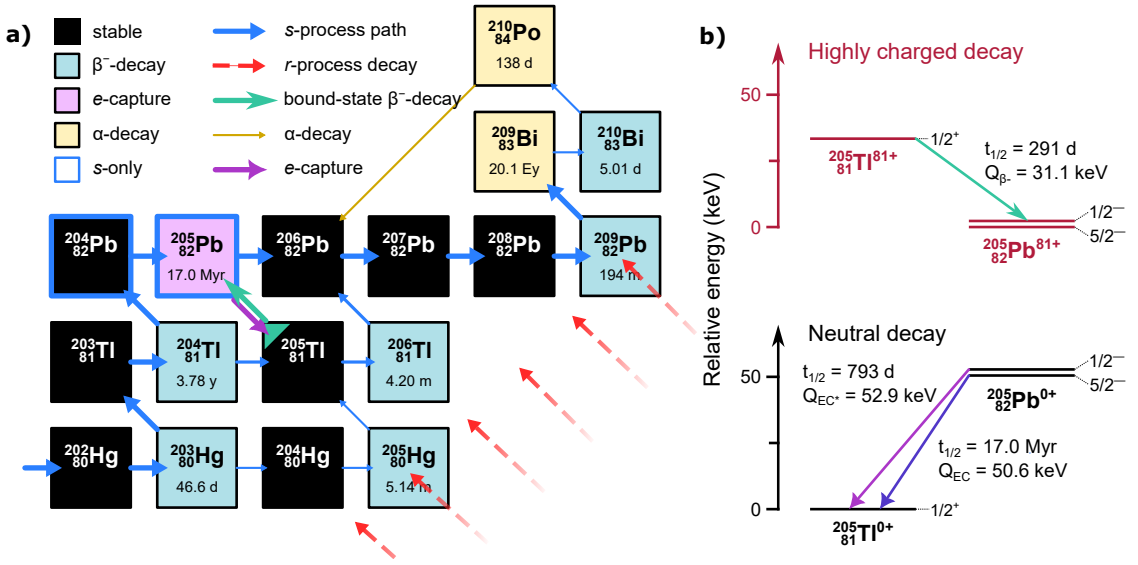

Figure 4.1: **a)** The termination of the *s*-process path in the Pb region, which is indicated by the blue arrows. The size of the *s*-process arrows roughly indicates the decay branchings. The *r*-process freezeout lines are shown by red arrows, demonstrating that ^{205}Pb is shielded by ^{205}Tl and ^{204}Pb is shielded by ^{204}Hg. **b)** The low-lying structure of the ^{205}Pb–^{205}Tl decay pair, alongside the partial half-lives for each state. Note that the ^{205}Pb 2.3 keV excited state never decays via electron capture at terrestrial temperatures, so fully temperature/density-dependent decay rates must be used. Figure reproduced from Leckenby *et al.* (2024) [164].

Blake & Schramm (1975) [196] concluded that meteorite measurements may be more useful in constraining the *s* process than constraining the formation of the Solar System.

Yokoi *et al.* (1985) [177] revived the possibility of ^{205}Pb as an SLR by pointing out that at even higher temperatures, where the K-shell of ^{205}Tl becomes ionised (> 100 MK), bound-state β-decay could produce ^{205}Pb to counterbalance its elevated decay rate. However, they acknowledged that the unknown nuclear matrix element between the two spin-1/2 states limited the precision of the astrophysical decay rates they calculated, both for the EC of ^{205}Pb* and the β_b decay of ^{205}Tl$^{80/81+}$. We note that Takahashi & Yokoi (1987) [184] (hereafter TY87) used a smaller Q_{β_b} value of 42.6 keV for their evaluation of stellar weak decay rates than what is now accepted (50.6(5) keV) in AME2020 [83].

Mowlavi *et al.* (1998) [198] were the first to apply the TY87 rates to a full model of a thermally-pulsing AGB star, and even today most modern AGB models are based on the TY87 rates. The primary nuclear physics limitation in the accuracy of the astrophysical rates to date has been the unknown nuclear matrix element, which resulted in rates that were uncertain by over an order of magnitude. With our experimental result, the accuracy of the astrophysical rates can now be determined by within our uncertainty of $\approx 10\%$.

4.2 Astrophysical weak decay rates

The details of the theory used to calculate the astrophysical weak decay rates of ^{205}Tl and ^{205}Pb are provided in the Methods section of our *Nature* publication [164] and an upcoming publication. A summary of the key points is provided here.

The β_b decay rate is connected to the nuclear shape factor C_K by

$$\lambda_{\beta_b} = \ln(2)\frac{C_K f_K}{\mathcal{K}}, \tag{4.1}$$

with $\mathcal{K} = 2\overline{F}t = 6145(4)$ s the decay constant determined from super-allowed β decay [199], $f_K = \pi Q_{\beta_b}^2 \beta_K^2 \mathcal{B}_K / 2m_e^2$ the phase space for β_b decay, β_K the Coulomb amplitude of the K-shell electron wavefunction, and $\mathcal{B}_K$ the exchange and overlap correction [200]. Note that the nuclear shape factor C_K is the same shape factor introduced in Section 1.5.2; it is not necessarily related to the shape or deformation of the nucleus, but rather describes the additional corrections required to describe the shape of β spectrum. From the measured decay rate determined in Chapter 3, a nuclear shape factor of $C_K = 7.6(8) \times 10^{-3}$ can be calculated, which gives an associated $\log(ft)$ of

$$\log(ft) = \log(\mathcal{K}/C_K) = 5.91(5). \tag{4.2}$$

The uncertainties on the theoretical quantities are an order of magnitude smaller than the experimental uncertainty on the β_b-decay rate [201], so the above uncertainty is experimental.

Depending on the temperature of the stellar plasma, ^{205}Tl and ^{205}Pb ions will be present in varying charge-state distributions. We follow the prescription outlined by Takahashi & Yokoi (1983) [202] where the Saha statistical equation is used to describe the charge-state distributions in thermal equilibrium:

$$\frac{n_{i,j+1}}{n_{i,j}} = \frac{b_{i,j+1}}{b_{i,j}} \left(\frac{m_{i,j+1}}{m_{i,j}}\right)^{\frac{3}{2}} e^{-\chi_{i,j}/kT - \eta}. \tag{4.3}$$

Here $n_{i,j}$ is the number density of isotope i in its j^{th} ionisation state, $b_{i,j}$ the atomic partition function, $m_{i,j}$ the mass, $\chi_{i,j}$ the ionisation potential, k the Boltzmann constant, T the temperature, and η is the electron degeneracy parameter (derived in ref. [202]) determined by the electron density.

In addition to the charge-state distribution, each species in the plasma also follows a distribution of nuclear excited states determined by Boltzmann statistics. The properties of these excited states, in particular the nuclear matrix elements for the relevant decays, are determined by our collaborators via shell-model calculations with the NATHAN code [203] and the Kuo-Herling interaction [178] that are calibrated to measured decay rates. In this way, the full phase space of forbidden decays is accounted for. The total decay rate for an

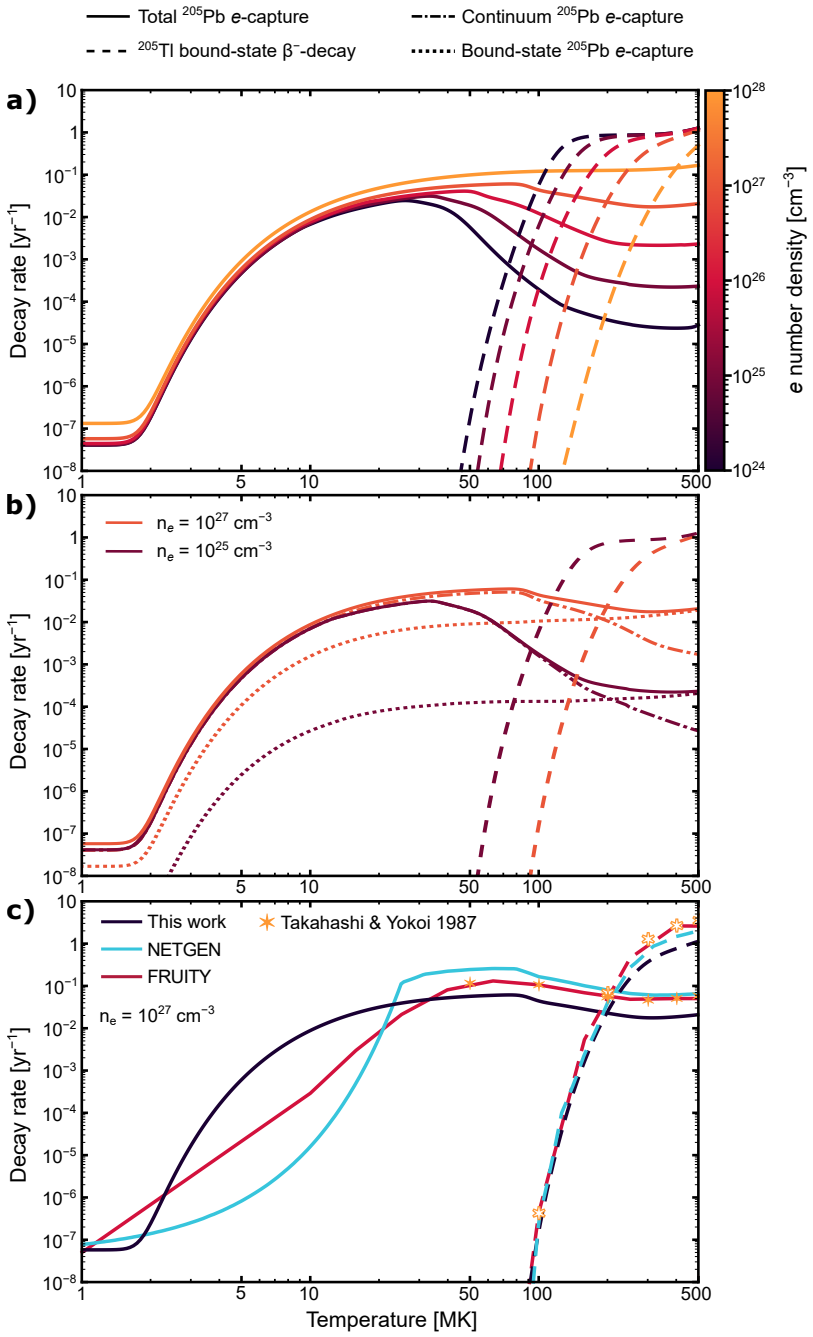

Figure 4.2: **a)** Total weak decay rates for ^{205}Pb and ^{205}Tl as a function of temperature and electron number density. **b)** A comparison of our new experimental rates with the rates currently used in AGB models. **c)** The bound and continuum contributions to electron capture. The bound contribution dominates for most conditions considered. Figure reproduced from Leckenby *et al.* (2024) [164].

individual species is given by the population-weighted sum of the partial decay rates from the charge-state and excited-state distribution.

The derived, total astrophysical weak decay rates for ^{205}Pb and ^{205}Tl are plotted in Figure 4.2a as a function of temperature and electron number density. The EC rate increases from 2 MK to 50 MK as the 2.3 keV excited state is thermally populated. Beyond 50 MK, the EC rate drops as ionisation reduces the available bound electrons to capture. The magnitude of this suppression depends on the electron density, as increased electron density both suppresses ionisation and increases continuum electron capture. The contributions of bound and continuum electron capture can be seen in Figure 4.2b.

In Figure 4.2c, our new rates are compared with the rates currently being used in AGB models. The NETGEN library [204] is a popular compilation of reaction rates, with the ^{205}Pb/^{205}Tl rates following the rates tabulated by Goriely (1999) [205]. Goriely made some modifications to the code used in TY87, and we believe this is the cause of the departure from the TY87 rates shown in Figure 4.2c. However, we were unable to reproduce Goriely's values. For low temperatures, NETGEN uses an interpolation in linear space to the terrestrial value of $\lambda(^{205}\mathrm{Pb})_0 = 1.29 \times 10^{-15}$ s^{-1}. The rates used to produce the FRUITY database [206], a popular database of AGB yields, are a spline interpolation of the TY87 rates with an interpolation to the terrestrial value in log space. With modern computing power, our calculation of the rates connects all the way down to the terrestrial value, so no interpolation is required. We see that for our new experimentally-backed rates, both the ^{205}Pb and ^{205}Tl rates are reduced compared to these present rates due to the fact that the measured β_b-decay rate was substantially smaller than predicted by TY87.

With the experimental nuclear matrix element, our new rates are substantially more accurate than what was available before. We have also incorporated the latest Q_{β_b} value of 31.1(5) keV, calculated in equation (1.20). In addition, we expanded the temperature and density grid with modern computing power from 5×4 to 200×200. As we shall see when discussing the production of ^{205}Pb in AGB stars in Section 4.3, this resolution in temperature and density space is crucial for achieving accurate production values.

To complement the new weak decay rates, updated neutron capture cross-section recommendations were calculated for nine key isotopes to complement the KADoNiS database [207]. These isotopes were $^{202–204}$Hg, $^{203–205}$Tl, and $^{204–206}$Pb, and featured new data like the (presently unpublished) ^{204}Tl(n,γ) measurement from n_TOF [208]. The details of these cross-section recommendations are available in the Methods section of ref. [164], whilst the impact of these new values is discussed at the end of Section 4.3.

4.3 AGB models

The large majority of the ^{205}Pb in the universe was synthesised in the main s process in AGB stars (see Section 1.4.2). A minor contribution can arise from neutron captures in core-collapse supernovae [209] and from Wolf-Rayet stars [210, 211], but these do not

significantly contribute to the abundances of live ^{205}Pb in the interstellar medium. Modern simulations of the main s process fully track the evolution of the AGB phase to inform the temperature, density, and neutron conditions of the material. To determine the impact of our new weak decay rates, we implemented them in three, state-of-the-art AGB models:

1. **Monash nucleosynthesis tools** [212] is a post-processing code, where an astrophysical trajectory is established from a 1D stellar model, and a nuclear reaction network is then solved following the trajectory conditions. This works if the post-processed nucleosynthesis does not contribute to the trajectory, which is true for the s process. Monash tools use the NETGEN compilation for weak decay rates.
2. **Nucleosynthesis Grid (NuGrid) model** uses the NuGrid post-processing network [213] applied to AGB stellar models from the MESA stellar evolution code [214] to simulate the s process in AGB stars [215]. NuGrid also use the NETGEN database.
3. **FUll Network Stellar (FUNS) evolutionary code** [216, 217] produces the FRUITY database for isotopic yields of AGB stars [206]. The most updated FUNS models implement coupled nucleosynthesis, so the reaction network grid is solved with the evolution of the star. FUNS models use an interpolation of TY87 rates.

As a reminder, the s process occurs in two phases in AGB stars. The first occurs during the interpulse period when a ^{13}C pocket develops at the top of the intershell region from mixing with the envelope at the third dredge-up causing the $^{13}\mathrm{C}(\alpha, n)^{16}\mathrm{O}$ neutron source to be activated creating low neutron densities. The second burst occurs during the thermal pulse where the He flash drives temperatures high enough for the $^{22}\mathrm{Ne}(\alpha, n)^{25}\mathrm{Mg}$ source to be activated generating medium neutron densities. See Section 1.4.2 for more details.

4.3.1 ^{205}Pb production in the thermal pulse cycle

For ^{205}Pb production, the exact nucleosynthesis path taken in Figure 4.1 is complicated to comprehend due to the weak decays of ^{205}Pb and ^{205}Tl that flow in both directions. This flow depends on the temperature and the interplay with neutron capture rates, which operate on the same timescale as the weak decays. The branching point at ^{204}Tl is also temperature dependent. This complexity is why ^{205}Pb production needs to be handled by full AGB stellar models and cannot be described by simple classical models.

By examining the abundance levels throughout the thermal pulse cycle, we can understand ^{205}Pb production. The key stages of the TP cycle are displayed in Figure 4.3, which shows the evolution of a $3M_{\odot}$, metallicity $Z = 0.02$ AGB star from the FUNS evolutionary code. In these figures, the mass coordinate is simply the mass spherically enclosed for a given radius. The structural species (H, He, C, etc.) are dashed and illustrate the structure of the intershell and thermal pulse cycle. Orders of magnitude lower in abundance are the key s-process isotopes for understanding ^{205}Pb production: ^{204,205}Tl and ^{204,205}Pb. The important mechanisms are described in the sub-captions of Figure 4.3. Additionally, this narrated video [218] describes the same principles with the full set of evolutionary frames.

Figure 4.3: Abundances of key species throughout the 21st thermal pulse cycle (of 22) of a $3M_\odot$, $Z = 0.02$ AGB star modelled by the FUNS code. The structural species (H, He, C, etc.) are shown as dashed lines, key third-peak isotopes (namely ^{205}Pb) are solid lines, and temperature/neutron density are dashed-dotted lines. Figure created in collaboration with Dr. Diego Vescovi.

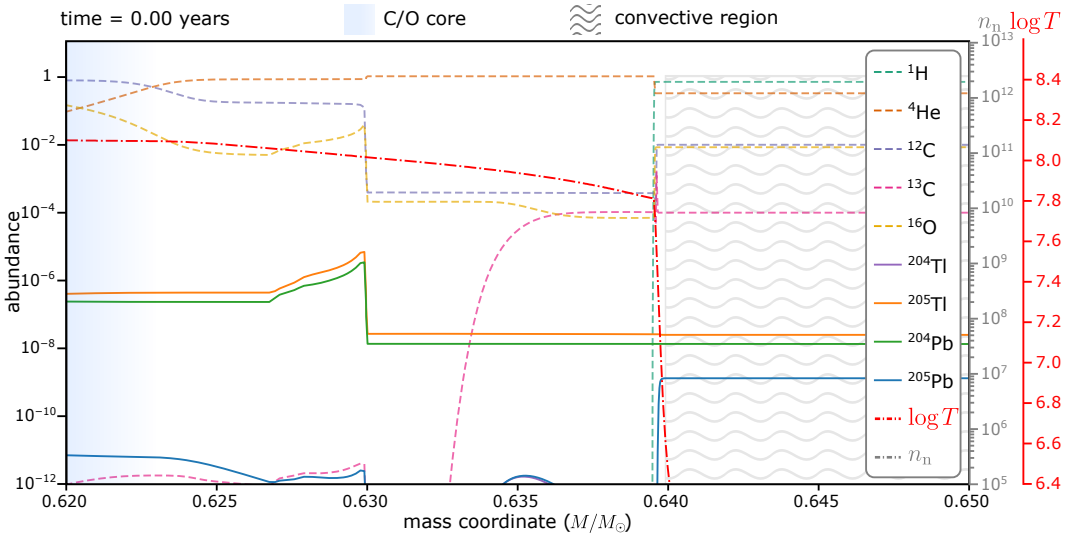

(a) The ignition of the thermal pulse is set to $T = 0$ years. The structure of the intershell region includes the C/O core, the dormant He burning shell, the ^{12}C-rich intershell region, the thin H-burning shell and the convective envelope. Initially no ^{205}Pb has survived in the intershell region.

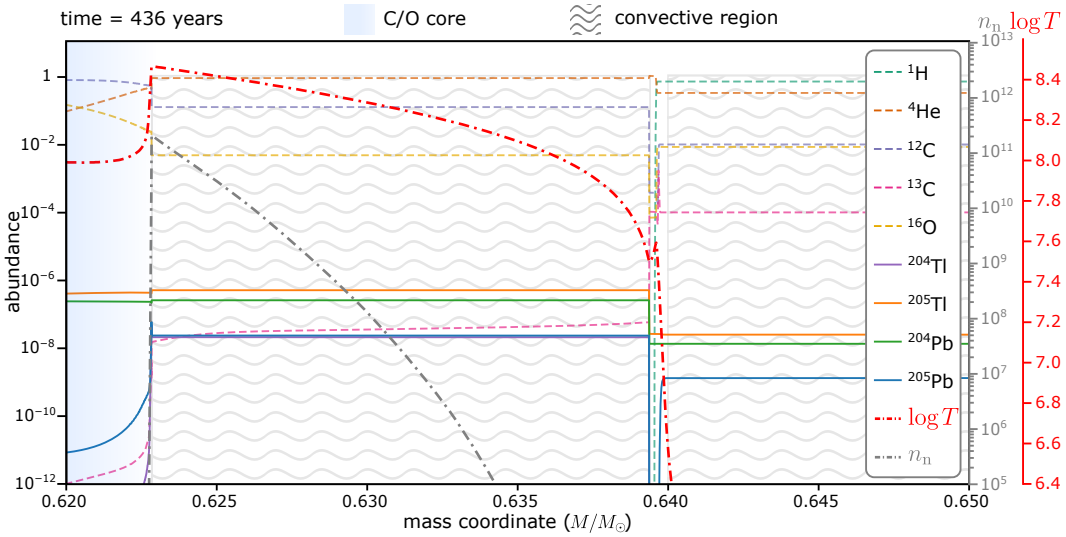

(b) The thermal pulse has fully engulfed the intershell region with convection powered by He burning at the bottom of the intershell. The ^{22}Ne(α, n) reaction is the source of neutrons. ^{205}Pb is being produced by both the s process and the β_b decay of ^{205}Tl. Because everything is mixed convectively, it is hard to know what production process is dominant, but it is clear that the ^{205}Tl decay is important as the ^{205}Pb abundance continues to rise even after the neutron production stops. During this phase, the H burning shell has been pushed out and extinguished.

Figure 4.3: Abundances of key species throughout the 21st thermal pulse cycle (of 22) of a $3M_\odot$, $Z = 0.02$ AGB star modelled by the FUNS code. The structural species (H, He, C, etc.) are shown as dashed lines, key third-peak isotopes (namely ^{205}Pb) are solid lines, and temperature/neutron density are dashed-dotted lines. Figure created in collaboration with Dr. Diego Vescovi.

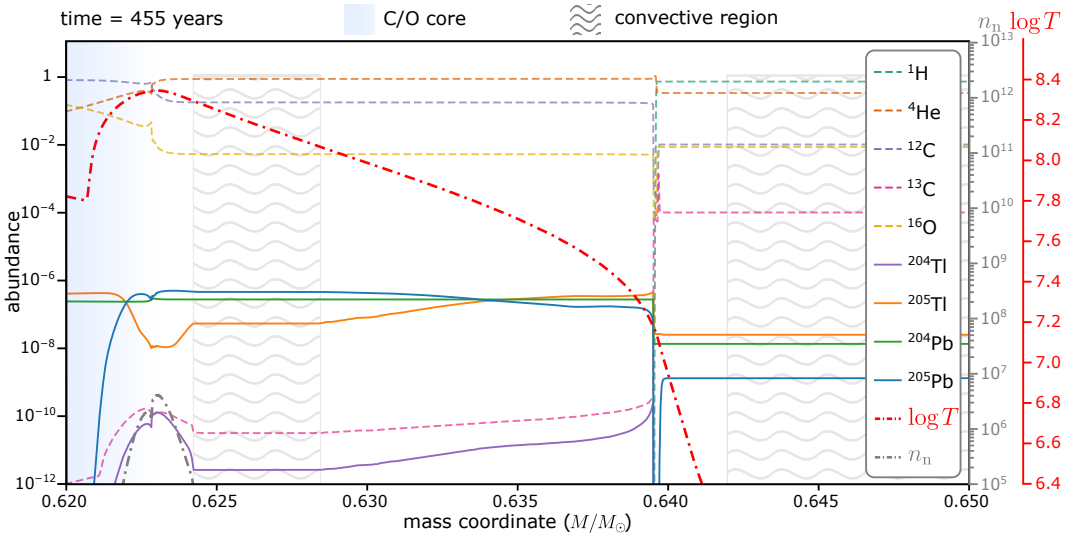

(c) He burning ends after the fuel is exhausted and neutron production stops with the drop in temperature. The convective zone recedes and is replaced by a radiative intershell, which begins to cool through radiative transfer. This power-down phase is crucial for the final ^{205}Pb yield of the star as this is where the ^{205}Pb abundance is set before the third dredge-up.

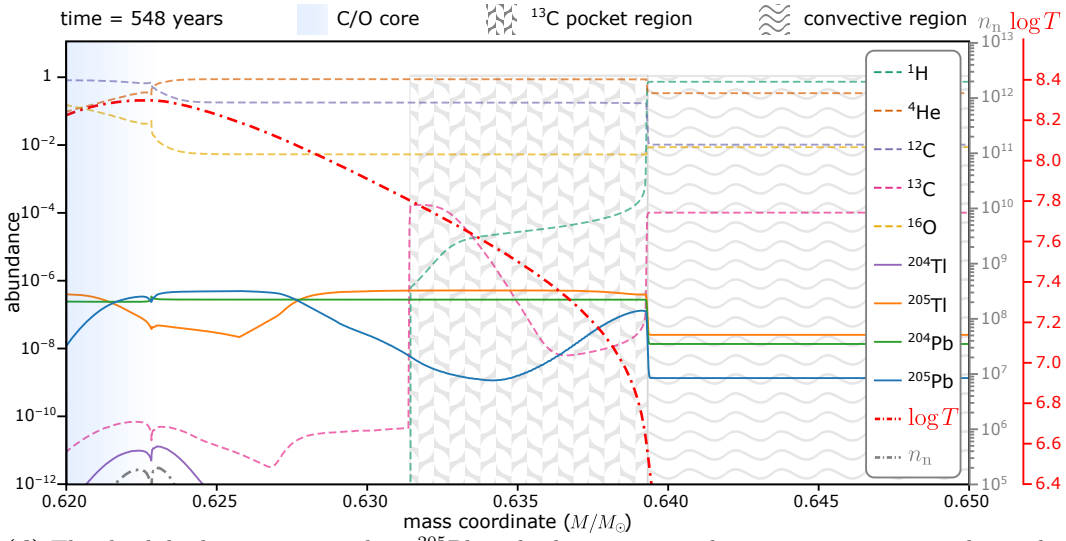

(d) The third dredge-up occurs where ^{205}Pb and other s-process elements are incorporated into the convective envelope. Once in the envelope, ^{205}Pb will survive due to the low temperatures. The ^{13}C pocket is formed during the third dredge-up by H mixing that reacts with the abundant ^{12}C to form ^{13}C (modelling details in text). The temperature is too low ($\log T < 7.95$) for the ^{13}C(α, n) neutron source to be activated yet.

Figure 4.3: Abundances of key species throughout the 21st thermal pulse cycle (of 22) of a $3M_\odot$, $Z = 0.02$ AGB star modelled by the FUNS code. The structural species (H, He, C, etc.) are shown as dashed lines, key third-peak isotopes (namely ^{205}Pb) are solid lines, and temperature/neutron density are dashed-dotted lines. Figure created in collaboration with Dr. Diego Vescovi.

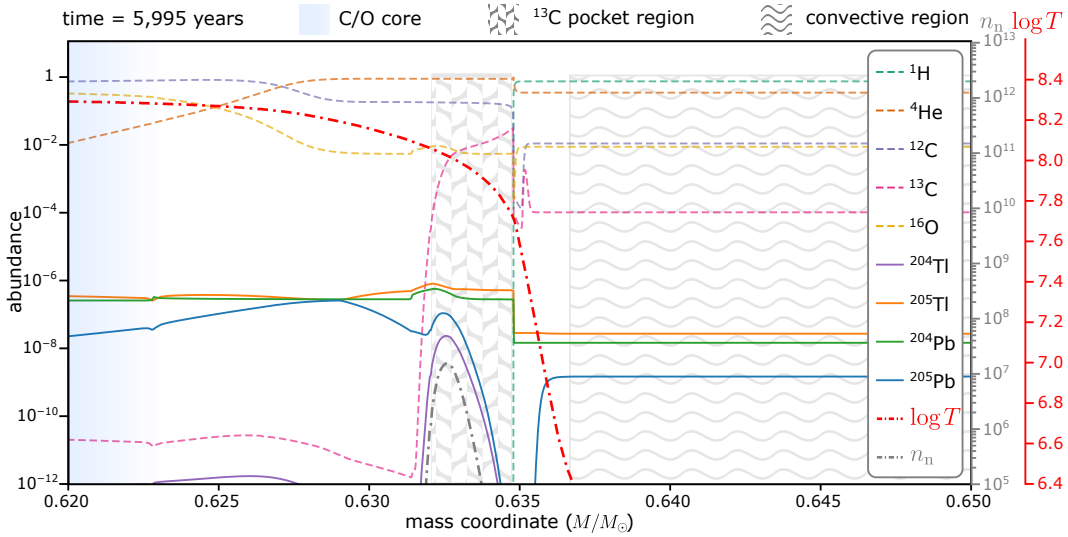

(e) As the intershell contracts and heats up after the thermal pulse, the H burning shell reignites pushing out the convective envelope. Once the temperature reaches 90 MK, the ^{13}C(α, n) source also ignites, providing neutrons. The main s process begins and ^{205}Pb is produced again in the ^{13}C pocket.

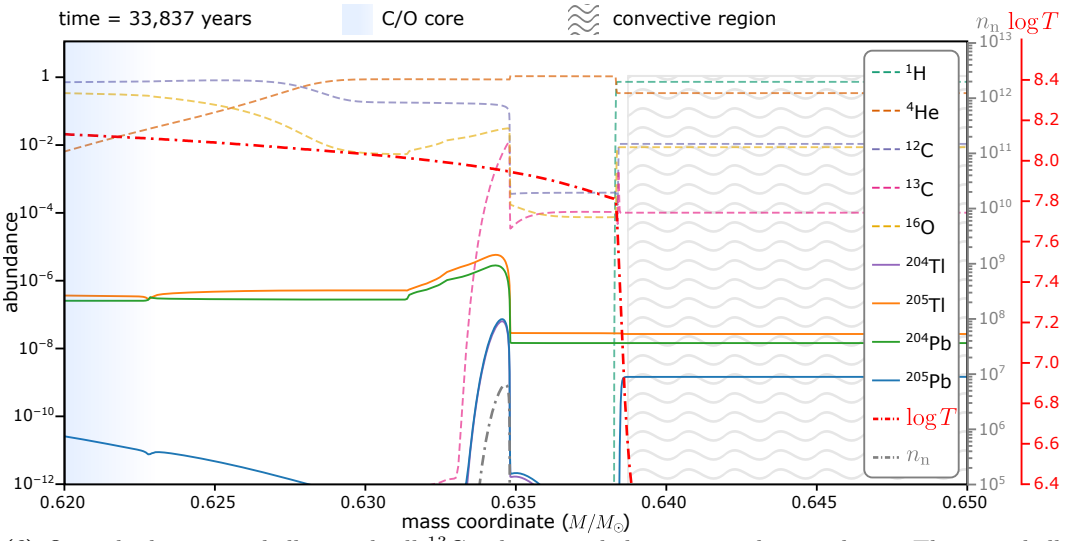

(f) Over the long intershell period, all ^{13}C is burnt and the neutron density drops. The intershell is sufficiently cool ($\log T < 8.30$) such that all ^{205}Pb produced in the thermal pulse and the ^{13}C pocket decays, leaving only ^{205}Tl. Eventually enough He ashes accumulate for the thermal pulse to begin again and the cycle repeats.

The takeaway from this analysis is that any active ^{205}Pb yield from the star originates from the thermal pulse, with the high-temperature β_b decay of ^{205}Tl accounting for a large fraction. The total yield of the star is very sensitive to the temperature gradient established during the power-down phase, as this determines the abundance of ^{205}Pb available to be extracted by the third dredge-up. This highlights how important accurate temperature dependent rates are for accurate ^{205}Pb production yields.

4.3.2 Model comparison

To compare the three AGB models, we considered an AGB star of 3 solar masses ($M_\odot$) and metallicity $Z = 0.02$. The resulting mass ejection yields are shown in Table 4.2, and the yields for a full range of masses are shown for Monash models in Figure 4.4. We can see that the updated weak decay rates have different impacts on the overall ^{205}Pb/^{204}Pb yield, which is unsurprising given each model operates at slightly different temperatures (and ^{205}Pb production is very sensitive to temperature).

This temperature trend can be seen explicitly in Figure 4.4, where higher masses cause higher temperatures resulting in higher ^{205}Pb yields. Eventually, ^{205}Pb yields tail off at the highest masses because the higher thermal pulse temperatures reduce the effectiveness of the third dredge-up, thus mixing less s-process products into the convective shell. This is true for all s-process elements; the AGB stars responsible for the bulk of the s process are those of 1–4$M_\odot$ due to the reduced effectiveness of the third dredge-up [56]. However, our results indicate that ^{205}Pb yields from a 4.5$M_\odot$ star are still significant, demonstrating the competition between the high-temperature production of ^{205}Pb and the efficiency of the third dredge-up.

In terms of the mechanics of the stellar models, the handling of the convective–radiative boundary mixing is the most relevant modelling uncertainty. The mixing determines not only the effectiveness of the third dredge-up, but also the temperature drop off at various boundaries, which crucially sets the ^{205}Pb abundance.

Convective boundary mixing is one of the most complicated topics in stellar modelling in general, and there is not an established prescription. The NuGrid models use a time-dependent convective overshoot prescription, where the momentum of the convection carries protons into the intershell. This is a physically self-consistent description of the mixing, albeit still using a free parameter β to characterise the extent of the exponential overshoot [206, 219]. The overshoot at the base of the thermal pulse results in an increase in the overall temperature of the thermal pulse, making the NuGrid models substantially hotter than the other two models resulting in the much higher ^{205}Pb yield [215].

The Monash models do not use convective overshoot, but instead search for a 'neutral border' by using interpolation in the radiative-to-adiabatic gradient ratio to decide how the convective region grows (see Karakas (2014) [220] for details). This method results in deeper third dredge-up dynamics than just defining a hard border, whilst not invoking any additional mixing.

Table 4.2: Yields for the three AGB models of a $3M_\odot$, $Z = 0.02$ star. Two sets of weak rates are used: the original rate library for each model, and the new rates from our collaboration (Mancino24).

Model	Weak Rates	^{205}Pb ($M_\odot$)	^{204}Pb ($M_\odot$)	^{205}Tl ($M_\odot$)	^{205}Pb/^{204}Pb
Monash	NETGEN	3.07×10^{-11}	3.17×10^{-9}	5.89×10^{-9}	0.0096
	Mancino24	2.29×10^{-10}	3.21×10^{-9}	5.48×10^{-9}	0.0710
NuGrid	NETGEN	4.67×10^{-11}	3.57×10^{-9}	5.34×10^{-9}	0.0130
	Mancino24	6.00×10^{-10}	3.41×10^{-9}	2.52×10^{-9}	0.1760
FUNS	FRUITY	1.01×10^{-9}	1.17×10^{-8}	2.05×10^{-8}	0.0859
	Mancino24	2.50×10^{-10}	1.17×10^{-8}	2.14×10^{-8}	0.0212

Figure 4.4: Calculated yields for ^{204,205}Pb, their ratio, and ^{205}Tl for Monash models of AGB stars of solar metallicity $Z = 0.014$. Salpeters mass function is overlayed displaying the associated population probability. Plot data is given in Table 4 of Leckenby *et al.* (2024) [164].

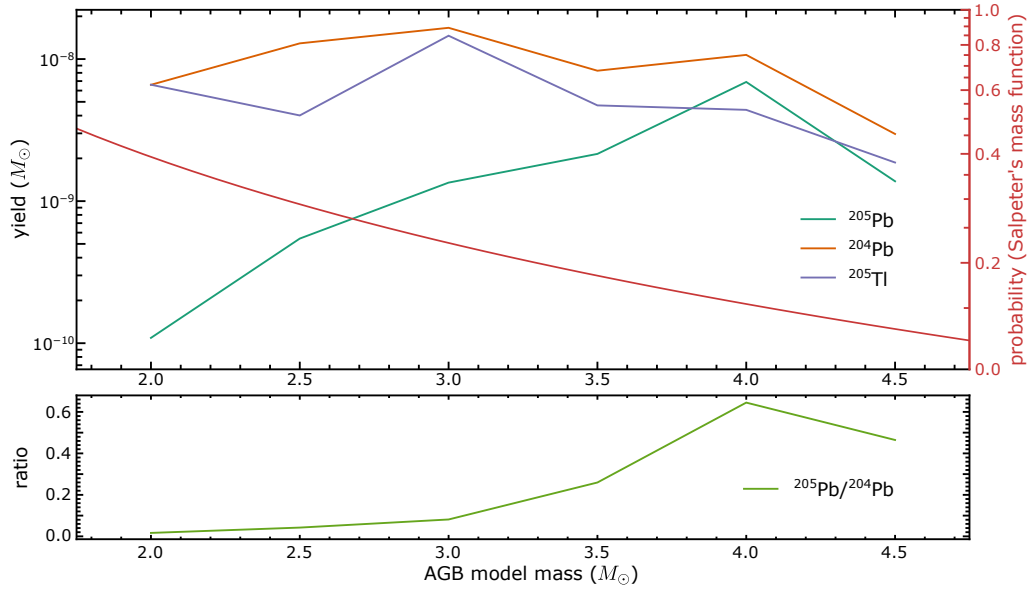

The FUNS models, having noted that convective overshoot was no longer reproducing the SiC isotopic grain distributions well, now use a magnetically-induced-buoyancy mixing mechanism, where magnetic 'flux tubes' in the He intershell are buoyant and cause mixing into the envelope [216, 217]. Each of these prescriptions has their own advantages and

challenges since boundary mixing is still an active problem. This is the primary reason for the factor-8 range in ^{205}Pb/^{204}Pb ratios, although of course many other modelling differences that impact the temperature are also consequential.

Modelling choices including different opacities, abundance compositions, and the still uncertain ^{22}Ne$(\alpha, n)^{25}$Mg reaction rate, all have a $< 10\%$ impact on the final abundances. Similarly, the updated neutron capture rates also had $< 10\%$ impact across all models.

4.4 ^{205}Pb in the interstellar medium

Once *s*-process products are mixed into the convective envelope, they are ejected into the interstellar medium by strong stellar winds that peel off the envelope throughout the AGB phase. The exact mechanism of these winds is complicated and not yet settled, but the broad consensus is that radiation pressure accelerates microscopic solid-state particles, called dust grains, that are formed in the atmosphere of the star and elevated with the expansion of the envelope during the thermal pulse [221]. The AGB star will thus enrich the surrounding interstellar medium (ISM) with *s*-process products.

For short-lived radionuclides (SLRs), the radioactive species will decay in the interstellar medium. To use an SLR as a cosmochronometer, it is crucial we have a good understanding of the abundance of the SLR in the ISM, as that is used as the start value of the clock. The change in the ISM abundance of an SLR is given by the radioactive decay of the SLR counterbalanced against the production rate dP/dt:

$$\frac{dN_{\rm SLR}}{dt} = -\frac{N_{\rm SLR}}{\tau} + \frac{dP_{\rm SLR}}{dt}, \tag{4.4}$$

where $N_{\rm SLR}$ is the abundance of the SLR and $\tau = t_{1/2}/\ln(2)$ is the mean life of the radioisotope. Lugaro *et al.* (2018) [106] note that this is a self-regulating equation in that if the production rate increases, the decay term also increases until a *steady-state* value is reached such that $dN_{\rm SLR}/dt = 0$. Then the SLR abundance is simply given by

$$N_{\rm SLR} = \frac{dP_{\rm SLR}}{dt}\tau. \tag{4.5}$$

The accumulation of the stable reference isotope is just given by

$$N_{\rm stable} = \frac{dP_{\rm stable}}{dt}T_{\rm Gal}, \tag{4.6}$$

where $T_{\rm Gal}$ is the age of the galaxy, so the abundance ratio for the SLR is given by

$$\frac{N_{\rm SLR}}{N_{\rm stable}} = \frac{dP_{\rm SLR}/dt}{dP_{\rm stable}/dt}\frac{\tau}{T_{\rm Gal}} = P_{\rm rat} \times \frac{\tau}{T_{\rm Gal}}, \tag{4.7}$$

where $P_{\rm rat}$ is the relative production ratio between the SLR and its stable reference isotope. This function decreases inversely with galactic age as the SLR reaches its steady state whilst the stable reference accumulates.

It was noted by Clayton (1984) [222] that production rates change over time as a response to the infall of primordial gas, which affects the local star formation rate (determining the SLR steady state) and the integrated stellar mass (determining the stable reference accumulation) whilst also diluting the SLR abundance [106]. Clayton (1985) [223] proposed an analytic model where the gas infall was parametrised by k, giving analytic solutions for the galactic chemical evolution (GCE) functions. This resulted in the steady-state formula requiring a simple multiplication by the factor $(k+1)$ if the nuclei are produced by primary nucleosynthesis (not requiring metallicity) or $(k+2)$ if the nuclei were produced by secondary nucleosynthesis (requiring metallicity). Dauphas *et al.* (2003) [224] determined a value of $k = 2.7(4)$ from galactic observations.

This analysis was modernised by Côté *et al.* (2019a) [19], who used a numerical GCE code that could track GCE parameters with more consistency than the analytic formulation of Clayton. In particular, they used a simple one-zone GCE code called `OMEGA`, coupled with the stellar-population-yield code `SYGMA` that is available as part of the NuPyCEE and JINAPyCEE packages on GitHub. Whilst the GCE analysis is more sophisticated, as a one-zone model, the ejecta of stars is assumed to be instantly well mixed into the ISM so no delay time to account for the lifetime of low-mass stars is included. They determined that multiplying by a single factor K reproduced the steady-state abundance of SLRs with a mean life below ~ 20 Myr, such that:

$$\frac{N_{\mathrm{SLR}}}{N_{\mathrm{stable}}} = K \times P_{\mathrm{rat}} \times \frac{\tau}{T_{\mathrm{Gal}}}, \tag{4.8}$$

From parameters of various Milky Way models fitted to observations from the compilation of Kubryk *et al.* (2015) [225], the best fit was $K = 2.3$, with a minimum value of 1.6 and a maximum value of 5.7. Note that these are not 1σ errors, but rather a range of possible values, and that each value represents a different realisation of the Milky Way, so results from a single K must be considered together.

This analysis, however, does not consider the fact that enrichment events of the ISM are discrete, with sharp jumps in N_{SLR} as a nucleosynthesis event releases fresh radionuclides into the ISM. This is especially important to consider when trying to use the initial ISM abundance as the starting value for a cosmochronometer. The SLR abundance from a set of n discrete enrichment events separated by a constant time between enrichment events δ_C is given by [106]

$$\begin{aligned} N_{\mathrm{SLR}}(t) &\propto p_{\mathrm{SLR}} \times \left(1 + e^{-\delta_C/\tau} + \cdots + e^{-(n-1)\delta_C/\tau}\right) \times e^{-(t-n\delta_C)/\tau} \\ &= p_{\mathrm{SLR}} \Big(\sum_{j=0}^{n-1} e^{-j\delta_C/\tau} \Big) e^{-(t-n\delta_C)/\tau} = p_{\mathrm{SLR}} \Big(\frac{1 - e^{-(n+1)\delta_C/\tau}}{1 - e^{-\delta_C/\tau}} \Big) e^{-(t-n\delta_C)/\tau}, \end{aligned} \tag{4.9}$$

where p_{SLR} is the production yield from a discrete event and the $e^{-(t-n\delta_C)/\tau}$ term describes the decay from the last event. The proportionality arises from the fact that infalling gas

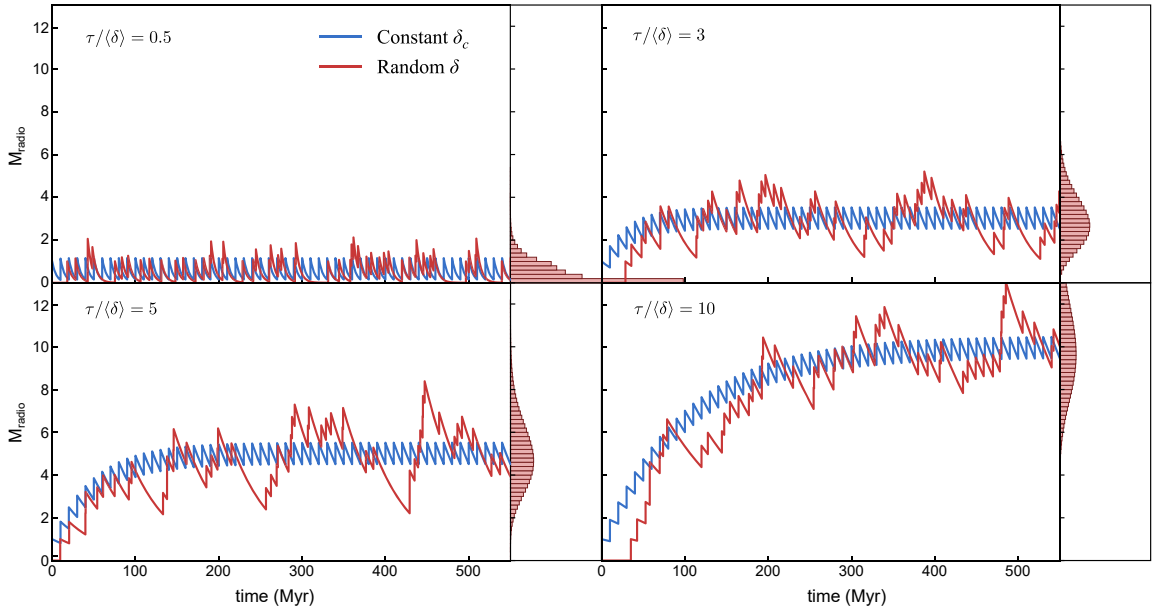

Figure 4.5: The steady-state value for the mass of an SLR in the ISM for both a constant time between enrichment events (blue) and a stochastic sampling of the time between enrichment events (red). Projections on the right show the long-time distribution of a stochastic sampling. Figure adapted from Côté *et al.* (2019b) [226].

can dilute the SLR abundance. This discrete growth is shown in the blue functions of Figure 4.5 for a variety of τ/δ_C values.

To make this discrete enrichment formalism more realistic, Côté *et al.* (2019b) [226] used Monte Carlo simulations to randomly sample the time between enrichment events δ. This stochastic enrichment generates a wider but more realistic range in the possible values of the ISM ratio. Some example Monte Carlo runs are shown by the red functions in Figure 4.5, where the histograms on the right show projections of the long-term stochastic distribution. Because we are dealing with stochastic discrete enrichments now, there are combinations of the mean life τ and the average time between enrichments $\langle\delta\rangle$ that don't result in a steady-state value. In particular, if $\tau/\langle\delta\rangle \gtrsim 2$, which Côté *et al.* [226] referred to as Regime I, then a steady state distribution is reached. This is the scenario where the ISM ratio can be used to define an isolation time of the Solar System from the ISM, because the ISM value is well defined. Note that the distribution is only symmetric if $\tau/\langle\delta\rangle \gtrsim 5$. If $\tau/\langle\delta\rangle \lesssim 0.3$, known as Regime III, then the probability that any ISM ratio arises from just one event is greater than 50%. This allows us to define the time from a single last event with reasonable confidence. If $0.3 \lesssim \tau/\langle\delta\rangle \lesssim 2$, known as Regime II, then the ISM ratio most probably arises from a small number of events and the distribution is highly

asymmetric, which is not ideal for use as a cosmochronometer.

For Regime I, the steady-state case, Côté *et al.* (2019b) [226] find that if $T_{\rm Gal} \gg \tau$, then the mean value is well approximated by

$$\langle N_{\rm SLR} \rangle \propto p_{\rm SLR} \frac{\tau}{\langle \delta \rangle}, \tag{4.10}$$

which is equivalent to equation (4.5). Note that the proportionality is now to acknowledge that complexities like dilution are considered. The stable reference isotope is simply

$$N_{\rm stable} \propto p_{\rm stable} \frac{T_{\rm Gal}}{\langle \delta \rangle}, \tag{4.11}$$

which is similarly equivalent to equation (4.6). Thus, the steady state formula is returned

$$\frac{N_{\rm SLR}}{N_{\rm stable}} = K \times P_{\rm rat} \times \frac{\tau}{T_{\rm Gal}} \times \xi(\tau/\langle \delta \rangle) \tag{4.12}$$

with an added function $\xi(\tau/\langle \delta \rangle)$ that is a probability distribution representing the numerical scatter arising from the stochastic enrichment. By definition, ξ has a mean of 1, and the shape of the distribution will be determined by the Monte Carlo results of Côté *et al.* (2019b) [226] for a given $\tau/\langle \delta \rangle$ value.

The use of the modified steady-state formula, i.e. equation (4.12), is a good starting point in predicting the value of the ISM ratio for an SLR. To apply the formula, one must determine the value of $\langle \delta \rangle$, which represents the average time between enrichment events for a given parcel of gas. Estimates of $\langle \delta \rangle$ for various nucleosynthetic events are poorly known, but it can be estimated from first principles by considering how much galactic mass is swept out by the ejecta of any given enrichment source, in what is called the 'snowplough' approach by Meyer & Clayton (2000) [193]. By considering energy conservation for the winds from an AGB star, one derives a value of $\sim$ 50 Myr [106, 189]. Given the mean-lives of the *s*-process SLRs (see Table 4.1), this would put their $\tau/\langle \delta \rangle$ value firmly into Regime III. However, it has been proposed that other processes in the ISM, like core-collapse supernova shock waves [227] and turbulent gas diffusion [228, 229] are likely to cause further distribution of AGB products.

With this in mind, Côté *et al.* (2019b) [226] and Trueman *et al.* (2022) [186] chose a value of $\langle \delta \rangle = 3.16$, which puts most *s*-process SLRs into Regime I for which an isolation time can be derived. It should be noted that as long as the $\langle \delta \rangle$ value puts the SLR in Regime I, then the choice of $\langle \delta \rangle$ only affects that size of the stochastic variation in the ISM, not the mean value. In fact, given the potential for ISM mixing to reduce the value of $\langle \delta \rangle$ to quite small values, the value of 3.16 was chosen as the most conservative choice that still left the *s*-process SLRs in Regime I.

This choice of $\langle \delta \rangle = 3.16$ works for ^{205}Pb ($\tau/\langle \delta \rangle = 7.8$), ^{107}Pd (3.0), and ^{182}Hf (4.06), but does not work for ^{135}Cs (0.60). In particular, it puts ^{135}Cs in Regime II, which makes it

challenging to place meaningful constraints on either a steady-state or last-event scenario. Given the value of $\langle\delta\rangle = 3.16$ was chosen to be conservative, we separately consider $\langle\delta\rangle = 1.0$ for ^{135}Cs. In theory, the value of $\langle\delta\rangle$ should be consistent across all s-process SLRs because each isotope is co-produced in low-mass AGB stars. However, as mentioned previously, as long as each isotope is in Regime I, only the size of the stochastic variation is affected, not the mean value.

Following these choices, we applied equation (4.12) to ^{205}Pb and the other s-process SLRs ^{107}Pd, ^{182}Hf, and ^{135}Cs, in line with the previous study by Trueman *et al.* (2022) [186]. We used the values of K proposed by Côté *et al.* (2019a) [19] to explore variation across different Milky Way parameters. To calculate the production ratios $P_{\rm rat}$, we considered a population of AGB stars with masses from 2–4.5 $M_\odot$ with an initial metallicity of $Z = 0.014$. The yields were calculated with the Monash AGB models, and the individual yields were weighted using Salpeter's mass function, which is a simple power law description of the initial mass function for a population of stars. We integrated the yields over Salpeter's mass function to get a ^{205}Pb/^{204}Pb production ratio of 0.167 using number abundance.

To get the ISM ratio from the production ratio $P_{\rm rat}$ for that s-process SLRs that have an r-process contribution, one must correct for the r-process contribution to the stable isotope (assuming, as we have, that the radioactive r-process contribution is negligible). We use the fractions presented in Table 3 of Trueman *et al.* (2022) [186] to scale the stable isotope abudance, which we achieve by multiplying the s-process production ratio by the s-process fraction for the stable reference. These fractions, and the resulting ISM ratios of s-process isotopes, are provided in Table 4.3.

The modified steady-state formula is only an approximation, and a full galactic chemical evolution (GCE) treatment is required to get accurate ISM values. This is what Trueman *et al.* (2022) [186] did for the s-process SLRs available at the time: ^{107}Pd, ^{182}Hf, and ^{135}Cs. They used the `OMEGA+` GCE code to track the abundances of SLRs over the course of galactic evolution to determine the ISM values at the birth of the sun at $T_{\rm Gal} = 8.4$ Gyr. `OMEGA+` is an extension of the one-zone code `OMEGA`, featuring a cold, star-forming gas reservoir (a.k.a. the Galaxy) and a hot, non-star-forming reservoir (a.k.a. the circum-galactic medium). In this model, time-dependent galactic parameters (e.g. gas inflows, etc.) and metallicity dependent stellar yields can be used that give a more accurate ISM value than the steady-state formula, although variation due to local inhomogeneities are not accounted for.

Comparing the results of the steady-state approximation to the full GCE treatment, we found that the ^{107}Pd/^{108}Pd ratio is 36% higher using the steady-state formula, the ^{182}Hf/^{180}Hf ratio is 55% lower, and the ^{135}Cs/^{133}Cs is 16% higher. The fact that no trend can be discerned based on lifetime indicates that the origin of these differences probably lies in the metallicity-dependent yields, which vary differently for each isotope. Thus, another full GCE calculation of all the s-process SLRs is warranted given the considerable new information gathered over the last few years. However, we can say that equation (4.12) reproduces the GCE results within 50%.

Table 4.3: ISM ratios calculated (using Equation (4.12)) and isolation times for s-process short-lived radionuclides using the Monash AGB models. τ is the SLR mean-life, $P_{\rm rat}$ is the SLR-to-stable production ratio, and $\langle\delta\rangle$ is the mean time between enrichment events. The uncertainty factors correspond to the $\pm1\sigma$ quantile values given the distributions are asymmetric.

	^{205}Pb/^{204}Pb	^{107}Pd/^{108}Pd	^{182}Hf/^{180}Hf	^{135}Cs/^{133}Cs
ESS ratio	$1.8(12)\times10^{-3}$	$6.6(4)\times10^{-5}$	$1.02(4)\times10^{-4}$	$<2.8\times10^{-6}$
τ [Myr]	24.5(13)	9.4(4)	12.84(13)	1.9(3)
s-process $P_{\rm rat}$	0.167	0.141	0.111	1.059
$\langle\delta\rangle$ [Myr]	3.16	3.16	3.16	1.0
$\tau/\langle\delta\rangle$	7.8	3.0	4.06	1.9
Unc. factors	0.76, 1.27	0.62, 1.46	0.67, 1.39	0.53, 1.58
Value of K	s-process fraction of stable reference			
1.6 (min)	1	0.37	0.88	0.14
2.3 (best)	1	0.45	0.86	0.17
5.7 (max)	1	0.60	0.85	0.21
	ISM ratio			
1.6 (min)	$\left(7.7^{+2.1}_{-1..9}\right)\times10^{-4}$	$\left(9.0^{+4.2}_{-3.5}\right)\times10^{-5}$	$\left(2.3^{+0.9}_{-0.8}\right)\times10^{-4}$	$\left(5.1^{+3.0}_{-2.5}\right)\times10^{-5}$
2.3 (best)	$\left(1.10^{+0.30}_{-0.27}\right)\times10^{-3}$	$\left(1.57^{+0.73}_{-0.62}\right)\times10^{-4}$	$\left(3.3^{+1.3}_{-1.1}\right)\times10^{-4}$	$\left(8.9^{+5.3}_{-4.3}\right)\times10^{-5}$
5.7 (max)	$\left(2.7^{+0.8}_{-0.7}\right)\times10^{-3}$	$\left(5.2^{+2.4}_{-2.0}\right)\times10^{-4}$	$\left(8.0^{+3.1}_{-2.7}\right)\times10^{-4}$	$\left(2.7^{+1.6}_{-1.3}\right)\times10^{-4}$
	Isolation time [Myr]			
1.6 (min)	$-20.7^{+11.5}_{-10.0}$	$2.9^{+3.6}_{-4.7}$	$10.6^{+4.3}_{-5.3}$	$>5.6^{+0.9}_{-1.3}$
2.3 (best)	$-11.8^{+11.5}_{-10.0}$	$8.1^{+3.6}_{-4.7}$	$14.9^{+4.3}_{-5.3}$	$>6.6^{+0.9}_{-1.3}$
5.7 (max)	$10.5^{+11.5}_{-10.0}$	$19.3^{+3.6}_{-4.7}$	$26.4^{+4.3}_{-5.3}$	$>8.8^{+0.9}_{-1.3}$

Uncertainty factors are 1σ equivalent (i.e. $\pm1\sigma = 68.2\%$) to represent the probability distributions shown in Fig. 4.7. Choice of δ and uncertainty factors are described in the text based on refs. [186, 226]. ESS ratios (with 2σ uncertainties) are taken from ref. [106], τ values from ref. [53]. Note that we updated the s-process production ratios P to those from the Monash AGB models computed with the the most recent nuclear inputs, relative to the yields used in refs. [186]. The stable s-process fractions are taken from the Monash GCE models of ref. [186], except for ^{204}Pb, which is an s-only isotope.

4.5 Isotopic ratios from meteorites

The long-since extinct value of the SLR ratio in the early Solar System can be extracted from meteorites by determining if the daughter isotope abundance correlates with the reference isotope abundance over meteorite inclusions of different chemistry. In particular, a linear regression is performed between the daughter isotope relative to a reference of the same element (e.g. ^{205}Tl/^{203}Tl) and the SLR reference isotope relative to the same denominator (e.g. ^{204}Pb/^{203}Tl). The inclusions in the meteorite (and also across different meteorites) will sample different ^{204}Pb/^{203}Tl ratios as a result of their varying chemistry. If the meteorite inclusions all formed at the same time, which can be determined by other dating systems like U-Pb dating, then a correlation between the daughter isotope and its reference isotope indicates that this correlation is driven by the radioactive decay of the SLR. This correlation line is called an *isochron*, since all points are associated with the same time, and the slope of the line determines the SLR ratio in the early Solar System, as more ^{204}Pb would imply more ^{205}Pb as well that decayed to ^{205}Tl.

The method is quite robust in theory, but is particularly vulnerable to systematic uncertainties. The radiogenic component of the stable isotope abundance is very small, often in the third or fourth significant digit, so measurement systematics can very easily affect the signal. A natural systematic arises from the fact that some chemical processes are mass dependent, referred to as *mass fractionation*, which can obscure the radiogenic correlation or introduce systematic bias. This is typically accounted for by looking to other isotopes of the element to calibrate any mass fractionation, but this is not possible for Tl, which only has two stable isotopes (^{203,205}Tl), nor Pb, whose other three stable isotopes (^{206,207,208}Pb) are affected by radiogenic contributions from the U/Th decay chains. Additionally, Pb abundances are easily polluted by terrestrial Pb during the collision with Earth. As a result, early studies looking for live ^{205}Pb in meteorites were unable to observe a signal [230].

It was not until the early 2000s that a signal was observed, and since then four studies have observed ^{205}Pb ratios in iron meteorites and various chondrites:[15]

1. Nielsen *et al.* (2006) [231] were the first to demonstrate live ^{205}Pb existed in the early Solar System by determining a strong isochron for IAB iron meteorites.
2. Baker *et al.* (2010) [232] measured the only set of carbonaceous chondrites to date, and established an initial isochron of $^{205}\text{Pb}/^{204}\text{Pb}_{SS,0} = (1.0 \pm 0.4) \times 10^{-3}$ at 2σ uncertainty.

[15]Meteorites are classified in three types: iron meteorites made mostly of metal, stony meteorites made mostly of silicate minerals, and stony-iron meteorites with roughly equal parts metal and silicates. Chondrites are stony meteorites that have not melted, and form the bulk of meteorites that fall to Earth. Carbonaceous chondrites are among the first solids to have condensed in the early Solar System, whilst enstatite and ordinary chondrites (the other two classes of chondrites) formed later. Both iron meteorites and chondrites have further subcatagories based on their structure and chemistry.

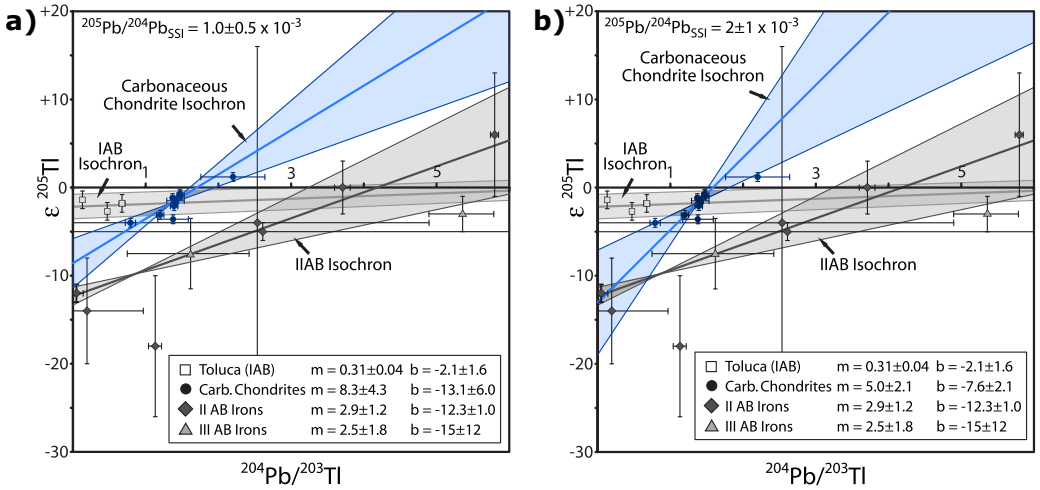

Figure 4.6: The isochron fits to all Tl meteorites including the carbonaceous chondrites [232] and the IAB [231], IIAB, and IIIAB [233] iron meteorites. **a)** shows the original fit from Baker *et al.* [232], whilst **b)** shows the adjustment to the carbonaceous chondrite isochron by Andreasen *et al.* [233] where the intercepts are improved. Figure reproduced from Andreasen *et al.* [233].

3. Andreasen *et al.* (2012) [233] followed up with measurements of IIAB and IIIAB iron meteorites.
4. Palk *et al.* (2018) [234] measured enstatite and ordinary chondrites, and evaluated the previous literature for their calibration.

Iron meteorites typically form 10–20 Myr later than carbonaceous chrondrites, which are thought to be among the first solids that condensed in the early Solar System. Whilst older meteorites cannot help set the initial SLR ratio due to uncertainties in their formation time, they are crucial in checking the consistency of the carbonaceous chondrites data. The isochron from Nielsen *et al.* requires either a much longer formation time (~ 60 Myr) than is typical, or a lower initial ratio than determined by Baker *et al.* [232]. However, the isochron from Andreasen *et al.* [233] provides consistent ages, supporting the value from Baker *et al.* [232].

Andreasen *et al.* [233] took the further step of rejecting "the three samples that suffer from large terrestrial Pb contamination or are desert finds" in the Baker *et al.* [232] sample. This was motivated by the observation that the $^{204}\mathrm{Pb}/^{203}\mathrm{Tl} = 0$ intercepts do not agree for the carbonaceous chondrites and the iron meteorites, which they argue is significant due to the fact that they say mass fractionation is unlikely to be able to explain an effect of this size. By removing the suspect samples, they find better agreement between the intercepts of the two isochrons and correspondingly suggest an adjusted value for the carbonaceous chondrite isochron of $^{205}\mathrm{Pb}/^{204}\mathrm{Pb}_{SS,0} = (2 \pm 1) \times 10^{-3}$. The data and best fit isochrons

from Andreasen *et al.* [233] are shown in Figure 4.6. Note that ε notation is given by

$$\varepsilon\,^{205}\mathrm{Tl} = \left(\frac{(^{205}\mathrm{Tl}/^{203}\mathrm{Tl})_{\mathrm{sample}}}{(^{205}\mathrm{Tl}/^{203}\mathrm{Tl})_{\mathrm{standard}}} - 1 \right) \times 10^4. \tag{4.13}$$

To address the systematic effects from mass fractionation, Baker *et al.* [232] and Andreasen *et al.* [233] also measured Cd isotopes. The idea is that Cd behaves similarly to Tl chemically, so Cd isotopic analysis can be used as a monitor for potential Tl fractionation. In particular, Cd and Tl have similar condensation temperatures and are known to be volatised during heating and metamorphic processes. A study of enstatite and ordinary chondrites by Palk *et al.* (2018) [234] confirmed that the correlation in Cd and Tl fractionation is excellent across two orders of magnitude. Baker *et al.* [232] also measured the Pb isotopes to identify terrestrial contamination. Thus, we can be reasonably confident that the ^{205}Pb signal is well-founded, even if the data set is still small.

Palk *et al.*[234] use the isochron of carbonaceous chondrites to calibrate the isochrons of the enstatite and ordinary chondrites, so they can be used to determine the chondrite ages. As a result, they also needed to evaluate a value for the carbonaceous chondrites, and chose to use of $^{205}\mathrm{Pb}/^{204}\mathrm{Pb}_{SS,0} = (1.8 \pm 1.2) \times 10^{-3}$ to cover the full 2σ range from both Baker *et al.* [232] and Andreasen *et al.* [233]. In our study of ^{205}Pb, we have chosen to consider both the value suggested by Palk *et al.* [234] and the original value given by Baker *et al.* [232].

4.6 Isolation time

The final step is to calculate the isolation time of the early Solar System (ESS). In particular, the isolation time is the length of time between the isolation of the Solar System from further enrichment by the interstellar medium to the formation of the first solids such as the carbonaceous chondrites. By using the ISM ratio as the start and the ESS ratio as the stop, we can derive the isolation time such that

$$T_{\mathrm{iso}} = \ln \left[\frac{(N_{\mathrm{SLR}}/N_{\mathrm{stable}})_{\mathrm{ISM}}}{(N_{\mathrm{SLR}}/N_{\mathrm{stable}})_{\mathrm{ESS}}} \right] \tau. \tag{4.14}$$

Monte Carlo simulations were used to propagate both the stochastic variation of the ISM and the uncertainty in the ESS meteorite values to produce a probability distribution function (PDF) for the isolation time of each of s-process SLR. For ^{205}Pb, the ESS result suggested by both Palk *et al.* [234] and Baker *et al.* [232] were considered. The resulting PDFs are shown in Figure 4.7 for the minimum/best/maxixmum values of K.

Using the full ESS range suggested by Palk *et al.* [234], the predicted isolation time for the best estimate of K is positive for 25% of the distribution. Negative isolation times are obviously unphysical, and it was previously impossible to produce positive isolation times for ^{205}Pb using Monash models, which was attributed to the uncertain nuclear physics

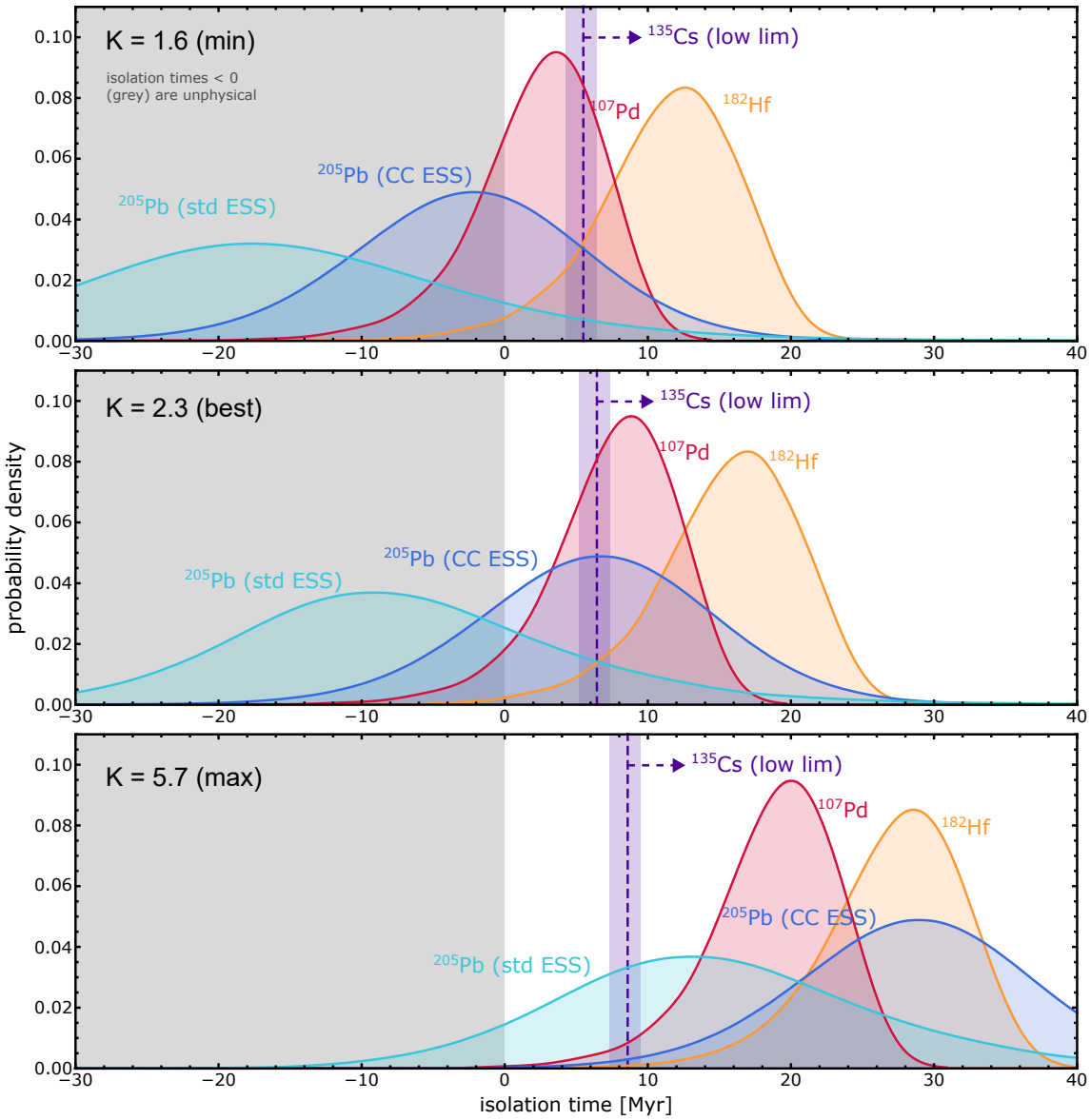

Figure 4.7: Probability distribution functions (PDF) for the Solar System isolation time given the min/best/max value of K. Std ESS refers to the ESS value from Palk *et al.* [234], CC ESS from Baker *et al.* [232]. For ^{107}Pd and ^{182}Hf, the meteorite measurements are well constrained (uncertainties are 2–3%), so the PDF widths are due to the stochastic ISM. For ^{205}Pb, the meteorite uncertainty is much larger ($\sim$ 30%) so the PDF width arises roughly equally from the meteorite uncertainty and the stochastic ISM. ^{135}Cs only has a lower limit for meteorite measurements, so is dotted to highlight the different mean enrichment spacing $\langle\delta\rangle$ assumed. Broadly speaking, the three s-process SLRs are consistent with an isolation time arising from just GCE.

inputs. With our newly measured β_b-decay rate for $^{205}Tl^{81+}$ and the associated new astrophysical weak rates, we have eliminated the major nuclear physics limitation of ^{205}Pb. Our ^{205}Pb isolation time PDF is consistent with the giant molecular cloud theory proposed by the other *s*-process SLRs. In particular, our PDF supports the use of the lower value for the ESS ^{205}Pb/^{204}Pb ratio originally determined by Baker *et al.* [232].

When considering the probability distributions in Figure 4.7, we must consider if there is correlation between the isotopes. In particular, the largest source of uncertainty in the PDFs is the stochastic variation in the ISM, but the *s*-process SLRs are co-produced in AGB stars and thus should vary together. However, the situation is not so simple. The stochastic model presented by Côté *et al.* [226] considers 'events' that enrich a parcel of gas, but it was deliberately kept vague as to what these events were so that their results could be applied to the continuous enrichment functions generated by most GCE models.

In the case of AGB stars, it is not obvious what an 'enrichment event' is, whether it is a single thermal pulse, the lifetime of a single AGB phase, or the AGB output from a full population of stars. We have chosen to use the production ratio from a whole population of stars as representative of the expected production ratio. If instead, the enriching events were single stars, then the production ratios can vary significantly depending on the mass of the AGB star, as as shown in Figure 4.4. For single stars, the *s*-process production ratios are not well correlated as ^{107}Pd, ^{182}Hf, and ^{205}Pb each come from different *s*-process peaks and are thus separated by different bottlenecks in the steady flow, associated with the neutron shell closures. On top of this, the yields of ^{205}Pb, ^{181}Hf, and ^{134}Cs are temperature dependent, so additional variation in production ratio should be considered. This complexity is currently beyond the scope of SLR analysis, but highlights areas where there is variation that is not currently accounted for, making the independence of the stochastic variation in the ISM presented here appear more reasonable.

Whilst the presented scenario is self-consistent, we also considered the situation if the mean enrichment spacing $\delta\rangle$ was long enough to put us in Regime III ($\langle\delta\rangle \gtrsim$ 30–70 Myr) where the ESS abundance was likely due to a single last event. For just ^{107}Pd and ^{182}Hf, it had been possible to identify some AGB models that provided a self-consistent last event occurring roughly 25 Myr before the formation of the first solids. However, with the addition of ^{205}Pb, stellar masses below $3M_\odot$ do not produce enough ^{205}Pb whilst models above this mass typically produce too much ^{205}Pb and ^{182}Hf, relative to ^{107}Pd. The $3M_\odot$, $Z = 0.014$ model with $K = 5.7$ and the lowest ^{205}Pb/^{204}Pb value for the 2σ range still gives a self-consistent isolation time of about 30 Myr, but this clearly requires more fine-tuning than the continuous enrichment assumption because there is no stochastic variation in the ISM ratios. This scenario needs to be further constrained with predictions from the ratios of the SLRs relative to each other, i.e. ^{107}Pd/^{182}Hf and ^{182}Hf/^{205}Pb.

Finally, the potential pollution from massive stars forming within the giant molecular cloud during the isolation time was also considered. Wolf-Rayet stars are very massive ($> 40M_\odot$) and very short-lived ($<$ 5 Myr), and can produce ^{107}Pd and ^{205}Pb, but cannot produce ^{182}Hf due to insufficient neutron density. Contributions from these stars would be

added on top of the GCE contribution from AGB stars, but this contribution is currently not needed. Core-collapse supernovae could also add to the abundance s-process SLRs in the ISM, but CCSNe cause overproduction of ^{135}Cs, ^{60}Fe, and ^{53}Mn, so this also seems unlikely.

In summary, with our new experimental result and more accurate astrophysical rates, the scenario of the s-process SLRs being explained by self-consistent isolation from standard GCE in a giant molecular cloud appears to have withstood the test from ^{205}Pb. However, the steady-state formula is only an approximation, and a full GCE study should be repeated including ^{205}Pb. Additionally, it would be most realistic if a physically motivated $\langle\delta\rangle$ value could be chosen, and then the production ratios of individual AGB stars could be sampled during the Monte Carlo simulation to accurately handle the correlations between the s-process SLRs. However, this future work is beyond the scope of this thesis.

Chapter 5

The PLEIADES Detector

Having now explored the nuclear astrophysics pipeline that takes us from experimental measurements to the production of the elements and the origins of our Solar System, we return to experimental nuclear physics to discuss the construction of a particle detector that will be used in future exotic decay measurements. As introduced in Section 2.6, particle detectors located inside stainless steel pockets—separated from the ultra-high vacuum by thin, stainless-steel windows—are used in the Experimental Storage Ring (ESR) to record particles that leave the momentum acceptance of the storage ring. These particle detectors are crucial in characterising the products of decays or reactions in the storage ring. The capability of these pocket detectors has continued to develop, and this chapter discusses the construction and characterisation of the most advanced ESR pocket detector yet, the ParticLE sIlicon-scintillAtor DEtector for Storage rings (PLEIADES)[16].

PLEIADES is one of a set of detectors used by the Isomeric states, LIfetimes, and MAsses (ILIMA) collaboration. The ILIMA collaboration aims to study the masses and decay pathways of the cocktail beams of many fragments produced at GSI. In addition to the nuclear properties outlined in the name, the collaboration also hopes to characterise particle-emission branching ratios at the GSI facilities. These fundamental nuclear data will have a large variety of applications, including extending the experimental data for neutron-rich regions crucial for understanding the r process. To cover such a wide range of decay modes across many species simultaneously, particle detectors that can separate individual isotopes are necessary. The particle detectors will provide complementary information to the Schottky detectors, allowing for better particle identification and cross-checking of lifetimes. To provide isotopic identification, a δE–E telescopic particle detector is required.

PLEIADES follows a prototype δE–E detector called the CsI–Silicon Particle detector for Heavy ions Orbiting in Storage rings (CsISiPHOS). The upgrades implemented in PLEIADES have also been applied to CsISiPHOS, so the ILIMA collaboration now has two versatile pocket detectors for decay spectroscopy. Both detectors can be operated together allowing for detection of ion decays in both straight sections of the ESR for twice the efficiency. This chapter summarises the design philosophy put forward by the ILIMA collaboration outlined in the FAIR Technical Design Report [235], and describes the construction and commissioning of PLEIADES with a ^{208}Pb beam in June 2022.

[16]The name PLEIADES was chosen because it connects the new detector to the prototype CsISiPHOS. Not only does PLEIADES invoke connections of the heavens to the earth through the ascension of the seven sisters, but the seventh Pleiades sister Merope was the wife of Sisyphus in Greek mythology.

5.1 Silicon detector physics

Silicon detectors are a favoured choice for charged particle spectroscopy for a few reasons: they provide precise energy resolution for charged particles, they allow simultaneous energy and position readout using detector strips, and the direct electronic signal generated by the silicon diode interfaces easily with electronic signal processing. For these reasons, and additionally the compactness of silicon chips, silicon detectors make an ideal choice for measuring the energy loss in the ESR pockets where space is highly constrained.

Charge flow in materials and the classification of insulators, conductors, and semiconductors are often described in terms of a *valence* and *conduction band* describing the ability for electrons to move in the lattice. In the valence band, electrons are bound to the atoms in the lattice, whilst in the conduction band, they are free to flow around the lattice and are not localised to any one ion. Insulating materials have a large energy gap between the valence and conduction band requiring large energy input before valence electrons can be liberated. Conducting materials have an overlap between the valence and conduction bands such that higher energy valence electrons are delocalised in the lattice. Semiconductor materials have just a small band gap such that low energy input can cause movement of charge. Whilst a few naturally-occurring semiconductors exist, silicon is by far the most commonly used. The different band gaps are shown schematically in Figure 5.1.

Intermediate charges in the band gap can be added by *doping* the semiconductor with impurities that have either excess or deficient electrons in their valence structure, creating free charges or holes respectively. Semiconductors doped with excess (e.g. arsenic) or deficient (e.g. boron) valence electrons are known as n- or p-type semiconductors respectively. Combining a p- and n-type semiconductor creates a p-n junction, where the excess electrons diffuse and recombine with the holes. This creates a separation of charge that builds up an intrinsic potential difference across the junction, generating a diode effect where charge can only flow in one direction. Such a diode can also be created using two

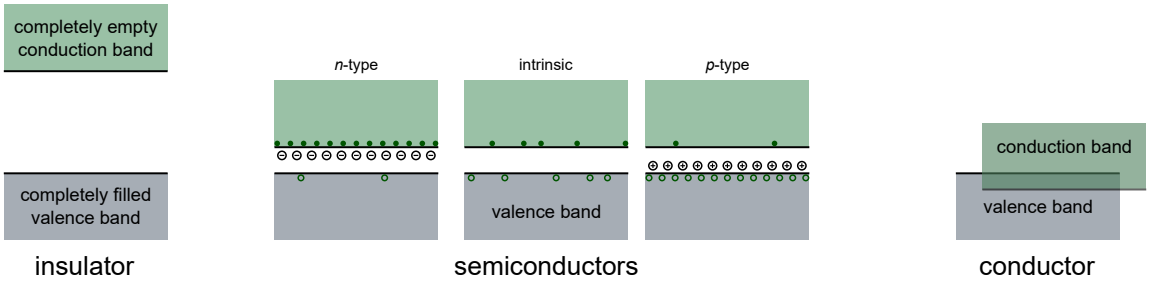

Figure 5.1: The band gap between the valence and conduction bands is shown schematically for insulators, semiconductors, and conductors. Different doping creates p- and n-type semiconductors featuring acceptor and donor ions respectively. Figure reproduced from Lutz (2007) [236].

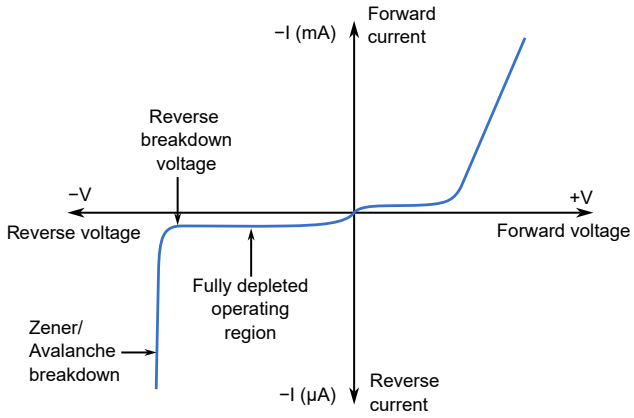

Figure 5.2: The bias response of a silicon p-n diode is shown. A flat region of small leakage current is achieved with a reverse bias until the breakdown voltage is reached, which is where the detector is operated.

doped crystals of the same type but with different impurity concentrations, written as a n^+-n junction.

The recombination of donor electrons and acceptor holes in the diode region means that it is free of charge carriers and is called the *depletion zone*. By applying *reverse bias* to the diode, the depletion zone can be extended as the added potential extends the reach of recombination. A reverse-biased diode is a much easier and more reliable way of creating a charge-free semiconducting material than synthesising a pure semiconductor crystal.

Energy deposited in the material excites electrons to the conduction band, and the electron and hole travel in opposite directions creating a current. Hence, radiation that deposits energy in the detector generates a current flow, and since the energy gap to the conduction band is constant, the number of charge carriers flowing is directly proportional to the energy deposited. Thermal vibrations will create a base current in the detector, known as the *leakage current*, that contributes random noise to the energy measurement. With radiation damage to the crystal structure of the silicon detector, the leakage current will increase and the energy resolution will decrease, so leakage current is often used as a monitor for the performance of a detector.

When reverse biasing a silicon detector, it is ideal to reach a state where the entire detector is depleted of charges, known as full depletion, as this gives the best energy resolution. At some point, the bias will become large enough that the leakage current rapidly increases. This is known as the *breakdown voltage* and arises from spontaneous charge production due to quantum tunnelling through the band gap (*Zener breakdown*) and when charge carriers gain enough energy to knockout more charge carriers (*avalanche breakdown*). The bias zone between full depletion and breakdown is where silicon detectors are operated. The current response across a range of biases is illustrated in Figure 5.2.

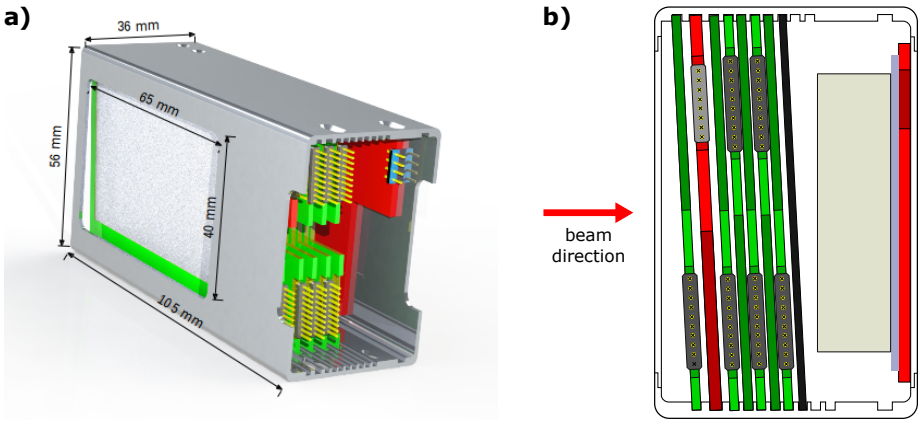

Figure 5.3: a) A CAD rendering of the detector housing shows the dimensions of the detector. **b)** A cross-sectional diagram of the detector of the δE–E telescope. The green boards hold the silicon pads, whilst the red board holds the DSSD. The scintillator crystal is glued onto a photodiode on the backplate of the housing. Figure reproduced from Najafi *et al.* (2016) [159].

5.2 Design philosophy

The design philosophy for CsISiPHOS and PLEIADES is based on the previous TU Munich Si-stack detector and was modified for use by the ILIMA collaboration. Originally the detectors were designed for operation in the FAIR Collector Ring (CR) at slightly higher energies. Since the CR has been delayed indefinitely, these detectors will be operated at the ESR for the foreseeable future. The design features a stack of six 60×40 mm^2 silicon pad detectors for energy loss measurement (green PCBs in Figure 5.3), a 60×40 mm^2 double-sided silicon strip detector (DSSD) with 1 mm strips for position measurement (left red PCB in Figure 5.3), and a 10 mm thick scintillator stopper at the back (khaki block + right red PCB in Figure 5.3). In CsISiPHOS, this scintillator stopper was a 24×24 mm^2 block; PLEIADES now uses 55×38 mm^2 blocks for essentially full coverage of the silicon detector active area.

The housing design (see Figure 5.3) enables the detector layout to be fully modular. This means any detector can be swapped in and out if it is damaged or not performing acceptably. Additionally, it means high-Z passive degraders can be added to slow down the particles if the active mass of the detector is not sufficient to stop the ions of interest (black board in Figure 5.3). A 1 mm thick Ta passive degrader, which has density of 16.4 g/cm^3 was used for CsISiPHOS.

The following design philosophy tries to optimise δE–E separation, whilst abiding by the very tight space constraints imposed by the ESR pocket cross-section of just 37×57 mm^2. The dimensions of the detector housing at 36×56 mm^2 gives just a 0.5 mm clearance. The window aperture in the housing is 65×40 mm^2.

5.2.1 Silicon pads for energy loss

To understand the design choices to measure energy loss, we must first understand the basics of energy loss in matter. Energy loss of charged particles in matter arises from a finite series of random collisions with the matter. The randomness of the interaction generates statistical distributions in the energy, angle, and range of the particle. These statistical distributions are called *straggling*, and the properties of the distribution vary widely depending on the energy due to the large number of interaction mechanisms possible across a range of energies.

Focusing on high-energy heavy ions in the storage ring, the energy loss of relativistic ions in matter can be parameterised by the smooth function [237]:

$$-\frac{dE}{dx'} = 4\pi N_A m_e c^2 r_e^2 \frac{Z_1^2 Z_2}{A_1 A_2} \frac{1}{\beta^2} L, \tag{5.1}$$

where the energy loss is given in units of $\mathrm{A\,MeV\,g^{-1}\,cm^2}$ to explicitly make it a function of density, N_A is Avogadro's number, m_e and $r_e = e^2/4\pi\epsilon_0 m_e c^2$ is the mass and classical radius of the electron, subscript 1 refers to the projectile and 2 the target, and $\beta = v/c$ is the relativistic velocity. The complexity of the physics in this formulation is bundled into the *stopping logarithm* L, but the takeaway is that energy loss is proportional to Z_1^2.

For relativistic energies ($\gtrsim 100$ MeV/u), ions are typically fully stripped and the energy loss is dominated by ionisation in the material. At medium energies (0.1–100 MeV/u), the ion is no longer fully stripped and the charge of the ion depends on electron recombination and stripping throughout the material, resulting in a more complicated energy loss behaviour. At low energies ($\lesssim 0.1$ MeV/u), the energy loss is dominated by nuclear recoils. As a result, angular straggling does not become significant until low energies where nuclear recoils contribute significantly. Additionally, the angular distribution of the incoming beam in the ESR is also negligible compared to the forward momentum (Najafi *et al.* (2016) [159] quote the angular spread at $< 0.17°$). Thus, energy straggling determines the fundamental resolution limit for the determination of energy loss in heavy ions leaving the ESR.

At the relativistic energies of 400 MeV/u at which the ESR is operated for decay measurements, a lot of energy is available for particle identification. Because of the large signal size, the contribution of electronic noise to the energy resolution in our detector is small, so the resolution of the detector is limited by energy straggling in the detector. To minimise the impact of energy straggling, it is desirable to deposit as much energy as possible to build up $1/\sqrt{N}$ statistics on the number of charge carriers generated by the beam. This is the first reason why we have chosen to use a stack of silicon detectors, as multiple detectors can acquire a larger total energy loss.

Silicon diodes are operated by applying a reverse bias such that the detector is depleted of free charge carriers and only those charge pairs produced by the detected particle can carry the electronic signal. This depletion voltage is proportional to the detector thickness squared, $V_{\mathrm{dep}} \propto d_{\mathrm{det}}^2$ [236, p.102], so thicker detectors require substantially higher bias volt-

ages. As a result, most silicon detectors are between 100–500 μm thick. Both CsISiPHOS and PLEIADES use 6 silicon pad detectors that are 500 μm thick. For example, ^{214}Tl ions at 400 MeV/u would deposit 11.4 GeV or 13% of their energy in the corresponding 3 mm of silicon.

The use of multiple silicon pads has another advantage. The energy straggling in a silicon detector follows a highly asymmetrical distribution with long high-energy tails [236, p.25] that was first described by Landau [238] and Vavilov [239]. This is because whilst the energy loss is typically dominated by ionisation, hard scattering of electrons known as delta electrons can deposit more energy than typical. By sampling the energy loss with multiple detectors, we get an average of the samples of the Landau distribution, which suppresses the impact of the extreme tails on our energy loss measurement.

Finally, the detector housing is designed such that the silicon detectors sit at a 3° tilt to the incoming beam. This reduces the so-called *channelling effect*, which causes different energy loss signals for those ions that are channelled along symmetries of the crystal lattice of the silicon, compared with those who cut across the crystal lattice [240]. The p and n sides of the detectors are also mounted in an alternating fashion, which means the detector sides facing each other have the same potential, reducing the risk of sparking.

5.2.2 Scintillator stopper for total energy

To measure the total energy of an incident particle, it needs to be stopped in the detector. At high energies of 400 MeV/u and with a pocket depth of just 36 mm, this is a non-trivial requirement. To achieve a large stopping power, a high-density scintillator was chosen to be the active stopper. Scintillating crystals emit visible light as energy is deposited in the crystal by radiation. In particular, the electron–hole pairs created by ionising radiation are trapped in defects on the crystal lattice, often induced by deliberate doping, and these defects then decay via emission of visible light. Thus, just like silicon detectors, the number of electron–hole pairs and hence the emitted scintillation light is proportional to the energy deposited in the detector. Because we have a large energy signal but tight space requirements, we measure the scintillation light by coupling the scintillation crystal to a large-area photodiode, which is a silicon detector optimised for photon detection.

Silicon photodiodes (SiPD) have a well defined response function, which increases with longer wavelengths for visible light. Hence, scintillating crystals that emit at longer wavelengths will induce a larger signal in the SiPD. To maximise the light collection on the photodiode, the exposed sides of the scintillator are wrapped in reflective foil. It was calculated that leaving an air gap between the foil and the crystal to maximise total internal reflection would result in higher light collection than gluing the reflective foil with optical cement. Additionally, crystals with fast light-decay times will reduce the charge collection time for the SiPD, which should improve the energy resolution of the charge-sensitive amplifier that integrates the signal.

For CsISiPHOS, a $24 \times 24 \times 10$ mm^3 CsI(Tl) scintillator was used. For PLEIADES,

Table 5.1: Properties of the three scintillation crystals. Data from Hilger & Epic Crystals.

Property	**CsI(Tl)**	**BGO**	**GAGG(Ce)**
Density ($\mathrm{g\,cm^{-3}}$)	4.51	7.13	6.6
Peak emission wavelength (nm)	550	480	530
Refractive index at peak emission	1.79	2.15	1.91
Photons per MeV	54 000	8500	40 000
Decay constant (ns)	1000	300	90
Hygroscopic?	Slightly	No	No
Hardness (Mohs)	2	5	8

two additional types of scintillating crystal have been chosen, BGO and GAGG crystals, to test a wider variety of scintillator properties. The new crystals are much denser and have higher average Z than CsI, so provide better stopping power. In addition, the PLEIADES crystals—including two additional CsI(Tl) crystals—are $55 \times 38 \times 10$ mm^3 to better match the size of the δE detectors to maximise the usable aperature. We compare the three scintillators below, with important physical properties tabulated in Table 5.1:

1. CsI(Tl) is a CsI crystal doped with Tl to improve the light output. CsI(Tl) is commonly used because of its high density and excellent light output, however the decay time at 1 ms is quite long. CsI is slightly hygroscopic, which quantifies its tendency to absorb water, but not enough to require special protection from atmospheric water vapour. The CsI crystal is soft, so support structures can damage the crystal.
2. BGO is a crystal formed from Bi and Ge oxides with a chemical structure $Bi_4Ge_3O_{12}$. It is the densest of the three crystals, but suffers significantly on both light output and peak emission wavelength. The emission decay constant is relatively fast and the crystal is also comparatively hard.
3. GAGG(Ce) is a crystal formed from Gd-Al-Ga garnet with a chemical structure of $Gd_3Al_2Ga_3O_{12}$ and doped with Ce. It has comparable light output to CsI(Tl) whilst being 50% denser, much faster, significantly harder, and not hygroscopic. However, because it is a newer and less common crystal, it is significantly more expensive.

On paper, the GAGG crystal should be the best with its excellent light output, long emission peak, very fast decay time, and robust hardness. CsI does well on light output, but suffers from a long decay time. Finally, BGO has excellent density and reasonable decay time, but suffers on light output. A primary goal of the PLEIADES commissioning was to determine which scintillating crystal is optimal going forward. The conclusions of the characterisation are presented in Section 5.5.5.

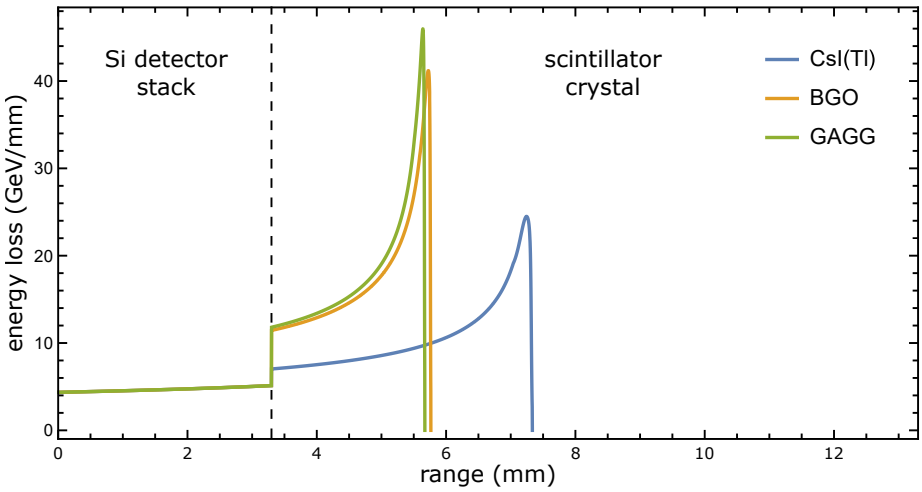

Figure 5.4: SRIM simulations of energy lost to ionisation in 3.3 mm of silicon and 10 mm of scintillator material for ^{208}Pb ions at 279 MeV/u.

Stopping power simulations

To determine what ion species can be measured in the detector, simulations using the Stopping Ranges of Ions in Matter (SRIM) code were performed [241]. Because the stopping power scales with Z^2 whilst the energy scales with A, lighter ions are much more challenging to stop. CsISiPHOS used a 1 mm Ta passive energy degrader to assist with the stopping of ^{142}Nd/Pm^{59+} ions during its commissioning experiment [159]. If possible, it would be ideal to avoid the use of a passive degrader as the degrader contributes to the straggling whilst not contributing to the measurement.

A range of ions in the different scintillator materials were tested to determine the lightest element at 400 MeV/u that each setup could stop (3.3 mm of Si includes the DSSD):[17]

1. 3.3 mm Si + 10 mm CsI(Tl) was only able to stop ^{174}Yb.
2. 3.3 mm Si + 1 mm Ta + 10 mm CsI(Tl) was able to stop ^{120}Sn.
3. 3.3 mm Si + 10 mm BGO was able to stop ^{90}Zr.
4. 3.3 mm Si + 10 mm GAGG was able to stop ^{82}Kr.

The stopping powers of the BGO and GAGG are comparable in the simulations, with both being much better than what is achievable with CsI(Tl). Figure 5.4 shows the energy loss of ^{208}Pb ions at 279 MeV/u in the PLEIADES silicon detectors and three crystal materials. This clearly demonstrates the improved stopping power of BGO and GAGG crystals.

[17] Note that the choice of isotopes is illustrative only. Obviously neutron-rich isotopes will be slightly harder to stop.

5.3 Detector construction

The PLEIADES detector was constructed at TRIUMF, taking advantage of the in-house expertise at various phases during the construction. Some construction was also done at GSI, notably infrastructure for mounting the detectors in the pockets. Improvements on the CsISiPHOS design were made at several stages.

5.3.1 Micron silicon pads

For PLEIADES, eight silicon pad detectors (with one mechanical sample) were purchased from Micron Semiconductor Ltd. CsISiPHOS used a silicon pad known as Design-I, which had a 60×40 mm^2 active area with 7-fold segmentation on the front side and a single area on the back. The new silicon pads are an updated model called the MS Pad 1x7, with the same dimensions and segmentation.

Micron silicon detectors, like most others, are constructed on n-type silicon with the front side featuring a p^+-n^- junction whilst the back side features an n^+-n^- junction. The p^+-n^- junction, also called the *junction window*, creates the diode by supplying many acceptor ions, whilst the n^+-n^- layer, also called the *ohmic window*, generates good ohmic contact with the metallisation and allows the detector to be overdepleted [236, p.100]. The front side with the junction window is called the p-side of the detector, whilst the back side with the ohmic window is called the n-side. Both the junction and ohmic windows on the MS Pad detectors are 0.5 μm thick. The metallisation is a continuous coverage of 0.5 μm sputtered aluminium that allows for good ohmic contact with the substrate of the detector.

The MS Pads feature upgrades over the Design-I pads with multiple *guard rings* and *field plates*. Guard rings are designed to absorb dark current from material beyond the active area of the detector. They also control the potential drop off at the edge of the detector, allowing for high voltage operation and improved stability over time. Ideally the innermost guard ring will be biased to the same potential as the active area to remove collected charges, and the following guard rings are left floating to distribute the edge fields via the "punch-through effect" described in Avset & Evensen (1996) [242]. However, we chose to just leave all guard rings floating [243]. Field plates are used to stabilize the "potential spreading" in guard rings due to the conduction of charge by SiO_2. The guard rings and field plates can be seen as fine rings around the p-strips in Figure 5.5a.

The printed circuit boards (PCB) for the pad detectors were reproduced from the CsISiPHOS design. We attached the detectors with a drop of epoxy in each corner to allow some flexibility if the boards flexed. Unfortunately, we did not account for the fact that some boards were naturally slightly warped. This warping now puts stress on the silicon chip when the board needs to be mounted or secured in a flat plane. Future silicon detectors should be mounted on more rigid PCBs that are less likely to be warped.

Wire bonding connects the metalised surface of the detector to the plates of the PCB

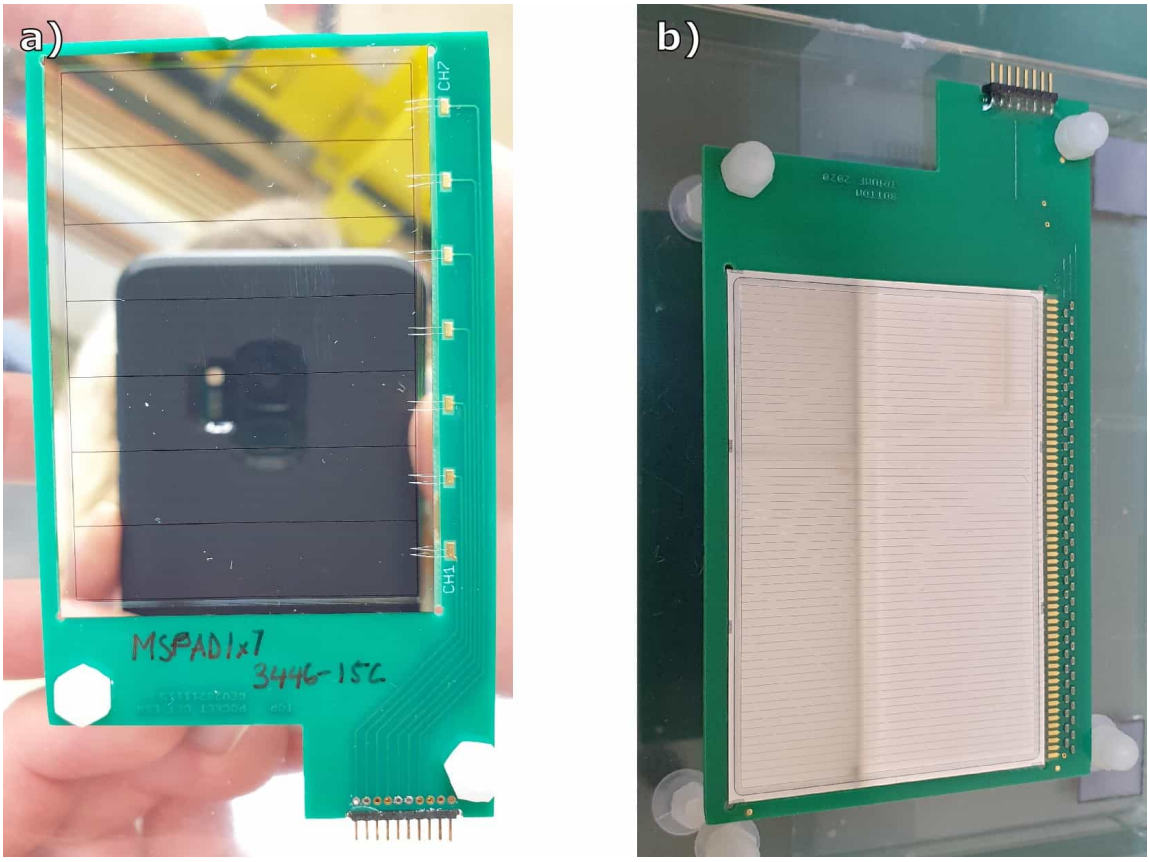

Figure 5.5: a) the p-side of MS Pad #15C with its 7-fold segmentation and surrounding guard ring structure. **b)** The p-side of Mirion DSSD with 60 1 mm vertical strips for horizontal position determination. The resistive chain and wire bonding pads are on the right.

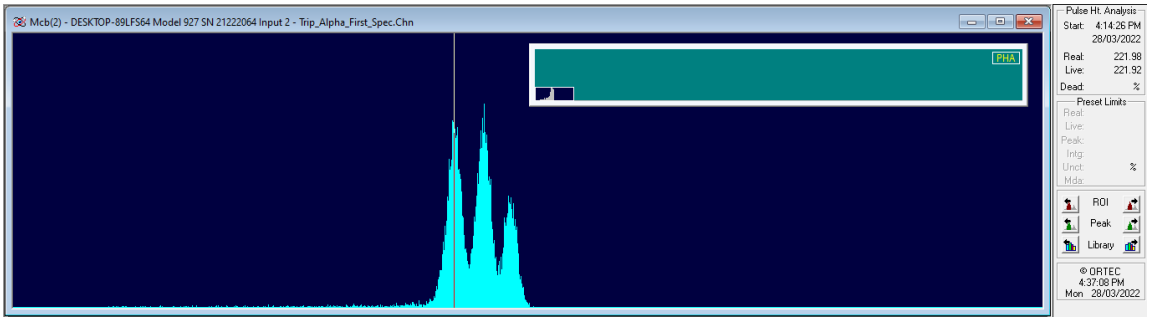

Figure 5.6: The triple α spectrum (see text) recorded by an MS Pad detector. The minor peak structure is not visible due to the 1 GeV range of the preamplifier chosen for heavy-ion signals.

for signal readout. The wire bonding was done using a ultra sonic bonding machine that uses vibrational energy to weld the bond wires to the metallisation layer in a very clean and heat-free way. Because of the tight packing of the detectors, the wire bond profile needed to be quite flat, which put the bond under stress. In some cases, wire bonds are encapsulated in an epoxy to protect them from being broken. We chose not to encapsulate our bonds to ensure that we could repair any bonds broken by the flexing of the PCB.

Micron determined the depletion voltage for most MS Pads to be 40 V. It is important to operate silicon detectors in an overdepleted mode because current generated by the impinged beam will reduce the voltage, but the bias should also be minimised to improve the lifetime of the detector. The voltage drop can be derived from the expected current

$$I_D = \text{event rate} \times \Delta E \times q_e/3.6 \text{ eV}, \tag{5.2}$$

where ΔE is the energy loss, q_e the electron charge, and the 3.6 eV is the energy per charge carrier in silicon. For the silicon detectors, our preamplifiers have bias resistors of 20 or 60 MΩ. In the β_b-decay measurement of $^{205}Tl^{81+}$, the CsISiPHOS detectors had peak rates of 10 kHz, and this resulted in a current of 966 nA on top of the leakage current, causing a $>$ 20 V bias drop. Higher bias resistances produce better electrical noise but larger bias drops, so the bias resistor and overdepletion amount should be appropriately selected based on the experiment.

The MS Pads were tested at TRIUMF with a triple α source in a vacuum chamber. We used a ^{239}Pu, ^{241}Am, ^{244}Cm source, which has primary alpha peaks of 5.155, 5.486, and 5.085 MeV respectively. Since our preamplifiers have a minimum range of 1 GeV, we were unable to separate the minor peaks of the triple-α spectrum, as shown in Figure 5.6, but the test demonstrated all detectors worked before the commissioning beamtime. During α testing, the new MS Pad detectors had leakage currents on the order of 30 nA.

Relevant properties of the silicon pads, alongside the other silicon detectors described below, are given in Table 5.2.

5.3.2 Mirion DSSD detector

PLEIADES utilises a double-sided silicon strip detector (DSSD) for a position measurement to give information on the particle's magnetic rigidity. DSSDs work by having high segmentation on both the front and back of the detector in orthogonal directions so that when a particle strikes the detector, the front and back strips hit identify a unique position pixel. The DSSD used in PLEIADES is a 300 μm thick detector with 60 vertical strips of 1 mm pitch on the front p-side and 40 horizontal strips of 1 mm pitch on the back n-side.

Since our signals are quite large, we read out the DSSD strips using a resistive chain where each strip is connected between a chain of resistors. The resistance, and thus the signal height, that a pulse sees between the end of the chain thus depends on the position. The position of the particle is then proportional to the difference between the two ends of the chain. This simplifies the readout out from 100 individual strips down to just 4

channels. The p-side chain features 60 surface-mounted 50 Ω resistors whilst the n-side feature 40 75 Ω resistors. The resistive chain and associated bonding pads can be seen on the right of Figure 5.5b.

Exactly like the silicon pads, the DSSDs also have multiple guard rings and field plates, and similarly we do not bias the guard rings. At just 300 μm, the detector is fully depleted at 30 V.

5.3.3 Scintillator stopper

For the scintillator stopper, a custom large area photodiode was purchased from CiS Forschungsinstitut für Mikrosensorik GmbH. Four of these SiPDs were provided to us, each with varying quality, to use for scintillator stoppers. To optimise performance, we coupled the highest performing photodiodes to the BGO and GAGG crystals to make the best use of their superior stopping power.

The CsISiPHOS prototype photodiode was bonded to its PCB with regular epoxy for strength and a conductive epoxy to connect the backside of the photodiode to the contact of the PCB. The same bonding scheme was followed for SiPD 7. A concern with this design was the potential degradation of the conductive epoxy over time and how that would affect charge collection. However, the CiS PIN40x60 photodiodes have an outer guard ring with an electrical connection through the substrate to the backside, so it is possible to attach the bond wires to this guard-ring on the front side, rather than using the conductive epoxy on the backside. This method was chosen for SiPDs 4, 5, and 6, and the specific wirebond locations for the front- and back-sides of the detector are shown inFigure 5.7. Note that the darker surface of the SiPD is not conductive and thus cannot be bonded to. With the new wirebonding scheme, the new photodiodes were bonded to a very simple PCB design with just small wirebond pads. We scratched and sanded the PCB surface considerably to provide the best adhesive surface given the very smooth surface of the photodiode makes good adhesion challenging.

The scintillator crystals were then attached to the photodiodes with Eljen EJ-500 optical cement, which is specially designed for bonding scintillating crystals. The transmission of this cement is $> 99\%$ for light above 450 nm. The recommended bond layer was < 125 μm, which equated to 0.26 mL of optical cement. Through testing, we determined 0.14 mL to be the optimal amount, and application with a syringe allowed for repeatable volume delivery. We applied the glue in a 'Feynman diagram' shape so the optical cement reached the corners evenly. The gluing process is shown in Figure 5.8.

The crystals were wrapped in 3M Vikuiti Enhanced Specular Reflector foil, which provides $> 98\%$ reflectivity across the visible spectrum. As mentioned already, leaving an air gap improves light collection via total internal reflection. The foil was then folded into shape and secured with Kapton tape (non-conductive) on the outside, as shown in Figure 5.8.

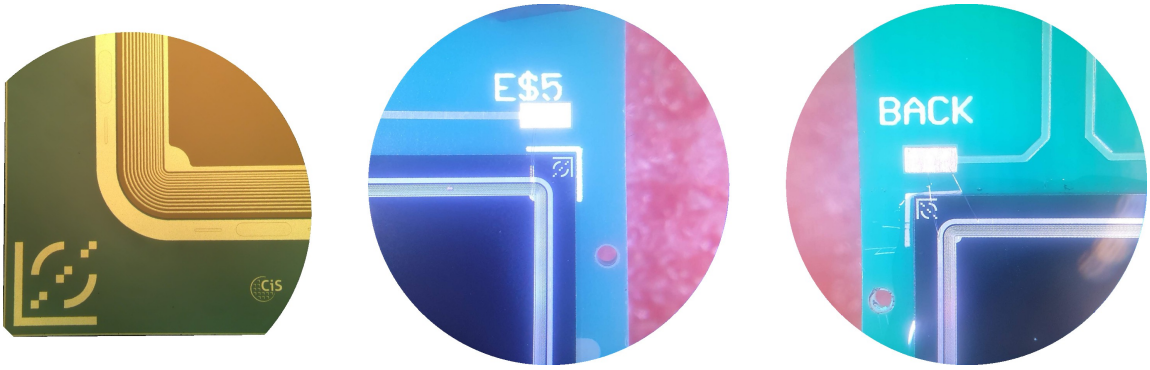

Figure 5.7: Microscope images of the guard ring structure of the CiS photodiodes, with the location of wirebonds to the front and back bonding regions. Note the dark areas are nonconductive.

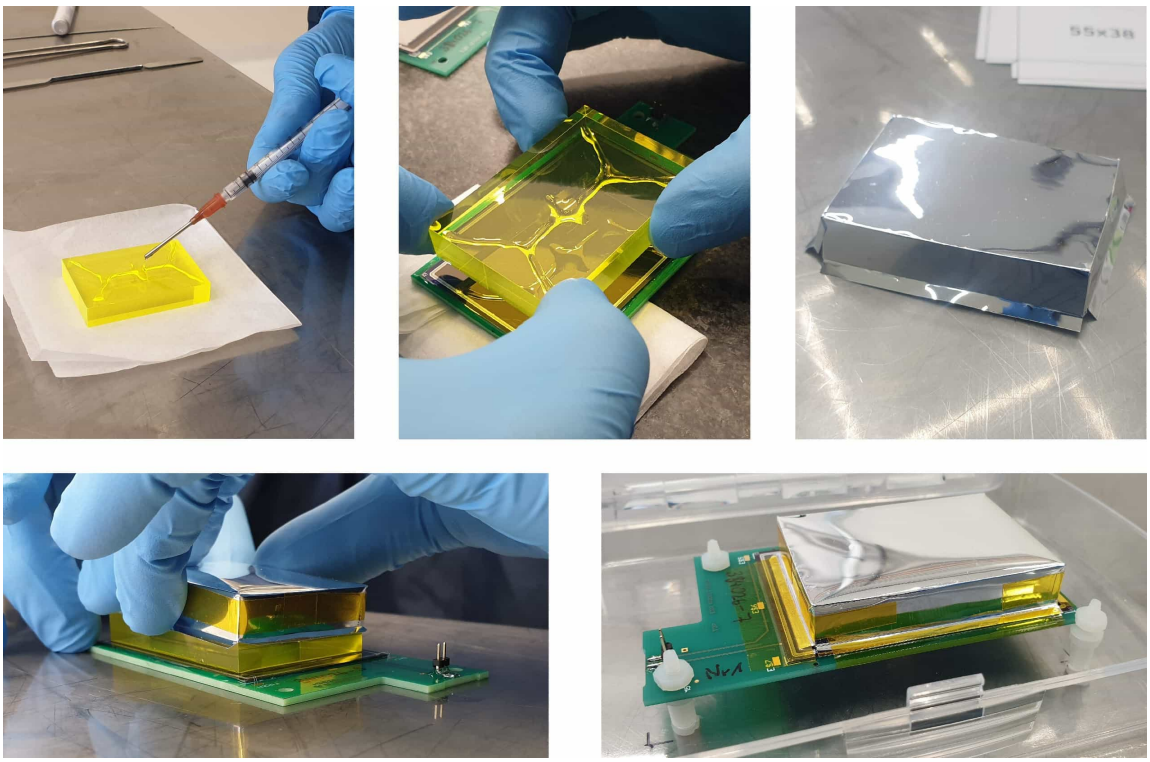

Figure 5.8: The mounting of the scintillator crystals (the GAGG crystal in this case) to their photodiodes included adhesion with optical cement and wrapping with a reflective foil.

5.3.4 Detector housing

The previous aluminium frame that held the detectors for CsISiPHOS was glued together into one solid piece. For structural reasons, and to provide more flexibility for mounting different stopper crystals, we altered the housing design to use screws. The new design required delicate balancing to fit the new screw design around the existing constraints of both the ESR pockets and the detector PCBs. The new housing is backwards compatible with all the CsISiPHOS components, so the old detectors and mounting frames can still be used.

The stopper crystals were secured into the backplate of the housing with 2-ton epoxy. Thus, there are four backplates to the housing corresponding to the four stopper crystals. The rest of the housing is then screwed onto the crystal of choice, as shown in Figure 5.9 (left), and silicon detectors are slid into the appropriate slot (right).

There was initially concern that the torque on the crystals produced by the fast-moving ESR pockets could cause one of the three layers of epoxy to shear off. This would be particularly catastrophic given the density of the crystals and the fact that the UHV of the ESR is protected by just a 25 μm window. However, testing in the ESR pocket successfully demonstrated the bonds held without the need for additional mechanical support. Such tests should be repeated if the detectors have not been used for a longer time to ensure the integrity of the epoxy remains acceptable.

5.3.5 Flange mounting arm

The detector housing is mounted on an arm that connects it to the flange that is secured to the ESR pocket. The arm provides mechanical support against the movement of the pocket, although the tight tolerances inside the pocket mean that the housing is already held quite securely. To ensure compatibility, we reused the design created for CsISiPHOS, and the parts were manufactured at GSI. The full assembly is shown in Figure 5.10.

The detectors in the housing connect to an adaptor PCB that slots into the end of the housing and routes the pin connections to two 50 Ω, high-density coaxial ribbon cables (Samtec HQCD-030-23.62-SED-SBR-1-N). The adaptor PCB also has the dual purpose of holding the detectors in place at the end of their slots, which is achieved by a screw in the h-shaped 'hand' of the arm that is tightened into place. The Samtec cables connect at the other end to the flange PCB, which routes the Samtec cables to LEMO and D-sub connectors on the outside of the pocket.

Finally, a thin pipe can direct dry nitrogen gas into the pocket. The nitrogen reduces the humidity in the pocket (the CsI crystals are slightly hygroscopic), and reduces the extent to which surface currents develop on highly biased detectors. The new, denser crystals are no longer hygroscopic and we will not need 1 mm thick silicon detectors for which the surface current is an issue, thus the flushing with dry nitrogen may not be needed in the future.

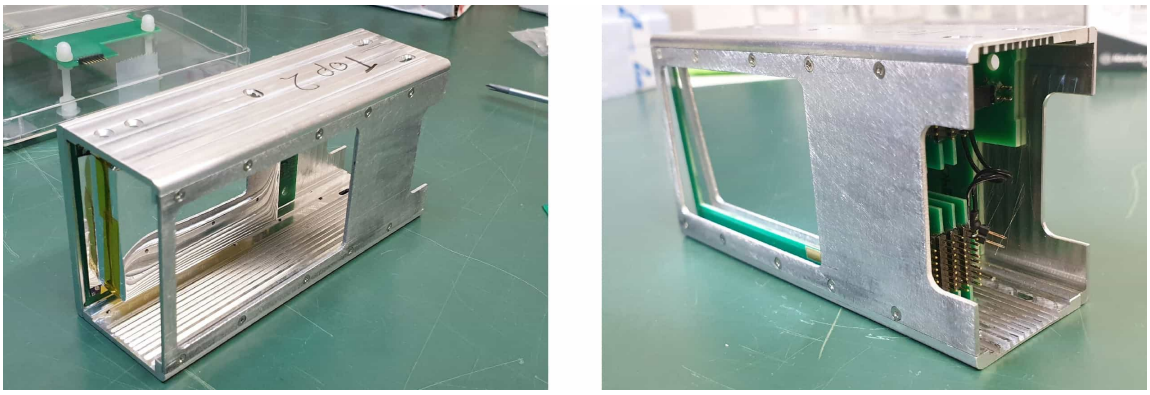

Figure 5.9: Two images of the housing showing the scintillator crystal mounted on the backplate and the silicon detectors slotted into their grooves.

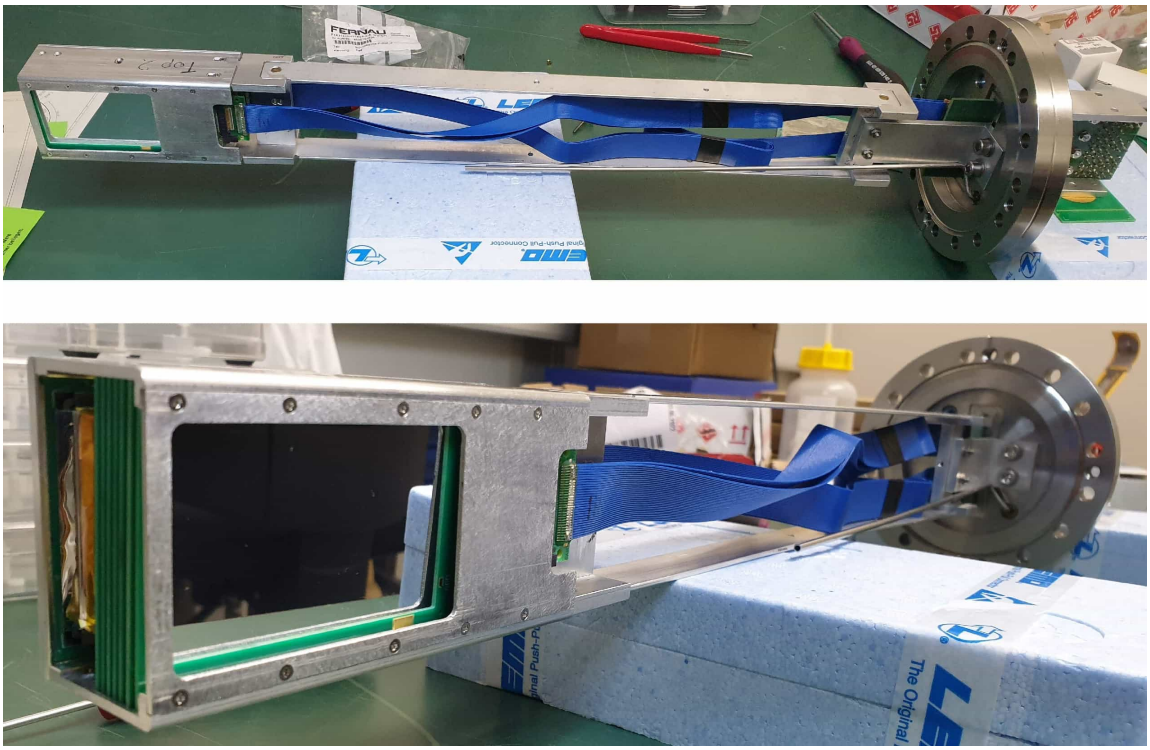

Figure 5.10: The full detector mounted on the flange arm assembly. The signals are carried by the blue high density Samtec cables to the flange PCB. Note the thin tube for dry nitrogen flushing.

5.4 Front end electronics

The *front end electronics* are responsible for processing the raw detector signals into something that can be stored digitally by the back end. The raw detector signals from the flange PCB are handled in two stages, as is customary for silicon detectors, a preamplification of the narrow detector pulse and then an analysis to extract the pulse height. The preamplifier serves to convert the small detector signal into a large signal that can be analysed whilst preserving the signal-to-noise ratio of the original pulse. In silicon detectors, the charge in the signal is directly proportional to the energy deposited, so a *charge sensitive amplifier* is used to collect the charge and convert it into a signal whose height is proportional to the charge. Careful choice of the amplifier and feedback capacitor is required to ensure that complete charge collection is achieved whilst balancing the preamplifier decay time to ensure minimal pileup of detector signals.

For the analysis of the preamplifier pulse, the preamplifier is traditionally shaped into a Gaussian pulse that can be counted by an analogue-to-digital converter (ADC) that bins the signal based on its height. This traditional analogue pulse analysis is what was used for CsISiPHOS. PLEIADES instead directly uses a high-rate sampling ADC to directly store the preamplifier pulse in the digital data acquisition (DAQ) system. The recording of preamplifier *traces* allows the pulse to be analysed with *digital pulse processing* algorithms that can use signal filters that cannot be built with analogue electronics. These digital filters come close to achieving the theoretical optimum for resolution and throughput when analysing preamplifier pulses [244] (more details in Section 5.5.2). Additionally, the recording of traces allows for analysis of the shape of the preamplifier pulse to separate different types of radiation that deposit energy differently with *pulse shape analysis*. Finally, digital pulse processing allows for considerably easier extraction of pileup events than analogue shaping.

5.4.1 Mesytec preamplifiers

Both CsISiPHOS and PLEIADES use Mesytec preamplifiers. The 7 p-side strips for up to 8 silicon pad detectors are read out into two MPR-32 modules, which use the same settings for all 32 channels. Mesytec MMPR preamplifiers have a factor-5 attenuator switch to give two gain ranges, and we opted for a 1/5 GeV range given the expected energy deposition in the silicon detectors of $\sim$ 2 GeV. The MMPR decay time is 25 μs and the zero-load rise time is 12 ns. The input signals arrive from a 25-pin D-sub connector from the flange PCB, whilst the output signals are 100 Ω differential signals with a $\pm$1.2 V max range and are transported with a 34-pin twisted pair ribbon cable to the digital DAQ.

The n-sides of the silicon pads, the four DSSD channels, and both sides of the scintillator photodiode are read into two MSI-8 modules. The MSI-8 modules are quite flexible and have both a MMPR preamplifier and a MMSH shaping module with individual bias and shaping options for all channels. Because the MSI-8 has individual preamplifier cards, the

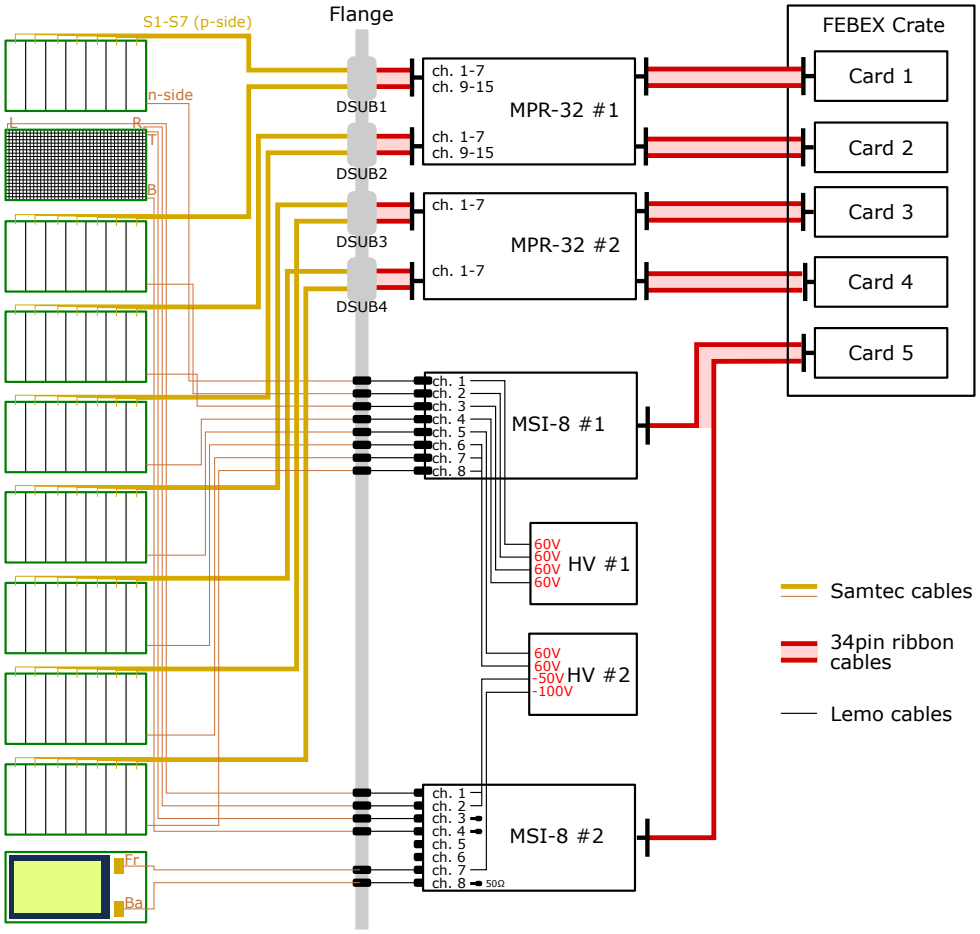

Figure 5.11: The channel mapping from individual detectors to the front end electronics is shown schematically.

silicon detectors use 1/5 GeV ranges whilst the crystal uses 4/20 GeV ranges. The inputs for signals and bias are via individual LEMO cables from the flange PCB. We do not use the shaping module, but instead read out the 100 Ω differential preamplifier outputs using two 20-pin twisted pair cables that combine into a single 34-pin cable for the DAQ. The differential output has a ±1.8 V max range for the MSI-8s.

The bias to the MSI-8 modules is supplied by two MHV-4 high-voltage NIM modules. The bias resistors in the MSI-8s are 20/60 MΩ, controlled by a jumper in the module. With eight bias channels, we can get individual leakage current monitoring for each detector. The MHV-4 also has remote control options for bias control and leakage current logging. This channel mapping setup is shown schematically in Figure 5.11

5.4.2 FEBEX digital data acquisition

PLEIADES utilises the DAQ created by the NUSTAR collaboration's DAQ group to modernise the data acquisition of experiments run at the FAIR facility. The NUSTAR DAQ system was chosen for the ILIMA particle detectors to access the benefits of digital data processing, but also to ensure minimal maintenance and be compliant to interface with other systems. The NUSTAR DAQ features several front end boards that work together, depicted in Figure 5.13, to construct events that are given to the MBS.

The Multi Branch System (MBS) is GSI's standard DAQ protocol that handles data transport. A core design principle is flexibility at every stage so almost everything is modular. The MBS process is shown schematically in Figure 5.12 and features the following components:

- the **Readout Process** is controlled entirely by the user, depending on the architecture they have, through a file called `f_user.C`. It dictates how to readout the ADCs, etc. to form an MBS sub-event.
- the **Collector Process** takes sub-events and assembles them into MBS physics events, also specified by `f_user.C`. PLEIADES does not require sub-events because we just have a single heavy ion implanting, so our MBS event is just 1 sub-event reading out all channels.
- the **Transport Process** describes how data is transferred and recorded.
- the **Monitor Server** is a stream server that allows for online monitoring of the DAQ.

Returning to the front end, the centrepiece of the NUSTAR DAQ is the FEBEX sampling ADC that records the preamplifier traces. The FEBEX3b ADC (Front End Board with optical link EXtension) is a 16-channel, 14-bit, digital ADC that samples at 50 MS/s (i.e. time resolution of 20 ns). This allows it to record a trace of the analogue signal from the preamplifiers, that can be analysed for pulse shape discrimination. The board contains trigger logic, time stamp logic, and external clock input, and the data is processed by an on-board FPGA. Our FEBEX boards take a 34-pin input twisted pair ribbon cable from the preamplifiers with a ± 2 V range. Up to 19 FEBEX boards are mounted in a FEBEX crate, which is connected to the DAQ computer via an optical fibre for high data throughput. The ILIMA pocket detectors typically run using four FEBEX boards.

The PEXOR card (PCI-Express Optical Receiver) receives the data from the FEBEX and transfers it to the MBS for data output [245]. The PEXOR card receives data from up to four SFP ports, which correspond to the daisy-chained FEBEX crates. The PEXOR card also handles triggers coming from TRIXOR; it will only read out data to MBS in response to a TRIXOR trigger.

The EXPLODER is a trigger logic box that can be used for common dead-time blocking, complex trigger logics, and interfacing external devices [246]. It is the module that allows us to turn many possible trigger inputs into a single trigger to be given to the TRIXOR

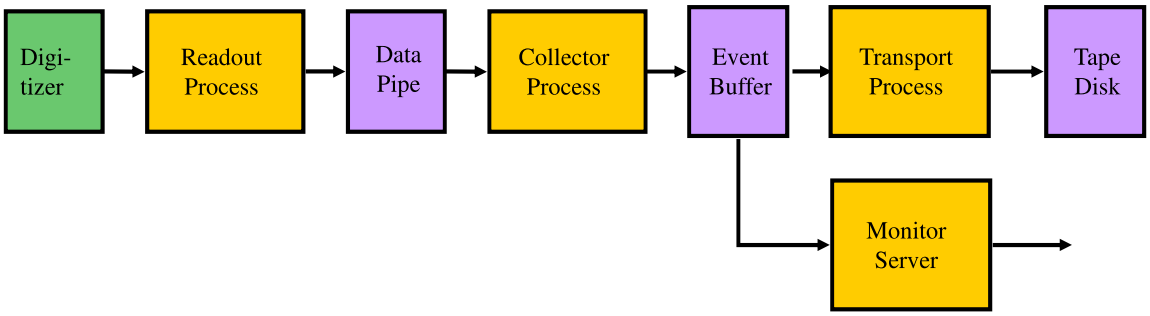

Figure 5.12: The MBS DAQ software proves a flexible process for constructing and recording events. Descriptions of the individual steps are provided in the text. Diagram courtesy of N. Kurz (GSI Darmstadt).

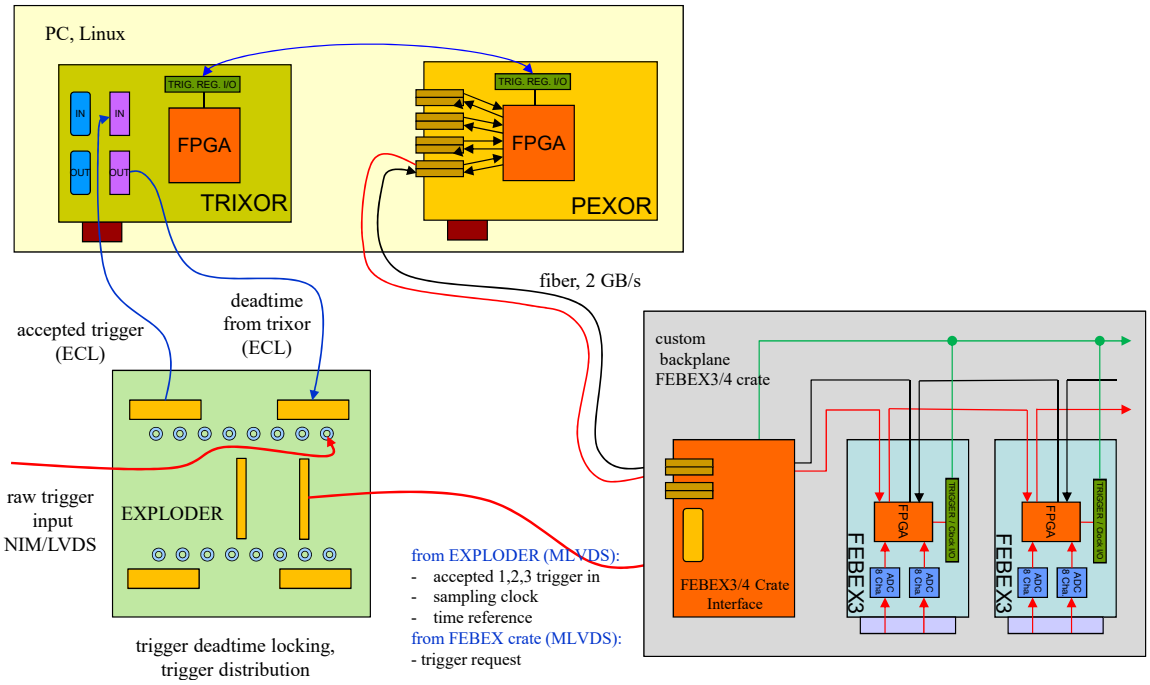

Figure 5.13: The NUSTAR DAQ uses a variety of front-end boards to store the trace readout of the preamplifier pulses and upload that to the back end electronics. The FEBEX is the sampling ADC itself, the EXPLODER module provides trigger logic and communicates between the FEBEX and the TRIXOR. TRIXOR directs the PEXOR board to write data to the MBS from the FEBEX boards. Diagram courtesy of N. Kurz (GSI Darmstadt).

card—the MBS trigger master. The TRIXOR board, another front end board in the DAQ computer, is the MBS trigger master that controls how MBS commands PEXOR to read out data from the FEBEX crates. An accepted trigger from the EXPLODER will be distributed to the TRIXOR and FEBEX boards. While the FEBEX boards are preparing the data to be sent to the computer, TRIXOR issues an interrupt request to the MBS software, which controls the readout. MBS causes PEXOR to send a digital token down the GOSIP chain successively to each FEBEX module. After receiving the token, the FEBEX modules send the collected data upstream before finally the token returns to PEXOR to indicate the complete readout. MBS collects the received data and provides a network data stream for online monitoring and disk storage.

To interface with any NUSTAR DAQ system, the FEBEX system uses a global White Rabbit time stamping protocol that attaches a global time stamp to MBS events. The White Rabbit clock is distributed by optical fibers to the DAQ computers via the PEXARIA card. When triggered, PEXARIA appends an MBS event with a timestamp, and then the events are sent to the time-sorter computer. The time-sorter is an independent system to the other DAQ sub-systems. This enables one to set up the subsystems and test them independently, and then connect them to the time-sorter after testing to combine the systems. The time-sorter requires event headers from each system to sort events, which is why a trigger to consistently send events (keep-alive trigger) is important so that the time-sorter can continue to make sorting decisions.

To operate both CsISiPHOS and PLEIADES together, we have two DAQ systems using four FEBEX boards connected to a DAQ computer with the PEXOR, TRIXOR, and PEXARIA front end boards. The full DAQ crate is shown in Figure 5.14. For the foreseen use cases, PLEIADES only requires simple trigger logic and so the EXPLODER module is currently setup to self-trigger based on the FPGA hit finder in the FEBEX boards. The MBS streams with White Rabbit stamps from the two DAQ systems are then combined using a time-sorter. The one capability that is still missing is a method for monitoring dead time, but this will be discussed more in Chapter 6.

5.5 June 2022 commissioning

To test the upgraded ILIMA detectors, we were able to use an 8-hour shift during the NECTAR experiment to measure ^{208}Pb through inelastic proton scattering. At that stage of the tuning, the beam was $^{208}Pb^{82+}$ at 269 MeV/u with $\sim 2 \times 10^7$ ions stored in the ESR. PLEIADES was placed in the pocket behind the first dipole after the gas target on the outside of the storage ring (same pocket as the MWPC in Figure 3.5), where we detected electron recombination products, i.e. $^{208}Pb^{81+}$. We confirmed these products originated from electron recombination in the electron cooler because the rate measured in PLEIADES was positively correlated to the electron cooler current.

The purpose of the test was to commission the detector by determining energy resolu-

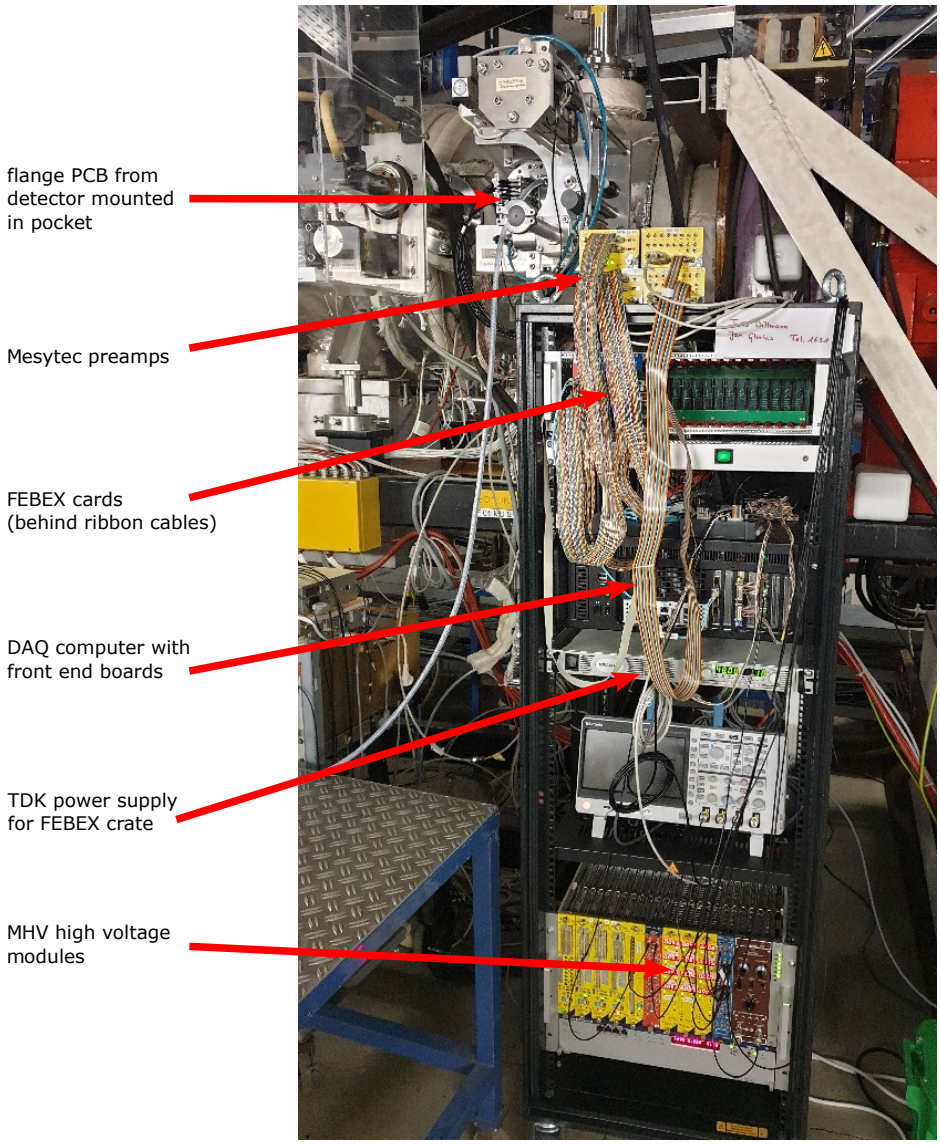

Figure 5.14: The data acquisition crate used during the test is shown, including all DAQ components described in Section 5.4. The detector is mounted in the detector pocket.

Table 5.2: Detector properties determined from the June 2022 commissioning. Some properties could not be determined for various reasons.

Detector	**Thickness**	**Leakage**	**Resolution (FWHM @ dE)**
MS Pad 17A	505 μm	310 nA	3.16%, 71 MeV @ 2.20 GeV
MS Pad 17B	505 μm	316 nA	3.15%, 73 MeV @ 2.27 GeV
MS Pad 17C	505 μm	334 nA	2.88%, 68 MeV @ 2.32 GeV
MS Pad 16A	504 μm	339 nA	2.81%, 69 MeV @ 2.38 GeV
MS Pad 16B	504 μm	361 nA	3.60%, 91 MeV @ 2.45 GeV
MS Pad 16C	504 μm	361 nA	2.44%, 63 MeV @ 2.52 GeV
MS Pad 15B	505 μm	78 nA	2.99%, 71 MeV @ 2.38 GeV
MS Pad 15C	505 μm	-	3.83%, 94 MeV @ 2.44 GeV
Design I 3	-	-	4.67%, 111 MeV @ 2.38 GeV
Design I 5	-	-	4.01%, 98 MeV @ 2.44 GeV
Design I 6	-	586 nA	3.35%, 84 MeV @ 2.51 GeV
Design I 8	-	518 nA	3.13%, 81 MeV @ 2.59 GeV
Design I 13	-	583 nA	3.83%, 89 MeV @ 2.32 GeV
Design I 14	-	135 nA	2.99%, 67 MeV @ 2.24 GeV
Design I 81	-	-	5.41%, 121 MeV @ 2.24 GeV
Design I 82	-	-	4.38%, 102 MeV @ 2.32 GeV
Mirion 121812	-	-	-
Mirion 121813	306 μm	30 nA	-
Mirion 161054	309 μm	249 nA	3.32%, 44 MeV @ 1.34 GeV
CsI (small) + SiPD 4	-	-	-
GAGG + SiPD 5	-	293 nA	1.16%, 467 MeV @ 40.11 GeV
CsI (large) + SiPD 6	-	-	1.12%, 448 MeV @ 40.11 GeV
BGO + SiPD 7	-	162 nA	1.02%, 434 MeV @ 40.11 GeV

MS Pad 15C is the mechanical sample so is not guaranteed for good resolution. Design I 14 popped out of its carrier PCB, so may have microfractures.

tions for all detectors and to quantify the isotopic separation of the δE–E telescope. We used three different layouts in the housing to test every detector except the small CsI + SiPD 4. The performance of each detector is summarised in Table 5.2. The test setup showing the DAQ crate is given in Figure 5.14.

5.5.1 Go4 data analysis

The data was collected from the front end electronics by the MBS, which stores data in its own specialised "`lmd`" format. `lmd` files are best unpacked using GSI's in-house Go4 analysis framework, which is an extension to CERN's famous ROOT software package. Go4 is a class-based analysis framework that uses successive analysis 'steps' to process data. Each step can pass on objects to the next step in a modular way, which synergises well with the modularity of MBS's design for complex event building. Furthermore, Go4 is often used for online monitoring of the MBS data stream, and the same analysis code can be used on a `lmd` file or the live monitoring stream from the MBS.

The GSI experiment electronics group provided us with an out-of-the-box Go4 class for basic analysis of the FEBEX ADC channels. We used this `TFeb3Full` class with minimal modification to monitor the traces and hit patterns during the beam test. The `TFeb3Full` class unpacks the MBS stream or `lmd` file event by event with knowledge of how the FEBEX uses the `f_user.C` file to store the event data.

To analyse the data offline, a full Go4 analysis suite was written called `TPLEIADES` that can be used in future ILIMA experiments to provide a framework for comprehensive unpacking of the data. The `TPLEIADES` analysis class uses three Go4 analysis steps:

1. `TPLEIADESRawUnpacking` that uses a modified version of `TFeb3Full` to unpack the MBS data into a FEBEX-based class structure. This step stores the data in their direct FEBEX channels, so the raw ADC format can be accessed.
2. `TPLEIADESDetEventBuilding` that takes the ADC format and constructs a class `TPLEIADESDetector` that stores the data in detector objects based on their structure. These detectors are built dynamically from a list in the `set_PLEIADESParam.C` file, so only one file needs to be edited to setup the detector structure for an experiment.
3. `TPLEIADESPhysicsProcessing` that takes the detector classes and does some preliminary processing of the data. Currently, this involves an algorithm to select the p-strip to use for the energy and a basic pulse shape analysis on the MSI-8 traces (see Section 5.5.3). For the future, this step is flexible based on the experiment, but the purpose is to provide a step to select how a single p- and n-side energy will be stored for each detector, resulting in a much simpler and cleaner final ROOT file.

Each Go4 analysis step output can be written to a ROOT file, and each step can also take a ROOT file of the previous step as input, so it is possible to do the unpacking or detector event building once, and then run different physics processes on those unpacked ROOT files allowing for a much more computationally efficient analysis.

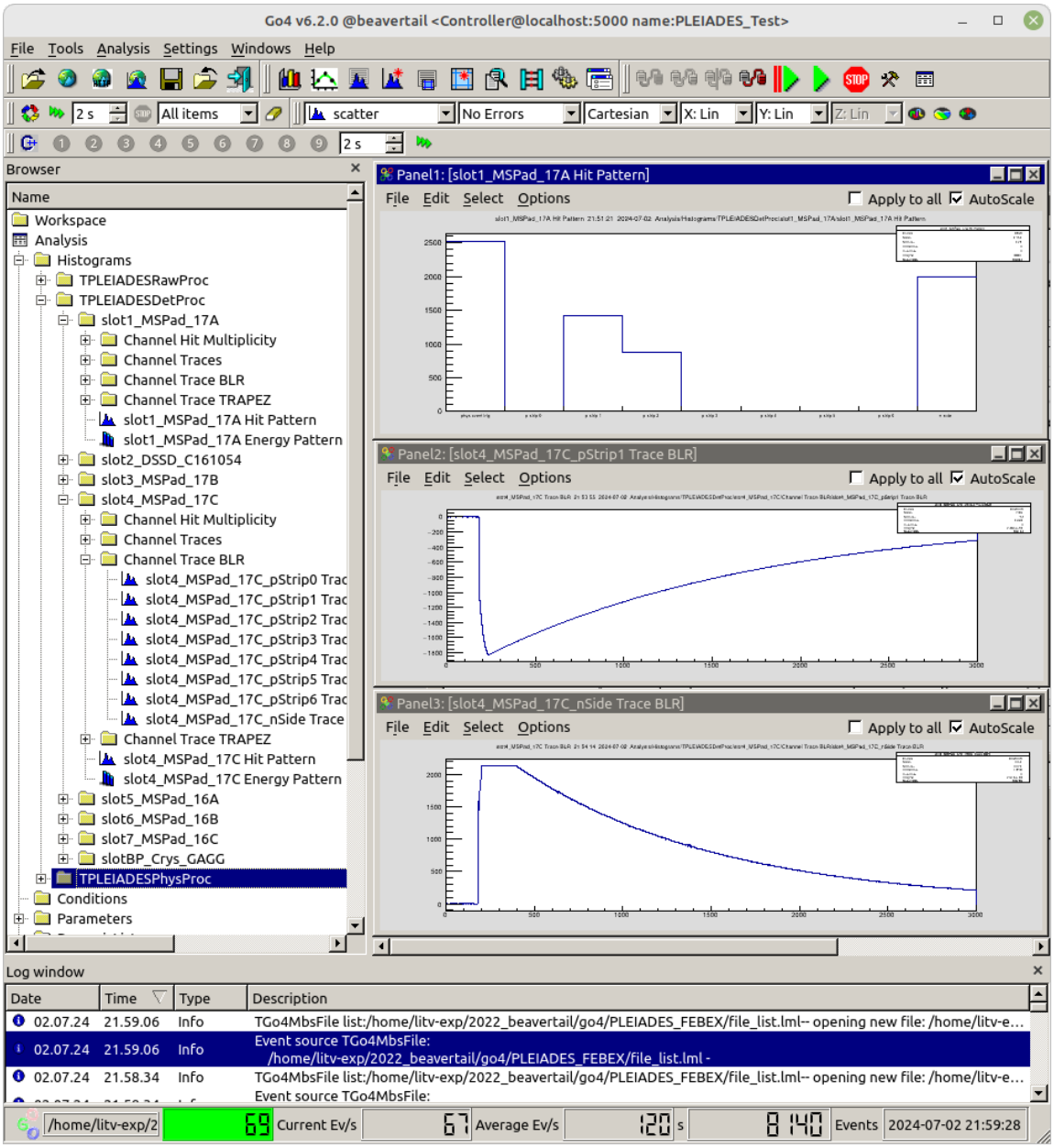

Figure 5.15: Screenshot of the TPLEIADES Go4 analysis in action. The displayed histograms show the detector hit pattern for MS Pad 17A, showing p-strips 2 and 3 being hit, with traces for p-strip 2 and the n-side of MS Pad 17C.

More details on the `TPLEIADES` Go4 analysis suite can be found on the GitHub and in the software publication ref. [247]. A screenshot of the analysis in action is provided in Figure 5.15.

5.5.2 Trace Analysis

For hit finding and real-time calculation of pulse heights, the FEBEX ADC uses a simple filter, which we call a *bi-box* filter, that is programmed on the FPGA of the FEBEX. This filter uses the difference of two moving averages to integrate the step function that is produced by the preamplifier. The bi-box filter is a simplified version of the industry standard *trapezoidal filter*. The trapezoidal filter will be explained first to highlight the key techniques used in trace analysis.

The trapezoidal digital filter was proposed by Radeka (1972) [248] and adapted for digital pulse processing by Georgiev *et al.* (1993) [244, 249] and Jordanov & Knoll (1994) [250, 251] throughout the 1990s. Whilst both algorithms are equivalent, Georgiev *et al.* called theirs a *moving window deconvolution* whilst Jordanov & Knoll called theirs a trapezoidal filter, so both terms are often used interchangeably. The trapezoidal filter is specifically designed for a digital sampling ADC since it is *causal* in that it only relies on present and previous values of the input signal. Different parameters are traditionally used for hit detection versus pulse-height evaluation.

Whilst producing essentially the same trapezoidal output, the trapezoidal filter and the moving window deconvolution implement the recursive algorithm slightly differently, but both feature two crucial steps: 1) a rolling average to integrate the rise time of the preamplifier signal, and 2) a pole-zero correction, that accounts for the exponential decay of the preamplifier pulse and produces the flat top of the trapezoidal output.

As discussed when introducing charge-sensitive amplifiers, the rise time of the preamplified signal is due both to the non-ideal nature of the amplifier and the non-zero capacitance of the silicon detector. Additionally, the non-zero width of the pulse from the sensor, which can be broadened with crystal defects from radiation damage, result in a preamplifier signal rise that is not a step function. This imperfection is referred to as *ballistic deficit*, but its effect can be minimised by good pulse shaping. In particular, if the window length is longer than the rise time, the ballistic deficit is fully integrated out. Furthermore, the window gap needs to also be longer than the rise time to integrate the entire pulse. However, the overall filter length needs to be balanced against avoiding pile up inside the filter.

As introduced above, the bi-box filter is a simplified version of the trapezoidal filter. It uses two moving averages for integration, but does not include a pole-zero correction, so does not achieve a flat top. This means that the advantages of the trapezoidal filter cannot be fully realised (i.e averaging the flat top). However, it has been demonstrated that both filters perform comparably. Considering our traces have a rise time of 60 samples (1.2 μs), we have chosen a window length of 100 samples (2.0 μs) and a window gap of 200 samples (4.0 μs). An example trace and output of the filter can be seen in Figure 5.16,

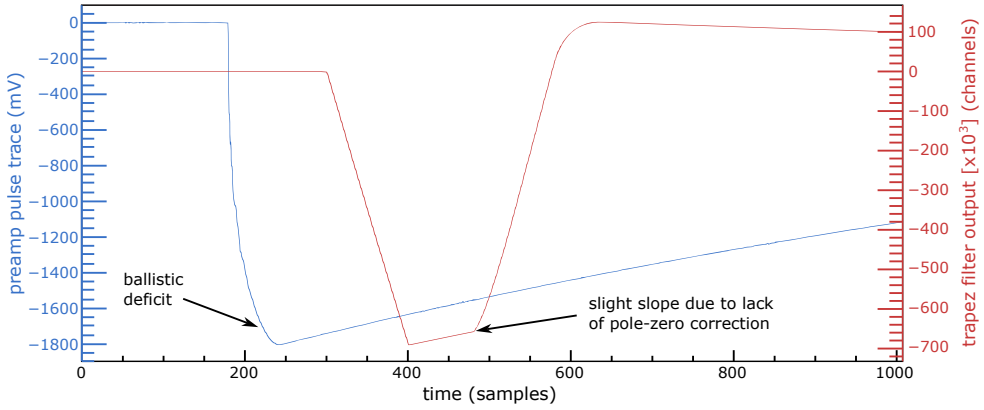

Figure 5.16: A comparison of a trace from a silicon pad p-strip with the accompanying bi-box filter, window = 100 samples and gap = 200 samples (1 sample = 20 ns). Because the window length is greater than the rise time, the ballistic deficit does not impact the filter. The lack of pole-zero correction means we do not achieve a flat top.

where the rounding effect of the ballistic deficit and the lack of pole-zero correction have been highlighted. The bi-box filter with these settings has been used for the offline trace analysis to extract the energy of our pulses, and will also be used going forward on the FPGA.

5.5.3 Trace Clipping

One unexpected issue occurred when the traces coming from the MSI-8s extended beyond the max range of the FEBEX ADCs causing the trace to be clipped, as shown in Panel 3 of Figure 5.15. Both the MPR-32 and MSI-8 datasheets from Mesytec incorrectly claim that the differential preamplifier output is ±1 V. As a result, our original FEBEX boards were purchased with a ±1 V input range. Upon checking the preamplifier outputs with a pulser after the test, we contacted Mesytec and found out that the MPR-32s have a ±1.2 V differential output and the MSI-8s have a ±1.8 V, with a 10% tolerance. This meant that the clipping we observed *was not* from the energy signals being too large and causing the preamplifiers to go over-range, but rather just a mismatch with between the preamplifier output and the digital ADC.

To solve this issue for future experiments, we had all our FEBEX boards modified to accept a ±2 V input range. This choice was motivated by balancing the desire to have all FEBEX boards use the same range for simplicity, whilst also considering need for good resolution and the ability to record pileup traces without clipping.

For the test analysis, this meant most MSI-8 traces were clipped and as a result neither the FPGA nor trace-based bi-box filters would give accurate energies. To check that all

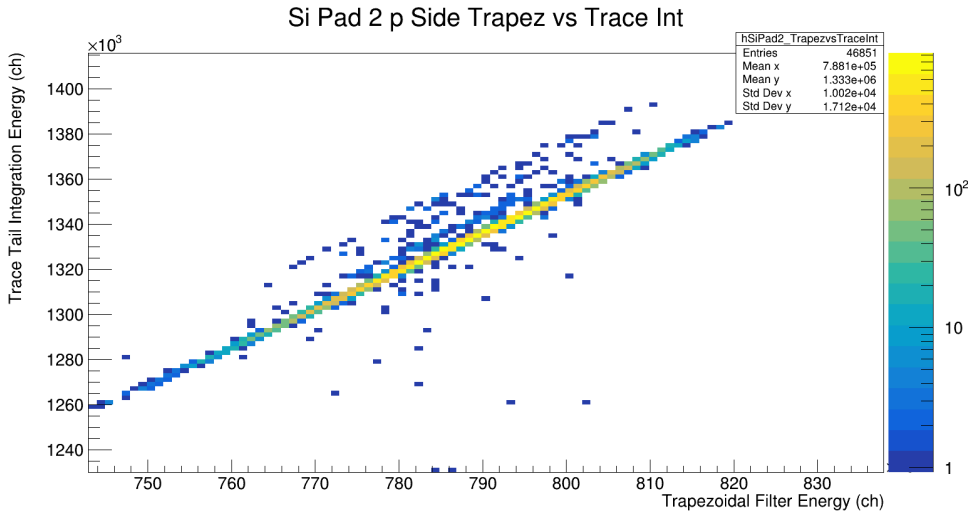

Figure 5.17: A comparison of the trapezoidal filter and the trace tail integration for determining the pulse height. The very strong positive correlation indicates that both methods measure the same energy.

pulses had similar shapes, some statistics on the clipped traces were collected including the rise time to clipping and the time of pulse reentry. Once it was established there was indeed only one species, several possibilities for extracting the energy from a clipped trace were considered. A simple time-over-threshold calculation was considered, but ultimately a late-time-integration was chosen because of its simplicity and the fact it required no calibration. We tested that the preamplifier decay was well modelled by an exponential, and then the integration is directly proportional to the peak height:

$$\int_{t_1}^{t_2} Ae^{-t/\tau} = A\tau(e^{-t_1/\tau} - e^{-t_2/\tau}) \propto A. \tag{5.3}$$

The start time of the trace was determined by a leading edge trigger, and then the trace was integrated between 900 and 2800 samples (18 and 56 μs) after the leading edge, which was outside the clipping range for all affected channels.

Figure 5.17 shows the bi-box filter against the trace integration for an unclipped p-strip trace. The very strong positive correlation indicates this is an appropriate substitute for the more accurate bi-box filter.

5.5.4 Isotopic selection performance

From the energy loss measured in individual silicon detectors, the signals can be summed to get a total energy loss measurement. Due to advantages of multi-sampling described in

Section 5.2.1, the resolution should improve with the number of detectors used. Figure 5.18 shows how the resolution increases with the number of silicon pads included in the sum. The relative resolution appears to plateau at four detectors, so if detector conservation was a consideration, just four silicon pads could still give the optimal resolution.

The tests were conducted with three different arrangements of detectors in order to test all detectors. Using all six pads, the energy loss resolution for the three setups was:

- Setup 1: 108 MeV at 15.82 GeV, or $d(dE)/dE = 1.61\%$;
- Setup 2: 118 MeV at 12.06 GeV, or $d(dE)/dE = 2.31\%$;
- Setup 3: 243 MeV at 14.51 GeV, or $d(dE)/dE = 3.94\%$.

Setup 3 shows considerably worse energy resolution then Setup 1 or 2. In particular, Design I detectors 6 and 8 were used in both Setups 2 and 3, and had significantly better resolution in Setup 2. One explanation is that Setup 3 had extensive pileup due to the high rates, and so the baseline of the signal was still recovering as new hits were analysed. This would cause low energy events, which would explain the reduced performance and the low energy tails seen for Setup 3. This result motivates the investigation of a filter with a pole-zero correction to mitigate these effects.

Analysing Setup 1, since $E \propto Z^2$, the above energy resolution corresponds to a Z resolution of $dZ/Z = 0.81\%$. For the test beam of ^{208}Pb with $Z = 82$, this corresponds to a $dZ = 0.66$. This is comparable to the reported resolution for CsISiPHOS, given its commissioning resolution was $dZ/Z = 0.45\%$, which is expected since they essentially use the same silicon detectors.

For the total energy measurement, the resolution at FWHM for the three setups was:

- Setup 1 (BGO): 130 MeV at 55.95 GeV, or $dE_{\text{tot}}/E_{\text{tot}} = 0.55\%$;
- Setup 2 (GAGG): 179 MeV at 52.18 GeV, or $dE_{\text{tot}}/E_{\text{tot}} = 0.81\%$;
- Setup 3 (CsI): 215 MeV at 54.789 GeV, or $dE_{\text{tot}}/E_{\text{tot}} = 0.92\%$.

Since the total energy is directly proportional to the mass, the resolution in A is the same, which for the test beam is $dA = 1.14$ u. Thus, the detector can separate 1 mass unit with a small amount of overlapping tails. Again, all values are comparable to the previous results from CsISiPHOS, where the total energy resolution was $dE_{\text{tot}}/E_{\text{tot}} = 0.57\%$.

It is worth noting that direct comparisons to the CsISiPHOS data can be challenging. The CsISiPHOS experiment detected ^{142}Pm/Pd^{52+} ions [159] as compared to our ^{208}Pb^{81+} ions. Because this is a real beam test, the momentum distribution of the beam will have a considerable impact of the measured resolutions. For the above tests, the electron cooler current was $I_e = 20$ mA for Setup 1 and $I_e = 100$ mA for Setup 2 and 3. The cooler current for the CsISiPHOS test was not reported, so a comparison is difficult.

The total energy vs energy loss histogram is shown in Figure 5.19. The main peak is nicely resolved, apart from a small tail to the bottom right from events who deposited

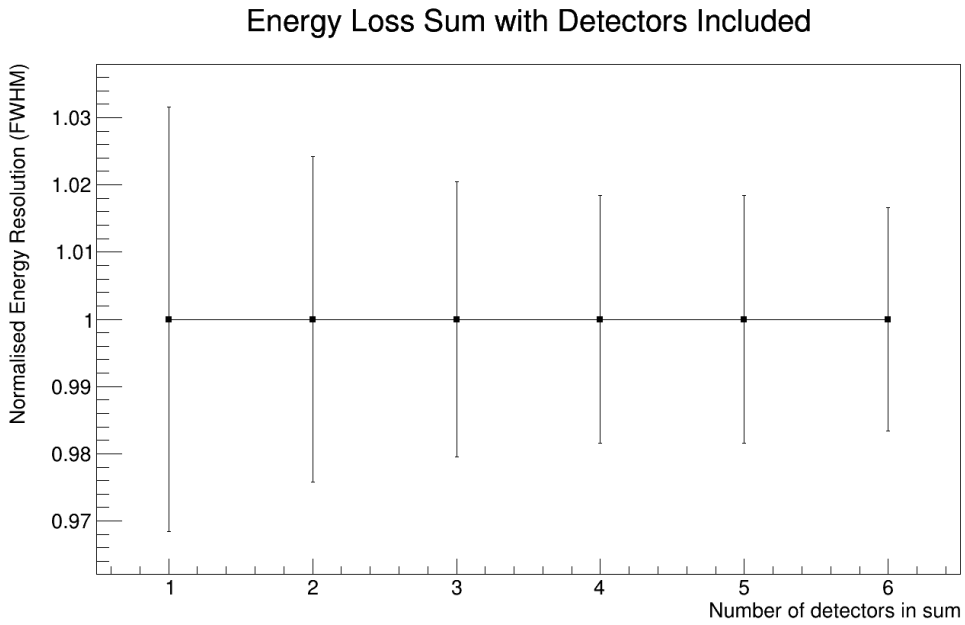

Figure 5.18: The energy loss resolution, given in FWHM with the energy loss normalised to 1 for comparison, is shown with an increasing number of detectors included. The resolution sees little improvement after 4 detectors are summed.

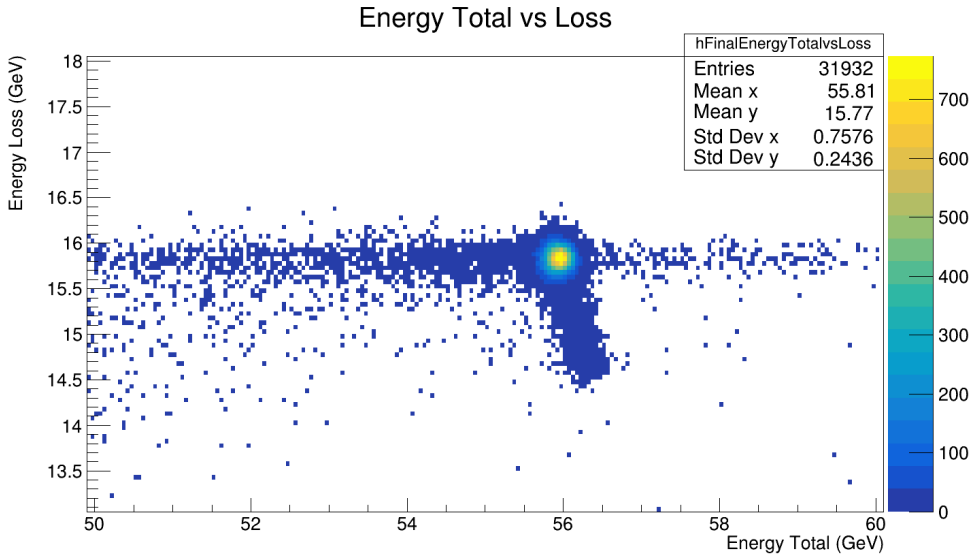

Figure 5.19: The energy total vs loss histogram for $^{208}Pb^{81+}$ ions intercepted by PLEIADES with Setup 1 of the commissioning test. As only primary beam was in the ring, a single peak is observed.

less energy in the silicon and more in the crystal. This tail was initially believed to be a clipping artefact, however, close examination of the traces show a small fraction of ions have a single silicon pad that has a signal trace with a much smaller amplitude whilst the corresponding crystal trace has a larger amplitude, with the shape of the traces looking completely normal. Since it is unphysical for an ion to deposit substantially less energy in just one, otherwise identical detector, close examination and potentially a further test should be done to understand this effect. However, since it does not the impact the energy resolution, such an investigation is beyond the scope of this thesis.

5.5.5 Crystal stopper comparison

Despite significantly different properties, in particular different light outputs, Table 5.2 shows that the three different scintillator materials performed comparably, with 1.12%, 1.16%, and 1.02% resolution for the CsI, GAGG, and BGO, respectively. Given the large signals from the large amount of energy deposited in these scintillators, and the very low electronic noise we observed for this run, this is an unsurprising but reassuring result.

One confounding factor that could impact a fair comparison of the energy resolution is the amount of pileup in each test. For the BGO crystal, the rate was low and as such the baseline was stable. This was not the case for the CsI or GAGG crystals, where some events still had a decaying baseline. Because the bi-box filter does not include a pole-zero correction, the integrated signal will be slightly smaller for such events. Whilst the bi-box filter was appropriate for this commissioning run, this can be fixed in future work by implementing a moving window deconvolution (MWD) filter.

It was possible to observe the effects of the decay constants of the crystals on the ballistic deficit of the traces (see Section 5.5.2) for the CsI and GAGG, but not the BGO as the traces were clipped for the BGO. The CsI detector had a rise time of 4.12 ms, whilst the GAGG detector had 2.50 ms. The fact that this had no impact on the energy resolution indicates that the faster rise time is not important in our situation.

This means that future editions of this detector can prioritise cost efficiency, robustness, and density by using BGO crystals, despite the reduced light output and slightly shorter peak wavelengths. Moving forward with PLEIADES, it gives us confidence that the new, denser crystals can be used without reduced performance in comparison to the very reliable CsI stopper.

Despite all signals being large, it is important to compare the peak signal height:

- CsI(Tl): signal height 1120 mV on 4 GeV card $\implies$ 2.49 GeV signal.
- GAGG(Ce): signal height 790 mV on 4 GeV card $\implies$ 1.76 GeV signal.
- BGO: signal height 1160 mV on 330 MeV card $\implies$ 212 MeV signal.

These signal heights are close to what was predicted (1.27, 0.87, and 0.13 GeV respectively) using just the responsivity at peak emission wavelength and photon output of the crystals, albeit off by a factor of 2 due to the previously stated mix up with the preamplifier output.

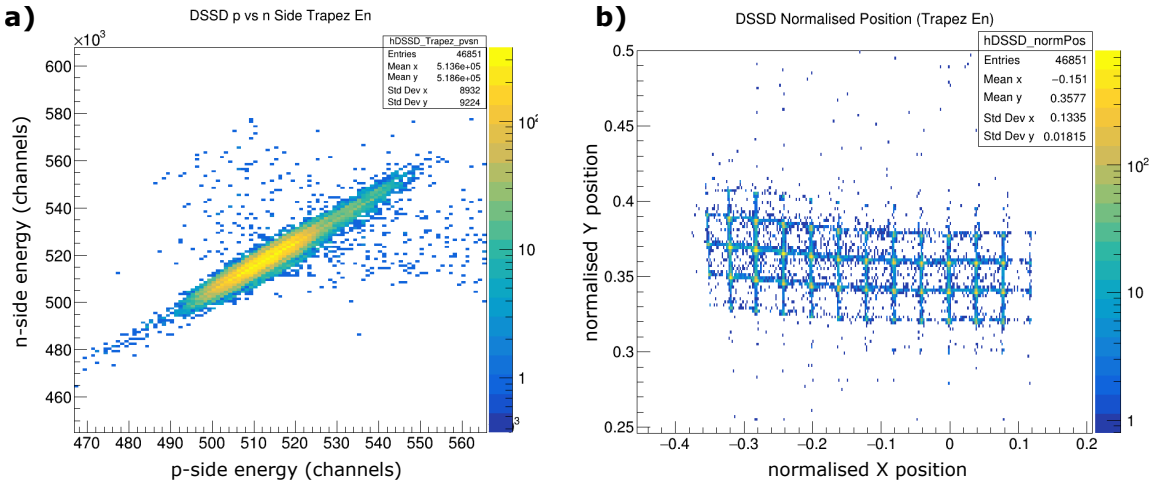

Figure 5.20: a) The p- and n-side energies of the DSSD are compared, showing strong correlation. **b)** The normalised position spectrum clearly shows the pixel accuracy of the resistive chain readout.

5.5.6 DSSD position spectrum

Finally, as discussed in Section 5.3.2, the DSSD strips are read out by a resistive chain. The ends of the resistive chain are referred to as 'left' and 'right' for the horizontal chain (vertical strips) on the p-side, and 'top' and 'bottom' for the vertical chain (horizontal strips) on the n-side. Note that these assignments depend on your frame of reference so for consistency, left and top are both closest to the pin connector shown in Figure 5.5b.

The height of the signal is directly proportional to how many resistors are between the strip that collected the charge and the readout electronics. For the sum of both ends of the resistive chain, this number is constant and proportional to the energy, so the left + right is proportional to the p-side energy and top + bottom is proportional to the n-side energy. As shown in Figure 5.20a, the p- and n-side energies are well correlated.

The difference of the two ends are directly proportional to the position, but to compare multiple events, the difference needs to be normalised by the energy. An example normalised position spectrum is shown in Figure 5.20b, which demonstrates the precise pixel resolution that can be achieved with the resistive chain. To calibrate the normalised position to give a scale in millimetres, the signal height produced by the last strip in the chain needs to be known as a reference point. This was done in the June 2022 test, but unfortunately the signals were assigned the wrong polarity, so no signals were recorded for those runs. Such a calibration is not required for the position spectrum to be useful though; a single beam spot is shown in Figure 5.20b that is well focused in Y but diffuse in X, as expected.

5.5.7 Summary of commissioning

The commissioning has demonstrated that all detectors are operational and that sufficeint energy resolution can be achieved to separate isotopes. All scintillators showed excellent resolution. In particular, even with the reduced light output, the BGO scintillator had the best resolution. This supports its use going forward as the primary detector, as the better stopping power allows PLEIADES to be used with lighter ions.

The commissioning also demonstrates the flexibility of the digital DAQ in diagnosing problems in offline analysis. Despite the saturation of signals, the recording of traces allowed us to extract good energy resolutions. However, pileup appears to cause problems with the bi-box filter, so a full moving window deconvolution filter should be implemented in the future. We were not able to do a beam test using two setups simultaneously using the timesorter, but this capability has been demonstrated with pulser tests. Thus, PLEIADES is ready for potential upcoming experiments.

Chapter 6

Summary and Outlook

6.1 Summary of the contributions of this thesis

This thesis has discussed the use of heavy-ion storage rings to address uniquely challenging measurements in the field of nuclear astrophysics. Experimental analysis, astrophysical impacts, and hardware developments have been presented. This chapter summarises these contributions, and places them in the broader context of the field of nuclear astrophysics.

Measurement of the bound-state β-decay rate of $^{205}Tl^{81+}$

The bound-state β-decay rate of $^{205}Tl^{81+}$ has been highly sought after due to its impact on two long-standing problems in astrophysics: the origin of ^{205}Pb in the early Solar System and the use of ^{205}Tl as a solar neutrino dosimeter. The experiment and analysis of the measurement of the bound-state β decay of $^{205}Tl^{81+}$ has been presented in Chapter 3. The experiment was technically very ambitious, and additional difficulties introduced by conducting the experiment during the COVID-19 lock-down made the analysis particularly challenging. The six corrections that needed to be applied to the raw Schottky data required careful handling to ensure that all systematic uncertainties were well understood. The β_b-decay rate was determined to be $\lambda_{\beta_b} = 2.76(25)_{\text{stat}}(13)_{\text{syst}} \times 10^{-8}$ s^{-1}, corresponding to a half-life of 291^{+33}_{-27} days and a $\log(ft)$ of 5.91(5). This $\log(ft)$ is larger than what was being used by the astrophysical community, highlighting the importance of making an experimental measurement.

^{205}Pb in the early Solar System

Chapter 4 presents the impact of the $^{205}Tl^{81+}$ measurement. The experimentally measured $\log(ft)$ for β_b decay of $^{205}Tl^{81+}$ determined the nuclear matrix element between the lowest spin-1/2 states of ^{205}Tl and ^{205}Pb [177]. This quantity is crucial for calculating accurate astrophysical weak decay rates of ^{205}Tl and ^{205}Pb. With these new rates, three state-of-the-art AGB models were used to predict ^{205}Pb yields from AGB stars. The yields resulted in a new ratio for the abundances of ^{205}Pb/^{204}Pb in the ISM, from which the isolation time of our Solar System from the ISM could be derived. Our measurement provided positive values for the isolation period, with 25% or 78% of the probability distribution being positive depending on the meteorite value used. This was the first time a positive value was achieved for ^{205}Pb.

The nuclear matrix element was also a crucial piece in determining the viability of the LOREX project for measuring the solar *pp* neutrino flux [90, 97, 185]. Unfortunately, the larger experimental $\log(ft)$ value (when compared to predictions) means that only 15(4) ^{205}Pb atoms per gram found in the lorandite can be attributed to the solar neutrino flux (compared to the prediction of 22(7) atoms g^{-1}), making the signal-to-background ratio statistically weaker.

Construction and commissioning of PLEIADES

In Chapter 5, the construction and commissioning of the PLEIADES multi-purpose detector, the successor to the CsISiPHOS δE–E telescope, has been presented. The detector was built at TRIUMF and commissioned at GSI with $^{208}\mathrm{Pb}^{82+}$ ions at 269 MeV/u in the Experimental Storage Ring. The detector performs comparably to CsISiPHOS, with improved flexibility and better handling of pulse pileup as a result of the new digital data acquisition. The new scintillator crystals allow for the full stopping of lower-Z ions (down to Kr, $Z = 36$) due to their higher density with no drop in performance. As a result, the ILIMA collaboration now has two powerful δE–E detectors that can be used for exotic decay measurements at GSI Darmstadt and the future FAIR facility.

6.2 Outlook

The study of ^{205}Pb in the early Solar System is just the first step in implementing the results of the new $^{205}\mathrm{Tl}^{81+}$ β_b-decay rate. The proposed scenario of the live ^{205}Pb observed in meteorites having arisen naturally from the galactic chemical evolution (GCE) of the interstellar medium needs to be better tested against other scenarios. In particular, the new astrophysical decay rates of ^{205}Pb and ^{205}Tl should be implemented in Wolf-Rayet star models to see whether a single, last event scenario could explain the observed abundances of the *s*-process short-lived radionuclides. In addition, our analysis based on the steady-state assumption should be upgraded with a GCE simulation to account for metallicity-dependent yields. This GCE analysis should also include a full comparison between multiple AGB models to account for the modelling uncertainty.

In parallel, we are testing the AGB models to see if the $^{205}\mathrm{Pb}(n,\gamma)$ cross section has any impact of the final ^{205}Pb yields. If the impact is large, then direct or indirect measurements of the $^{205}\mathrm{Pb}(n,\gamma)$ cross section should be prioritised to further reduce the nuclear physics uncertainties in this important prediction.

The ESR pocket detector PLEIADES is now commissioned and ready for use. One last outstanding capability that is missing is the ability to record the deadtime of the detector. Whilst the TRIXOR handles deadtime communication between the EXPLODER module and the PEXOR control unit, the MBS does not record the triggers that the TRIXOR rejects. In principle, this counting can be done by another FEBEX module, or through

an analogue scalar system. Both options are relatively simple, but need to be sorted out before the detector can be used for absolute counting of ions.

In the first physics experiment at the ESR requiring PLEIADES, it has been proposed to make a symbiotic measurement of the masses, half-lives, and β-delayed neutron (βn) branching ratios of ^{137,138}I. This experiment would be a proof-of-principle for a new method of measuring βn decay without detecting the neutron. This is a great strength of the proposed method given the low efficiencies for the direct detection of neutrons and the scarce amount of available beamtime. The β^--decay products (in this case $^{137,138}Xe^{54+}$) would stay within the acceptance of the ESR allowing them to be monitored by the Schottky detectors, whilst the βn-decay products (in this case $^{136,137}Xe^{54+}$ for β-delayed one-neutron emission) would be captured by the particle detectors in the ESR pockets. Given the low expected count rates of just 0.4 decays from $\sim$ 23 ions per storage for ^{138}I, the isotopic identification of PLEIADES and CsISiPHOS will be crucial in the success of this experiment. The isotopes ^{137,138}I were chosen for their high production rates at GSI allowing for a high-statistics proof-of-principle experiment, and because the isotopes are βn reference standards with well-measured neutron-branching ratios, making them ideal calibration points for the new method.

In conclusion, heavy-ion storage rings are powerful tools for studying exotic decays and reactions for nuclear astrophysics. The ability to trap millions of highly-charged ions for several hours allows for the measurement of exotic decay modes that can only be measured with a storage ring. The next decade will bring exciting new advances for radioactive beam facilities, and storage rings will provide a crucial experimental tool to collect the nuclear data required to understand the production of the elements.

Bibliography

[1] Eddington, A.S. The Internal Constitution of the Stars. *Nature*, **106**:14–20, (1920).

[2] Bethe, H.A. Energy Production in Stars. *Physical Review*, **55**:434–456, (1939).

[3] von Weizsacker, C.F. Über Elementumwandlungen in Innern der Sterne I. *Physikalische Zeitschrift*, **38**:176–191, (1937).

[4] von Weizsacker, C.F. Über Elementumwandlungen in Innern der Sterne II. *Physikalische Zeitschrift*, **39**:633–646, (1938).

[5] Hoyle, F. The Synthesis of the Elements from Hydrogen. *Monthly Notices of the Royal Astronomical Society*, **106**:343–383, (1946).

[6] Hoyle, F. On Nuclear Reactions Occuring in Very Hot Stars. I. The Synthesis of Elements from Carbon to Nickel. *The Astrophysical Journal Supplement Series*, **1**: 121, (1954).

[7] Burbidge, E.M., Burbidge, G.R., Fowler, W.A. and Hoyle, F. Synthesis of the Elements in Stars. *Reviews of Modern Physics*, **29**:547–650, (1957).

[8] Cameron, A.G.W. Stellar Evolution, Nuclear Astrophysics, and Nucleogenesis. (1957).

[9] Grevesse, N. and Noels, A. Cosmic abundances of the elements. In *Proc. Origin and Evolution of the Elements*, p. 15–25, (Cambridge Univ. Press, 1993).

[10] Asplund, M., Grevesse, N., Sauval, A.J. and Scott, P. The Chemical Composition of the Sun. *Annual Review of Astronomy & Astrophysics*, **47**:481–522, (2009).

[11] Lodders, K. Solar Elemental Abundances. *Oxford Research Encyclopedia*, (Oxford Univ. Press, 2020).

[12] Lodders, K. Relative Atomic Solar System Abundances, Mass Fractions, and Atomic Masses of the Elements and Their Isotopes, Composition of the Solar Photosphere, and Compositions of the Major Chondritic Meteorite Groups. *Space Science Reviews*, **217**:44, (2021).

[13] Lodders, K. Solar System Abundances and Condensation Temperatures of the Elements. *The Astrophysical Journal*, **591**:1220, (2003).

[14] Diehl, R., Korn, A.J., Leibundgut, B., Lugaro, M. and Wallner, A. Cosmic nucleosynthesis: A multi-messenger challenge. *Progress in Particle and Nuclear Physics*, **127**:103983, (2022).

[15] Travaglio, C. *et al.* Galactic Chemical Evolution of Heavy Elements: From Barium to Europium. *The Astrophysical Journal*, **521**:691, (1999).

[16] Travaglio, C. *et al.* Galactic Evolution of Sr, Y, and Zr: A Multiplicity of Nucleosynthetic Processes. *The Astrophysical Journal*, **601**:864, (2004).

[17] Prantzos, N., Abia, C., Limongi, M., Chieffi, A. and Cristallo, S. Chemical evolution with rotating massive star yields – I. The solar neighbourhood and the *s*-process elements. *Monthly Notices of the Royal Astronomical Society*, **476**:3432–3459, (2018).

[18] Prantzos, N., Abia, C., Cristallo, S., Limongi, M. and Chieffi, A. Chemical evolution with rotating massive star yields II. A new assessment of the solar *s*- and *r*-process components. *Monthly Notices of the Royal Astronomical Society*, **491**:1832–1850, (2020).

[19] Côté, B. *et al.* Galactic Chemical Evolution of Radioactive Isotopes. *The Astrophysical Journal*, **878**:156, (2019).

[20] Cyburt, R.H., Fields, B.D., Olive, K.A. and Yeh, T.H. Big bang nucleosynthesis: Present status. *Reviews of Modern Physics*, **88**:015004, (2016).

[21] Boesgaard, A.M. and Steigman, G. Big Bang Nucleosynthesis: Theories and Observations. *Annual Review of Astronomy & Astrophysics*, **23**:319–78, (1985).

[22] Rolfs, C.E. and Rodney, W.S. *Cauldrons in the cosmos: nuclear astrophysics.* (The Univ. of Chicago Press, 1988).

[23] Iliadis, C. *Nuclear Physics of Stars.* (Wiley-VCH, 2007).

[24] Karakas, A.I. and Lattanzio, J.C. The Dawes Review 2: Nucleosynthesis and Stellar Yields of Low- and Intermediate-Mass Single Stars. *Publications of the Astronomical Society of Australia*, **31**:e030, (2014).

[25] Arcones, A. and Thielemann, F.K. Origin of the elements. *The Astronomy & Astrophysics Review*, **31**:1, (2022).

[26] Hoyle, F. and Fowler, W.A. Nucleosynthesis in Supernovae. *The Astrophysical Journal*, **132**:565, (1960).

[27] Johnson, J.A., Fields, B.D. and Thompson, T.A. The origin of the elements: a century of progress. *Philosophical Transactions of the Royal Society A: Mathematical, Physical and Engineering Sciences*, **378**:20190301, (2020).

[28] Märkisch, B. *et al.* Measurement of the Weak Axial-Vector Coupling Constant in the Decay of Free Neutrons Using a Pulsed Cold Neutron Beam. *Physical Review Letters*, **122**:242501, (2019).

[29] Käppeler, F. The origin of the heavy elements: The *s* process. *Progress in Particle and Nuclear Physics*, **43**:419–483, (1999).

[30] Sneden, C., Cowan, J.J. and Gallino, R. Neutron-Capture Elements in the Early Galaxy. *Annual Review of Astronomy & Astrophysics*, **46**:241–288, (2008).

[31] Qian, Y.Z. The origin of the heavy elements: Recent progress in the understanding of the *r*-process. *Progress in Particle and Nuclear Physics*, **50**:153–199, (2003).

[32] Arnould, M., Goriely, S. and Takahashi, K. The *r*-process of stellar nucleosynthesis: Astrophysics and nuclear physics achievements and mysteries. *Physics Reports*, **450**: 97–213, (2007).

[33] Martínez-Pinedo, G. *et al.* The role of fission in the *r*-process. *Progress in Particle and Nuclear Physics*, **59**:199–205, (2007).

[34] Cowan, J.J. *et al.* Origin of the heaviest elements: The rapid neutron-capture process. *Reviews of Modern Physics*, **93**:015002, (2021).

[35] Abbott, B. *et al.* GW170817: Observation of Gravitational Waves from a Binary Neutron Star Inspiral. *Physical Review Letters*, **119**:161101, (2017).

[36] Abbott, B.P. *et al.* Multi-messenger Observations of a Binary Neutron Star Merger*. *The Astrophysical Journal Letters*, **848**:L12, (2017).

[37] Villar, V.A. *et al.* The Combined Ultraviolet, Optical, and Near-infrared Light Curves of the Kilonova Associated with the Binary Neutron Star Merger GW170817: Unified Data Set, Analytic Models, and Physical Implications. *The Astrophysical Journal Letters*, **851**:L21, (2017).

[38] Chen, H.Y., Landry, P., Read, J.S. and Siegel, D.M. Inference of multi-channel *r*-process element enrichment in the Milky Way using binary neutron star merger observations. (arXiv, 2024).

[39] Woosley, S.E. and Howard, W.M. The *p*-processes in supernovae. *The Astrophysical Journal Supplement Series*, **36**:285–304, (1978).

[40] Pignatari, M., Göbel, K., Reifarth, R. and Travaglio, C. The production of proton-rich isotopes beyond iron: The γ-process in stars. *International Journal of Modern Physics E*, **25**:1630003, (2016).

[41] Rauscher, T. *et al.* Constraining the astrophysical origin of the p-nuclei through nuclear physics and meteoritic data. *Reports on Progress in Physics*, **76**:066201, (2013).

[42] Cowan, J.J. and Rose, W.K. Production of C-14 and neutrons in red giants. *The Astrophysical Journal*, **212**:149, (1977).

[43] Herwig, F. *et al.* Convective-reactive proton-^{12}C combustion in Sakurai's object (V4334 SagittarII) and implications for the evolution and yields from the first generations of stars. *The Astrophysical Journal*, **727**:89, (2011).

[44] Denissenkov, P.A. *et al.* i-process Nucleosynthesis and Mass Retention Efficiency in He-shell Flash Evolution of Rapidly Accreting White Dwarfs. *The Astrophysical Journal Letters*, **834**:L10, (2017).

[45] Choplin, A., Siess, L. and Goriely, S. The intermediate neutron capture process - III. The i-process in AGB stars of different masses and metallicities without overshoot. *Astronomy & Astrophysics*, **667**:A155, (2022).

[46] Jones, S. *et al.* H ingestion into He-burning convection zones in super-AGB stellar models as a potential site for intermediate neutron-density nucleosynthesis. *Monthly Notices of the Royal Astronomical Society*, **455**:3848–3863, (2016).

[47] Pritychenko, B., Mughaghab, S.F. and Sonzogni, A.A. Calculations of Maxwellian-averaged cross sections and astrophysical reaction rates using the ENDF/B-VII.0, JEFF-3.1, JENDL-3.3, and ENDF/B-VI.8 evaluated nuclear reaction data libraries. *Atomic Data and Nuclear Data Tables*, **96**:645–748, (2010).

[48] Clayton, D.D., Fowler, W.A., Hull, T.E. and Zimmerman, B.A. Neutron capture chains in heavy element synthesis. *Annals of Physics*, **12**:331–408, (1961).

[49] Seeger, P., Fowler, W. and Clayton, D. Nucleosynthesis of Heavy Elements by Neutron Capture. *The Astrophysical Journal*, **11**:121–126, (1965).

[50] Clayton, D.D. and Ward, R.A. s-Process Studies: Exact Evaluation of an Exponential Distribution of Exposures. *The Astrophysical Journal*, **193**:397–400, (1974).

[51] Käppeler, F., Gallino, R., Busso, M., Picchio, G. and Raiteri, C.M. s-Process Nucleosynthesis: Classical Approach and Asymptotic Giant Branch Models for Low-Mass Stars. *The Astrophysical Journal*, **354**:630, (1990).

[52] Wisshak, K., Guber, K., Voss, F., Käppeler, F. and Reffo, G. Neutron capture in ^{148,150}Sm: A sensitive probe of the *s*-process neutron density. *Physical Review C*, **48**: 1401–1419, (1993).

[53] Kondev, F.G., Wang, M., Huang, W.J., Naimi, S. and Audi, G. The NUBASE2020 evaluation of nuclear physics properties*. *Chinese Physics C*, **45**:030001, (2021).

[54] Käppeler, F., Beer, H. and Wisshak, K. *s*-process nucleosynthesis-nuclear physics and the classical model. *Reports on Progress in Physics*, **52**:945, (1989).

[55] Arlandini, C. *et al.* Neutron Capture in Low-Mass Asymptotic Giant Branch Stars: Cross Sections and Abundance Signatures. *The Astrophysical Journal*, **525**:886, (1999).

[56] Käppeler, F., Gallino, R., Bisterzo, S. and Aoki, W. The *s* process: Nuclear physics, stellar models, and observations. *Reviews of Modern Physics*, **83**:157–193, (2011).

[57] Busso, M., Gallino, R. and Wasserburg, G.J. Nucleosynthesis in Asymptotic Giant Branch Stars: Relevance for Galactic Enrichment and Solar System Formation. *Annual Review of Astronomy & Astrophysics*, **37**:239–309, (1999).

[58] Lugaro, M., Pignatari, M., Reifarth, R. and Wiescher, M. The *s* Process and Beyond. *Annual Review of Nuclear and Particle Science*, **73**:315–340, (2023).

[59] Merrill, P.W. Spectroscopic Observations of Stars of Class S. *The Astrophysical Journal*, **116**:21, (1952).

[60] Wallner, A. *et al.* Accelerator mass spectrometry measurements of the ^{13}C$(n,\gamma)^{14}$C and ^{14}N$(n,p)^{14}$C cross sections. *Physical Review C*, **93**:045803, (2016).

[61] Bisterzo, S., Travaglio, C., Gallino, R., Wiescher, M. and Käppeler, F. Galactic Chemical Evolution and Solar *s*-Process Abundances: Dependence on the ^{13}C-Pocket Structure. *The Astrophysical Journal*, **787**:10, (2014).

[62] The, L.S., Eid, M.F.E. and Meyer, B.S. *s*-Process Nucleosynthesis in Advanced Burning Phases of Massive Stars. *The Astrophysical Journal*, **655**:1058, (2007).

[63] Raiteri, C.M., Busso, M., Gallino, R., Picchio, G. and Pulone, L. *s*-Process Nucleosynthesis in Massive Stars and the Weak Component. I. Evolution and Neutron Captures in a 25 $M_\odot$ Star. *The Astrophysical Journal*, **367**:228, (1991).

[64] Raiteri, C.M., Busso, M., Gallino, R. and Picchio, G. *s*-Process Nucleosynthesis in Massive Stars and the Weak Component. II. Carbon Burning and Galactic Enrichment. *The Astrophysical Journal*, **371**:665, (1991).

[65] Pignatari, M. *et al.* The weak s-process in massive stars and its dependence on the neutron capture cross sections. *The Astrophysical Journal*, **710**:1557, (2010).

[66] Pignatari, M., Gallino, R. and Reifarth, R. The s process in massive stars, a benchmark for neutron capture reaction rates. *The European Physical Journal A*, **59**:302, (2023).

[67] Fermi, E. Tentativo di una Teoria Dei Raggi . *Il Nuovo Cimento (1924-1942)*, **11**: 1–19, (1934).

[68] Krane, K.S. *Introductory Nuclear Physics.* (John Wiley & Sons, 1988).

[69] Severijns, N., Beck, M. and Naviliat-Cuncic, O. Tests of the standard electroweak model in nuclear beta decay. *Reviews of Modern Physics*, **78**:991–1040, (2006).

[70] Behrens, H. and Bühring, W. *Electron Radial Wave Functions and Nuclear Beta-decay.* (Clarendon Press, 1982).

[71] Holstein, B.R. Induced Coulomb corrections to nuclear beta decay. *Physical Review C*, **10**:1215–1219, (1974).

[72] Hayen, L., Severijns, N., Bodek, K., Rozpedzik, D. and Mougeot, X. High precision analytical description of the allowed β spectrum shape. *Reviews of Modern Physics*, **90**:015008, (2018).

[73] Daudel, R., Jean, M. and Lecoin, M. Sur la possibilité d'existence d'un type particulier de radioactivité phénomène de création e. *Journal de Physique et le Radium*, **8**:238–243, (1947).

[74] Bahcall, J.N. Theory of Bound-State Beta Decay. *Physical Review*, **124**:495–499, (1961).

[75] Litvinov, Y.A. and Bosch, F. Beta decay of highly charged ions. *Reports on Progress in Physics*, **74**:016301, (2011).

[76] Takahashi, K., Boyd, R.N., Mathews, G.J. and Yokoi, K. Bound-state beta decay of highly ionized atoms. *Physical Review C*, **36**:1522–1528, (1987).

[77] Jung, M. *et al.* First observation of bound-state β^- decay. *Physical Review Letters*, **69**:2164–2167, (1992).

[78] Bosch, F. *et al.* Observation of Bound-State β^- Decay of Fully Ionized ^{187}Re: ^{187}Re-^{187}Os Cosmochronometry. *Physical Review Letters*, **77**:4, (1996).

[79] Ohtsubo, T. *et al.* Simultaneous Measurement of β^- Decay to Bound and Continuum Electron States. *Physical Review Letters*, **95**:052501, (2005).

[80] Pengra, J.G., Genz, H. and Fink, R.W. Orbital electron capture ratios in the decay of ^{205}Pb. *Nuclear Physics A*, **302**:1–11, (1978).

[81] Lindner, H. *et al.* The Q-value of the electron capture in ^{205}Pb measured with transfer reactions. *Nuclear Instruments and Methods in Physics Research Section A: Accelerators, Spectrometers, Detectors and Associated Equipment*, **297**:217–222, (1990).

[82] Sidky, M.H. *et al.* Precise atomic mass differences in Pb and Tl and the decay energy for ^{205}Pb. *Nuclear Instruments and Methods in Physics Research Section A: Accelerators, Spectrometers, Detectors and Associated Equipment*, **330**:195–198, (1993).

[83] Wang, M., Huang, W.J., Kondev, F.G., Audi, G. and Naimi, S. The AME 2020 atomic mass evaluation (II). Tables, graphs and references*. *Chinese Physics C*, **45**: 030003, (2021).

[84] Kondev, F.G. Nuclear Data Sheets for A = 205. *Nuclear Data Sheets*, **166**:1–230, (2020).

[85] Rodrigues, G.C., Indelicato, P., Santos, J.P., Patté, P. and Parente, F. Systematic calculation of total atomic energies of ground state configurations. *Atomic Data and Nuclear Data Tables*, **86**:117–233, (2004).

[86] Huang, K.N., Aoyagi, M., Chen, M.H., Crasemann, B. and Mark, H. Neutral-atom electron binding energies from relaxed-orbital relativistic Hartree-Fock-Slater calculations $2 \leq Z \leq 106$. *Atomic Data and Nuclear Data Tables*, **18**:243–291, (1976).

[87] Johnson, W.R. and Soff, G. The lamb shift in hydrogen-like atoms, $1 \leq Z \leq 110$. *Atomic Data and Nuclear Data Tables*, **33**:405–446, (1985).

[88] Plante, D.R., Johnson, W.R. and Sapirstein, J. Relativistic all-order many-body calculations of the $n = 1$ and $n = 2$ states of heliumlike ions. *Physical Review A*, **49**: 3519–3530, (1994).

[89] Krečak, Z. *et al.* Measurement of the half-life of the first excited state of ^{205}Pb. *Physical Review C*, **50**:1319–1320, (1994).

[90] Freedman, M.S. *et al.* Solar Neutrinos: Proposal for a New Test. *Science*, **193**: 1117–1119, (1976).

[91] Davis, R. Solar Neutrinos. II. Experimental. *Physical Review Letters*, **12**:303–305, (1964).

[92] Davis, R., Harmer, D.S. and Hoffman, K.C. Search for Neutrinos from the Sun. *Physical Review Letters*, **20**:1205–1209, (1968).

[93] Anselmann, P. *et al.* Solar neutrinos observed by GALLEX at Gran Sasso. *Physics Letters B*, **285**:376–389, (1992).

[94] Abdurashitov, J.N. *et al.* Measurement of the solar neutrino capture rate with gallium metal. III. Results for the 2002–2007 data-taking period. *Physical Review C*, **80**: 015807, (2009).

[95] Bahcall, J.N. Solar Neutrinos. I. Theoretical. *Physical Review Letters*, **12**:300–302, (1964).

[96] Bahcall, J.N., Bahcall, N.A. and Shaviv, G. Present Status of the Theoretical Predictions for the ^{37}Cl Solar-Neutrino Experiment. *Physical Review Letters*, **20**:1209–1212, (1968).

[97] Freedman, M.S. Measurement of low energy neutrino absorption probability in thallium 205. *Nuclear Instruments and Methods in Physics Research Section A: Accelerators, Spectrometers, Detectors and Associated Equipment*, **271**:267–276, (1988).

[98] Kienle, P. Studies of radioactive decays of completely ionized nuclei in a heavy ion storage ring. *Nuclear Instruments and Methods in Physics Research Section A: Accelerators, Spectrometers, Detectors and Associated Equipment*, **271**:277–279, (1988).

[99] Pavićević, M.K. Lorandite from Allchar — A low energy solar neutrino dosimeter. *Nuclear Instruments and Methods in Physics Research Section A: Accelerators, Spectrometers, Detectors and Associated Equipment*, **271**:287–296, (1988).

[100] Subotic, K.M., Pavicevic, M.K. and Sherrill, B.M. Status of the LOREX: Geochemical ^{205}Tl solar neutrino experiment. *AIP Conference Proceedings*, **455**:912–915, (1998).

[101] Pavićević, M.K. *et al.* Lorandite from Allchar as geochemical detector for pp-solar neutrinos. *Nuclear Instruments and Methods in Physics Research Section A: Accelerators, Spectrometers, Detectors and Associated Equipment*, **895**:62–73, (2018).

[102] Sidhu, R.S. *et al.* Bound-State Beta Decay of $^{205}Tl^{81+}$ Ions and the LOREX Project. *Physical Review Letters*, **133**:232701, (2024).

[103] Dillmann, I. *et al.* KADoNiS - the Karlsruhe Astrophysical Database of Nucleosynthesis in Stars. In *Proc. Capture Gamma-Ray and Related Topics: 12th International Symposium*, p. 123–127, (AIP Conference Proceeding, 2006).

[104] Liu, N., Cristallo, S. and Vescovi, D. Slow Neutron-Capture Process: Low-Mass Asymptotic Giant Branch Stars and Presolar Silicon Carbide Grains. *Universe*, **8**: 362, (2022).

[105] Palmerini, S. *et al.* Low Mass Stars or Intermediate Mass Stars? The Stellar Origin of Presolar Oxide Grains Revealed by Their Isotopic Composition. *Frontiers in Astronomy and Space Sciences*, **7**:607245, (2021).

[106] Lugaro, M., Ott, U. and Kereszturi, Radioactive nuclei from cosmochronology to habitability. *Progress in Particle and Nuclear Physics*, **102**:1–47, (2018).

[107] Zhang, Y.H., Litvinov, Y.A., Uesaka, T. and Xu, H.S. Storage ring mass spectrometry for nuclear structure and astrophysics research. *Physica Scripta*, **91**:073002, (2016).

[108] Steck, M. and Litvinov, Y.A. Heavy-ion storage rings and their use in precision experiments with highly charged ions. *Progress in Particle and Nuclear Physics*, **115**:103811, (2020).

[109] Franzke, B. Review of heavy ion storage rings. In *Proc. EPAC 92: Third European Particle Accelerator Conference*, p. 367–371, (Editions Frontières, 1992).

[110] Budker, G.I. An effective method of damping particle oscillations in proton and antiproton storage rings. *Soviet Atomic Energy*, **22**:438–440, (1967).

[111] Skrinsky, A. Proton - antiproton colliding beams. In *Proc. 8th International Conference on High-Energy Accelerators*, p. 72–78, (Fermilab Library, 1971).

[112] van der Meer, S. Stochastic damping of betatron oscillations in the ISR. Technical Report CERN-ISR-PO-72-31, CERN, (1972).

[113] Carron, G., Myers, S. and Thorndahl, L. The 50 MHz Transverse Feedback System in the CERN ISR. *IEEE Transactions on Nuclear Science*, **24**:1833–1835, (1977).

[114] Wolf, A. Heavy-Ion Storage Rings. In *Atomic Physics with Heavy Ions*, (eds. Beyer, H.F. and Shevelko, V.P.), p. 3–29, (Springer, 1999).

[115] Franzke, B. The heavy ion storage and cooler ring project ESR at GSI. *Nuclear Instruments and Methods in Physics Research Section B: Beam Interactions with Materials and Atoms*, **24-25**:18–25, (1987).

[116] Lestinsky, M. *et al.* Physics book: CRYRING@ESR. *The European Physical Journal Special Topics*, **225**:797–882, (2016).

[117] Lestinsky, M. *et al.* First Experiments with CRYRING@ESR. *Atoms*, **10**:141, (2022).

[118] Xia, J.W. *et al.* HIRFL-CSR complex. *Chinese Physics C*, **33**:804–810, (2009).

[119] Wakasugi, M. The Rare RI Ring Facility at the RIKEN RI Beam Factory. In *Proc. Conference on Advances in Radioactive Isotope Science (ARIS2014)*, (Journal of the Physical Society of Japan, 2015).

[120] Beckert, K. *et al.* Charge Exchange Extraction at the Experimental Storage Ring ESR at GSI. In *Proc. EPAC 98: Sixth European Particle Accelerator Conference*, p. 559–561, (Institute of Physics Publishing, 1998).

[121] Edwards, D.A. and Syphers, M.J. *An Introduction to the Physics of High Energy Accelerators.* (John Wiley & Sons, 1993).

[122] Conte, M. and Mackay, W.W. *Introduction To The Physics Of Particle Accelerators, An (2nd Edition).* (World Scientific Publishing Company, 2008).

[123] Steinhagen, R.J. Transverse Dynamics. In *Proc. Operateursschulung Betrieb*, (Indico, 2016).

[124] Steck, M. Beam Cooling. In *Proc. Advanced Accelerator Physics Course*, (CERN Accelerator School, 2015).

[125] Schottky, W. Über spontane Stromschwankungen in verschiedenen Elektrizitätsleitern. *Annalen der physik*, **362**:541–567, (1918).

[126] Möhl, D. Stochastic Cooling of Particle Beams. In *Stochastic Cooling of Particle Beams*, (ed. Möhl, D.), p. 1–3, (Springer, 2013).

[127] Nolden, F. *et al.* Stochastic cooling at the ESR. *Nuclear Instruments and Methods in Physics Research Section A: Accelerators, Spectrometers, Detectors and Associated Equipment*, **441**:219–222, (2000).

[128] Steck, M., Beller, P., Beckert, K., Franzke, B. and Nolden, F. Electron cooling experiments at the ESR. *Nuclear Instruments and Methods in Physics Research Section A: Accelerators, Spectrometers, Detectors and Associated Equipment*, **532**: 357–365, (2004).

[129] Morgner, J. *et al.* Stringent test of QED with hydrogen-like tin. *Nature*, **622**:53–57, (2023).

[130] Beyer, H.F., Liesen, D. and Guzman, O. On the total recombination between cooling electrons and heavy ions. *Particle Accelerators*, **24**:163–175, (1989).

[131] Eichler, J. and Stöhlker, T. Radiative electron capture in relativistic ion–atom collisions and the photoelectric effect in hydrogen-like high-Z systems. *Physics Reports*, **439**:1–99, (2007).

[132] Badnell, N.R. Dielectronic Recombination. In *Proc. Spectroscopic Challenges of Photoionized Plasmas*, p. 37–52, (ASP Conference Series, 2001).

[133] Dimopoulou, C. *et al.* Longitudinal accumulation of ion beams in the ESR supported by electron cooling. In *Proc. Proceeding of COOL 2007*, p. 21–24, (JACoW, 2007).

[134] Steck, M. *et al.* Demonstration of longitudinal stacking in the ESR with barrier buckets and stochastic cooling. In *Proc. Proceeding of COOL'11*, p. 140–143, (JACoW, 2011).

[135] Glorius, J. *et al.* Storage, accumulation and deceleration of secondary beams for nuclear astrophysics. *Nuclear Instruments and Methods in Physics Research Section B: Beam Interactions with Materials and Atoms*, **541**:190–193, (2023).

[136] Herfurth, F. *et al.* The HITRAP facility for slow highly charged ions. *Physica Scripta*, **2015**:014065, (2015).

[137] Gruber, A., Bourgeois, W., Franzke, B., Kritzer, A. and Treffert, C. Internal gas-jet target for the ESR at GSI. *Nuclear Instruments and Methods in Physics Research Section A: Accelerators, Spectrometers, Detectors and Associated Equipment*, **282**: 87–93, (1989).

[138] Reich, H., Bourgeois, W., Franzke, B., Kritzer, A. and Varentsov, V. The ESR internal target. *Nuclear Physics A*, **626**:417–425, (1997).

[139] Kühnel, M. *et al.* Low-Z internal target from a cryogenically cooled liquid microjet source. *Nuclear Instruments and Methods in Physics Research Section A: Accelerators, Spectrometers, Detectors and Associated Equipment*, **602**:311–314, (2009).

[140] Reifarth, R. and Litvinov, Y.A. Measurements of neutron-induced reactions in inverse kinematics. *Physical Review Special Topics - Accelerators and Beams*, **17**:014701, (2014).

[141] Reifarth, R. *et al.* Spallation-based neutron target for direct studies of neutron-induced reactions in inverse kinematics. *Physical Review Accelerators and Beams*, **20**:044701, (2017).

[142] Dillmann, I. *et al.* Measuring neutron capture cross sections of radioactive nuclei. *The European Physical Journal A*, **59**:105, (2023).

[143] Webber, R.C. Tutorial on beam current monitoring. In *Proc. Beam Instrumentation Workshop 2000*, p. 83–104, (AIP Conference Proceedings, 2000).

[144] Caspers, F. Schottky signals for longitudinal and transverse bunched-beam diagnostics. In *Proc. Course on Beam Diagnostics*, p. 407–425, (CERN Accelerator School, 2008).

[145] Nolden, F. Instrumentation And Diagnostics Using Schottky Signals. In *Proc. Fifth European Workshop on Diagnostics and Beam Instrumentation*, p. 6–10, (JACoW, 2001).

[146] Franzke, B., Geissel, H. and Münzenberg, G. Mass and lifetime measurements of exotic nuclei in storage rings. *Mass Spectrometry Reviews*, **27**:428–469, (2008).

[147] Bosch, F., Litvinov, Y.A. and Stöhlker, T. Nuclear physics with unstable ions at storage rings. *Progress in Particle and Nuclear Physics*, **73**:84–140, (2013).

[148] Litvinov, Y.A. *et al.* Nuclear physics experiments with ion storage rings. *Nuclear Instruments and Methods in Physics Research Section B: Beam Interactions with Materials and Atoms*, **317**:603–616, (2013).

[149] Beckert, K., Cocher, S., Franzke, B. and Schaaf, U. The ESR Schottky-Diagnosis-System. In *Proc. EPAC 90: Second European Particle Accelerator Conference*, p. 777–779, (JACoW, 1990).

[150] Sanjari, M.S. *Resonant pickups for non-destructive single-particle detection in heavy-ion storage rings and first experimental results.* PhD thesis, (J.W. Goethe University, 2013).

[151] Nolden, F. *et al.* A fast and sensitive resonant Schottky pick-up for heavy ion storage rings. *Nuclear Instruments and Methods in Physics Research Section A: Accelerators, Spectrometers, Detectors and Associated Equipment*, **659**:69–77, (2011).

[152] Sanjari, M.S. *et al.* A 410 MHz resonant cavity pickup for heavy ion storage rings. *Review of Scientific Instruments*, **91**:083303, (2020).

[153] Trageser, C. *et al.* A new data acquisition system for Schottky signals in atomic physics experiments at GSI's and FAIR's storage rings. *Physica Scripta*, **2015**:014062, (2015).

[154] Klepper, O. *et al.* First steps towards radioactive beams in the experimental storage ring at GSI. *Nuclear Instruments and Methods in Physics Research Section B: Beam Interactions with Materials and Atoms*, **70**:427–433, (1992).

[155] Klepper, O. and Kozhuharov, C. Particle detectors for beam diagnosis and for experiments with stable and radioactive ions in the storage-cooler ring ESR. *AIP Conference Proceedings*, **512**:269–274, (2000).

[156] Klepper, O. and Kozhuharov, C. Particle detectors for beam diagnosis and for experiments with stable and radioactive ions in the storage-cooler ring ESR. *Nuclear Instruments and Methods in Physics Research Section B: Beam Interactions with Materials and Atoms*, **204**:553–556, (2003).

[157] Stelzer, H. Multiwire chambers with a two-stage gas amplification. *Nuclear Instruments and Methods in Physics Research Section A: Accelerators, Spectrometers, Detectors and Associated Equipment*, **310**:103–106, (1991).

[158] Maier, L.W. *Speicherringexperiment zum gebundenen Beta-Zerfall vollständig ionisierter* ^{207}Tl *Kerne*. PhD thesis, (Technischen Universität München, 2007).

[159] Najafi, M. *et al.* CsI–Silicon Particle detector for Heavy ions Orbiting in Storage rings (CsISiPHOS). *Nuclear Instruments and Methods in Physics Research Section A: Accelerators, Spectrometers, Detectors and Associated Equipment*, **836**:1–6, (2016).

[160] Litvinov, Y.A. *et al.* Observation of non-exponential orbital electron capture decays of hydrogen-like 140Pr and 142Pm ions. *Physics Letters B*, **664**:162–168, (2008).

[161] Schmelzer, C. Study of a Variable Energy Heavy Ion Linear Accelerator. In *Proc. 1968 Proton Linear Accelerator Conference*, p. 735–744, (JACoW, 1968).

[162] Blasche, K. and Franczak, B.J. The heavy ion synchrotron SIS. In *Proc. EPAC 92: Third European Particle Accelerator Conference*, p. 9–14, (Editions Frontières, 1992).

[163] Scheidenberger, C. *et al.* Charge states of relativistic heavy ions in matter. *Nuclear Instruments and Methods in Physics Research Section B: Beam Interactions with Materials and Atoms*, **142**:441–462, (1998).

[164] Leckenby, G. *et al.* High-temperature ^{205}Tl decay clarifies ^{205}Pb dating in early Solar System. *Nature*, **634**:321–326, (2024).

[165] Sidhu, R.S. *Measurement of the bound-state beta decay of bare* $^{205}Tl^{81+}$ *ions at the ESR*. PhD thesis, (Heidelberg University, 2021).

[166] Goldhaber, A.S. Statistical models of fragmentation processes. *Physics Letters B*, **53**:306–308, (1974).

[167] Weick, H. *et al.* Energy-loss straggling of (200–1000) MeV/u uranium ions. *Nuclear Instruments and Methods in Physics Research Section B: Beam Interactions with Materials and Atoms*, **193**:1–7, (2002).

[168] Sümmerer, K. and Blank, B. Modified empirical parametrization of fragmentation cross sections. *Physical Review C*, **61**:034607, (2000).

[169] Weick, H. *et al.* Slowing down of relativistic few-electron heavy ions. *Nuclear Instruments and Methods in Physics Research Section B: Beam Interactions with Materials and Atoms*, **164-165**:168–179, (2000).

[170] Leckenby, G. *et al.* Measurement of the bound-state beta decay of 205Tl(81+): intermediate and result data. (Zenodo, 2024).

[171] Pajek, M. and Schuch, R. Radiative recombination of bare ions with low-energy free electrons. *Physical Review A*, **45**:7894–7905, (1992).

[172] Pajek, M. and Schuch, R. Total radiative recombination rates for ions interacting with electrons from an electron cooler. *Nuclear Instruments and Methods in Physics Research Section B: Beam Interactions with Materials and Atoms*, **93**:241–248, (1994).

[173] Kramers, H.A. XCIII. On the theory of X-ray absorption and of the continuous X-ray spectrum. *The London, Edinburgh, and Dublin Philosophical Magazine and Journal of Science*, **46**:836–871, (1923).

[174] Weick, H. Private communication. (2022).

[175] Cox, M.G. and Siebert, B.R.L. The use of a Monte Carlo method for evaluating uncertainty and expanded uncertainty. *Metrologia*, **43**:S178, (2006).

[176] Ogawa, K. and Arita, K. Shell-model study of the first forbidden $^{205}\mathrm{Tl} \rightarrow {}^{205}\mathrm{Pb}$ transition and solar neutrino detection. *Nuclear Instruments and Methods in Physics Research Section A: Accelerators, Spectrometers, Detectors and Associated Equipment*, **271**:280–285, (1988).

[177] Yokoi, K., Takahashi, K. and Arnould, M. The production and survival of ^{205}Pb in stars, and the ^{205}Pb-^{205}Tl *s*-process chronometry. *Astronomy & Astrophysics*, **145**: 339–346, (1985).

[178] Warburton, E.K. First-forbidden β decay in the lead region and mesonic enhancement of the weak axial current. *Physical Review C*, **44**:233–260, (1991).

[179] Braun, E. and Talmi, I. On the β-Transition of ^{205}Tl to ^{205}Pb. In *Proc. Weak and Electromagnetic Interactions in Nuclei*, p. 47–48, (Springer, 1986).

[180] Xiao, Y. and Wang, L.J. Calculations of bound-state beta-decay half-lives of highly ionized $^{163}\mathrm{Dy}^{66+}$, $^{187}\mathrm{Re}^{75+}$, and $^{205}\mathrm{Tl}^{81+}$. *Physical Review C*, **110**:054308, (2024).

[181] Liu, S., Gao, C. and Xu, C. Investigation of bound state β^- decay half-lives of bare atoms. *Physical Review C*, **104**:024304, (2021).

[182] Freedman, M.S. 205Tl as a low energy neutrino detector. In *Proc. Proceedings of Conference on Status and Future of Solar Neutrino Research*, (US Dept. of Energy, 1978).

[183] Bahcall, J.N. Solar neutrino experiments. *Reviews of Modern Physics*, **50**:881–903, (1978).

[184] Takahashi, K. and Yokoi, K. Beta-decay rates of highly ionized heavy atoms in stellar interiors. *Atomic Data and Nuclear Data Tables*, **36**:375–409, (1987).

[185] Pavićević, M.K. *et al.* New data for the geochemical determination of the solar pp-neutrino flux by means of lorandite mineral. *Nuclear Instruments and Methods in Physics Research Section A: Accelerators, Spectrometers, Detectors and Associated Equipment*, **621**:278–285, (2010).

[186] Trueman, T.C.L. *et al.* Galactic Chemical Evolution of Radioactive Isotopes with an *s*-process Contribution. *The Astrophysical Journal*, **924**:10, (2022).

[187] Krause, M.G.H. *et al.* Surround and Squash: the impact of superbubbles on the interstellar medium in Scorpius–Centaurus OB2. *Astronomy & Astrophysics*, **619**: A120, (2018).

[188] Maddalena, R.J., Morris, M., Moskowitz, J. and Thaddeus, P. The Large System of Molecular Clouds in Orion and Monoceros. *The Astrophysical Journal*, **303**:375, (1986).

[189] Lugaro, M. *et al.* Stellar origin of the ^{182}Hf cosmochronometer and the presolar history of solar system matter. *Science*, **345**:650–653, (2014).

[190] Côté, B. *et al.* ^{129}I and ^{247}Cm in meteorites constrain the last astrophysical source of solar *r*-process elements. *Science*, **371**:945–948, (2021).

[191] Dauphas, N. and Chaussidon, M. A Perspective from Extinct Radionuclides on a Young Stellar Object: The Sun and Its Accretion Disk. *Annual Review of Earth and Planetary Sciences*, **39**:351–386, (2011).

[192] Chiera, N.M. *et al.* The ^{146}Sm half-life re-measured: consolidating the chronometer for events in the early Solar System. *Scientific Reports*, **14**:17436, (2024).

[193] Meyer, B.S. and Clayton, D.D. Short-Lived Radioactivities and the Birth of the sun. *Space Science Reviews*, **92**:133–152, (2000).

[194] Huss, G.R., Meyer, B.S., Srinivasan, G., Goswami, J.N. and Sahijpal, S. Stellar sources of the short-lived radionuclides in the early solar system. *Geochimica et Cosmochimica Acta*, **73**:4922–4945, (2009).

[195] Blake, J.B., Lee, T. and Schramm, D.N. Chronometer for S-Process Nucleosynthesis. *Nature Physical Science*, **242**:98–100, (1973).

[196] Blake, J.B. and Schramm, D.N. A consideration of the neutron capture time scale in the *s*-process. *The Astrophysical Journal*, **197**:615–620, (1975).

[197] Martinez-Pinedo, G. Private communication. (2024).

[198] Mowlavi, N., Goriely, S. and Arnould, M. The survival of ^{205}Pb in intermediate-mass AGB stars. *Astronomy & Astrophysics*, **330**:206–214, (1998).

[199] Hardy, J.C. and Towner, I.S. Superallowed $0^+ \to 0^+$ nuclear β decays: 2020 critical survey, with implications for V_{ud} and CKM unitarity. *Physical Review C*, **102**:045501, (2020).

[200] Bambynek, W. *et al.* Orbital electron capture by the nucleus. *Reviews of Modern Physics*, **49**:77–221, (1977).

[201] Mancino, R. Private communication. (2023).

[202] Takahashi, K. and Yokoi, K. Nuclear -decays of highly ionized heavy atoms in stellar interiors. *Nuclear Physics A*, **404**:578–598, (1983).

[203] Caurier, E., Martínez-Pinedo, G., Nowacki, F., Poves, A. and Zuker, A.P. The shell model as a unified view of nuclear structure. *Reviews of Modern Physics*, **77**:427–488, (2005).

[204] Aikawa, M., Arnould, M., Goriely, S., Jorissen, A. and Takahashi, K. BRUSLIB and NETGEN: the Brussels nuclear reaction rate library and nuclear network generator for astrophysics. *Astronomy & Astrophysics*, **441**:1195–1203, (2005).

[205] Goriely, S. Uncertainties in the solar system r-abundance distribution. *Astronomy & Astrophysics*, **342**:881–891, (1999).

[206] Cristallo, S., Straniero, O., Piersanti, L. and Gobrecht, D. Evolution, Nucleosynthesis, and Yields of AGB Stars at Different Metallicities. III. Intermediate-Mass Models, Revised Low-Mass Models, and the pH-FRUITY Interface. *The Astrophysical Journal Supplement Series*, **219**:40, (2015).

[207] KADoNiS: The Karlsruhe Astrophysical Database of Nucleosynthesis in Stars, version 1.0. (Goethe Universität Frankfurt, 2014).

[208] Casanovas-Hoste, A. *et al.* Shedding Light on the Origin of ^{204}Pb, the Heaviest s-Process–Only Isotope in the Solar System. *Physical Review Letters*, **133**:052702, (2024).

[209] Lawson, T.V. *et al.* Radioactive nuclei in the early Solar system: analysis of the 15 isotopes produced by core-collapse supernovae. *Monthly Notices of the Royal Astronomical Society*, **511**:886–902, (2022).

[210] Arnould, M., Paulus, G. and Meynet, G. Short-lived radionuclide production by non-exploding Wolf-Rayet stars. *Astronomy & Astrophysics*, **321**:452–464, (1997).

[211] Arnould, M., Goriely, S. and Meynet, G. The production of short-lived radionuclides by new non-rotating and rotating Wolf-Rayet model stars. *Astronomy & Astrophysics*, **453**:653–659, (2006).

[212] Karakas, A.I. and Lugaro, M. Stellar yields from metal-rich Asymptotic Giant Branch models. *The Astrophysical Journal*, **825**:26, (2016).

[213] Pignatari, M. and Herwig, F. The NuGrid Research Platform: A Comprehensive Simulation Approach for Nuclear Astrophysics. *Nuclear Physics News*, **22**:18–23, (2012).

[214] Paxton, B. *et al.* Modules for Experiments in Stellar Astrophysics (MESA). *The Astrophysical Journal Supplement Series*, **192**:3, (2010).

[215] Battino, U. *et al.* NuGrid stellar data set – III. Updated low-mass AGB models and s-process nucleosynthesis with metallicities Z= 0.01, Z = 0.02, and Z = 0.03. *Monthly Notices of the Royal Astronomical Society*, **489**:1082–1098, (2019).

[216] Vescovi, D., Cristallo, S., Busso, M. and Liu, N. Magnetic-buoyancy-induced mixing in AGB Stars: Presolar SiC Grains. *The Astrophysical Journal Letters*, **897**:L25, (2020).

[217] Vescovi, D., Cristallo, S., Palmerini, S., Abia, C. and Busso, M. Magnetic-buoyancy-induced mixing in AGB stars: Fluorine nucleosynthesis at different metallicities. *Astronomy & Astrophysics*, **652**:A100, (2021).

[218] Leckenby, G. How is ^{205}Pb produced in the thermal pulses of AGB stars? (Youtube, 2024). URL: youtu.be/NYo9oVwcZqE?si=M8h7U2Uu0Z0Umy7S .

[219] Cristallo, S. *et al.* Evolution, Nucleosynthesis, and Yields of low-mass Asymptotic Giant Branch Stars at Different Metallicities. *The Astrophysical Journal*, **696**:797, (2009).

[220] Karakas, A.I. Helium enrichment and carbon-star production in metal-rich populations. *Monthly Notices of the Royal Astronomical Society*, **445**:347–358, (2014).

[221] Höfner, S. and Olofsson, H. Mass loss of stars on the asymptotic giant branch. *The Astronomy & Astrophysics Review*, **26**:1, (2018).

[222] Clayton, D.D. Galactic chemical evolution and nucleocosmochronology - Standard model with terminated infall. *The Astrophysical Journal*, **285**:411–425, (1984).

[223] Clayton, D.D. Galactic Chemical Evolution and Nucleocosmochronology: A Standard Model. In *Nucleosynthesis: Challenges and New Developments*, (eds. Amen, W.D. and Truran, J.W.), p. 65–88, (Univ. of Chicago Press, 1985).

[224] Dauphas, N., Rauscher, T., Marty, B. and Reisberg, L. Short-lived p-nuclides in the early solar system and implications on the nucleosynthetic role of X-ray binaries. *Nuclear Physics A*, **719**:C287–C295, (2003).

[225] Kubryk, M., Prantzos, N. and Athanassoula, E. Evolution of the Milky Way with radial motions of stars and gas - I. The solar neighbourhood and the thin and thick disks. *Astronomy & Astrophysics*, **580**:A126, (2015).

[226] Côté, B., Yagüe, A., Világos, B. and Lugaro, M. Stochastic Chemical Evolution of Radioactive Isotopes with a Monte Carlo Approach. *The Astrophysical Journal*, **887**: 213, (2019).

[227] Wehmeyer, B. *et al.* Inhomogeneous Enrichment of Radioactive Nuclei in the Galaxy: Deposition of Live ^{53}Mn, ^{60}Fe, ^{182}Hf, and ^{244}Pu into Deep-sea Archives. Surfing the Wave? *The Astrophysical Journal*, **944**:121, (2023).

[228] Hotokezaka, K., Piran, T. and Paul, M. Short-lived ^{244}Pu points to compact binary mergers as sites for heavy r-process nucleosynthesis. *Nature Physics*, **11**:1042–1042, (2015).

[229] Beniamini, P. and Hotokezaka, K. Turbulent mixing of r-process elements in the Milky Way. *Monthly Notices of the Royal Astronomical Society*, **496**:1891–1901, (2020).

[230] Huey, J.M. and Kohman, T.P. Search for extinct natural radioactivity of ^{205}Pb via thallium-isotope anomalies in chondrites and lunar soil. *Earth and Planetary Science Letters*, **16**:401–412, (1972).

[231] Nielsen, S.G., Rehkämper, M. and Halliday, A.N. Large thallium isotopic variations in iron meteorites and evidence for lead-205 in the early solar system. *Geochimica et Cosmochimica Acta*, **70**:2643–2657, (2006).

[232] Baker, R.G.A., Schönbächler, M., Rehkämper, M., Williams, H.M. and Halliday, A.N. The thallium isotope composition of carbonaceous chondrites — New evidence for live ^{205}Pb in the early solar system. *Earth and Planetary Science Letters*, **291**: 39–47, (2010).

[233] Andreasen, R. *et al.* Lead-Thallium Chronology of IIAB and IIIAB Iron Meteorites and the Solar System Initial Abundance of Lead-205. In *Proc. 43rd Lunar and Planetary Science Conference*, p. 2902, (Lunar and Planetary Institute, 2012).

[234] Palk, E. *et al.* Variable Tl, Pb, and Cd concentrations and isotope compositions of enstatite and ordinary chondrites—Evidence for volatile element mobilization and decay of extinct ^{205}Pb. *Meteoritics & Planetary Science*, **53**:167–186, (2018).

[235] The ILIMA Collaboration. The ILIMA ring detector for particle identification, life time measurement and beam diagnostics. Technical Design Report, (2017).

[236] Lutz, G. *Semiconductor radiation detectors: device physics.* (Springer, 2007).

[237] Weaver, B.A. and Westphal, A.J. Energy loss of relativistic heavy ions in matter. *Nuclear Instruments and Methods in Physics Research Section B: Beam Interactions with Materials and Atoms*, **187**:285–301, (2002).

[238] Landau, L.D. On the energy loss of fast particles by ionization. *Journal of Physics*, **8**:201–205, (1944).

[239] Vavilov, P.V. Ionization losses of high-energy heavy particles. *Soviet Physics JETP*, **5**:749–751, (1957).

[240] Bardelli, L. *et al.* Influence of crystal-orientation effects on pulse-shape-based identification of heavy-ions stopped in silicon detectors. *Nuclear Instruments and Methods in Physics Research Section A: Accelerators, Spectrometers, Detectors and Associated Equipment*, **605**:353–358, (2009).

[241] Biersack, J.P. and Haggmark, L.G. A Monte Carlo computer program for the transport of energetic ions in amorphous targets. *Nuclear Instruments and Methods*, **174**: 257–269, (1980).

[242] Avset, B.S. and Evensen, L. The effect of metal field plates on multiguard structures with floating p+ guard rings. *Nuclear Instruments and Methods in Physics Research Section A: Accelerators, Spectrometers, Detectors and Associated Equipment*, **377**: 397–403, (1996).

[243] Davinson, T. Private communication. (2021).

[244] Stein, J., Scheuer, F., Gast, W. and Georgiev, A. X-ray detectors with digitized preamplifiers. *Nuclear Instruments and Methods in Physics Research Section B: Beam Interactions with Materials and Atoms*, **113**:141–145, (1996).

[245] Minami, S., Hoffmann, J., Kurz, N. and Ott, W. Design and Implementation of a Data Transfer Protocol Via Optical Fiber. *IEEE Transactions on Nuclear Science*, **58**:1816–1819, (2011).

[246] Adamczewski-Musch, J., Kurz, N. and Linev, S. MBSPEX and PEXORNET—Linux Device Drivers for PCIe Optical Receiver DAQ and Control. *IEEE Transactions on Nuclear Science*, **65**:788–795, (2018).

[247] Leckenby, G., Adamczewski-Musch, J. and Kurz, N. Clazaryn/PLEIADES_FEBEX: TPLEIADES Pre Release. (Zenodo, 2024).

[248] Radeka, V. Trapezoidal filtering of signals from large germanium detectors at high rates. *Nuclear Instruments and Methods*, **99**:525–539, (1972).

[249] Georgiev, A. and Gast, W. Digital pulse processing in high resolution, high throughput, gamma-ray spectroscopy. *IEEE Transactions on Nuclear Science*, **40**:770–779, (1993).

[250] Jordanov, V.T., Knoll, G.F., Huber, A.C. and Pantazis, J.A. Digital techniques for real-time pulse shaping in radiation measurements. *Nuclear Instruments and Methods in Physics Research Section A: Accelerators, Spectrometers, Detectors and Associated Equipment*, **353**:261–264, (1994).

[251] Jordanov, V.T. and Knoll, G.F. Digital synthesis of pulse shapes in real time for high resolution radiation spectroscopy. *Nuclear Instruments and Methods in Physics Research Section A: Accelerators, Spectrometers, Detectors and Associated Equipment*, **345**:337–345, (1994).

[252] Williamson, R. Lecture 6 - Longitudinal Dynamics. In *Proc. Graduate Accelerator Physics Course*, (John Adams Institute for Accelerator Science, 2019).

[253] Dolinskii, A., Valkov, A., Eickhoff, H., Franczak, B. and Franzke, B. Operation of the ESR (GSI, Darmstadt) at the transition energy. In *Proc. EPAC 98: Sixth European Particle Accelerator Conference*, p. 596–598, (JACoW, 1996).

[254] Steinhagen, R.J. Tune and chromaticity diagnostics. In *Proc. Course on Beam Diagnostics*, p. 317–359, (CERN Accelerator School, 2008).

[255] Bisoffi, G., Grieser, M., Jaeschke, E., Krämer, D. and Noda, A. Radiofrequency stacking experiments at the Heidelberg test storage ring. *Nuclear Instruments and Methods in Physics Research Section A: Accelerators, Spectrometers, Detectors and Associated Equipment*, **287**:320–323, (1990).

[256] Tecker, F. Injection and Extraction. (arXiv, 2021).

Appendix A

Storage Ring Dynamics

The basic principles of how the beam behaves in a storage ring were introduced in Section 2.1. This appendix introduces some additional important storage ring dynamics and terminology for a deeper understanding of storage rings.

A.1 Synchrotron oscillations

Storage rings are synchrotron accelerators, and the beam dynamics in storage rings are directly analogous. To accelerate a charged particle, a radiofrequency (RF) potential is applied to the orbiting ions as they pass through an RF cavity with each revolution. If the ion arrives in sync with the RF signal, it will continuously pick up energy from the electric field.[18] If the magnetic rigidity is increased synchronously with the RF signal, the synchronous orbit will gain energy and advance in phase ϕ_s. Near the synchronous orbit, if particles are early, they will see a smaller electric field and will not gain as much phase, whilst if they are late, they will see a larger field and gain more phase. Thus, stable deviations from the synchronous frequency are allowed, highlighted in Figure A.1, and this *phase stability* is a crucial feature of how synchrotrons keep beams together.

The stability of the two sides of the RF signal depend on the sign of η; if $\eta < 0$ then $\phi_s < \pi$ is stable and $\phi_s > \pi$ is unstable, and vice versa. This is a result of how extra energy changes the orbital dynamics, relative to the design orbit, with the velocity increase from γ competing with momentum compaction from γ_t. If we plot the change in energy against the phase, then solutions to the differential equation of motion are shown in Figure A.2 (a full derivation can be found in Edwards & Syphers (2008) [121, p.31]). Oscillations in phase occur around ϕ_s, with some trajectories being bound by the RF potential whilst others diverge. These oscillations around the synchrotron phase are called *synchrotron oscillations*. The boundary between stable oscillation and divergence is called the *separatrix*, and the region of stability is called an *RF bucket*. Figure A.2a shows the RF field and associated RF bucket for $\phi_s = 0$ (i.e. no acceleration), whilst Figure A.2b shows how the separatrix changes for $\phi_s = \pi/6$ (some acceleration).

[18] This also applies to linear accelerators, where an orbit period is replaced by the time between accelerating stations.

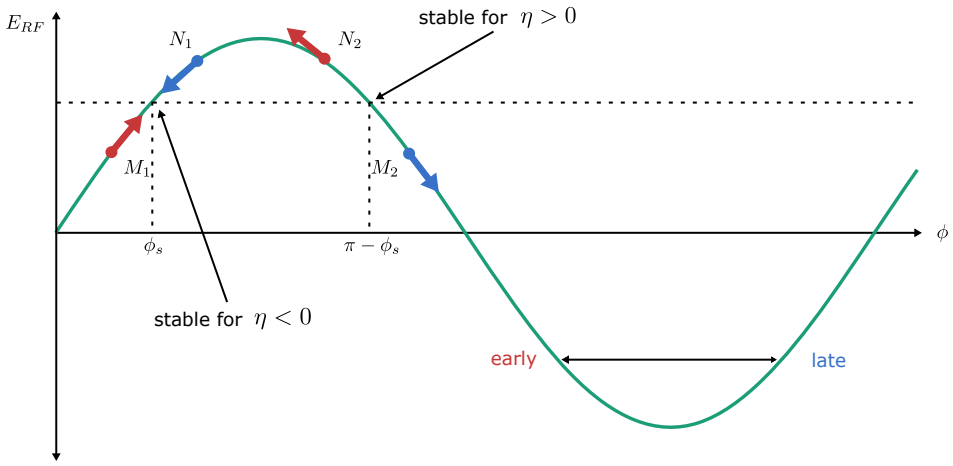

Figure A.1: The phase stability of RF fields is demonstrated. Early particles receive smaller acceleration fields, and vice versa. The point of phase stability depends on the sign of η, since η determines how the orbital frequency changes in response to changes in energy. Figure inspired by Williamson (2019) [252].

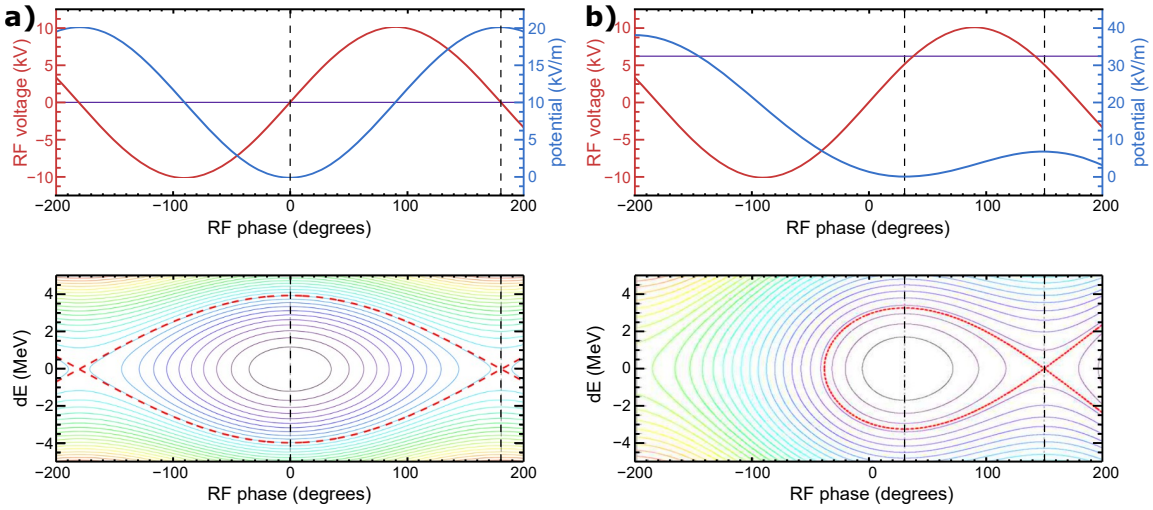

Figure A.2: a) The RF field and potential for $\phi_s = 0$ generates a symmetrical RF bucket. **b)** The RF field and potential for $\phi_s = \pi/6$ generates an asymmetrical potential and smaller RF bucket. Figure reproduced from Williamson (2019) [252].

A.2 Betatron equations of motion

As discussed in Section 2.1.2, betatron oscillations are generated from the strong focusing of the beam when using quadrupole magnets. A simple form of the equations of motion for betatron oscillations can be written down because the focusing and defocusing of the lenses is linear to the first order. In particular, the equations of motion are

$$\begin{aligned} \frac{d^2x}{ds^2} + \left(\frac{1}{\rho^2} + \frac{1}{B\rho}\frac{\partial B_y(s)}{\partial x}\right) x = 0 \\ \frac{d^2y}{ds^2} - \frac{1}{B\rho}\frac{\partial B_y(s)}{\partial x} y = 0, \end{aligned} \tag{A.1}$$

where ρ is the bending radius in the dipoles. These equations of motion both have the form

$$\frac{d^2x}{ds^2} + K(s)\, x = 0, \tag{A.2}$$

where $K(s)$ acts as a "spring constant" that varies around the ring. Since every synchrotron is periodic, often with a period smaller than a full rotation due to the symmetry of the ring, this equation has the form of an homogeneous Hill's equation and thus has the solution

$$x(s) = A\, w(s) \cos\left(\psi(s) + \psi_0\right), \tag{A.3}$$

where $\psi(s)$ is the phase of the pseudo-harmonic betatron oscillation and $w(s)$ is the normalised amplitude function. A schematic of this pseudo-harmonic oscillation is shown in Figure A.3a.

As the ring components are often formulated as matrices, this solution can be formulated as a matrix representing the transformation of the transverse coordinates along the periodic section of the ring C:

$$\begin{bmatrix} x \\ x' \end{bmatrix}_{s_0+C} = \begin{bmatrix} \cos\Delta\psi_C + \alpha\sin\Delta\psi_C & \beta\sin\Delta\psi_C \\ -\gamma\sin\Delta\psi_C & \cos\Delta\psi_C - \alpha\sin\Delta\psi_C \end{bmatrix} \begin{bmatrix} x \\ x' \end{bmatrix}_{s_0}, \tag{A.4}$$

$$\text{where} \quad \beta(s) \equiv \frac{w^2(s)}{k}, \quad \alpha(s) \equiv -\frac{1}{2}\frac{d\beta(s)}{ds}, \quad \gamma \equiv \frac{1+\alpha^2}{\beta}.$$

The parameters α, β, γ are called the *Courant-Snyder parameters*, and they characterise the betatron oscillations. The parameter $\beta(s)$ is called the amplitude function and describes how the amplitude of the beam packet varies throughout the ring [121, p.75]. Thus, each synchrotron (or symmetric sub-component) will have its own set of Courant-Snyder parameters, determined by the optical layout of the lattice, that will determine the exact shape of the betatron oscillations in the ring. The betatron amplitude calculated for both the vertical and horizontal planes of the ESR is shown in Figure A.3.

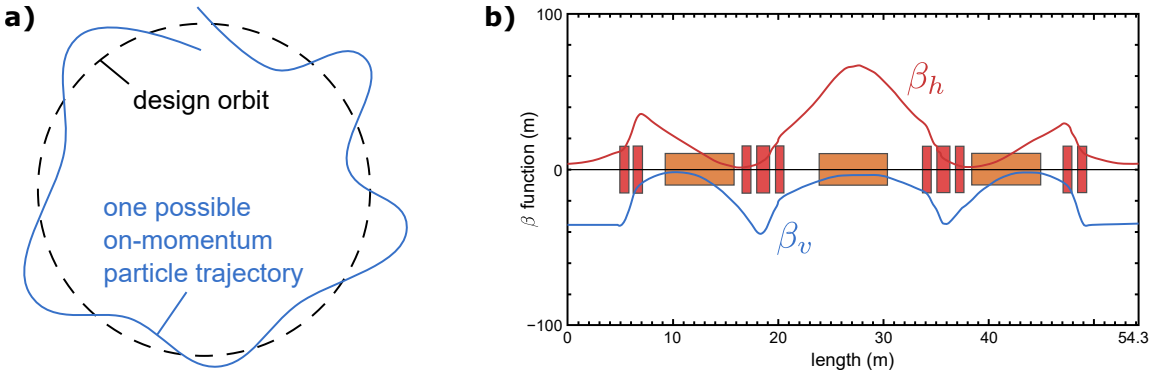

Figure A.3: a) The schematic outline of betatron oscillations around the design orbit. Note that the phase advance is not integer to avoid resonances. **b)** Calculations for the amplitude function $\beta(s)$ are shown for the ESR in isochronous mode, as calculated by Dolinskii *et al.* (1996) [253]. The calculations show the periodic section of the ring, since the north and south halves are identical (see Figure 2.1).

The number of betatron oscillations per revolution through the storage ring, i.e. the frequency of the oscillation in terms of the ideal orbit, is called the *tune* of the ring,

$$Q \equiv \frac{1}{2\pi} \oint \frac{ds}{\beta(s)}. \tag{A.5}$$

The tune of the ring should be such that simple integers or fractions are avoided to prevent resonances that may amplify instabilities, causing beam losses [254]. In particular, this requirement is parameterised by $mQ_x + nQ_y \neq \ell$, where m, n, ℓ are integers and the order of the resonance is given by $m + n$. Note that this equation specifically requires the horizontal and vertical tune to be different to avoid planar coupling.

A.3 Emittance

Now that the Courant-Snyder parameters α, β, γ have been introduced, the emittance ε discussed in Section 2.1.3 can be formally defined:

$$\frac{\varepsilon}{\pi} = \gamma\, x^2 + 2\alpha\, x\, x' + \beta\, x'^2, \tag{A.6}$$

The emittance describes the area of the ellipse in phase space, and thus has units of length $\times$ angle.

Since the emittance is most commonly a Gaussian distribution that has infinite tails, one needs to decide what fraction of the distribution the emittance should enclose. Edwards

& Syphers [121, p.82] derive that for a beam with a standard deviation σ in x, the emittance ε encloses a fraction F related by

$$\varepsilon = -\frac{2\pi\sigma^2}{\beta}\ln(1-F). \tag{A.7}$$

The maximum squeezing of the emittance throughout a betatron oscillation, in both dimensions of phase space, is given by [121, p.83]

$$x_{\max} = \sqrt{\frac{\varepsilon\beta_{\max}}{\pi}} \quad \text{and} \quad x'_{\max} = \sqrt{\frac{\varepsilon\gamma_{\max}}{\pi}}. \tag{A.8}$$

A.4 Momentum dispersion function

In Section 2.1.4, it was observed that momentum spread of the beam also causes transverse deviations, which was identified as momentum dispersion. To solve for this momentum spread, the equation of motion in equation (A.1) needs to be adjusted:

$$\frac{d^2x}{ds^2} + \left(\frac{1}{\rho^2}\frac{2p_0 - p}{p} + \frac{1}{B\rho}\frac{\partial B_y(s)}{\partial x}\frac{p_0}{p}\right)x = \frac{1}{\rho}\frac{\Delta p}{p}, \tag{A.9}$$

where $\Delta p \equiv p - p_0$. This is an inhomogenous Hill's equation, and the solution $D(p, s)$ is called the *dispersion function* of the storage ring. It will introduce some pseudo-harmonic oscillations very similar to the betatron oscillations. In fact, the betatron oscillations, which are the solution to the homogenous Hill's equation, can be included by simply adding the homogenous solution given in equation (A.3) [121, p.87]. Thus, the full transverse equation of motion is

$$x = D\frac{\Delta p}{p} + x_\beta. \tag{A.10}$$

Connecting the dispersion function back to the transition energy, it is now possible to define the *compaction factor* α_p that defines the transition energy:

$$\alpha_p \equiv \frac{1}{\gamma_t^2} = \left\langle \frac{D}{p} \right\rangle. \tag{A.11}$$

The compaction factor relates the change in orbital circumference to the deviation in momentum, $\Delta C/C = \alpha_p \Delta p/p$. The compaction factor is individual to each synchrotron or storage ring, and needs to be chosen carefully as it is difficult to accelerate particles through the transition energy.

The sensitivity of the tune of the ring to the change in momentum spread is called the *chromaticity*, defined by

$$Q^{(n)} \equiv \frac{\partial^{(n)} Q}{\partial \delta}, \tag{A.12}$$

where $\delta \equiv \Delta p/p$ and (n) denotes the order typically listed in prime notation. All strong-focusing accelerators have some level of *natural chromaticity* caused by their dipole and quadrupole elements, but additional chromaticity is introduced by field imperfections. The chromaticity can be reduced with sextupole magnets, that have a focal length that is inversely proportional to the beam axis offset, the opposite of quadrupoles. If the sextupoles are placed at locations where the particles are sorted according to their momenta, then the sextupole strength can be matched to the quadrupole strength such that reasonable momentum dispersion is corrected for.

A.5 Accumulation methods

With the storage ring vocabulary now established, we can better understand the accumulation methods introduced in Section 2.3.2.

The *multiturn injection* method was developed at the Heidelberg Test Storage Ring (TSR), where the transverse acceptance of the storage ring was filled with beam. With each turn, the injected beam moves in phase space due to the non-integer betatron tune. Additionally, special bumper magnets alter the closed orbit at the injection, and then are rapidly decreased to zero (in 300 μs) such that each injection starts with a different betatron amplitude. Over multiple turns, the beam then fills up the full acceptance ellipse of the storage ring. In the procedure described by Bisoffi *et al.* (1990) [255], a factor 40 beam accumulation was achieved in ~ 70 turns by filling the entire transverse acceptance, as shown in Figure A.4a. This process works well if the injected beam already has a low emittance compared to the storage ring acceptance.

The second method commonly used is *RF stacking*. In this case, radiofrequency stability is used to accumulate the beam in the RF buckets. When taking hot fragments from the Fragment Separator (FRS), i.e. with a large emittance from the nuclear reaction in the FRS, the emittance is initially large in the RF bucket but stochastic and electron cooling can condense the beam onto a well-defined stack. Phase space is cleared by tightening the width of the bucket, and a new fragment is injected into the free space [133, 134], as shown in Figure A.4b. Because the beam is stacked in longitudinal phase space using synchrotron oscillations, this is sometimes referred to as *longitudinal stacking*. RF stacking plateaus when the loss mechanisms counterbalance the injection of new beams. The effectiveness of stochastic cooling decreases with the number of stored ions, and electron cooling is limited by beam heating and electron capture losses.

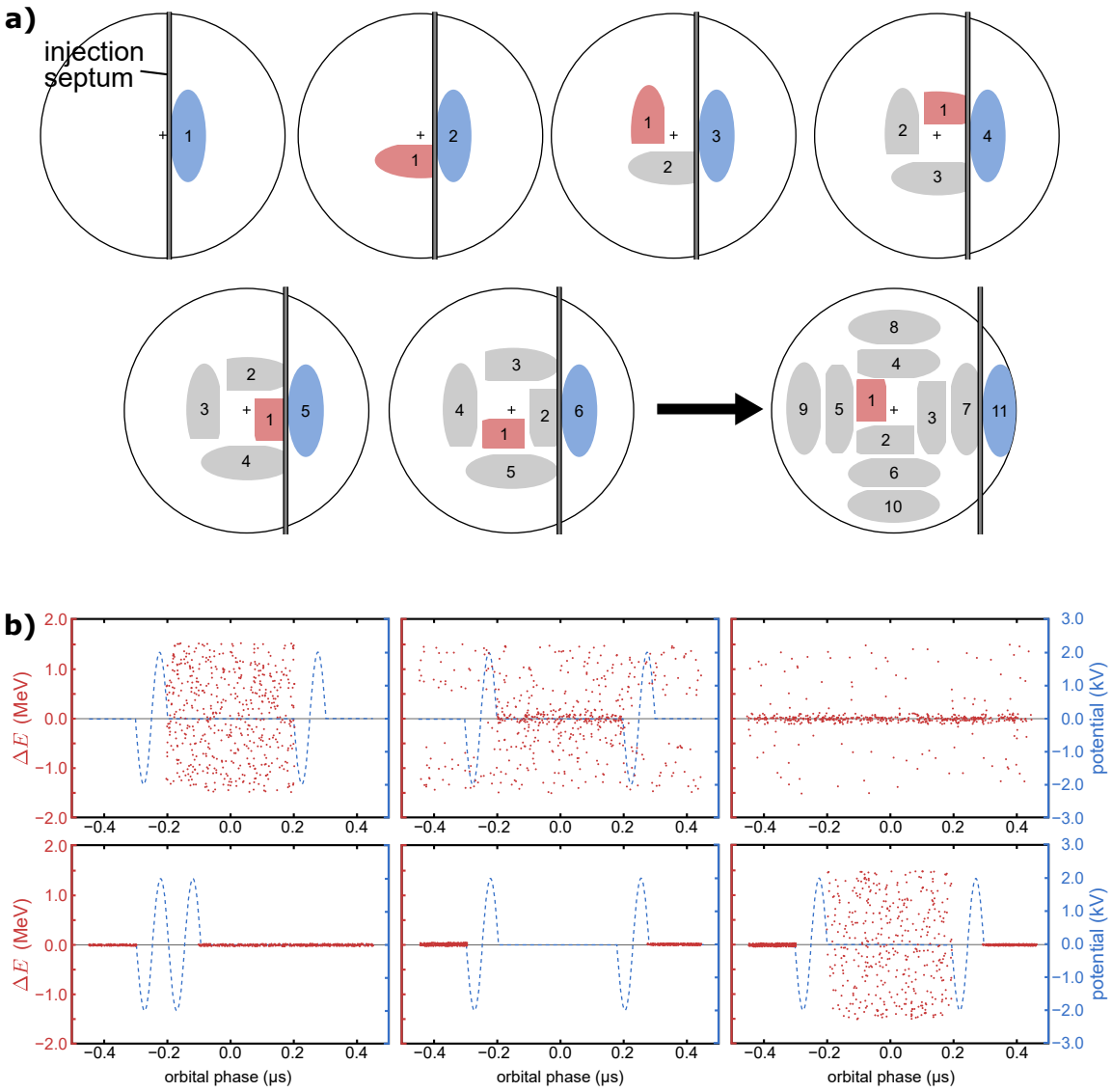

Figure A.4: a) A schematic of the multiturn injection process. If the fractional tune is a quarter, then for each turn a new injection is placed. The placement moves to a larger betatron amplitude as the bumper magnets go to zero. In this way, the phase space can be painted. Figure inspired by Tecker (2019) [256]. **b)** In longitudinal stacking, from left to right: (i) beam is injected, (ii) hot beam debunches, (iii) electron cooling, (iv) barrier buckets are introduced, (v) the buckets squeeze the beam, opening a gap, and (vi) new beam is injected. Figure reproduced from Dimopoulou *et al.* (2007) [133].